Modelling the Transition from Channel-Veins to PSBs in the Early Stage of Fatigue Tests



Yichao Zhu

The Queen's College

University of Oxford

A thesis in preparation for

Doctor of Philosophy

Hilary 2012

To my grandparents, my parents, my girlfriend Xiaoou Yi and all other family members, who have been supporting me for the past 29 years.

Acknowledgements

I would like to thank my supervisor Professor S.J. Chapman for his valuable support and advice. This thesis is completed by following his splendid ideas. I would also like to thank Professor J.R. Ockendon for recommending me to study in Oxford and for many helpful discussions. Additionally, I would like to thank Dr. C.L. Hall for many contributive discussions.

Simultaneously, I would also like to express my sincere gratitude to Prof. Yongji Tan from Fudan University, for his strongly supporting me to pursue a PhD degree in Oxford with great selflessness.

My colleagues, especially Yiming Zhong, Cara Morgan, Gemma Fey, David Hewitt, Sarah Macburnie, Chris Lustri, Alex Shabala, Sofia Piltz and Mohit Dalwadi, have my gratitude both for academic help freely given, and for their friendship.

I would also like to thank my family and friends for their unstinting support and encouragement.

I also gratefully acknowledge the financial support from EPSRC via OxMOS and the Chinese Scholarship Council.

Abstract

Dislocation channel-veins and persistent slip bands (PSBs) are characteristic dislocation configurations that are of interest to both industry and academia. However, existing mathematical models are not adequate to describe the mechanism of the transition between these two states. In this thesis, a series of models are proposed to give a quantitative description to such a transition. The full problem has been considered from two angles.

Firstly, the general motion and instabilities of arbitrary curved dislocations have been studied both analytically and numerically. Then the law of motion and local expansions are used to track the shapes of screw segments moving through channels, which are believed to induce dislocation multiplication by cross-slip.

The second approach has been to investigate the collective behavior of a large number of dislocations, both geometrically necessary and otherwise. The traditional method of multiple scales does not apply well to describe the pile-up of two arrays of dislocations of opposite signs on a pair of neighbouring glide planes in two dimensional space. Certain quantities have to be more accurately defined under the multiple-scale coordinates to capture the much more localised resultant stress caused by these dislocation pairs. Through detailed calculations, one-dimensional dipoles can be homogenised to obtain some insightful results both on a local scale where the dipole pattern is the key diagnostic and on a macroscopic scale on which density variations are of most interest. Equilibria of dislocation dipoles in a two-dimensional regular lattice have been also studied. Some natural transitions between different patterns can be found as a result of geometrical instabilities.

Contents

1 Introduction **1**

1.1 Basic Mathematical Representations 2

1.1.1 Basic Concepts Concerning Discrete Dislocations 2

1.1.2 The Fatigue Tests 14

1.1.3 Review of Previous Continuum and Discrete Models 18

1.2 Mathematical Introduction to Dislocations 21

1.2.1 The 'Force' on a Dislocation 21

1.2.2 Velocities of Dislocations 22

1.2.3 Some Mathematical Representations 23

1.2.4 Stress by Dislocations 24

1.3 The Outline of this Thesis 29

2 Mathematical Modelling of Individual Dislocations **33**

2.1 Self-Induced Dislocation Motion 34

2.1.1 Geometric Parameters for a Dislocation in Three Dimensional Space 34

2.1.2 The Law of Motion 35

2.1.3 The Local Stress Field of a Curvilinear Dislocation 38

2.1.4 Motion of a Curvilinear Dislocation 43

2.2 Linear Stability Analysis 45

2.2.1 Perturbation to a Mixed Dislocation ($b_1 = \mathcal{O}(1)$) 46

2.2.2 Perturbation to an Almost-Screw Dislocation ($b_1 = \mathcal{O}(\epsilon)$) . . . 47

2.2.3 Perturbation to a Screw-Dominant Dislocation ($b_1 = \mathcal{O}(\epsilon^2)$) . 50

2.2.4 A Uniformly Valid Dispersion Relation 52

2.3 Nonlinear Evolution of the Instability 55

2.3.1 Numerical Results 56

2.3.2 Discussion 60

2.3.3 Implication for Non-Schmid Yield Criterion and Non-Associated Flow . . . 61
2.3.4 Spacing and Orientation of Active Slip Planes . . . 62
2.4 Conclusion . . . 62

3 Screw Segments **65**
3.1 Introduction . . . 65
3.2 Travelling Wave Solutions to Screw Segments . . . 67
3.2.1 Governing Equations . . . 68
3.2.2 Shapes of Screw Segments . . . 70
3.2.3 Relating Traveling Wave Solutions to Experiments . . . 74
3.3 Estimation of the Rate of Dislocation Multiplication . . . 77
3.3.1 The Mechanism of Cross-Slip in Fatigue Test . . . 78
3.3.2 Cross-Slip Components . . . 78
3.3.3 Driving Forces on Cross-slip Components . . . 80
3.3.4 Self-Forces on Cross-Slip Components . . . 82
3.3.5 A Criterion for the Completion of Cross-Slip Motion . . . 83
3.4 Fitting Experimental Data into the Model . . . 84
3.4.1 Translation from the Crystallographic Notation to Cartesian System . . . 85
3.4.2 Experimental Parameters . . . 86
3.4.3 Comparisons with Experimental Data . . . 86
3.5 Conclusion . . . 88

4 Homogenisation of One-Dimensional Monopole Arrays **91**
4.1 The Idea of Homogenisation of One-Dimensional Monopoles . . . 91
4.1.1 Unstressed Single Pile-ups . . . 91
4.1.2 Quantities on Different Scales . . . 93
4.1.3 Introduction of the Fast Scale Variable . . . 94
4.1.4 Density Distribution . . . 96
4.2 Homogenisation of a Row of Screw Monopoles . . . 97
4.2.1 Governing Equations . . . 97
4.2.2 Expansions under the Multiple-Scale Coordinates . . . 98
4.2.3 The Leading Order . . . 102
4.3 Homogenisation of a Row of Edge Monopoles . . . 107
4.3.1 Governing Equations . . . 107
4.3.2 Expansions under the Multiple-Scale Coordinates . . . 108

4.3.3 The Leading Order . . . 111
4.4 Comparison of Results of Monopole Pile-ups among Various Method . 114
4.4.1 Analytical Results . . . 114
4.4.2 Numerical Schemes . . . 115
4.4.3 Comparison of Results . . . 115
4.5 Conclusion . . . 116

5 Homogenisation of One Dimensional Arrays of Dipoles 117
5.1 Governing Equations . . . 118
5.2 Multiple Scales and Relevant Expansions . . . 119
5.2.1 Introduction of the Small-Scale Variable . . . 119
5.2.2 Targeting the Negative Dislocations with Multiple Scales . . . 120
5.2.3 The Inner Region . . . 121
5.2.4 Force-Balance Equations . . . 123
5.2.5 The Outer Region . . . 123
5.3 The Leading Order . . . 124
5.3.1 The Inner Region . . . 124
5.3.2 Force Balance . . . 125
5.3.3 The Outer Region . . . 128
5.3.4 Equilibria . . . 129
5.4 The First Order . . . 130
5.4.1 The Inner Region . . . 130
5.4.2 Force Balance . . . 133
5.4.3 Equilibria of Type II . . . 135
5.4.4 Pile-up of Dipoles with Super Small Gap Between Slip Planes 138
5.4.5 Summary . . . 142
5.5 Numerical Results . . . 143
5.5.1 Numerical Scheme . . . 143
5.5.2 Unstressed Dipolar Distribution . . . 143
5.5.3 Equilibria of Type II . . . 143
5.5.4 Pile-up of Dipoles Against Stress Gradient . . . 145
5.6 Analysis of Uniformly Distributed Dipoles . . . 147
5.7 Conclusion . . . 150

6 Two-Dimensional Dipole Patterns and Stability Analysis 153
6.1 Introduction . . . 153
6.2 Unit Square Lattice . . . 154

6.2.1 Equilibria . . . 155
6.2.2 Stability Analysis . . . 159
6.3 Rectangular Lattices . . . 162
6.3.1 Equilibria . . . 163
6.3.2 Stability Analysis . . . 166
6.4 Mechanism of the Formation of PSBs . . . 169
6.4.1 Evolution of Parameters under the Cyclic Loads . . . 169
6.4.2 Formation of Dipole Walls . . . 171
6.5 Comparisons to Experimental Data . . . 173
6.6 Conclusion . . . 174

7 Conclusions and Future Work **175**
7.1 Conclusion . . . 175
7.2 Further Work . . . 176
7.2.1 The Mechanism of Cross-slip Motions . . . 176
7.2.2 Density Distribution of Dipoles Throughout Two Dimensional Space . . . 177
7.2.3 Elements in Walls of PSBs . . . 178

A **179**
A.1 Derivation of (1.17) . . . 179
A.2 Proof of $\boldsymbol{\chi}$ satisfying (1.49) . . . 179
A.3 Derivation of equation (2.26) . . . 180
A.4 Derivation of equation (2.46) . . . 180
A.5 Derivation of the dispersion relation of (2.53) . . . 181
A.6 Derivation of (2.64) . . . 182
A.7 Proof of (4.52) . . . 182
A.8 Proof of (4.107) . . . 184
A.9 Derivation of (4.123) . . . 185
A.10 The Calculation of χ_F . . . 186
A.11 Proof of (6.8) . . . 189

Appendices **179**

Bibliography **191**

List of Figures

1.1 (a) A space lattice, (b) an fcc crystal with cubic unit-cell vectors $\boldsymbol{a}_i$ and primitive unit-cell vector $\boldsymbol{a}_i'$. 2

1.2 Deformation: for a point $\boldsymbol{x}$ in a three-dimensional body Ω_x, if it undergoes some continuous deformation, the mass at $\boldsymbol{x}$ in the reference configuration is moved to $\boldsymbol{y}(\boldsymbol{x})$ in the deformed body Ω_y. 4

1.3 The configuration of a dislocation at the atomistic level: if a column of atoms, starting from the third row, are removed, then an edge dislocation is created. 6

1.4 Definition of Burger vector $\boldsymbol{b}$ by FS/RH convention 7

1.5 Dislocations can be created through cut-and-weld operation. 8

1.6 Dislocation motions at the atomistic level: (a) starting with an edge dislocation, (b) an external stress pushes the atoms at the bottoms to realign with their neighbouring columns, (c) if the realignment finishes, the dislocation is moved an atomic spacing to the right, (d) as the dislocation glides away, the atoms restore to a regular pattern. . . . 10

1.7 The Frank-Read source: AB is a segment of a dislocation with two ends pinned by an unspecified barrier. When a stress $\boldsymbol{\sigma}$ is applied, the original segment bows out in response. At some stage two parts of the same dislocation (the green curve) are so close that they meet and form a single large loop together with the original segment AB (the yellow curve). 11

1.8 Double cross-slip source: (a) dislocation loop in its glide plane; (b) it moves to the adjacent of its glide plane M and cross slip plane N; (c) it does the cross slip motion; (d) it moves back to the original glide plane [33]. 11

1.9 Diagrams for a prismatic loop 12

1.10 Vacancies and interstitials: a vacancy corresponds to a missing atom; an interstitial is an excessive atom from the perfect lattice structure. 13

1.11 Formation of dislocation dipoles at the atomistic level: when two dislocation of opposite signs glide towards each other, they are likely to be bound together which has the minimum energy state, leaving an interstitial or vacancy site between the them. Outside two dislocations are all perfect lattice. According to [6], in the state of stress free, the line that connects two dislocations should form an angle of 45° with the glide plane. 14

1.12 Experimental equipment: a specimen (copper) undergoes push-pull at two ends by a control of stress or strain, which cyclically satisfies a fully reversed sine wave (abstracted from [2]). 15

1.13 Channel-vein structures: if the plastic strain amplitude $\gamma <\sim 10^{-4}$, the saturation stress grows with the plastic strain amplitude. A schematic plot of the material microstructure is drawn in the middle circle at the same angle as in the image in the right hand side by using the ECCI technique. It can be observed that most dislocations are of straight edge type, which take a 'vein structure'. These veins are surrounded by 'channels', there are mainly screw segments connecting edge dislocations in different veins. It is noted that dislocations correspond to the dark region in the image by using the ECCI technique (abstracted from [2]). 16

1.14 Persistent slip band (PSB) structure: the dislocations start to change their group pattern significantly by forming a ladder shape structure known as a PSB (abstracted from [2]). 17

1.15 PSBs observed in fatigue tests. This time, the light regions correspond to dislocations (abstracted from [2]). 17

1.16 An element of dislocation line d$\boldsymbol{l}$ sweeps out an area d$\boldsymbol{S}$ by moving a distance $\delta\boldsymbol{r}$. 21

1.17 Outline of the thesis. 30

2.1 Geometric parameters of a single dislocation: two most representative dislocations are sketched here. $\boldsymbol{l}$, $\boldsymbol{n}$, $\boldsymbol{m}$ and $\boldsymbol{\beta}$ are the dislocation tangent, normal, binormal and normal to its glide plane, respectively. $\boldsymbol{\rho}$ is the direction of the edge component at $\boldsymbol{x}(s)$. 35

2.2 The rescaled maximum growth rate $\Re(\hat{\lambda})_{\max}$ as a function of $\bar{b}_1/b$ and $\sigma_{23}^2/\sigma_{13}^2$. The dislocation is unstable in the region below the solid white curve. The maximum growth rate is 0.18 and occurs for $\sigma_{23} = 0$, $\bar{b}_1/b \approx 0.981$ with a corresponding wavenumber $\hat{k} \approx 0.54$. 49
2.3 The maximum growth rate as a function of $\tilde{b}_1/b$. The solid curve corresponds to $\sigma_{23}/\sigma_{13} = 1$, $\sigma_{33}/\sigma_{13} = 2$; the dashed curve corresponds to $\sigma_{23}/\sigma_{13} = 1$, $\sigma_{33}/\sigma_{13} = -2$; the dotted curve corresponds to $\sigma_{23}/\sigma_{13} = 4$, $\sigma_{33}/\sigma_{13} = -2$; the dash-dotted curve corresponds to $\sigma_{23}/\sigma_{13} = 4$, $\sigma_{33}/\sigma_{13} = 2$. The dislocation is always unstable for $\tilde{b}_1$ small. For large $\tilde{b}_1$ it is stable if and only if $\sigma_{23}/\sigma_{13} \geq \sqrt{8}$. Even when the dislocation is unstable for small and large $\tilde{b}_1$ there may be a region of stability at moderate $\tilde{b}_1$ depending on the relative size and signs of σ_{13}, σ_{23} and σ_{33}. 52
2.4 The maximum growth rate as a function of $\bar{b}_1$ for various combinations of applied stress. The solid curve corresponds to $\sigma_{23}/\sigma_{13} = 1$, $\sigma_{33}/\sigma_{13} = 4$; the dashed curve corresponds to $\sigma_{23}/\sigma_{13} = 4$, $\sigma_{33}/\sigma_{13} = 1$; the dotted curve corresponds to $\sigma_{23}/\sigma_{13} = 1$, $\sigma_{33}/\sigma_{13} = 1$; the dash-dotted curve corresponds to $\sigma_{23}/\sigma_{13} = -1$, $\sigma_{33}/\sigma_{13} = -1$. For all plots $\epsilon = 0.01$. . . 54
2.5 Non-linear evolution of a perturbed rectilinear dislocation. (a) three-dimensional view; (b) projection onto the x_1-x_2 plane; (c) projection onto the x_1-x_3 plane; (d) projection to the x_2-x_3 plane. The only nonzero component of the external stress is $\sigma_{13} = 1$. 56
2.6 The left plot gives the proportion of velocity in $\boldsymbol{\beta}$ (normal to the glide plane) direction against the spatial parameter z, showing that most parts of the dislocation do in-plane motion. The right plot depicts the proportion of screw segment at every point parameterized by z, showing that the edge components grow when evolving. 57
2.7 Glide plane family: dislocation segments sharing the same d reside in one glide plane. Most dislocation segments will evolve to a family of mutually parallel glide planes. 58
2.8 Evolution of the dislocation when $\sigma_{13} = 5$. (a) 3-D plot for the evolution; (b) projection onto the x_1-x_2 plane (c) projection onto the x_1-x_3 plane; (d) projection onto the x_2-x_3 plane. 59
2.9 (a) shows that the dislocation will evolve to a family of glide planes; (b) draws the magnitude of the velocity at each point. 59
2.10 Schematic diagram of the nonlinear evolution. 60

2.11 Comparison with the theoretical results: the curve is drawn from (2.65), the diamonds are from the simulation 62

3.1 A screw segment is a mixed dislocation, which connects two edge dislocations from different veins. When an external stress $\boldsymbol{\sigma}$ is applied, it moves in the channels in response. Its motion can be formulated by travelling waves with a speed u_0. In this way, the evolution of the curve can be written as $(x(\theta) + u_0 t, y(\theta))$, where θ is the angle between its tangent and x-axis. Here d is the width of the screw segment; $\boldsymbol{b}$ is the Burgers vector. 66

3.2 A proposed mechanism of dislocation multiplication in the early stage of fatigue: (a) A screw segment is moving in response to the cyclic applied stress in its primary slip plane. (b) Since the tip of the segment is purely a screw character, it may initiate a cross-slip motion induced by some unspecified sources. If such sources are strong enough, the screw segment will cross-slip to another slip plane. (c) The screw segment may move back to another slip plane, which is parallel to the original one to create a double cross-slip configuration. (d) As the cyclic load proceeds, the stress is reversed, which may trigger another cross-slip motion to bring the dislocation back to its original primary slip plane. According to the anisotropic nature of dislocations (most motion is restricted in their slip planes), the cross-slip-back motion does not follow the same path. Such irreversibility then leaves two prismatic loops in veins. 67

3.3 Schematic plots for screw segments when $U^2 < 1$: when $-1 < U < 0$, it is an external driven motion; when $0 < U < 1$, it is a self-driven motion. ν here is taken to be 0.3. 72

3.4 The schematic diagrams for screw segments when $U^2 > 1$: when $U > 1$, it is self-driven motion; when $U < -1$, rather than joining tangentially to two edge dislocations in veins, the travelling wave will shoot to infinity at an angle $-\arcsin(1/U)$. 73

3.5 D is uniquely determined by U. 76

3.6 For fixed $d = 10^4$, the greater σ_{23} is, the more proportion of screw components a screw segment has. 77

3.7 Mechanism of the initiation of a cross-slip motion: if applied an anti-plane stress σ_{12} by some unspecified sources, the tip of the screw segment will be pushed out of its glide plane. The cross slip component then will generate a self stress σ_s to impede the cross slip motion. . . 78
3.8 Cross-slip components under various σ_{23}: the thick blue curves are the cross-slip components, where d is fixed to be 10^4. 80
3.9 For fixed $d = 10^4$, the fraction of the width of the cross-slip component over that of its corresponding screw segment grows with an increasing σ_{23}. ξ is the critical cross-slip angle defined in (3.40). 80
3.10 Cross-slip components: when applied an anti-plane stress component σ_{12} in addition to σ_{23}, the cross-slip component will start its motion in the plane that resolves both σ_{12} and σ_{23}. In this case, the new glide plan M_2 is normal to $(-k, 0, 1)$. For simplification, the cross-slip component is assumed to be in arc shape of radius cutting AB throughout the whole process. 81
3.11 Cross-slip in a cycle: the space spanned two most crucial experimental parameters, σ_{23} and d can be separated by $D^* = d\sigma_{23}$ which corresponds to the blue curve. Only when (σ_{23}, d) is on the left hand of the curve, the cross-slip occurs. Within a cycle, the width of a channel is fixed. When σ_{23} is small, the screw segment will propagate in its primary slip plane as a travelling wave until the stress exceeds the critical value (when the arrow hits the curve). Then the cross-slip starts and part of the screw segment moves in the cross-slip plane. After reaching the stress amplitude resolved in the primary plane, denoted by $\sigma_{23}^{\max}$ (the blue curve), σ_{23} is reversed. When σ_{23} is not big enough to keep the cross-slip motion (when the arrow hits the curve again), the cross-slip component will start their motion in a slip plane parallel to its original glide plane. 85
3.12 Dislocation multiplication under cyclic loads: for a given stress amplitude, the dots the width of screw segment after n-th cycle. of cross-slip motion derived from (3.55). It can be seen that the screw segment will keep cross-slipping until the dot falls below the dashed curve, which is the minimum distance required for the occurrence. 89

4.1 Quantities of different scales: when observation is made at a macroscopic level, say, $\mathcal{O}(1)$ by scale, the dislocations are so close to each other that they can be treated as continuously distributed. At this level, people are interested in the quantities, such as dislocation density. Isolated dislocations cannot be seen unless the observation is made at a microscopic level, i.e. $\mathcal{O}(\epsilon)$ by scale. 93

4.2 Correlation between $\bar{x}$ and x: in the $(\bar{x}, X)$ space, the problem is actually being looked at along the curve $X = B(\bar{x})/\epsilon$. In each cell, which is an orange box, the variation in $\bar{x}$ is at $\mathcal{O}(\epsilon)$ while that in X is $\mathcal{O}(1)$. The evolution in x can be expressed as a superposition of that in $\bar{x}$ and X as depicted in the right hand side. Since the derivatives with respect to $\bar{x}$ and X are not in the same scale, we can treat them independently throughout the calculation. However, as we will see later, when we evaluate at some specific point, the correlation between $\bar{x}$ and X has to be considered. 95

4.3 The inner and outer region: if the observation is made near the dislocation array, where $y \sim \mathcal{O}(\epsilon)$, we are in the inner region, where dislocations look discretely; if the observation is made away from the array, where $y \sim \mathcal{O}(1)$, we are in the outer region, where dislocations look continuously distributed. 99

4.4 Comparison of densities obtained by different methods: The grey bars are drawn by the counting method within each small interval $(x - \Delta x, x + \Delta x)$; the curve is drawn by the result in (4.126) from the multiple-scale calculation; the diamonds depict $2/(N(p_k - p_{k-1}))$ against p_k. For the full problem, we use the numerical scheme in §4.4.2 with $N = 50$. 116

5.1 A row of dislocation pairs: it composes of two arrays of dislocation monopoles with opposite signs. The spacing between two glide planes is $s \sim \mathcal{O}(\epsilon)$. Each positive dislocation is located at $(p_k, 0)$, $k \in \mathbb{Z}$ and $0 \leq k < N$; each negative dislocation is located at (q_k, s). 118

5.2 Dipoles with super small gap between slip planes. 138

5.3 Comparison of unstressed dipole distribution of Type II between results from the multiple-scale method and numerics: (a) $\rho^{\text{num}} = 1/(p_k - p_{k-1})$, while the green curve is the density predicted by the method using multiple scales, which suggests $\rho^{t2} = N/(L_2 - L_1)$. (b) The diamonds are the horizon spacing within dislocation pairs. their corresponding theoretical values by the method of multiple scales are all 1/2. Throughout the simulation, $N = 101$, $s = 0.5$, $L_1 = -50$ and $L_2 = 50$. 144

5.4 Dipolar arrangement of Type II: $N = 101$, $s = 0.5$. 144

5.5 Comparison between numerical and theoretical results of density as well as $q_i - p_i$ of Type III: $N = 101$, $s = 0.1$ $L_1 = -50$ and $L_2 = 50$. 145

5.6 Dipole arrangement of Type III: $N = 101$, $s = 0.1$ 145

5.7 Dipole Pile-up Against Stress Gradient of Type II: $s = 0.2$, $\phi = 0.2$, N = 50. 146

5.8 Dipole Pile-up Against Stress Gradient of Type III: $\phi = 0.2$, N = 50. 146

5.9 Dipole pile-up against stress gradient of mixed type: near the lock, it is of Type II. As ρ decreases such that (5.137) holds, the system shift to Type III. The horizontal dash-dot line is where $\rho s = 0.2456$. Here $S = 0.08$ and $\phi = 0.2$. 148

5.10 Uniformly distributed dipoles: the solid curves are sets of (Q, S) such that the system is in equilibrium under an external stress σ_{ext}, which are correspondingly indicated on the curve. The diamonds denote (Q, S) for some specific equilibrium states. We can also see that for a given σ_{ext}, there exists a maximum S_c, such that all $S \leq S_c$. Finally, the two dashed curves are the boundaries between stable and unstable regions. Here ρ is set to be 1. 149

5.11 The maximum spacing S_c to retain dipoles under σ_{ext}. 150

5.12 When the external stress σ_{ext} is too large, the dislocations will recombine to form new dipoles, giving rise to the pile-ups of monopoles at both ends. Here in the simulation, $S = 0.4$ and $\sigma_{\text{ext}} = 0.4$. 150

6.1 Rectangular Lattice: the infinite region is divided by identical rectangle of size $\alpha \times \beta$. In each lattice, there two dislocations of opposite signs. Their mutual horizontal and vertical spacing are set to be Q and S, respectively. 154

6.2 Two dimensional monopoles: solving (6.7) is equivalent to finding the zero contour of $\sigma_{12}^{+}(X, Y)$ defined in (6.6). There are two ways to estimate $\sigma_{12}^{+}(X, Y)$. One way is to treat these monopoles as a collection of one-dimensional walls, then σ_{12}^{+} can be estimated as a sum of shear stress by these walls. The other way, vice versa, is to estimate σ_{12}^{+} by a sum of stress component by monopole rows. 156

6.3 Zero contour of σ_{12}^{+}: three types of equilibrium can be spotted. Type I and II correspond to the cases when Q is 0 and 1/2, respectively. These two types of equilibria exist regardless the value of S; Type III exists only when the mutual spacing between glide planes of dipoles is less than a critical value S^*, marked as the black dot. In this case, $S^* = 0.2170$. Also, the lattice patterns of some equilibrium states are sketched on top of their corresponding (Q, S). 158

6.4 Equilibrium pattern in two-dimensional unit lattice. 159

6.5 Idea of the stability analysis to equilibrium states: A set of periodically distributed positive monopoles exert a stress field such that $\sigma_{12}^{+}(X, Y) > 0$ in the green regions and $\sigma_{12}^{+}(X, Y) < 0$ in the white regions. The equilibrium states correspond to the boundaries that separate a green and a white region. A negative dislocation in this system will be pushed to the left in green regions and to the right in white regions This suggests that only equilibrium states that correspond to boundaries with white region on the left are stable. 160

6.6 Stabilities for the equilibria in unit lattices: for Type I, it is always unstable. For Type II, it is conditionally stable. The most stable configuration of this type arises when $S = 0.5$. When $S < S^*$(the black dot), Type III occurs. In this case, a dislocation will be coupled with one of its neighbouring opposite counterpart to form a pair of dipole. Another key observation can be made from Fig. 6.6 is that for any given S, there exists only one stable state. When $S > S^*$, it is of Type II; when $S < S^*$, the stable system bifurcates to Type III. . . . 161

6.7 Shear stress field by two dimensional dipoles in one cell: in the first plot, the stress is exerted by the Taylor Lattice of equilibrium Type II, where two dislocations are at $(0, 0)$ and $(1/2, 1/2)$, respectively; in the second plot, the dislocations are located at $(0, 0)$ and $(0.1, 0.1)$. The shear stress is localised between two dislocations, which gives rise to a stress free region away from the dipole. 163

6.8 Zero-contour of σ_{12}^{+} in $\hat{X}$-$\hat{Y}$ space: still three types of equilibria can be observed. 165
6.9 $\hat{S}^*$ against λ: $\hat{S}^*$ has an upper limit of 0.25. On the other hand, as $\lambda \to 0$, the system is equivalent to the case of one-dimensional array of dipoles. The slope at the origin is the critical value S^*. 166
6.10 Stability in rectangular lattices. 168
6.11 Comparison of stability under different combinations of β and S. . . 169
6.12 A simplified example of how dislocation multiplication influence the lattice stability: suppose S is a constant, then a surface can be drawn for f_r in $1/\alpha$-β space. Each point in the surface, satisfies $f_r = f_r(Q, S, \alpha, \beta)$. As the cyclic load proceeds, a paths in the parameter space is chosen by the process of dislocation multiplication. Then how f_r varies with the process can be identified on the surface. 170
6.13 Evolution into the instability as cyclic loads proceed: in (a), we start with $\rho_0 = 1$, and draw the evolution under different u_ρ; in (b), we start with different ρ_0, and draw the evolution under $u_\rho = 0.01$. Here, $\beta = 3 - 0.02t$ and $S = 1 - 0.01t$. 171
6.14 Mechanism of the formation of PSBs: In stage I, dislocations are sparsely distributed in veins of equilibrium Type II. As the cyclic loads proceed, the dislocations are multiplied. The result is a gradual reduction of β and S, accompanying with an increased density ρ. Such process raise the value of f_r, giving rise to a weakening of the stability of Type II. When the density rises to a critical value ρ^*, f_r reaches 0. Positive dislocations start to lock with negative dislocations to form dipole, and the system transits to equilibrium of Type III. In stage II, further dislocation multiplication will result in the cancelation of dislocations, leaving a row of dipole walls. 172
6.15 Parameters of PSBs. 173
6.16 PSB configuration predicted from our model. 174

7.1 Outline of the thesis. 175

Chapter 1

Introduction

Dislocation channel-veins and persistent slip bands (PSBs) are characteristic dislocation configurations that are of interest to both industry and academia. However, existing mathematical models are not adequate to describe the mechanism of the transition between these two states. The aim of this project is to develop a convincing model for these structures that is consistent with the experimental results obtained by Ahmed et al [3]. In order to achieve this aim, it is first essential to investigate both the motion of a single curved dislocation and the collective interaction of large numbers of dislocations. The detailed analysis of these two problems given in the early chapters of this thesis forms the foundation for the description of channel-veins and PSBs.

In this chapter, the aims of the present work are discussed in greater detail. Firstly we introduce several important concepts concerning dislocations, such as dislocation dynamics and mechanisms of dislocation creation. This is followed by a survey of previous discrete and continuum models of dislocation behaviour. Using the basic theory of linear elasticity, the stress fields of isolated straight dislocations are obtained, and the idea of incompatibility is introduced. After the introduction of generalised stress functions, which are analogous to vector potentials in electromagnetism, the stress distribution for a curved dislocation (the Peach-Koehler formula) is derived. At the end of Chapter 1, we give the outline of this thesis.

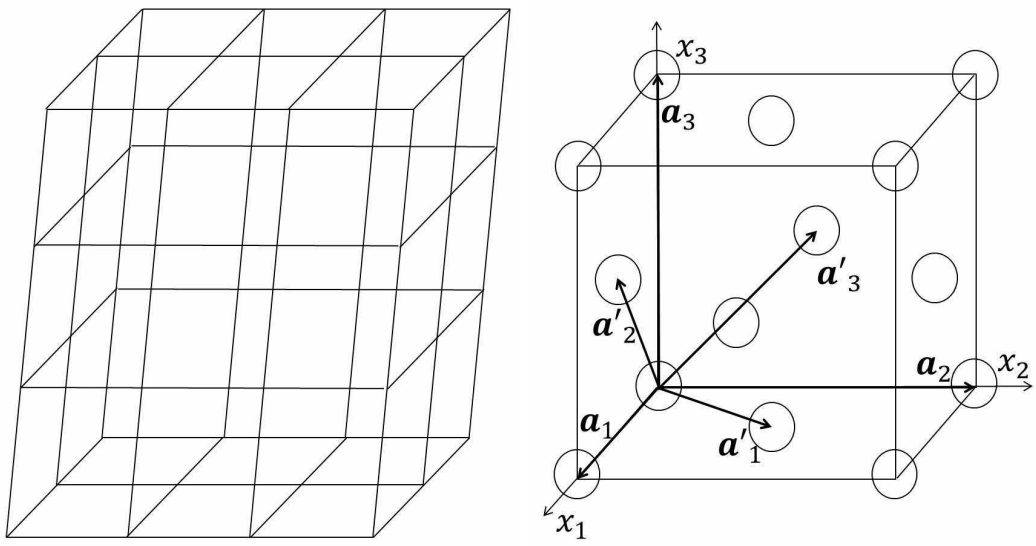
1.1 Basic Mathematical Representations

1.1.1 Basic Concepts Concerning Discrete Dislocations

Crystallinity of Metals

Dislocations are an important class of defects in crystalline solids, so an elementary understanding of crystallinity is required before dislocations can be introduced. Metals and many important classes of non-metallic solids are crystalline, i.e. the constituent atoms are arranged in a pattern that repeats itself periodically in three dimensions.

The arrangement of atoms in a crystal can be described with respect to a three-dimensional net formed by three sets of straight, parallel lines as shown in Fig. 1.1(a). The lines divide space into uniform parallelepipeds and the points at the intersection of the lines define a space lattice. Each parallelepiped is called a unit cell and the crystal is constructed by stacking identical unit cells face to face in perfect alignment in three dimensions.



(a) (b)

Figure 1.1: (a) A space lattice, (b) an fcc crystal with cubic unit-cell vectors $\boldsymbol{a}_i$ and primitive unit-cell vector $\boldsymbol{a}'_i$.

Here, we follow the crystallographic notation described in [33]. Every crystal lattice can be generated by the translation of a lattice point by multiples of three non-coplanar translation vectors $\boldsymbol{a}_1$, $\boldsymbol{a}_2$ and $\boldsymbol{a}_3$ as shown in Fig. 1.1(b). The lattice points

coincide with atoms in simple crystals such as fcc (face-centered cubic), or with groups of atoms in crystals with a basis, such as hcp (hexagonal close-packed). The direction notation $[n_1 n_2 n_3]$ represents the vector $n_1\boldsymbol{a}_1 + n_2\boldsymbol{a}_2 + n_3\boldsymbol{a}_3$, where n_i are integers. A bar on top of n_i means $-n_i$. A plane with Miller indices $(m_1 m_2 m_3)$ is parallel to a plane cutting the axes at $1/m_1$, $1/m_2$, $1/m_3$, where the m_i are integers. It can be proved that in the cubic system, a plane $(m_1 m_2 m_3)$ is normal to a direction $[m_1 m_2 m_3]$. The notation $< n_1 n_2 n_3 >$ represents the set that includes all $[k_1 k_2 k_3]$, where $k_i = \pm n_i$ and all possible permutation of $[k_1 k_2 k_3]$. For example, $< 100 >$ is the set that contains $[100]$, $[\bar{1}00]$, $[010]$, $[0\bar{1}0]$, $[001]$ and $[00\bar{1}]$. In the same sense, $\{n_1 n_2 n_3\}$ is defined to be the equivalent set for planes of the type $(n_1 n_2 n_3)$.

In this thesis, we mainly focus on crystals that have cubic cells, such as fcc and bcc (body-centered cubic) detailed in [35]. Thus the orthogonal vectors $\boldsymbol{a}_i$, $i = 1, 2, 3$, with equal magnitudes as shown in Fig. 1.1(b), are used to generate a unit cell. A primitive vector represents the vector translations from one atom centre to its nearest-neighbour atom centres. For example, the primitive vectors in Fig. 1.1(b) are $\boldsymbol{a}_i'$. In general, the primitive vectors in fcc are of type $\frac{1}{2} < 110 >$ and in bcc are of type $\frac{1}{2} < 111 >$. In crystals, the slip is most likely to happen along the primitive vector.

Preliminary Knowledge of the Linear Elasticity

Some basic concepts in the theory of linear elasticity are also required. As shown in Fig. 1.2, for a point $\boldsymbol{x}$ in a three-dimensional body Ω_x, undergoing some continuous deformation, the mass at $\boldsymbol{x}$ in the reference configuration is moved to $\boldsymbol{y}(\boldsymbol{x})$ in the deformed body Ω_y. Note that, throughout this thesis, bold symbols denote vectors except for $\boldsymbol{\sigma}$, the stress tensor, which will be introduced later in this chapter.

The displacement of the mass originally at $\boldsymbol{x}$ is defined to be

$$\boldsymbol{u}(\boldsymbol{x}) = \boldsymbol{y}(\boldsymbol{x}) - \boldsymbol{x}. \tag{1.1}$$

We will consider only linear elasticity in this thesis, in which the displacement $\boldsymbol{u}$ is taken to be infinitesimally compared to the scale of $\boldsymbol{x}$. Taking the gradient with respect to $\boldsymbol{x}$ of each of the components of $\boldsymbol{u}$ gives a matrix:

$$(\nabla \otimes \boldsymbol{u})_{ij} = u_{i,j} = \frac{\partial u_i}{\partial x_j}.$$

All indices will take the values 1, 2 and 3, unless otherwise stated.

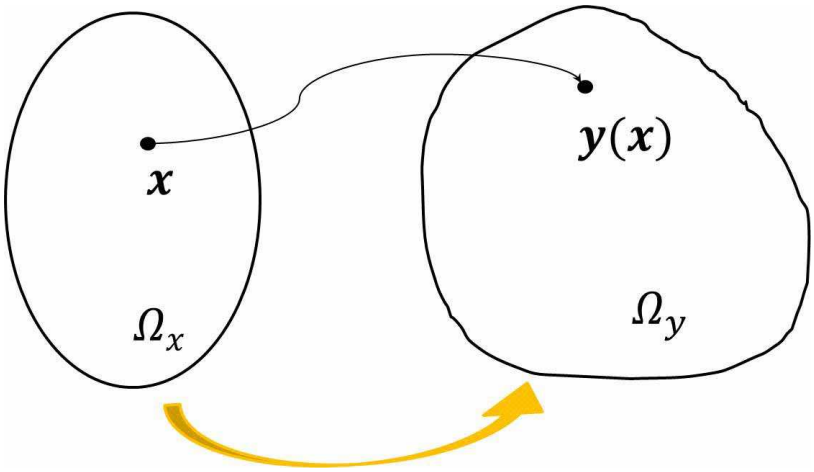


Figure 1.2: Deformation: for a point $\boldsymbol{x}$ in a three-dimensional body Ω_x, if it undergoes some continuous deformation, the mass at $\boldsymbol{x}$ in the reference configuration is moved to $\boldsymbol{y}(\boldsymbol{x})$ in the deformed body Ω_y.

Then a second order strain tensor

$$\mathcal{E} = \frac{1}{2}\left((\nabla \otimes \boldsymbol{u}) + (\nabla \otimes \boldsymbol{u})^T\right) \tag{1.2}$$

can be defined, wherever single-valued differentiable displacements $\boldsymbol{u}$ exist; "T" stands for the transpose of. The condition for the existence of such a single-valued displacement is known as the compatibility equation

$$\nabla^T \wedge \nabla \wedge \mathcal{E} = \mathbf{0}, \tag{1.3}$$

where '$\nabla\wedge$' denotes the row curl, that is, we treat each row of the 2nd order tensors as a vector, and take curl on them to obtain a new second order tensor; the '$\nabla^T\wedge$' is the column curl, respectively.

An equivalently crucial second order symmetric tensor in the theory of elasticity [34], is the stress tensor, denoted by $\boldsymbol{\sigma}$. When an elastic body is in equilibrium, the stress tensor should satisfy the equilibrium equation:

$$\nabla \cdot \boldsymbol{\sigma} = \mathbf{0}, \tag{1.4}$$

where we treat '$\nabla\cdot$' as row divergence.

In a linear isotropic elastic solid, the constitutive relation between the stress and strain is given by the Hookean law:

$$\boldsymbol{\sigma} = \lambda \mathbf{tr}(\mathcal{E})\mathbf{I} + 2\mu\mathcal{E}, \tag{1.5}$$

where $\mathbf{I}$ is the identity matrix; λ and μ are the Lame constants, the bulk and shear modulus respectively; and '$\mathbf{tr}$' denotes the 'trace of'.

We can also write the inverse relation of stress and strain as

$$\mathcal{E} = \frac{1}{2\mu}\left(\boldsymbol{\sigma} - \frac{\nu}{1+\nu}\mathbf{tr}(\boldsymbol{\sigma})I\right), \tag{1.6}$$

where ν is the Poisson ratio given by

$$\nu = \frac{\lambda}{2(\lambda+\mu)}.$$

Therefore, in theory, we have collected 12 equations from (1.3), (1.4) and (1.5) for the 12 unknowns from $\boldsymbol{\sigma}$ and $\mathcal{E}$. To reduce the number of both equations and unknowns, firstly substituting (1.5) into (1.4) gives

$$\lambda\nabla\left(\mathbf{tr}(\mathcal{E})\right) + 2\mu\nabla\cdot\mathcal{E} = \mathbf{0}.$$

Replace $\mathcal{E}$ by (1.2), and we have

$$(\lambda+\mu)\nabla(\nabla\cdot\boldsymbol{u}) + \mu\Delta\boldsymbol{u} = \mathbf{0}, \tag{1.7}$$

where 'Δ' is the Laplacian operator with respect to $\boldsymbol{x}$. The equation (1.7) is known as the Navier equation. Taking the divergence of (1.7), we obtain

$$\Delta(\nabla\cdot\boldsymbol{u}) = \Delta\mathbf{tr}(\mathcal{E}) = 0, \tag{1.8}$$

and so from Hooke's law

$$\Delta\mathbf{tr}(\boldsymbol{\sigma}) = (3\lambda+2\mu)\Delta\mathbf{tr}(\mathcal{E}) = 0.$$

Combining (1.8), we can apply the Laplacian operator on both sides of (1.7) to obtain

$$\Delta^2\boldsymbol{u} = \mathbf{0},$$

and so from (1.2)

$$\Delta^2\mathcal{E}_{ij} = 0,$$

which leads to

$$\Delta^2\sigma_{ij} = 0, \tag{1.9}$$

for all i, j. Thus, all the stress components are everywhere biharmonic functions.

Defining a Dislocation

Following the idea in [58], we give two alternative frameworks in which to think of a dislocation, before deciding which will be better for our purposes.

(a) **Displacements at the atomistic level.** At an atomistic level, dislocations are regarded as the line defects of crystals. Suppose we take one layer from a simple cubic crystal as shown in Fig. 1.3. If a column of atoms, starting from the third row, are removed, then an edge dislocation is created. Such a

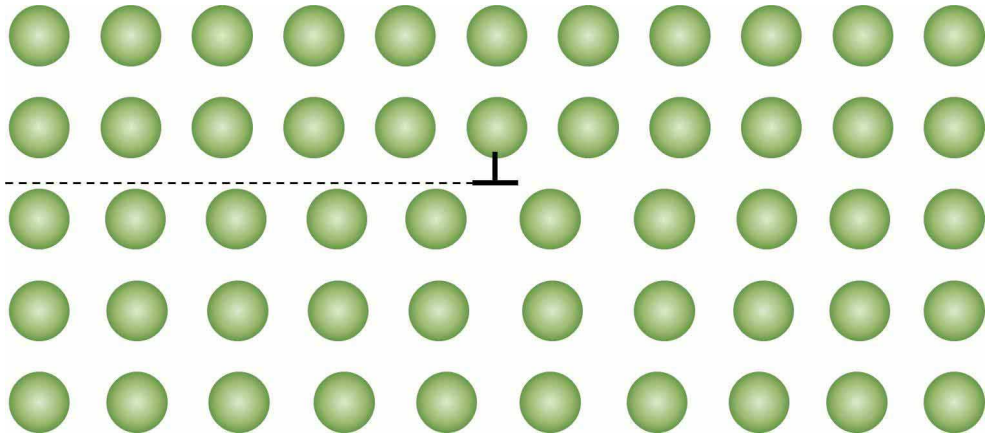
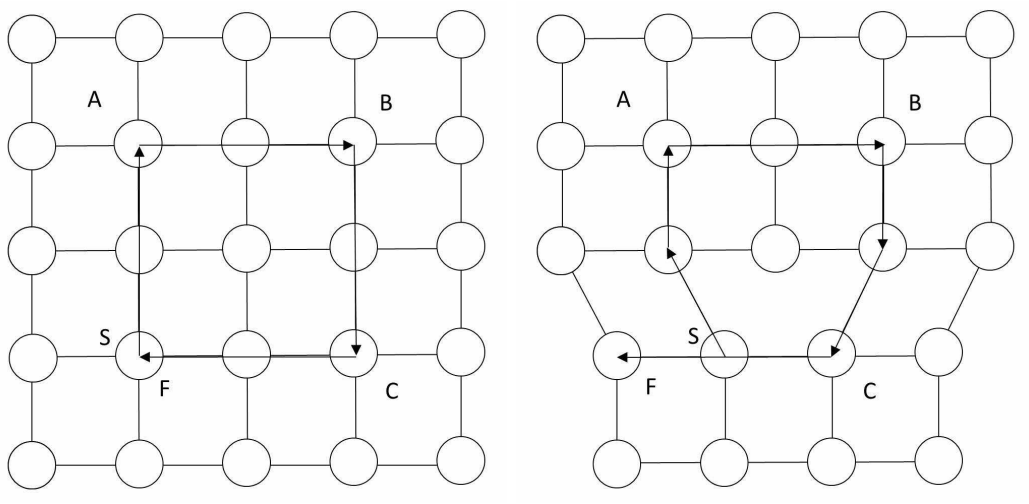


Figure 1.3: The configuration of a dislocation at the atomistic level: if a column of atoms, starting from the third row, are removed, then an edge dislocation is created.

configuration was proposed by Orowan [46], Taylor [57] and Polanyi [49]. It can be seen from Fig. 1.3 that the arrangement of atoms looks regular except that those in the third row on one side are displaced an atom spacing with respect to their counterparts from the second row. Thus we can give a more precise definition of a dislocation: in three dimensional space, a dislocation is the line (perpendicular to the paper) boundary of a planar region (the dashed line in Fig. 1.3) of slip over which the atoms on one side are displaced with respect to the atoms on the other side by an integral atomic spacing. The region where atoms do not appear regular, is called the dislocation core, which is several atomic spacings across. It follows from the definition that the line boundary is either a closed curve, or that it reaches the edge of the specimen. The jump in displacement across the dashed line in the diagram is quantified by the Burgers vector $\boldsymbol{b}$, which can be defined by the procedure illustrated in Fig. 1.4, where the dislocation tangent $\boldsymbol{l}$ is taken to be into the paper. First we form in a perfect



(a) Perfect Lattice (b) Defect Lattice

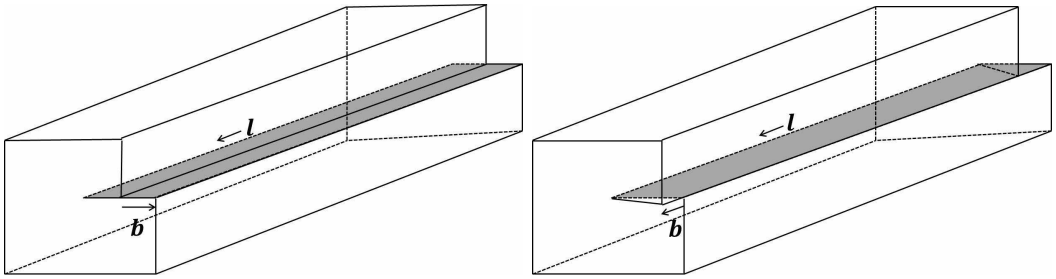
Figure 1.4: Definition of Burger vector $\boldsymbol{b}$ by FS/RH convention

reference crystal a closed, clockwise Burgers circuit SABCF, which encloses the dislocation (Fig. 1.4(a)). Then we draw the same circuit in the real crystal, as shown in Fig. 1.4(b). The excess vector SF from the latter circuit is defined as the local Burgers vector $\boldsymbol{b}$. Mathematically, it is given by the line integral, taken in a right handed sense relative to the dislocation tangent $\boldsymbol{l}$, of the elastic displacement $\boldsymbol{u}$ along any curve C that encloses the dislocation:

$$\boldsymbol{b} = \oint_C \frac{\partial \boldsymbol{u}}{\partial l} \mathrm{d}l. \tag{1.10}$$

It can be seen that the definition of $\boldsymbol{b}$ depends on the sense of the dislocation line, i.e. whether we take the tangent $\boldsymbol{l}$ to point outwards or inwards the paper in Fig. 1.4. Since the sense of the circuit is that of a right-handed screw RH, this convention for $\boldsymbol{b}$ is called the FS/RH convention. The definition of $\boldsymbol{b}$ can also be accomplished by first taking a right-handed circuit enclosing the dislocation in real material and measuring the vector required to close the circuit in perfect crystal. The details of such other ways of definition can be found in [33]. Thus we can define a dislocation more precisely as being characterised by a line direction $\boldsymbol{l}$ and a Burgers vector $\boldsymbol{b}$. From experimental observations, there are two basic types of dislocations: when $\boldsymbol{l}$ is perpendicular to $\boldsymbol{b}$, the dislocation is called an edge dislocation; when $\boldsymbol{l}$ is parallel to $\boldsymbol{b}$, the dislocation is called a screw dislocation. There are also dislocations that are neither edge nor screw, but any such dislocation can be envisaged as a combination of its edge and screw components.

Here it is noted that, in agreement with conventions, we use a "$\top$" or "$\perp$" shape as shown in Fig. 1.3 to denote the cross-section of an edge dislocation with the paper. The vertical segment of such "$\perp$" shape tells the position of the extra plane of atoms with respect to the dislocation.



(a) An Edge Dislocation (b) A Screw Dislocation

Figure 1.5: Dislocations can be created through cut-and-weld operation.

(b) **Cut-and-weld operations.** As discussed above, the atoms stay in perfect lattice only several atomic spacings away from a dislocation. From this point of view, if considering the material as an elastic continuum rather than a crystal with an ordered lattice, we can create a dislocation through the 'cut-and-weld' procedure, which was wonderfully described in [29]: "By arming an ingenious metal worker with a very fine saw which effectively wastes no material, a welding torch and a virgin piece of metal in which certain parallel planes (later to be interpreted as the slip planes) are inscribed, a macroscopic dislocation can be created by asking him to saw along an arbitrary region in one of the planes, then subject the cut metal to a constant jump in tangential displacement across the cut, and finally weld the metal together again." In such a way, a Volterra dislocation is created as the boundary of the cut as shown in Fig. 1.5. The constant jump here is effectively the Burgers vector $\boldsymbol{b}$.

This way of definition enables us to model dislocations using classical continuum elasticity theory. In a dislocated material, dislocations are considered as line singularities. In this scenario, the displacement $\boldsymbol{u}$ is no longer continuous across the dislocation curves. The consequence of this is that the compatibility equation (1.3) does not hold throughout the material. To be precise, the displacements in the material with a single dislocation can be thought as the solution to the Navier equations with zero body force, but with some non-zero function on the righthand side of the compatibility equation (1.3) at the dislocation curve. A mathematical interpretation will be given in §1.2.1.

Of these two definitions of a dislocation, the latter one, based on the cut-and-weld procedure, will be mostly used in this thesis, because it enables us to analyse dislocations by using the classical continuum theory of elasticity. The crystalline nature of metals will be incorporated (discussed below) the crystal lattice property into continuum elasticity through the designation of slip planes and the quantisation of the Burgers vector.

Dislocation Dynamics and Slip Planes

One aspect of the influence of the crystal lattice on a dislocation is its motion. Fig. 1.6 depicts the movement through the crystal lattice of an edge dislocation under an applied external stress $\boldsymbol{\sigma}$, which pushes the atoms at the bottom to realign with their neighbouring columns (Fig. 1.6(b)). If the realignment occurs, the dislocation is moved an atomic spacing to the right (Fig. 1.6(c)). As the dislocation glides away, the atoms restore to a regular pattern (Fig. 1.6(d)). For a dislocation with an edge component, the glide takes place in the plane spanned by $\boldsymbol{b}$ and $\boldsymbol{l}$. This plane is known as the slip (or glide) plane. In the case of screw dislocations where $\boldsymbol{b}$ and $\boldsymbol{l}$ are parallel, the slip plane is not unique[1]. A family of mutually parallel glide planes is defined as the glide system.

There is also another type of dislocation motion, called 'climb', when the dislocation moves out of its glide plane. At room temperature, climbing is much more difficult than gliding, as it relies on the diffusion of vacancies or interstitials, which will be introduced later.

Creation and Annihilation of Dislocations

Dislocations may be created through a number of different mechanisms, two of which are most common when a large plastic strain is present in crystals.

One of the most important dislocation sources, the Frank-Read source is depicted in Fig. 1.7. AB is a segment of a dislocation with two ends pinned by an unspecified barrier. When a stress $\boldsymbol{\sigma}$ is applied, the original segment bows out in response. At some stage two parts of the same dislocation (green curve) are so close that they

[1]In practice, pure screw dislocations are unlikely to occur; most dislocations are curved though they may have straight segments of pure screw character. We will discuss the motion of dislocations more in Chapter 2.

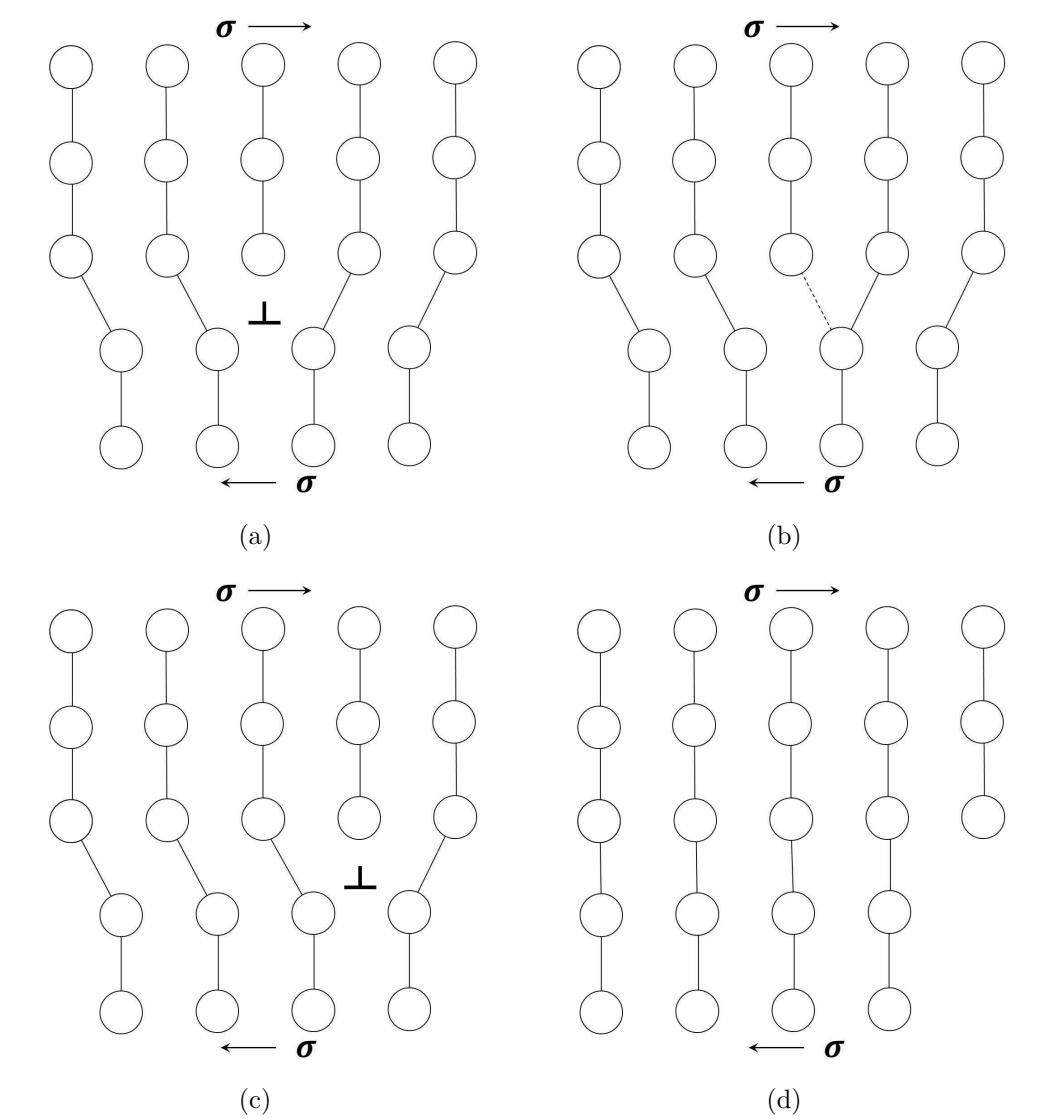


Figure 1.6: Dislocation motions at the atomistic level: (a) starting with an edge dislocation, (b) an external stress pushes the atoms at the bottoms to realign with their neighbouring columns, (c) if the realignment finishes, the dislocation is moved an atomic spacing to the right, (d) as the dislocation glides away, the atoms restore to a regular pattern.

meet and form a single large loop together with the original segment AB (the yellow curve).

Another mechanism that accounts for dislocation multiplication, is the double cross-slip source [33], sketched in Fig. 1.8. Induced by an anti-plane stress or meeting barriers, a screw segment of a dislocation, which have more than one slip planes, may move into another plane known as the cross-slip plane. Double cross-slip occurs when

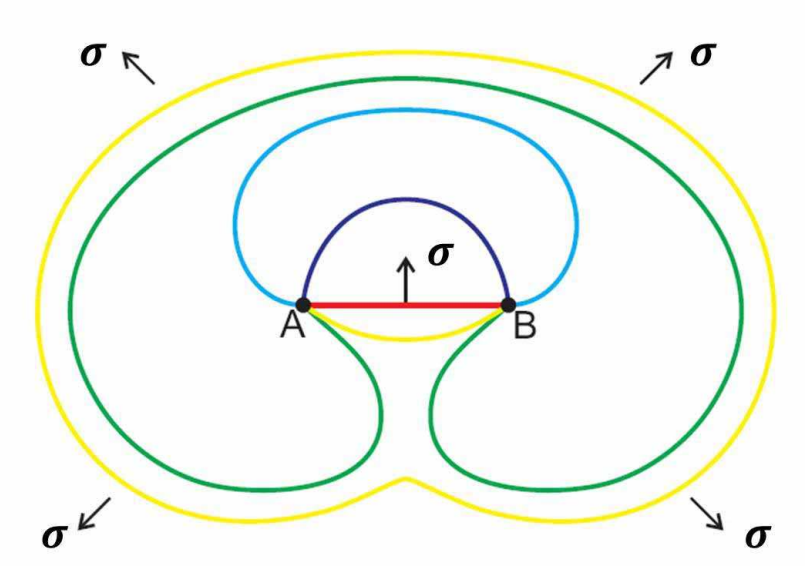


Figure 1.7: The Frank-Read source: AB is a segment of a dislocation with two ends pinned by an unspecified barrier. When a stress $\boldsymbol{\sigma}$ is applied, the original segment bows out in response. At some stage two parts of the same dislocation (the green curve) are so close that they meet and form a single large loop together with the original segment AB (the yellow curve).

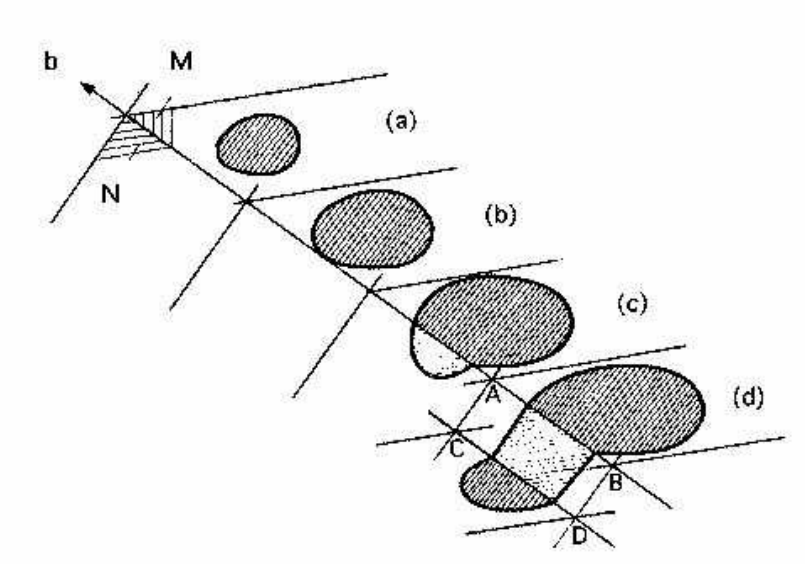


Figure 1.8: Double cross-slip source: (a) dislocation loop in its glide plane; (b) it moves to the adjacent of its glide plane M and cross slip plane N; (c) it does the cross slip motion; (d) it moves back to the original glide plane [33].

the screw segment then moves into a slip plane parallel to the original slip plane. In Fig. 1.8, the doubly cross-slipped segment (CD in Fig. 1.8(d)) can now operate exactly as a Frank-Read source. The segments of the original dislocation that did

not cross slip (AB in 1.8(d)) could in principle operate as another Frank-Read source bowing out in the opposite direction, but they may be prevented from doing so by an impenetrable obstacle.

We will see an extension of this mechanism to multiple loops when we consider the dislocation stability in Chapter 2.

In poly-crystals the boundaries separating different crystalline regions, known as grain-boundaries, are the places where large stress concentrations can arise to activate the sources described above. It is suggested in [41] that edge grain-boundary dislocations could be emitted into a grain, thereby acting as a source. A variety of other possibilities for grain boundary sources have been suggested, as reviewed in Chapter 20 of [33].

A dislocation is annihilated when it meets its exact opposite or when it meets the surface of the material. It is clear from Fig. 1.6, that if two half-sheets of atoms (one as shown in Fig. 1.6(a), lying above the glide plane, the other lying below the line) meet, a perfect lattice will be the result.

Prismatic Loops and Dislocation Dipoles

If a dislocation forms a loop in a plane and its Burgers vector $\boldsymbol{b}$ does not lie in that plane, the glide surface defined by the dislocation line and its Burgers vector is a cylindrical surface as shown in Fig. 1.9. The dislocation is called a prismatic

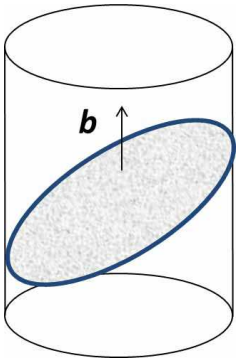
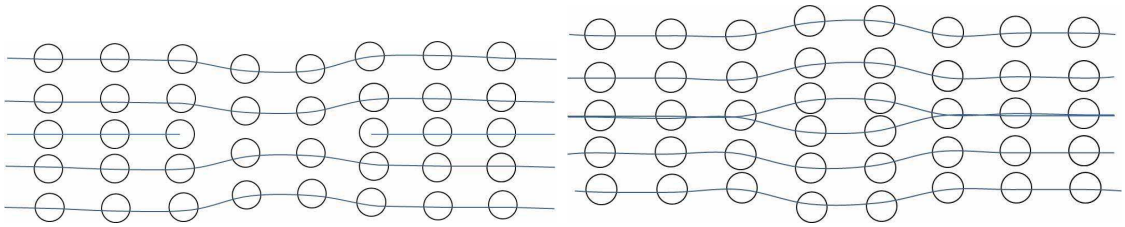


Figure 1.9: Diagrams for a prismatic loop

dislocation. Given the fact that dislocations can only move by glide along the glide surface in the case of prismatic loops, the expansion or shrinking of a dislocation loop must be coupled with climbing motion. A number of examples of prismatic loops have been observed using transmission electron microscopy (TEM). Their atomic

configuration can be associated with vacancies or interstitials as sketched in Fig. 1.10. A vacancy corresponds to a missing atom, while an interstitial is an excessive atom from the perfect lattice structure.



(a) Vacancies (b) interstitials

Figure 1.10: Vacancies and interstitials: a vacancy corresponds to a missing atom; an interstitial is an excessive atom from the perfect lattice structure.

A prismatic loop does not move in response to a uniform applied stress due to the cancelation effect from its opposite tangents in the loop. However, it can be moved by an applied stress which has a gradient between the two opposite tangents.

Another well-agreed dislocation pattern in materials is the dislocation dipole, whose formation is described in Fig. 1.11. When two dislocations of opposite signs in two slip planes glide towards each other by some unspecified source, then they will lock each other. If viewed at a continuum level, outside two dislocations are all perfect lattice (recalling the definition of a Volterra dislocation from the cut-and-weld operation). Correspondingly at the atomic level, the formation of dipoles gives rise to a column of interstials or vacancies as marked in Fig. 1.11. When there is an applied stress, the center of the dislocation pair does not move in response unless this applied stress is big enough to break the dipole. Instead, they only change their mutual angle to accommodate such an applied stress. As we will see later, a dipole will keep a 45° angle under no applied stress. Similarly as the prismatic loop, a pair of dislocation dipole can also be moved by some stress gradient across the two slip planes. Actually, if we compare the atomic configurations of dipoles and prismatic loops, we find that an elongated prismatic loop is equivalent to a pair of dislocation dipole.

Dislocation Density

In real crystals, a large number of dislocations are observed. Their distribution is quantified by the dislocation density ρ, which is defined as the total length of dislocation line per unit volume of crystal, normally quoted in units of cm^{-2} or m^{-2}. There is

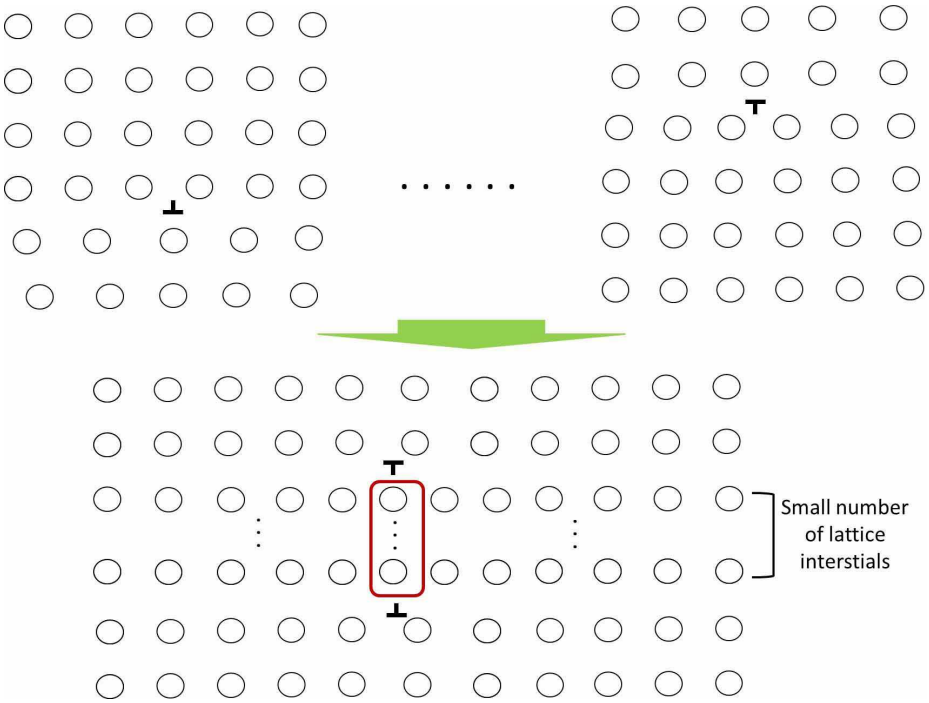


Figure 1.11: Formation of dislocation dipoles at the atomistic level: when two dislocation of opposite signs glide towards each other, they are likely to be bound together which has the minimum energy state, leaving an interstitial or vacancy site between the them. Outside two dislocations are all perfect lattice. According to [6], in the state of stress free, the line that connects two dislocations should form an angle of 45° with the glide plane.

also an alternative definition for the density: the number per unit area of dislocations intersecting a planar surface within the crystal. The density that is defined in such a manner is called the surface density. If all dislocations are parallel, the two density values are the same. But the values by the two definitions are in general different.

It is noted that compared to the other quantities introduced, the dislocation density is a concept at a macroscopic level, since it only concerns the collective behaviour of dislocations.

1.1.2 The Fatigue Tests

Experimental Equipment

The experimental results of the fatigue test we followed in this thesis are detailed in Chapter 4 of [2]. To briefly summerise, in their experiments as shown in Fig. 1.12, a specimen (copper) undergoes push-pull at two ends by a control of stress or strain,

which cyclically satisfies a fully reversed sine wave. All specimens after prescribed

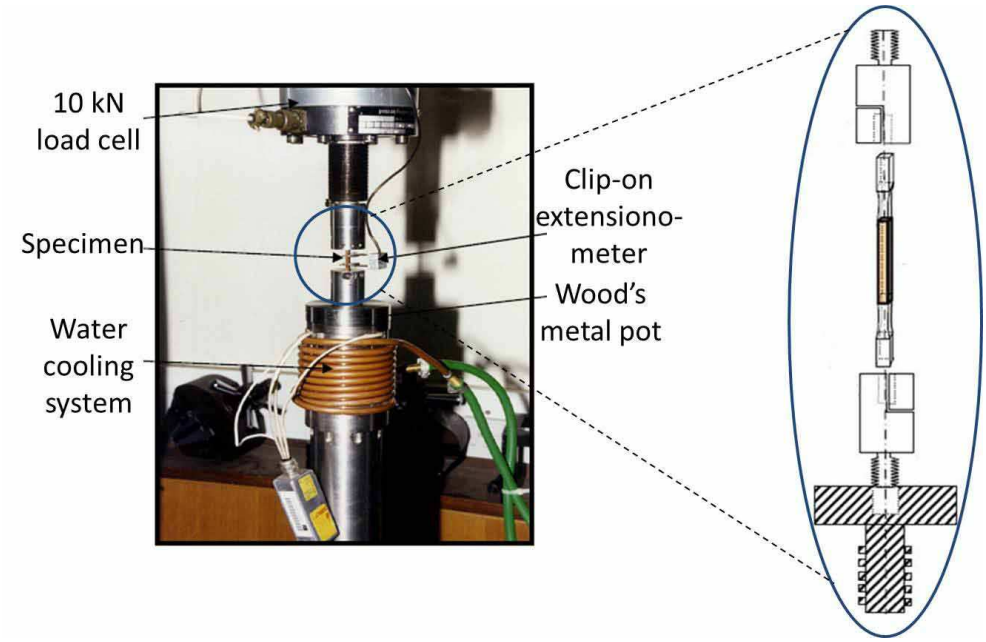


Figure 1.12: Experimental equipment: a specimen (copper) undergoes push-pull at two ends by a control of stress or strain, which cyclically satisfies a fully reversed sine wave (abstracted from [2]).

number of cycles are analysed by using the electron channelling contrast imaging (ECCI) technique.

The Channel-Vein Structure

From the experiments, it can be found that if the plastic strain amplitude $\gamma <\sim 10^{-4}$, the saturation stress (the peak stress that saturates at a constant value after a sufficiently large number of cycles.) grows with the plastic strain amplitude as shown in Fig. 1.13. It is noted that dislocations correspond to the dark region in the image in the right hand side of Fig. 1.13. A schematic plot of the material microstructure is drawn in the middle circle at the same angle as in the image. It can be observed that most dislocations are of straight edge type, which take a 'vein structure'. These veins are surrounded by 'channels', there are mainly screw segments connecting edge dislocations in different veins. When there is an applied stress, these segments will glide on their slip planes in response. The veins have a dislocation density of $3 \times 10^{15}\mathrm{m}^{-2}$ (see [23]) and a volume fraction of around 50% (see [21]). The dislocation density in the channels is about $10^{11}\mathrm{m}^{-2}$ (see [21]).

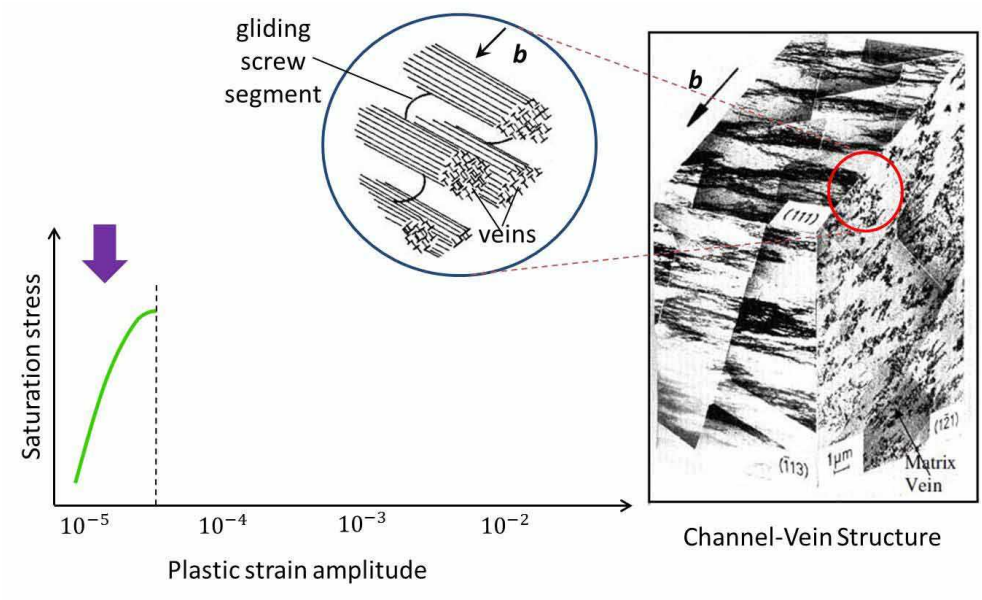


Figure 1.13: Channel-vein structures: if the plastic strain amplitude $\gamma <\sim 10^{-4}$, the saturation stress grows with the plastic strain amplitude. A schematic plot of the material microstructure is drawn in the middle circle at the same angle as in the image in the right hand side by using the ECCI technique. It can be observed that most dislocations are of straight edge type, which take a 'vein structure'. These veins are surrounded by 'channels', there are mainly screw segments connecting edge dislocations in different veins. It is noted that dislocations correspond to the dark region in the image by using the ECCI technique (abstracted from [2]).

Persistent Slip Bands

If the plastic strain amplitude γ exceeds $\sim 10^{-4}$, the saturation stress does not vary too much against the strain amplitude. In this case, the dislocations start to change their group pattern significantly by forming a ladder shape structure as highlighted in Fig. 1.14. These ladder shape structures are known the persistent slip bands (PSBs). In Fig. 1.15, more observations of PSBs by using the ECCI technique are given. It should be noted that in these diagrams the light regions correspond to dislocations.

In the rungs of PSBs reside a large number of straight edge dislocations, which have a dislocation density of around $6 \times 10^{15}\mathrm{m}^{-2}$ (see [23]). The regions between rungs are relatively dislocation free region with a density of approximately $10^{12}\mathrm{m}^{-2}$ (see [23]). Also some bowing-out edge segments can be observed growing from the edge dislocation walls. It is noted that although the dislocation density in the walls is much higher than in the veins, the overall dislocation density in the PSB is roughly half of the density in the channel-vein structure, because the volume fraction of the

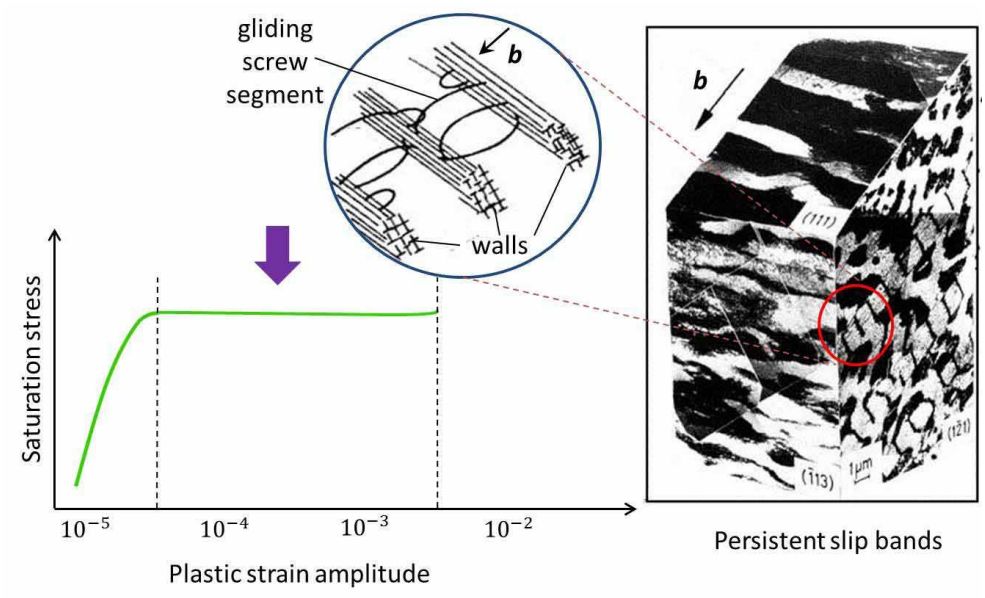


Figure 1.14: Persistent slip band (PSB) structure: the dislocations start to change their group pattern significantly by forming a ladder shape structure known as a PSB (abstracted from [2]).

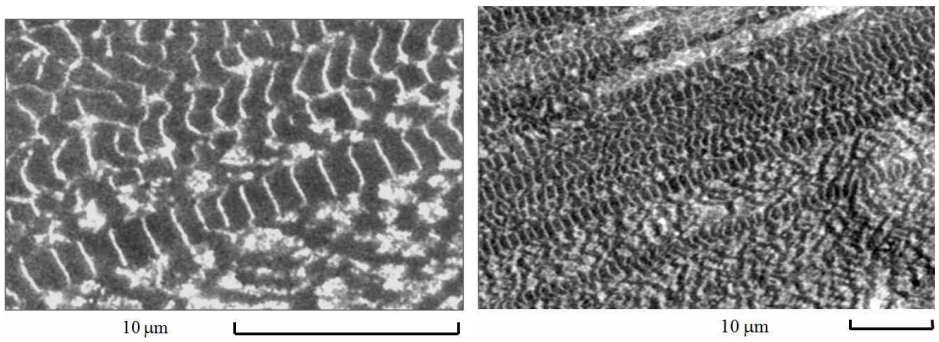


Figure 1.15: PSBs observed in fatigue tests. This time, the light regions correspond to dislocations (abstracted from [2]).

walls in the PSB, roughly 10%, is smaller than the volume fraction of the veins in the channel-vein structure.

A good understanding of the formation of PSBs is important, because they are widely believed to be the indication of crack initiation [54]. However, there are few results concerning such a mechanism. The aim of this thesis is trying to develop models which can answer the following questions. 'What controls the transition from veins to PSBs?' and 'What controls the characteristic spacings in these structures?'.

1.1.3 Review of Previous Continuum and Discrete Models

In the literature, dislocations have been analysed mathematically from various points of view. Here we contrast briefly some of the approaches.

- **Atomistic v.s. Elastic**

  From the two definitions of dislocations given in §1.1.1, the ways of modelling dislocations can be naturally divided into two. Since dislocations are atomic defects, it is sensible to track them by using mathematical methods for atoms, such as the molecular dynamics (MD) method. However, because the arrangement of atoms restores to a regular lattice several atomic spacings from the dislocation, it is also practical to treat dislocations as line singularities embedded in an elastic medium. As we can see later, which of these different approaches is most appropriate depends on which scale we are most interested in.

- **Energy v.s. Force**

  The comparison of these two issues can be regarded as an extension of that in classical elasticity. Given a system, the equilibrium state is that for which the total energy is minimised locally. The evolution of the system can also be driven by the variation of the energy. One advantage of the formulation in terms of energy is its rigour. A big box of tools of partial differential equations can be borrowed to analyse the well-posedness of solutions. Another advantage is that using the principle of energy minimisation, numerical methods such as the finite element method (FEM), can be easily implemented.

  On the other hand, dislocations can be tracked by examining the total force on them. This way is more intuitive compared to that of energy. If lucky, we may even achieve some explicit solutions. In the thesis, our approach is mainly force-based.

- **Discrete v.s. Homogenised**

  Discrete methods treat dislocations separately and see how each dislocation behaves in the presence of others and external effects. This method works well in lots of situations, and its usefulness is enhanced due to an increase in computing power. The method of homogenisation looks at the collective behaviour of microscopic properties to concentrate on those macroscopic quantities such as the dislocation density. Literature regarding both methods will be listed later.

In the rest of this section our literature review will be arranged from the microscopic scale to the macroscopic.

At an atomistic level, where the computational domain is measured by nm (10^{-9}m), two distinct approaches are used. First-principle or ab initio methods incorporate the quantum mechanical nature of bonding between atoms. The configuration of the system is determined by solving Schrödinger's equation for interacting electrons. Such a method is useful when determining the local atomic structure, such as vacancies, self-interstitials and small clusters (up to four or five) of these defects. Also it is valuable for providing a database of crystal properties for fitting the adjustable parameters in empirical interatomic potentials. For example, in [22], the atomic structure of the core of the screw dislocation in iron and some other bcc metals were described. However, one key disadvantage of this method is its high reliance on computer power, and for that reason, most of the models with this method, are restricted to systems containing typically 100 to 1000 atoms.

The other method based on the atomic level employs models that accurately describe the atomic structure of dislocations but are at a larger scale than the previous one to allow the effect from external strains. The methods are from the broad family of molecular dynamic methods, where the trajectories of molecules or atoms are determined by numerically solving the Newton's equations of motion for a system of interacting particles. MD methods allow people to investigate the short range interaction between dislocations or other defects by remaining at the atomic level. It should be noted that in order to accommodate space in the right scale, the temporal scale is taken to be $\sim 10^{-9}$s. There are a vast number of results with MD methods. For example, [15] simulates dislocation motion in bcc metals. Although at a slight larger scale, MD methods still share the disadvantage of the quantum mechanical simulation: the number of atoms they can deal with are restricted.

At a mesoscopic level (10^{-6}m), dislocations degenerate to one-dimensional curves surrounded by elastic media. In [33], the expressions for stress field and elastic energy by a single dislocation are summarized. Following the law of motion originating from experimental observations, many methods under the framework of dislocation dynamics (DD) simulation, have been developed to track the evolution of dislocations. As the representative eminent work among such methods, [11] explains the algorithm of the DD simulations in their ParaDis codes; [18] and [19] are two examples of work using the DD simulation to study the dislocation structures in the early stage of low-

amplitude fatigue by Fivel et al. The level-set method has also been used to track the dislocation motion [61].

At a larger scale ($\sim 10^{-5}$ to 10^{-4}m), dislocation models are associated with material microstructure, such as grains, whose collective features will determine the macroscopic mechanical properties of the material. At this level, continuum quantities such as the dislocation density ρ are the focus. One category of such models treat the evolution of ρ as a diffusive process [10]. Another set of models treat the dislocated material as a continuum with simple geometry or low dimension. As the simplest case, one dimensional arrays of discrete dislocations with the same sign have been widely studied (see [26], [27], [20], and [38]). If a group of infinitely long and parallel dislocations each lying in the same glide plane is represented in this way by a number density, the configuration is known as a 'dislocation sheet'. The static equilibrium of dislocation sheets was investigated in [25], while the time evolution of dislocation sheets was studied later (see [28], [31], [32], [51] and [44]). A more recent application of dislocations using this method, for example, can be found in the investigations on dislocation pile-ups (see [24] and [60]).

At a scale of 10^{-4}m or larger, the issue is about macroscopic material properties, such as the plasticity. Research at this scale usually involves giving certain yield conditions and flow rules for plastic flow. Some relevant results are introduced in [34]. In the thesis, we will not consider the properties at such scales.

The existence of such a wide range of scales in the models mentioned above has triggered a number of recent approaches to studying dislocations: models using the multiple-scale analysis. The basic idea is to combine the models of different scales. We here list some of the attempts that have been made. The quasi-continuum (QC) method builds models around the idea of linking the atomistic region to the continuum via a special set of transition region boundary conditions. At the dislocation core region, where linear elasticity breaks down, atomic models are employed. Away from the dislocations, linear elasticity is used. The method was introduced in [55] and [56], and has been built on in [47], [4] and [7], for example. Another example of using multiple-scale analysis is the phase field model of dislocations. By defining some phase function ψ, which assigns neighbouring integers to regions that share a dislocation, one can formulate the elastic energy for each region. At the dislocation core, the Peierls-Nabarro energy is used to smooth ψ. The system is then driven by the gradient flow of free energy ([39], [5] and [13]). In this thesis, we will present a

model to describe discrete dislocations and dislocation densities by the multiple-scales technique.

1.2 Mathematical Introduction to Dislocations

After introducing the background of dislocations, we now describe in more detail of the mathematical models of dislocations we will use.

1.2.1 The 'Force' on a Dislocation

Since a dislocation has no mass, it can not experience a Newtonian force. However, dislocations will move in the presence of an appropriate component of stress. If the total stress acting on the dislocation is $\boldsymbol{\sigma}$, then the work done by it can be thought of as arising from a force per unit length along the dislocation line.

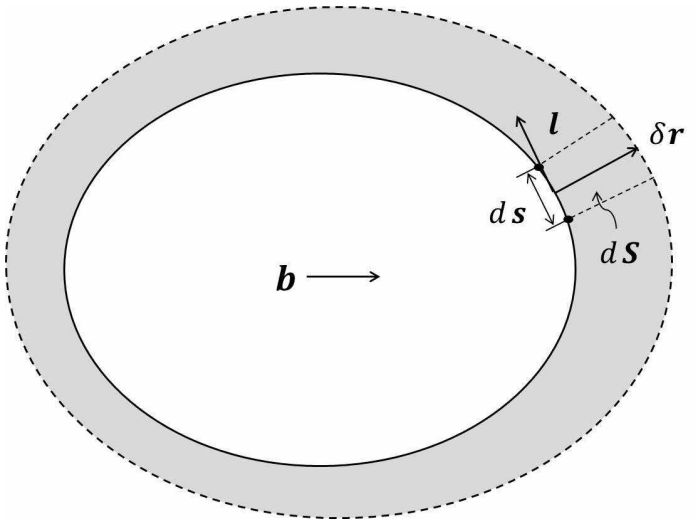


Figure 1.16: An element of dislocation line d$\boldsymbol{l}$ sweeps out an area d$\boldsymbol{S}$ by moving a distance $\delta\boldsymbol{r}$.

Suppose that the element of the dislocation line d$\boldsymbol{l}$ is displaced by $\delta\boldsymbol{r}$, under a stress $\boldsymbol{\sigma}$. Then, as shown in Fig. 1.16, the element sweeps out an area $|\mathrm{d}\boldsymbol{S}|$ where

$$\mathrm{d}\boldsymbol{S} = \delta\boldsymbol{r} \wedge \mathrm{d}\boldsymbol{l}.$$

The force acting on this area can be written

$$\boldsymbol{\sigma} \cdot \mathrm{d}\boldsymbol{S}.$$

Since the effect on the displacement is a difference of $\boldsymbol{b}$ across the planar area (in Fig. 1.16, this area is the plane), the work done by the stress on the dislocation line element is

$$\boldsymbol{b}\cdot\boldsymbol{\sigma}\cdot\mathrm{d}\boldsymbol{S} = (\boldsymbol{\sigma}\cdot\boldsymbol{b})\cdot(\delta\boldsymbol{r}\wedge\mathrm{d}\boldsymbol{l}) = -\delta\boldsymbol{r}\cdot((\boldsymbol{\sigma}\cdot\boldsymbol{b})\wedge\boldsymbol{l})\,\mathrm{d}s.$$

Therefore, the increase in strain energy of the dislocation, which is the work done against the stresses, is

$$\delta W = \delta\boldsymbol{r}\cdot((\boldsymbol{\sigma}\cdot\boldsymbol{b})\wedge\boldsymbol{l})\,. \tag{1.11}$$

Now, if the 'force per unit length' is $\boldsymbol{F}$, then

$$\delta W = (\boldsymbol{F}\mathrm{d}s)\cdot\delta\boldsymbol{r}. \tag{1.12}$$

By comparing (1.11) and (1.12), we relate the force per unit length on a dislocation to the stress by

$$\boldsymbol{F} = (\boldsymbol{\sigma}\cdot\boldsymbol{b})\wedge\boldsymbol{l}, \tag{1.13}$$

where $\boldsymbol{l}$ is the tangential direction.

In this thesis, the local orthogonal coordinate system $(\boldsymbol{n},\boldsymbol{m},\boldsymbol{l})$ is frequently used for convenience; $\boldsymbol{n}$ is the normal of the dislocation curve, and $\boldsymbol{m}$ is the binormal direction defined by

$$\boldsymbol{m} = \boldsymbol{l}\wedge\boldsymbol{n}. \tag{1.14}$$

Any vector $\boldsymbol{v}$ can be decomposed in this local coordinate system as

$$\boldsymbol{v} = (\boldsymbol{v}\cdot\boldsymbol{n})\boldsymbol{n} + (\boldsymbol{v}\cdot\boldsymbol{m})\boldsymbol{m} + (\boldsymbol{v}\cdot\boldsymbol{l})\boldsymbol{l}.$$

It should be noted that for a straight dislocation the stress $\boldsymbol{\sigma}$ in the Peach-Koehler force (1.13) is the total stress excluding the stress by the local part of the dislocation itself [58]. For curved dislocations, the situation is more complicated. In Chapter 2, we will obtain the self-induced stress of a curved dislocation by asymptotic expansion. The force exerted by a curved dislocation on itself can then be determined.

1.2.2 Velocities of Dislocations

As described above, a dislocation may move in response to the total stress on it. The first experimental attempt to measure the stress dependence of dislocation velocity were conducted by Johnston and Gilman [37] in 1959. From then on, a number of experiments were conducted for other metals; these results are collected in [35].

The experimental results have shown that the dislocation velocity satisfies

$$v = A\sigma^m, \tag{1.15}$$

where A is a material constant; σ is the corresponding stress component; m is approximately 1 at 300K in pure crystals [35]. In the literature many mobility laws have been proposed motivated by experimental observations. In this thesis we follow [26] and [53] to postulate a mobility law. More details will be discussed in Chapter 2.

1.2.3 Some Mathematical Representations

Incompatibility

From the definition of the Burgers vector, we find that the displacement $\boldsymbol{u}$ is no longer continuous. Thus the definition of the derivatives of $\boldsymbol{u}$ may not be meaningful. In other words, the compatibility equation (1.3) does not hold where there is a dislocation. To capture such singularities, we define

$$\boldsymbol{\eta} = -\nabla^T \wedge \nabla \wedge \mathcal{E}, \tag{1.16}$$

called the 'incompatibility tensor'. The function $\boldsymbol{\eta}$ vanishes where there is no dislocation. From Appendix A.1, we can express $\boldsymbol{\eta}$ as a function of $\mathcal{E}$ by

$$\eta_{ij} = e_{ij,kk} + e_{kk,ij} - (e_{ik,jk} + e_{jk,ik}) + (e_{kl,kl} - e_{kk,ll})\delta_{ij}. \tag{1.17}$$

The Einstein summation convention will be used throughout the first two chapters, that is, we sum over repeated indices.

The Delta Function

Before we derive any expression for the stress components of a single dislocation, we first introduce the one-dimensional Dirac distribution (or delta function) $\delta(x)$, which is defined by a linear mapping on a smooth enough function $f(x)$:

$$\int_{\mathbb{R}} \delta(x' - x) f(x') \mathrm{d}x' = f(x). \tag{1.18}$$

The n-dimensional δ-function is then defined as the product of one dimensional delta functions:

$$\delta(\boldsymbol{x} - \boldsymbol{x}') = \prod_{i=1}^{n} \delta(x_i - x_i'). \tag{1.19}$$

The derivative of delta function is defined by the mapping

$$\int_{\mathbb{R}} \delta'(x'-x)f(x')\mathrm{d}x' = -\frac{\mathrm{d}f}{\mathrm{d}x}. \tag{1.20}$$

1.2.4 Stress by Dislocations

The Screw Dislocation

For a straight screw dislocation, for example, $\boldsymbol{l} = (0,0,1)^T$ and $\boldsymbol{b} = (0,0,b)^T$, it is clear that the material is in a state of anti-plane strain, where the displacement can be assumed to be $\boldsymbol{u} = (0,0,u_3(x_1,x_2))^T$. Hence the strain tensor can be written as

$$\mathcal{E} = \begin{pmatrix} 0 & 0 & e_{13} \\ 0 & 0 & e_{23} \\ e_{13} & e_{23} & 0 \end{pmatrix} = \frac{1}{2} \cdot \begin{pmatrix} 0 & 0 & u_{3,1} \\ 0 & 0 & u_{3,2} \\ u_{3,1} & u_{3,2} & 0 \end{pmatrix}.$$

From the definition of the Burgers vector in (1.10), we have

$$b = \oint_\gamma \mathrm{d}u_3 = \oint_\gamma u_{3,1}\mathrm{d}x_1 + u_{3,2}\mathrm{d}x_2 = 2\oint_\gamma e_{13}\mathrm{d}x_1 + e_{23}\mathrm{d}x_2,$$

which, on using Green's theorem in the plane, becomes

$$e_{23,1} - e_{13,2} = \frac{b}{2}\delta(x_1)\delta(x_2). \tag{1.21}$$

Partially differentiating this with respect to x_1 and x_2 gives respectively

$$e_{23,11} - e_{13,21} = \frac{b}{2}\delta'(x_1)\delta(x_2) \tag{1.22}$$

and

$$e_{23,12} - e_{13,22} = \frac{b}{2}\delta(x_1)\delta'(x_2). \tag{1.23}$$

Comparing these with (1.17), we see that only η_{13} and η_{23} are non-zero, and they are just the left hand sides of (1.22) and (1.23), respectively.

Also, using the Hookean Law in (1.5), we can rewrite (1.21) as

$$\sigma_{23,1} - \sigma_{13,2} = \mu b\delta(x_1)\delta(x_2). \tag{1.24}$$

And in this case the equilibrium equation (1.4) becomes

$$\sigma_{13,1} + \sigma_{23,2} = 0. \tag{1.25}$$

Thus we can define a stress potential function φ, such that,

$$\sigma_{13} = -\varphi_{,2}, \qquad \sigma_{23} = \varphi_{,1}.$$

Substituting these expressions into (1.24), we can obtain

$$\Delta\varphi = \mu b \delta(x_1)\delta(x_2), \tag{1.26}$$

where the radially symmetric solution for φ is

$$\varphi = \frac{\mu b}{4\pi} \log\left(x_1^2 + x_2^2\right). \tag{1.27}$$

So the stress components are

$$\sigma_{13} = -\frac{\mu b}{2\pi} \cdot \frac{x_2}{x_1^2 + x_2^2}, \qquad \sigma_{23} = \frac{\mu b}{2\pi} \cdot \frac{x_1}{x_1^2 + x_2^2}. \tag{1.28}$$

The Edge Dislocation

The derivation of the stress due to edge dislocations follows the study of linear plane theory introduced in §4.6.5 of [34]. Suppose we have an isolated, infinitely long and straight edge dislocation with Burgers vector $(b, 0, 0)$, lying along the x_3-axis. The displacement then becomes

$$\boldsymbol{u} = \begin{pmatrix} u_1(x_1, x_2) \\ u_2(x_1, x_2) \\ 0 \end{pmatrix}.$$

In this case, the strain tensor can be expressed by

$$\mathcal{E} = \begin{pmatrix} e_{11} & e_{12} & 0 \\ e_{12} & e_{22} & 0 \\ 0 & 0 & 0 \end{pmatrix} = \begin{pmatrix} u_{1,1} & \frac{1}{2}\left(u_{1,2} + u_{2,1}\right) & 0 \\ \frac{1}{2}\left(u_{1,2} + u_{2,1}\right) & u_{2,2} & 0 \\ 0 & 0 & 0 \end{pmatrix} \tag{1.29}$$

Similarly to the screw dislocation, we have

$$b = \oint_\gamma \mathrm{d}u_1 = \oint_\gamma e_{11}\mathrm{d}x_1 + (2e_{12} - u_{2,1})\mathrm{d}x_2. \tag{1.30}$$

Since γ is arbitrary, by using Green's formula in the plane, we can obtain

$$2e_{12,1} - u_{2,11} - e_{11,2} = b\delta(x_1)\delta(x_2).$$

Differentiating this with respect to x_2 gives

$$2e_{12,12} - e_{22,11} - e_{11,22} = b\delta(x_1)\delta'(x_2). \tag{1.31}$$

A comparison with the incompability tensor (1.17) shows that, for an edge dislocation, the only component of the incompatibility tensor that does not vanish is

$$\eta_{33} = b\delta(x_1)\delta'(x_2). \tag{1.32}$$

On the other hand, for stress components, the equilibrium equation (1.4) becomes

$$\sigma_{11,1} + \sigma_{12,2} = 0;$$

$$\sigma_{12,1} + \sigma_{22,2} = 0,$$

which imply that these components can be written as the second order derivatives of the Airy stress function χ, which satisfies

$$\sigma_{11} = \chi_{,22}, \quad \sigma_{12} = -\chi_{,12}, \quad \sigma_{22} = \chi_{,11}. \tag{1.33}$$

And from (1.6), we can find that

$$\sigma_{33} = \nu(\sigma_{11} + \sigma_{22}).$$

Inplementing the inverse Hookean Law (1.6) gives

$$e_{11} = \frac{1}{2\mu}\left((1-\nu)\sigma_{11} - \nu\sigma_{22}\right);$$

$$e_{22} = \frac{1}{2\mu}\left((1-\nu)\sigma_{22} - \nu\sigma_{11}\right);$$

$$e_{12} = \frac{1}{2\mu}\sigma_{12}.$$

Using (1.33), we incorporate these into (1.31) to obtain

$$\nabla^4\chi = -\frac{2\mu b}{1-\nu}\delta(x_1)\delta'(x_2). \tag{1.34}$$

Substituting

$$\chi = -2\psi_{,2},$$

gives

$$\nabla^4\psi = -\frac{\mu b}{1-\nu}\delta(x_1)\delta(x_2), \tag{1.35}$$

whose radially symmetric solution is

$$\psi = \frac{\mu b}{16\pi(1-\nu)}\left(x_1^2 + x_2^2\right)\log\left(x_1^2 + x_2^2\right). \tag{1.36}$$

Thus the stress components are

$$\sigma_{11} = -\frac{\mu b}{2\pi(1-\nu)} \cdot \frac{x_2\left(3x_1^2 + x_2^2\right)}{\left(x_1^2 + x_2^2\right)^2}; \tag{1.37}$$

$$\sigma_{12} = -\frac{\mu b}{2\pi(1-\nu)} \cdot \frac{x_1\left(x_1^2 - x_2^2\right)}{\left(x_1^2 + x_2^2\right)^2}; \tag{1.38}$$

$$\sigma_{22} = \frac{\mu b}{2\pi(1-\nu)} \cdot \frac{x_2\left(x_1^2 - x_2^2\right)}{\left(x_1^2 + x_2^2\right)^2}. \tag{1.39}$$

The Curved Dislocation

The stress field of an arbitrary curved dislocation was firstly derived by Peach and Koehler [48] in 1950 by differentiating the components of displacement as given by Burgers [12] in 1939. We will follow the approach in [40], where the same result was achieved by means of the introduction of stress functions. Firstly, we need to generalise the results of the incompatibility tensor for screws and edges to a loop dislocation.

If the dislocation is screw with $\boldsymbol{l} = (0, 0, 1)$ and $\boldsymbol{b} = (0, 0, b_3)$, we have the non-zero components of incompatibility tensor as

$$\eta_{13} = -\frac{1}{2}[\varepsilon_{123} l_3 b_3 \delta(x_1)\delta(x_2)]_{,2}, \tag{1.40}$$

$$\eta_{23} = -\frac{1}{2}[\varepsilon_{213} l_3 b_3 \delta(x_1)\delta(x_2)]_{,1}. \tag{1.41}$$

If the dislocation is edge with $\boldsymbol{l} = (0, 0, 1)$ and $\boldsymbol{b} = (b_1, 0, 0)$, we have the non-zero components of incompatibility tensor as

$$\eta_{33} = -[\varepsilon_{321} l_3 b_1 \delta(x_1)\delta(x_2)]_{,2}. \tag{1.42}$$

For any curved dislocation, we can always treat it as a linear combination of its screw and edge characters. So based on these 3 equations, we may write the incompatibility tensor of an arbitrary curved dislocation as

$$\eta_{ij} = -[\varepsilon_{jmn} l_i b_n \delta(x_p - x'_p)\delta(x_{p+1} - x'_{p+1})]^S_{,m}, \tag{1.43}$$

for $i, j = 1, 2, 3$, $i < j$, where $p = (i + 1) \mod 3$, and the point $\boldsymbol{x}'$ lies on the dislocation. Here, the superscript 'S' denotes the 'symmetric part of'.

Substituting the components of the strain by that of the stress from (1.6) gives

$$\sigma_{ij,kk}+\sigma_{kk,ij}-(\sigma_{jk,ki}+\sigma_{ki,kj})+(\sigma_{kl,kl}-\sigma_{kk,ll})\delta_{ij}-\frac{\nu}{1+\nu}(\sigma_{kk,ij}-\sigma_{kk,ll}\delta_{ij}) = 2\mu\eta_{ij}. \quad (1.44)$$

Noticing that the stress components of the material in an equilibrium state under no body force satisfy

$$\sigma_{ik,k} = 0,$$

for $i = 1, 2, 3$, we can rewrite (1.44) as

$$\sigma_{ij,kk} + \frac{1}{1+\nu}(\sigma_{kk,ij} - \sigma_{kk,ll}\delta_{ij}) = 2\mu\eta_{ij}. \quad (1.45)$$

In order to solve (1.45) for $\boldsymbol{\sigma}$, we first define some potential functions related to $\boldsymbol{\sigma}$, which are generalisations of the stress function φ for screw dislocations, and ψ for edge dislocations. Then we can solve for these potentials by combining (1.43) and (1.45), and finally obtain the expression for the stress tensor.

Firstly, since $\boldsymbol{\sigma}$ is a symmetric, second-rank tensor, and the force balance equation (1.4) holds, then we may write

$$\boldsymbol{\sigma} = -\nabla^T \wedge \nabla \wedge \boldsymbol{\psi}, \quad (1.46)$$

where $\boldsymbol{\psi}$ is also a symmetric second rank tensor. The diagonal elements of $\boldsymbol{\psi}$ are the Morera's stress functions, and the off-diagonal elements are the Maxwell's stress functions.

Substituting (1.46) into (1.45) gives a cumbersome expression for $\boldsymbol{\psi}$, and yet we may expect, on the basis of the Airy stress function equation (1.36) for edge dislocations, that we may generalise to obtain $\boldsymbol{\eta}$ as the result of operating with the biharmonic operator Δ^2 on a stress function. This is done by introducing a different stress function $\boldsymbol{\chi}$ defined by

$$\boldsymbol{\psi} = 2\mu\left(\boldsymbol{\chi} + \frac{\nu}{1-\nu}\mathbf{tr}(\boldsymbol{\chi})\mathbf{I}\right),$$

where $\mathbf{I}$ is the identity matrix, so that we may write

$$\boldsymbol{\sigma} = -2\mu\left(\nabla^T \wedge \nabla \wedge \left(\boldsymbol{\chi} + \frac{\nu}{1-\nu}\mathbf{tr}(\boldsymbol{\chi})\mathbf{I}\right)\right). \quad (1.47)$$

Then substituting (1.47) into (1.45) gives

$$\chi_{ij,kkll} - (\chi_{jk,kill} + \chi_{ki,jkll}) + \frac{1}{1+\nu}\chi_{kl,klij} + \frac{\nu}{1+\nu}\chi_{kl,klmm}\delta_{ij} = \eta_{ij}. \quad (1.48)$$

From Appendix A.2, we have another 3 equations for $\boldsymbol{\chi}$ everywhere,

$$\chi_{ij,j} = 0. \tag{1.49}$$

So (1.48) becomes

$$\nabla^4 \boldsymbol{\chi} = \boldsymbol{\eta},$$

and (1.47) becomes

$$\sigma_{ij} = 2\mu \left(\chi_{ij,kk} + \frac{1}{1-\nu}(\chi_{kk,ij} - \chi_{kk,ll}\delta_{ij}) \right). \tag{1.50}$$

The solution of this for which the stress vanishes at infinity is

$$\boldsymbol{\chi} = -\frac{1}{8\pi} \int_{\mathbb{R}^3} \boldsymbol{\eta}(\boldsymbol{x}') R \mathrm{d}V', \tag{1.51}$$

where $R = |\boldsymbol{x}' - \boldsymbol{x}|$. So (1.50), in terms of the incompatibility, becomes

$$\boldsymbol{\sigma} = -\frac{\mu}{4\pi} \int_{R^3} \boldsymbol{\eta} \Delta R + \frac{1}{1-\nu} \mathbf{tr}(\boldsymbol{\eta}) \cdot ((\nabla \otimes \nabla) R - \Delta R \mathbf{I}) \, \mathrm{d}V'$$

after integrating by parts twice, where ∇ is the gradient with respect to $\boldsymbol{x}$. Using the property of the delta function and substituting the expression by (1.43) gives the Peach-Koehler stress tensor at point $\boldsymbol{x}$ as

$$\begin{aligned} \boldsymbol{\sigma}^{\mathrm{pk}}(\boldsymbol{x}) = \frac{\mu}{4\pi} \left(\int_C (\boldsymbol{b} \wedge \nabla) \frac{1}{Z} \otimes \mathrm{d}\boldsymbol{q} + \left(\int_C (\boldsymbol{b} \wedge \nabla) \frac{1}{Z} \otimes \mathrm{d}\boldsymbol{q} \right)^T \right) \\ + \frac{\mu}{4\pi(1-\nu)} \int_C (\mathrm{d}\boldsymbol{q} \cdot (\boldsymbol{b} \wedge \nabla)) (\nabla \otimes \nabla - \mathbf{I}\Delta) Z, \end{aligned} \tag{1.52}$$

where $\boldsymbol{q}$ is a point on dislocation curve; $\boldsymbol{z} = \boldsymbol{q} - \boldsymbol{x}$; $Z = |\boldsymbol{z}|$.

1.3 The Outline of this Thesis

Based on above information, we give the outline of this thesis as diagrammed in Fig. 1.17.

In Chapter 2, we try to find the local self-induced stress for a single dislocation by following the work in [16] to do a local expansion of the Peach-Koehler stress tensor. Combining the expression for the local force with an experimentally-motivated mobility law, we reach the governing formula for the motion of a curvi-linear dislocation. Then we follow the idea in [50] and perform a stability analysis of a uniformly translating rectilinear dislocation. We find that the outcome is more complicated than

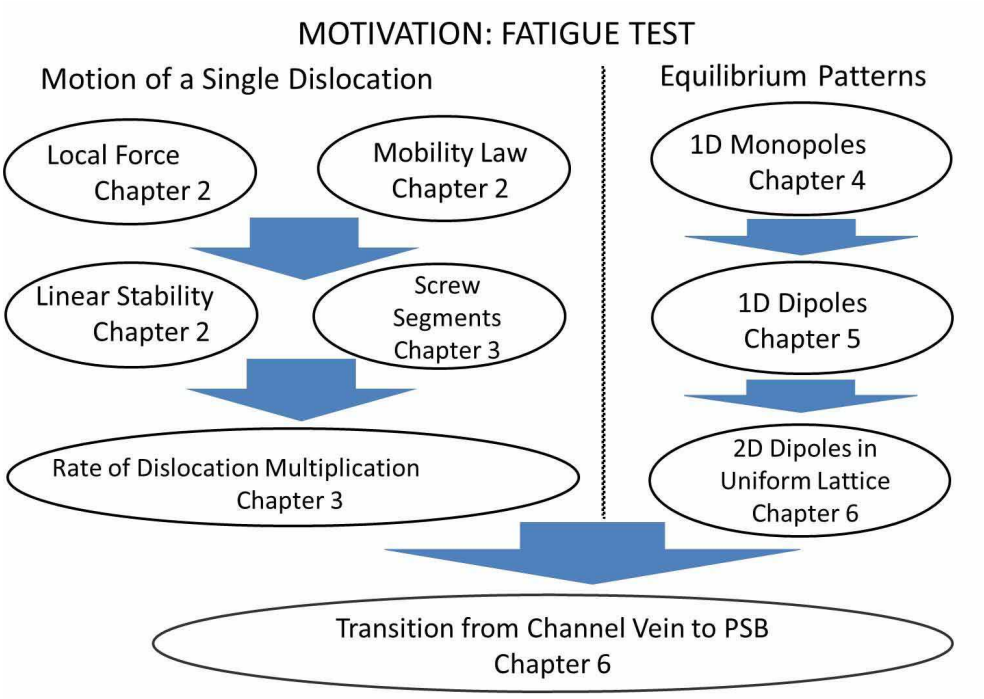


Figure 1.17: Outline of the thesis.

that in [50], due to the anisotropic nature of the motion of an edge dislocation. A counter-intuitive, but a posteriori understandable answer, will be presented. Finally we perform numerical experiments at the end of Chapter 2 which we find are in agreement with the results of the linear stability analysis, and which enable us to track the nonlinear evolution of the dislocation.

In Chapter 3, the screw segments which connect edge dislocations from different veins, are considered. According to experimentalists, their ability to cross slip is widely believed to be the key reason of the multiplication of dislocations in fatigue tests. By using the travelling wave formulations, we are able to quantify how experimental data, such as applied stress amplitude, dictate the geometries of screw segments. A criterion for cross-slip is then proposed in order to predict the rate of dislocation multiplication.

In Chapter 4, we change track and examine equilibria for a large number of straight dislocations. By using the multiple-scale technique, we manage to derive an equation describing the density distribution for a row of screw or edge monopoles, which is validated by comparing with the existing results and numerical simulations. Then in Chapter 5, equipped with this multiple-scale method, we carry out a similar procedure for a row of dislocation pairs. Here we are forced to proceed to higher order in the

expansion to determine an equation for the pair density. We find that the density is constant when the applied stress is uniform. At the end of this chapter, numerical results are presented to validate the theory.

In Chapter 6, we generalise our one dimensional result to two-dimensional unstressed periodic lattices. We find three types of equilibria. By performing a stability analysis, we see a natural change in stability as a bifurcation parameter is varied, which indicates a shift in equilibrium type to keep the whole system to be stable. This we believe is a key factor that triggers the transition from channel-veins to PSBs. At the end of this chapter, a model for the formation of PSBs is proposed.

Chapter 2

Mathematical Modelling of Individual Dislocations

Having summarised the existing results of dislocations in the previous chapter, we turn to dislocation motion and instability, which are believed to be crucial in understanding the formation of structures such as channel-veins and PSBs. This piece of work is initiated by studying the similarity between dislocations and superconducting vortices. It has been known for some time that superconducting vortices are susceptible to a helical instability if a component of the driving force lies along the vortex line. Such a component produces no motion while the vortex is straight, but will cause any deviation to grow in time.

Our initial thoughts were that dislocations would not be susceptible to the same instability since, unlike superconducting vortices, they are more or less required to lie in a slip plane. However, we will see that the helical instability does manifest itself in the dislocation case, with the evolution proceeding via cross-slip onto many slip planes.

The remainder of the chapter is organised as follows. We firstly introduce a law of motion which allows for but severely impedes climb. Such a law enables us to describe cross slip without needing to specify the slip planes a *priori*. Then an asymptotic expansion of the Peach-Koehler expression for the force produced by a general curvilinear dislocation, as the dislocation line is approached is performed to find the local self force and thus the law of motion. Then a linear stability analysis is performed to determine the most unstable configurations and the maximum growth rate. Finally, we present numerical results conforming to the instability and describe the long time evolution schematically.

2.1 Self-Induced Dislocation Motion

2.1.1 Geometric Parameters for a Dislocation in Three Dimensional Space

An arbitrary dislocation curve in three dimensional space can be parameterised by its arclength s:

$$\boldsymbol{x}(s) = (x_1(s), x_2(s), x_3(s))^T. \tag{2.1}$$

Then the dislocation tangent at $\boldsymbol{x}(s)$, denoted by $\boldsymbol{l}(s)$ can be defined by

$$\boldsymbol{l}(s) = (l_1(s), l_2(s), l_3(s))^T = \frac{\mathrm{d}\boldsymbol{x}}{\mathrm{d}s}. \tag{2.2}$$

By using the Frenet-Serret formulae, we can define the unit normal $\boldsymbol{n}(s)$ and curvature $\kappa(s)$ at $\boldsymbol{x}(s)$ as

$$\boldsymbol{n}(s) = (n_1(s), n_2(s), n_3(s))^T = \frac{\mathrm{d}\boldsymbol{l}/\mathrm{d}s}{|\mathrm{d}\boldsymbol{l}/\mathrm{d}s|} \tag{2.3}$$

and

$$\kappa(s) = \left|\frac{\mathrm{d}\boldsymbol{l}}{\mathrm{d}s}\right|, \tag{2.4}$$

respectively. Moreover, the binormal vector $\boldsymbol{m}(s)$ can also be defined by

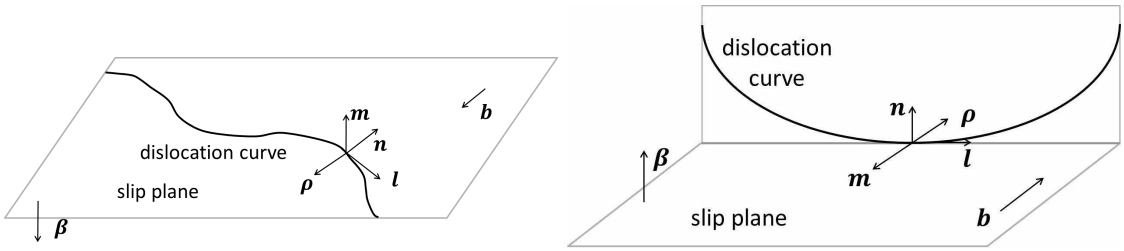
$$\boldsymbol{m}(s) = (m_1(s), m_2(s), m_3(s))^T = \boldsymbol{l}(s) \wedge \boldsymbol{n}(s). \tag{2.5}$$

The above definitions are general for any curve. In the dislocation case, some other geometric parameters are also of importance. It has been discussed in the previous section that a non-screw dislocation has its own slip plane, spanned by the dislocation tangent $\boldsymbol{l}(s)$ and $\boldsymbol{b}$. Hence

$$\boldsymbol{\beta}(s) = \frac{\boldsymbol{l}(s) \wedge \boldsymbol{b}}{|\boldsymbol{l}(s) \wedge \boldsymbol{b}|} \tag{2.6}$$

is a unit normal to the slip plane of the dislocation at $\boldsymbol{x}(s)$. Without causing any ambiguity, from now on, we denote $\boldsymbol{x}(s)$, $\boldsymbol{l}(s)$, $\boldsymbol{n}(s)$, $\boldsymbol{m}(s)$, $\kappa(s)$ and $\boldsymbol{\beta}(s)$ by $\boldsymbol{x}$, $\boldsymbol{l}$, $\boldsymbol{n}$, $\boldsymbol{m}$, κ and $\boldsymbol{\beta}$, respectively.

In Fig. 2.1, the geometric parameters defined above are sketched for two most representative configurations. In Fig. 2.1(a), for a planar mixed dislocation, the normal to the slip plane $\boldsymbol{\beta}$ is the same as $\boldsymbol{m}$, while in Fig. 2.1(b), for a part of a prismatic loop, the glide plane is normal to $\boldsymbol{n}$.



(a) Mixed Planar Dislocation (b) Prismatic Dislocation

Figure 2.1: Geometric parameters of a single dislocation: two most representative dislocations are sketched here. $\boldsymbol{l}$, $\boldsymbol{n}$, $\boldsymbol{m}$ and $\boldsymbol{\beta}$ are the dislocation tangent, normal, binormal and normal to its glide plane, respectively. $\boldsymbol{\rho}$ is the direction of the edge component at $\boldsymbol{x}(s)$.

It can be seen that the strength of the screw component of a dislocation is the projection of $\boldsymbol{b}$ onto $\boldsymbol{l}$:

$$b_l = \boldsymbol{b} \cdot \boldsymbol{l}, \tag{2.7}$$

and its edge component has the strength of $\sqrt{b_n^2 + b_m^2}$, where b_n and b_m are the projection of $\boldsymbol{b}$ onto $\boldsymbol{n}$ and $\boldsymbol{m}$, respectively. The direction of the edge component is then calculated by the projection of $\boldsymbol{b}$ onto the plane normal to the dislocation, which is

$$\boldsymbol{\rho} = \frac{\boldsymbol{b} - b_l \boldsymbol{l}}{|\boldsymbol{b} - b_l \boldsymbol{l}|}, \tag{2.8}$$

when the dislocation is non-screw. The orientation of $\boldsymbol{\rho}$ is also sketched in Fig. 2.1.

From (2.6), it can be easily checked that

$$\boldsymbol{l} \wedge \boldsymbol{\rho} = \frac{\boldsymbol{l} \wedge \boldsymbol{b}}{|\boldsymbol{b} - b_l \boldsymbol{l}|} = \boldsymbol{\beta}.$$

Thus, we have obtained two alternative local rectangular coordinate systems: $\{\boldsymbol{l}, \boldsymbol{n}, \boldsymbol{m}\}$ which is based on the shape of the dislocation curve and $\{\boldsymbol{l}, \boldsymbol{\rho}, \boldsymbol{\beta}\}$ which is based on the dislocation type. In the rest of this chapter, both coordinate systems will be used in order to describe the motion of a single dislocation.

2.1.2 The Law of Motion

Force on a Dislocation

In § 1.2.1, we saw that a dislocation will experience a Peach-Koehler force, deduced from the virtual work:

$$\boldsymbol{f} = (\boldsymbol{\sigma}^t \cdot \boldsymbol{b}) \wedge \boldsymbol{l}, \tag{2.9}$$

where $\boldsymbol{f}$ is the force per unit length; $\boldsymbol{\sigma}^t$ is the total stress acted on the dislocation.

This $\boldsymbol{\sigma}^t$ acts as a combination of three sources: the self-induced stress $\boldsymbol{\sigma}^s$, the external stress $\boldsymbol{\sigma}^e$ and stress from other dislocations $\boldsymbol{\sigma}^o$. From the previous chapter, we know that the stress field from a single dislocation curve is expressed by the Peach-Koelher stress tensor $\boldsymbol{\sigma}^{\mathrm{pk}}$ as in (1.52).

The Mobility Law

The motion of a dislocation in response to its applied force is governed by the mobility law. At room temperature, for an edge dislocation, gliding is much easier than climbing, so that the motion is effectively confined to the slip plane normal to $\boldsymbol{\beta}$, with a velocity approximately proportional to the force per unit length that is resolved in its slip plane, as discussed in § 1.2.2. However, for a screw dislocation its tangent vector and Burgers vector are parallel, so that it may have several glide planes depending on the crystal structure of the material. In the isotropic continuum model, the number of glide planes for a screw dislocation can be regarded as infinite; in effect any plane containing the tangent vector is a potential glide plane.

A common approximation takes the velocity of a dislocation to be proportional to the projection of the force per unit length onto its glide plane. Since a screw dislocation can have any glide plane, for a pure screw no projection is necessary. Thus, if we write

$$\boldsymbol{v} = M\boldsymbol{f},$$

where M is the mobility tensor, then

$$M = \begin{cases} m_g(\mathbf{I} - \boldsymbol{\beta} \otimes \boldsymbol{\beta}) & \text{non-screw;} \\ m_g\mathbf{I} & \text{screw,} \end{cases} \tag{2.10}$$

where m_g is the (constant) glide mobility; $\mathbf{I}$ is the 3-by-3 identity matrix.

An alternative law in which climb is allowed but difficult was given by [61], who wrote

$$M = \begin{cases} m_g(\mathbf{I} - \boldsymbol{\beta} \otimes \boldsymbol{\beta}) + m_c\boldsymbol{\beta} \otimes \boldsymbol{\beta} & \text{non-screw;} \\ m_g\mathbf{I} & \text{screw} \end{cases} \tag{2.11}$$

where m_c is the mobility constant for climb, with $m_c \ll m_g$. This definition resolves the force for an edge dislocation to its glide plane, but keeps the freedom of motion of a screw dislocation. However, there are still difficulties with such a law, due to its singular nature: a pure screw has an isotropic mobility, yet if we add an infinitesimal

edge component we change the mobility drastically. Thus for a curved dislocation on which there is a single point of pure screw with the remainder mixed, the mobility will have a discontinuity at that point. The behaviour of the law then crucially depends on the numerical discretisation used: if the neighbourhood of that point is treated as a small pure screw segment then cross-slip will be allowed, but if there is a small edge component then cross-slip will not occur.

To avoid this situation in which the numerical discretisation is used to regularise a singular law, we instead regularise the law mathematically. Effectively we are saying that cross-slip is possible providing the dislocation is sufficiently close to a pure screw, rather than requiring the dislocation to be exactly pure screw. Specifically we introduce a weighting function $\phi(x)$, such that

$$\phi(0) = 1; \qquad 0 \leq \phi(x) \leq 1; \qquad \phi'(x) < 0; \qquad \lim_{x\to\infty} \phi = 0,$$

and write

$$M = m_g \mathbf{I} + m_g \left(\phi \left(\frac{b^2 - b_l^2}{b^2 \epsilon^2} \right) - 1 \right) \boldsymbol{\beta} \otimes \boldsymbol{\beta}. \tag{2.12}$$

With the mobility tensor M, we can proceed to give our law of motion by

$$\boldsymbol{v} = m_g \left(\mathbf{I} + \left(\phi \left(\frac{b^2 - b_l^2}{b^2 \epsilon^2} \right) - 1 \right) \boldsymbol{\beta} \otimes \boldsymbol{\beta} \right) \boldsymbol{f}^t. \tag{2.13}$$

Here $\epsilon \ll 1$ can be thought as an angle measuring how close to screw a dislocation needs to be in order to cross slip. We choose

$$\phi(x) = e^{-x} \tag{2.14}$$

as our smoothing function. Note that we have taken $m_c = 0$ for simplicity, but that ϕ can easily be modified to allow for the climb of edge dislocations.

To calculate the self-induced law of motion for a dislocation curve we need to calculate the self-induced force. In the following subsection we find the local self-induced stress in the vicinity of an arbitrary curved dislocation through an asymptotic expansion of the Peach-Koehler expression (1.52).

2.1.3 The Local Stress Field of a Curvilinear Dislocation

As derived in the previous chapter, the stress at $\boldsymbol{x}$ exerted by an arbitrary curved dislocation C can be calculated by the Peach-Koehler stress tensor in (1.52):

$$\begin{aligned}\boldsymbol{\sigma}^{\mathrm{pk}}(\boldsymbol{x}) = \frac{\mu}{4\pi}\left(\int_C (\boldsymbol{b}\wedge\nabla)\frac{1}{Z}\otimes \mathrm{d}\boldsymbol{q} + \left(\int_C (\boldsymbol{b}\wedge\nabla)\frac{1}{Z}\otimes \mathrm{d}\boldsymbol{q}\right)^T\right) \\ + \frac{\mu}{4\pi(1-\nu)}\int_C (\mathrm{d}\boldsymbol{q}\cdot(\boldsymbol{b}\wedge\nabla))\left((\nabla\otimes\nabla - \mathbf{I}\nabla^2)\,Z,\right.\end{aligned} \tag{2.15}$$

where $\boldsymbol{q}$ is a point on dislocation curve; $\boldsymbol{z} = \boldsymbol{q} - \boldsymbol{x}$; $Z = |\boldsymbol{z}|$; '∇' is the gradient with respect to $\boldsymbol{q}$.

From the fact that

$$\nabla Z = -\frac{\boldsymbol{z}}{Z},$$

the Peach-Koehler stress tensor (2.15) can be rewritten as

$$\boldsymbol{\sigma}^{\mathrm{pk}} = \boldsymbol{\sigma}^1 + (\boldsymbol{\sigma}^1)^T + \boldsymbol{\sigma}^2, \tag{2.16}$$

where

$$\boldsymbol{\sigma}^1 = -\frac{\mu}{4\pi}\int_C \frac{\boldsymbol{b}\wedge\boldsymbol{z}}{Z^3}\otimes \mathrm{d}\boldsymbol{q} \tag{2.17}$$

and

$$\boldsymbol{\sigma}^2 = \frac{\mu}{4\pi(1-\nu)}\int_C (\mathrm{d}\boldsymbol{q}\cdot(\boldsymbol{b}\wedge\nabla))\left((\nabla\otimes\nabla)Z + \frac{2}{Z}\mathbf{I}\right). \tag{2.18}$$

The integrands in (2.17) and (2.18) are sufficiently singular that as the point $\boldsymbol{x}$ approaches the dislocation the dominant contribution to the stress arises from the integral over nearby points on the dislocation curve. We introduce a local curvilinear coordinate system (s, r, θ) by writing

$$\boldsymbol{x} = \boldsymbol{q}(s) + \boldsymbol{n}(s) r\cos\theta + \boldsymbol{m}(s) r\sin\theta,$$

where $\boldsymbol{q}(s)$ is the nearest point to $\boldsymbol{x}$ on the dislocation curve (parameterised by the arc length s); r is the distance from $\boldsymbol{x}$ to the dislocation. As discussed above, the vectors $(\boldsymbol{l}, \boldsymbol{n}, \boldsymbol{m})$ form an orthogonal triad, and r and θ are local polar coordinates in the $\boldsymbol{n}$-$\boldsymbol{m}$ plane.

We wish to evaluate the stress $\boldsymbol{\sigma}^{\mathrm{pk}}$ as $\boldsymbol{x}$ approaches a point on the dislocation curve $\boldsymbol{q}(s_0)$, that is, as $s \to s_0$ and $r \to 0$. To this end we rescale $r = \varepsilon R$ and consider the

limit $\varepsilon \to 0$. We split the dislocation curve into a local part and non-local part by writing

$$\int_C = \int_{s_0-L}^{s_0+L} + \int_{C_1},$$

where L is such that $1/|\log\varepsilon| \ll L \ll 1$. In the local integral the dislocation curve $\boldsymbol{q}$ can be expanded in the vicinity of s_0 as

$$\boldsymbol{q}(s) \sim \boldsymbol{q}_0 + \boldsymbol{l}_0\varepsilon l + \boldsymbol{n}_0\frac{1}{2}\kappa_0\varepsilon^2 l^2 + \cdots,$$

where $\varepsilon l = s - s_0$ is the arc length, κ_0 is the curvature at s_0, and $\boldsymbol{q}_0 = \boldsymbol{q}(s_0)$, etc. The terms in the integrand can be similarly expanded, such as

$$\boldsymbol{z} = \boldsymbol{q}(s_0+\varepsilon l) - \boldsymbol{x} \sim -\varepsilon(\boldsymbol{n}_0 R\cos\theta + \boldsymbol{m}_0 R\sin\theta - \boldsymbol{l}_0 l) + \varepsilon^2\boldsymbol{n}_0\frac{\kappa_0 l^2}{2} + \cdots, \quad (2.19)$$

and

$$\mathrm{d}\boldsymbol{q}(s_0+\varepsilon l) \sim \left(\varepsilon\boldsymbol{l}_0 + \varepsilon^2\boldsymbol{n}_0\kappa_0 l + \mathcal{O}(\varepsilon^3)\right)\mathrm{d}l. \quad (2.20)$$

We also decompose the Burgers vector into the local coordinate system at s_0 by

$$\boldsymbol{b} = b_n\boldsymbol{n}_0 + b_m\boldsymbol{m}_0 + b_l\boldsymbol{l}_0. \quad (2.21)$$

Henceforth, for ease of notation and without chance of confusion, we drop the subscript 0 from $\boldsymbol{q}$, $\boldsymbol{l}$, $\boldsymbol{n}$, $\boldsymbol{m}$, and κ. Now we can incorporate (2.19), (2.20), and (2.21) into (2.17) and (2.18), and express the result in terms of the local coordinate system $(\boldsymbol{n}, \boldsymbol{m}, \boldsymbol{l})$.

Expansion of $\boldsymbol{\sigma}^1$

Using the fact that

$$\frac{1}{Z^3} \sim \frac{1}{\varepsilon^3}\frac{1}{(R^2+l^2)^{3/2}} + \frac{1}{\varepsilon^2}\frac{3\kappa R\cos\theta l^2}{2(R^2+l^2)^{5/2}} + \mathcal{O}\left(\frac{1}{\varepsilon}\right),$$

the expansion for $\boldsymbol{\sigma}^1$ in (2.17) can be derived in terms of local coordinates. Instead of giving the cumbersome details of all the calculations, we only list the possible singular terms. From (2.20), we can see that the projection from $\mathrm{d}\boldsymbol{q}$ to $\boldsymbol{m}$ is $\mathcal{O}(\varepsilon^3)$, which makes all the terms arising from $\otimes\boldsymbol{m}$ in $\boldsymbol{\sigma}^1$ regular. Therefore, only the remaining

six entries for the second order tensor in the local coordinate system need to be considered, and these are:

$$\begin{aligned}
\sigma_{nn} &\sim -\frac{\mu}{4\pi}\int_{-L/\varepsilon}^{L/\varepsilon}\frac{b_m\kappa l^2}{(R^2+l^2)^{3/2}}\mathrm{d}l+\mathcal{O}(1)\sim\frac{\mu b_m\kappa}{2\pi}\log(R\varepsilon)+\mathcal{O}(1),\\
\sigma_{nl} &\sim -\frac{\mu}{4\pi\varepsilon}\int_{-L/\varepsilon}^{L/\varepsilon}\frac{b_l R\sin\theta}{(R^2+l^2)^{3/2}}\mathrm{d}l+\mathcal{O}(1)\sim-\frac{\mu}{2\pi R\varepsilon}b_l\sin\theta+\mathcal{O}(1),\\
\sigma_{mn} &\sim \frac{\mu}{4\pi}\int_{-L/\varepsilon}^{L/\varepsilon}\frac{\kappa(b_l R\cos\theta+b_n l)}{(R^2+l^2)^{3/2}}l\mathrm{d}l+\mathcal{O}(1)\sim-\frac{\mu b_n\kappa}{2\pi}\log(R\varepsilon)+\mathcal{O}(1),\\
\sigma_{ml} &\sim \frac{\mu}{4\pi\varepsilon}\int_{-L/\varepsilon}^{L/\varepsilon}\frac{b_l R\cos\theta+b_n l}{(R^2+l^2)^{3/2}}\mathrm{d}l-\frac{\mu}{8\pi}\int_{-L/\varepsilon}^{L/\varepsilon}\frac{b_l\kappa l^2}{(R^2+l^2)^{3/2}}\mathrm{d}l+\mathcal{O}(1)\\
&\sim \frac{\mu}{2\pi R\varepsilon}b_l\cos\theta+\frac{\mu b_l\kappa}{4\pi}\log(R\varepsilon)+\mathcal{O}(1),\\
\sigma_{ln} &\sim \frac{\mu}{4\pi}\int_{-L/\varepsilon}^{L/\varepsilon}\frac{b_n R\sin\theta\kappa}{(R^2+l^2)^{3/2}}l\mathrm{d}l+\mathcal{O}(1)=\mathcal{O}(1),\\
\sigma_{ll} &\sim \frac{\mu}{4\pi\varepsilon}\int_{-L/\varepsilon}^{L/\varepsilon}\frac{b_n R\sin\theta-b_m R\cos\theta}{(R^2+l^2)^{3/2}}\mathrm{d}l+\frac{\mu}{8\pi}\int_{-L/\varepsilon}^{L/\varepsilon}\frac{b_m\kappa l^2}{(R^2+l^2)^{3/2}}\mathrm{d}l+\mathcal{O}(1)\\
&\sim \frac{\mu}{2\pi R\varepsilon}(b_n\sin\theta-b_m\cos\theta)-\frac{\mu b_m\kappa}{4\pi}\log(R\varepsilon)+\mathcal{O}(1).
\end{aligned}$$

To summarise, the expansion $\boldsymbol{\sigma}^1$ in the local basis $(\boldsymbol{n},\boldsymbol{m},\boldsymbol{l})$ is

$$\boldsymbol{\sigma}^1\sim\frac{1}{\varepsilon R}\frac{\mu}{2\pi}\begin{pmatrix}0&0&-b_l\sin\theta\\0&0&b_l\cos\theta\\0&0&b_n\sin\theta-b_m\cos\theta\end{pmatrix}+\log(R\varepsilon)\frac{\mu\kappa}{2\pi}\begin{pmatrix}b_m&0&0\\-b_n&0&b_l/2\\0&0&-b_m/2\end{pmatrix}+\cdots, \tag{2.22}$$

as $\varepsilon\to 0$.

Expansion of $\boldsymbol{\sigma}^2$

By using the fact that

$$\frac{\partial^2 Z}{\partial q_i\partial q_j}=\delta_{ij}\frac{1}{Z}-\frac{z_i z_j}{Z^3},$$

where z_i is the i-th entry of $\boldsymbol{z}$ and δ_{ij} is the Kronecker delta, we can rewrite $\boldsymbol{\sigma}^2$ as

$$\begin{aligned}
\frac{4\pi(1-\nu)}{\mu}\boldsymbol{\sigma}^2&=\int_{-L/\varepsilon}^{L/\varepsilon}(\mathrm{d}\boldsymbol{q}\cdot(\boldsymbol{b}\wedge\nabla))\left((\nabla\otimes\nabla)Z+\frac{2}{Z}\mathbf{I}\right)\\
&=\int_{-L/\varepsilon}^{L/\varepsilon}\frac{\mathrm{d}\boldsymbol{q}}{Z^3}\cdot(\boldsymbol{b}\wedge\nabla Z)\,\mathbf{I}-\int_{-L/\varepsilon}^{L/\varepsilon}(\mathrm{d}\boldsymbol{q}\cdot(\boldsymbol{b}\wedge\nabla))\left(\frac{\boldsymbol{z}\otimes\boldsymbol{z}}{Z^3}\right).
\end{aligned} \tag{2.23}$$

From the first term of (2.23), we obtain

$$\begin{aligned}
&\int_{-L/\varepsilon}^{L/\varepsilon} \frac{\mathrm{d}\boldsymbol{q}}{Z^3} \cdot (\boldsymbol{b} \wedge \boldsymbol{z})\mathbf{I} \\
&\qquad \sim \quad -\frac{1}{\varepsilon}\int_{-L/\varepsilon}^{L/\varepsilon} \frac{b_n R\sin\theta - b_m R\cos\theta}{(R^2+l^2)^{3/2}}\mathrm{d}l\,\mathbf{I} - \frac{1}{2}\int_{-L/\varepsilon}^{L/\varepsilon} \frac{b_m \kappa l^2}{(R^2+l^2)^{3/2}} l^2 \mathrm{d}l\,\mathbf{I} + \mathcal{O}(1) \\
&\qquad = \quad \frac{2}{R\varepsilon}(b_n\sin\theta - b_m\cos\theta)\mathbf{I} - b_m\kappa\log(R\varepsilon)\mathbf{I} + \mathcal{O}(1). \qquad (2.24)
\end{aligned}$$

The second term of (2.23) can rewritten

$$\begin{aligned}
&-\int_{-L/\varepsilon}^{L/\varepsilon} (\mathrm{d}\boldsymbol{q}\cdot(\boldsymbol{b}\wedge\nabla'))\left(\frac{1}{Z^3}(\boldsymbol{z}\otimes\boldsymbol{z})\right) \\
&\qquad = \quad -\int_{-L/\varepsilon}^{L/\varepsilon} (\mathrm{d}\boldsymbol{q}\cdot(\boldsymbol{b}\wedge\nabla'))\frac{\boldsymbol{z}\otimes\boldsymbol{z}}{Z^3} - \int_{-L/\varepsilon}^{L/\varepsilon}\left(\frac{\mathrm{d}\boldsymbol{q}}{Z^3}\cdot(\boldsymbol{b}\wedge\nabla')\right)(\boldsymbol{z}\otimes\boldsymbol{z}) \\
&\qquad = \quad \int_{-L/\varepsilon}^{L/\varepsilon} \frac{3\mathrm{d}\boldsymbol{q}}{Z^5}\cdot(\boldsymbol{b}\wedge\boldsymbol{z})(\boldsymbol{z}\otimes\boldsymbol{z}) - \int_{-L/\varepsilon}^{L/\varepsilon}\left(\frac{\mathrm{d}\boldsymbol{q}}{Z^3}\cdot(\boldsymbol{b}\wedge\nabla')\right)(\boldsymbol{z}\otimes\boldsymbol{z}) \\
&\qquad = \quad \boldsymbol{\sigma}^{21} + \boldsymbol{\sigma}^{22},
\end{aligned}$$

say. From the expansion

$$\frac{\mathrm{d}\boldsymbol{q}}{Z^5}\cdot(\boldsymbol{b}\wedge\boldsymbol{z}) \sim -\frac{1}{\varepsilon^3}\frac{(b_n R\sin\theta - b_m\cos\theta)\mathrm{d}l}{(R^2+l^2)^{5/2}} + \frac{1}{\varepsilon^2}\frac{b_m\kappa l^2\mathrm{d}l}{(R^2+l^2)^{5/2}} + \mathcal{O}\left(\frac{1}{\varepsilon}\right),$$

$\boldsymbol{\sigma}^{21}$ can be calculated term-by-term in a similar way to $\boldsymbol{\sigma}^1$, giving

$$\begin{aligned}
\sigma_{nn} \quad &\sim \quad -\frac{1}{\varepsilon}\int_{-L/\varepsilon}^{L/\varepsilon} \frac{(b_n\sin\theta - b_m\cos\theta)R^3\cos^2\theta}{(R^2+l^2)^{5/2}}\mathrm{d}l + \mathcal{O}(1) \\
&\sim \quad -\frac{4\cos^2\theta(b_n\sin\theta - b_m\cos\theta)}{3R\varepsilon} + \mathcal{O}(1), \\
\sigma_{mn} = \sigma_{nm} \quad &\sim \quad -\frac{1}{\varepsilon}\int_{-L/\varepsilon}^{L/\varepsilon} \frac{(b_n\sin\theta - b_m\cos\theta)R^3\cos\theta\sin\theta}{(R^2+l^2)^{5/2}}\mathrm{d}l + \mathcal{O}(1) \\
&\sim \quad -\frac{4\cos\theta\sin\theta(b_n\sin\theta - b_m\cos\theta)}{3R\varepsilon} + \mathcal{O}(1), \\
\sigma_{nl} \sim \sigma_{ln} \quad &\sim \quad \int_{-L/\varepsilon}^{L/\varepsilon} \frac{b_l\kappa R^2\cos\theta\sin\theta}{(R^2+l^2)^{5/2}} l^2\mathrm{d}l + \mathcal{O}(1) \sim \mathcal{O}(1),
\end{aligned}$$

$$
\begin{aligned}
\sigma_{mm} &\sim -\frac{1}{\varepsilon}\int_{-L/\varepsilon}^{L/\varepsilon}\frac{(b_n\sin\theta - b_m\cos\theta)R^3\sin^2\theta}{(R^2+l^2)^{5/2}}\mathrm{d}l + \mathcal{O}(1)\\
&\sim -\frac{4\sin^2\theta(b_n\sin\theta - b_m\cos\theta)}{3R\varepsilon} + \mathcal{O}(1),\\
\sigma_{ml}\sim\sigma_{lm} &\sim \int_{-L/\varepsilon}^{L/\varepsilon}\frac{b_l\kappa R^2\sin^2\theta}{(R^2+l^2)^{5/2}}l^2\mathrm{d}l + \mathcal{O}(1)\sim\mathcal{O}(1),\\
\sigma_{ll} &\sim -\frac{1}{\varepsilon}\int_{-L/\varepsilon}^{L/\varepsilon}\frac{(b_n\sin\theta - b_m\cos\theta)Rl^2}{(R^2+l^2)^{5/2}}\mathrm{d}l + \frac{1}{2}\int_{-L/\varepsilon}^{L/\varepsilon}\frac{b_m\kappa l^4}{(R^2+l^2)^{5/2}}\mathrm{d}l + \mathcal{O}(1)\\
&\sim -\frac{2(b_n\sin\theta - b_m\cos\theta)}{3R\varepsilon} - b_m\kappa\log(R\varepsilon) + \mathcal{O}(1).
\end{aligned}
$$

Thus

$$
\begin{aligned}
\boldsymbol{\sigma}^{21} \sim\ & -\frac{4}{R\varepsilon}(b_n\cos\theta - b_m\sin\theta)\begin{pmatrix}\cos^2\theta & \cos\theta\sin\theta & 0\\ \cos\theta\sin\theta & \sin^2\theta & 0\\ 0 & 0 & 1/2\end{pmatrix}\\
&+\kappa\log(R\varepsilon)\begin{pmatrix}0&0&0\\0&0&0\\0&0&-3b_m\end{pmatrix} + \mathcal{O}(1). \qquad (2.25)
\end{aligned}
$$

From Appendix A.3, the integrand of $\boldsymbol{\sigma}^{22}$ can be written as

$$
\begin{aligned}
-\mathrm{d}\boldsymbol{q}\cdot\frac{1}{Z^3}(\boldsymbol{b}\wedge\nabla'(\boldsymbol{z}\otimes\boldsymbol{z})) &= \frac{\mathrm{d}l}{Z^3}(-\varepsilon b_n + \varepsilon^2 b_l\kappa l)\left((\boldsymbol{z}\otimes\boldsymbol{m}) + (\boldsymbol{m}\otimes\boldsymbol{z})\right)\\
&+\frac{\varepsilon b_m\mathrm{d}l}{Z^3}\left((\boldsymbol{z}\otimes\boldsymbol{n}) + (\boldsymbol{n}\otimes\boldsymbol{z})\right) - \frac{\varepsilon^2 b_m\kappa l}{Z^3}\left((\boldsymbol{z}\otimes\boldsymbol{l}) + (\boldsymbol{l}\otimes\boldsymbol{z})\right). \qquad (2.26)
\end{aligned}
$$

With the expansion

$$
-\frac{1}{Z^3}(\varepsilon b_n - \varepsilon^2 b_l\kappa l) \sim -\frac{1}{\varepsilon^2}\frac{b_n}{(R^2+l^2)^{3/2}} - \frac{1}{\varepsilon}\frac{3b_n\kappa R\cos\theta l^2}{2(R^2+l^2)^{5/2}} + \frac{1}{\varepsilon}\frac{b_l\kappa l}{(R^2+l^2)^{3/2}} + \cdots,
$$

the singular terms in $\boldsymbol{\sigma}^{22}$ can be evaluated as

$$
\begin{aligned}
\sigma_{nm} &\sim \frac{1}{\varepsilon}\int_{-L/\varepsilon}^{L/\varepsilon}\frac{b_n R\cos\theta}{(R^2+l^2)^{3/2}}\mathrm{d}l - \frac{1}{2}\int_{-L/\varepsilon}^{L/\varepsilon}\frac{b_n\kappa l^2}{(R^2+l^2)^{3/2}}\mathrm{d}l + \frac{3}{2}\int_{-L/\varepsilon}^{L/\varepsilon}\frac{b_n\kappa R^2\cos^2\theta}{(R^2+l^2)^{5/2}}l^2\mathrm{d}l + o(1)\\
&\sim \frac{2}{R\varepsilon}b_n\cos\theta + b_n\kappa\log(R\varepsilon) + \mathcal{O}(1),\\
\sigma_{mm} &\sim \frac{1}{\varepsilon}\int_{-L/\varepsilon}^{L/\varepsilon}\frac{b_n R\sin\theta}{(R^2+l^2)^{3/2}}\mathrm{d}l + \frac{3}{2}\int_{-L/\varepsilon}^{L/\varepsilon}\frac{b_n\kappa R^2\cos\theta\sin\theta}{(R^2+l^2)^{5/2}}l^2\mathrm{d}l + \mathcal{O}(1)\\
&\sim \frac{2}{R\varepsilon}b_n\sin\theta + \mathcal{O}(1),\\
\sigma_{lm} &\sim \int_{-L/\varepsilon}^{L/\varepsilon}\frac{b_l\kappa l^2}{(R^2+l^2)^{3/2}}\mathrm{d}l + \mathcal{O}(1) = -2b_l\kappa\log(R\varepsilon) + \mathcal{O}(1),
\end{aligned}
$$

$$
\begin{aligned}
\sigma_{nn} &\sim -\frac{1}{\varepsilon}\int_{-L/\varepsilon}^{L/\varepsilon}\frac{b_m R\cos\theta}{(R^2+l^2)^{3/2}}\mathrm{d}l+\frac{1}{2}\int_{-L/\varepsilon}^{L/\varepsilon}\frac{b_m\kappa l^2}{(R^2+l^2)^{3/2}}l^2\mathrm{d}l+\mathcal{O}(1)\\
&\sim -\frac{2}{R\varepsilon}b_m\cos\theta-b_m\kappa\log(R\varepsilon)+\mathcal{O}(1),\\
\sigma_{mn} &\sim -\frac{1}{\varepsilon}\int_{-L/\varepsilon}^{L/\varepsilon}\frac{b_m R\sin\theta}{(R^2+l^2)^{3/2}}\mathrm{d}l+\mathcal{O}(1)=-\frac{2}{R\varepsilon}b_m\sin\theta+\mathcal{O}(1),\\
\sigma_{ll} &\sim \int_{-L/\varepsilon}^{L/\varepsilon}\frac{b_m\kappa l^2}{(R^2+l^2)^{3/2}}\mathrm{d}l+\mathcal{O}(1)=-2b_m\kappa\log(R\varepsilon)+\mathcal{O}(1).
\end{aligned}
$$

Thus the expression for $\boldsymbol{\sigma}^{22}$ can be obtained as

$$
\begin{aligned}
\boldsymbol{\sigma}^{22} \sim\ & \frac{2}{R\varepsilon}\begin{pmatrix} -2b_m\cos\theta & b_n\cos\theta-b_m\sin\theta & 0\\ b_n\cos\theta-b_m\sin\theta & 2b_n\sin\theta & 0\\ 0 & 0 & 0\end{pmatrix}\\
&+2\log(R\varepsilon)\begin{pmatrix} -b_m & b_n/2 & 0\\ b_n/2 & 0 & -b_l\\ 0 & -b_l & 2b_m\end{pmatrix}+\cdots
\end{aligned}
\tag{2.27}
$$

Combining all of the expressions above, we finally obtain the local expansion for the Peach-Koehler stress tensor in the local coordinate system $(\boldsymbol{n},\boldsymbol{m},\boldsymbol{l})$ as

$$
\begin{aligned}
\boldsymbol{\sigma}^{\mathrm{pk}} \sim\ & \frac{1}{r}\frac{\mu}{2\pi}\begin{pmatrix} \frac{-b_n\sin\theta(1+2\cos^2\theta)+b_m\cos\theta\cos2\theta}{1-\nu} & \frac{b_n\cos\theta\cos2\theta-b_m\sin\theta\cos2\theta}{1-\nu} & -b_l\sin\theta\\ \frac{b_n\cos\theta\cos2\theta-b_m\sin\theta\cos2\theta}{1-\nu} & \frac{b_n\sin\theta\cos2\theta+b_m\cos\theta(1+2\sin^2\theta)}{1-\nu} & b_l\cos\theta\\ -b_l\sin\theta & b_l\cos\theta & -\frac{2\nu(b_n\sin\theta-b_m\cos\theta)}{1-\nu}\end{pmatrix}\\
&+\log\left(\frac{1}{r}\right)\cdot\frac{\mu\kappa}{2\pi}\begin{pmatrix} -\frac{b_m(1-4\nu)}{2(1-\nu)} & \frac{b_n(1-2\nu)}{2(1-\nu)} & 0\\ \frac{b_n(1-2\nu)}{2(1-\nu)} & -\frac{b_m}{2(1-\nu)} & \frac{b_l(1+\nu)}{2(1-\nu)}\\ 0 & \frac{b_l(1+\nu)}{2(1-\nu)} & -b_m\end{pmatrix}+\cdots
\end{aligned}
\tag{2.28}
$$

as $r\to 0$. The first term in (2.28) corresponds to the stress field induced by a rectilinear dislocation. The effect of the curvature of the dislocation is felt in the second term, which is proportional to κ.

2.1.4 Motion of a Curvilinear Dislocation

To determine the self-induced motion of a curvilinear dislocation we need to evaluate the local force given by (2.9) on the dislocation curve $r=0$. We see that the singular nature of the stress causes a problem: the force evaluates to infinity. This singularity is regularised by the finite size of the dislocation core: within a few Burgers vectors of the core the Volterra model of a dislocation breaks down, and an atomistic model should be used. For similar scenarios in the field of fluid or superconducting

vortex dynamics the inner model regularising the core is still a continuum model, and matched asymptotic expansions can be used to determine the self-induced law of motion. One interpretation of the resulting law is that the vortex moves in response to the average force over the core region, corresponding to $r < \varepsilon$ say.

Following the systematic procedure of matched inner and outer asymptotic expansions for the case of dislocations is much more difficult, due to the discrete nature of the inner core model. However, we can still regularise the singularity by supposing that the dislocation responds to the average stress over the core region. Performing this average, the first term in the expansion (2.28) vanishes, and so does not generate any dislocation motion: rectilinear dislocations in an unbounded material have no self-induced motion. The second term evaluates to

$$\boldsymbol{f}_{\rm loc} = (\boldsymbol{b}\cdot\boldsymbol{\sigma})\wedge\boldsymbol{l} = \log\left(\frac{1}{\varepsilon}\right)\cdot\frac{\mu\kappa}{4\pi(1-\nu)}\begin{pmatrix} b_n^2(1-2\nu)-b_m^2+b_l^2(1+\nu) \\ 2b_nb_m\nu \\ 0\end{pmatrix}+\cdots, \quad (2.29)$$

where ε is the dislocation core radius.

As discussed above, the projection of the Burgers vector onto the plane normal to the dislocation, (which, providing the dislocation is not pure screw, is given by $\boldsymbol{\rho}$) plays a key role in the law of motion; $\boldsymbol{\rho}$ is the direction normal to the dislocation in the glide plane. By replacing $b_m\boldsymbol{m}$ by $\sqrt{b^2-b_l^2}\boldsymbol{\rho}-b_n\boldsymbol{n}$, the local force can be decomposed into components parallel to $\boldsymbol{\rho}$ and $\boldsymbol{n}$ as

$$\boldsymbol{f}_{\rm loc} = \left(\frac{\mu\kappa}{4\pi(1-\nu)}\left((b_l^2(2+\nu)+2b_n^2(1-2\nu)-b^2)\boldsymbol{n}+2\nu b_n\sqrt{b^2-b_l^2}\boldsymbol{\rho}\right)\right)\log\left(\frac{1}{\varepsilon}\right)+\mathcal{O}(1). \quad (2.30)$$

We now consider that in addition to the self-induced force the dislocation is subject to a uniform external stress $\boldsymbol{\sigma}_{\rm ext}$. After rescaling time with $1/\log(1/\varepsilon)$ the law of motion is then

$$\begin{aligned}\boldsymbol{v} \;=\; & \frac{\mu\phi\left(\frac{b^2-b_l^2}{b^2\epsilon^2}\right)m_g\left(b_l^2(2+\nu)+2b_n^2(1-2\nu)-b^2\right)}{4\pi(1-\nu)}\kappa\boldsymbol{n} \\ & +\frac{2\mu\nu m_g\kappa b_n\sqrt{b^2-b_l^2}}{4\pi(1-\nu)}\boldsymbol{\rho}+\frac{\mu\kappa b_n m_g\left(1-\phi\left(\frac{b^2-b_l^2}{b^2\epsilon^2}\right)\right)\left(b_l^2(2+\nu)+2b_n^2(1-2\nu)-b^2\right)}{4\pi(1-\nu)\sqrt{b^2-b_l^2}}\boldsymbol{\rho} \\ & +m_g\left(1-\phi\left(\frac{b^2-b_l^2}{b^2\epsilon^2}\right)\right)(\boldsymbol{\rho}\cdot(\boldsymbol{F}\wedge\boldsymbol{l}))\,\boldsymbol{\rho}+\phi\left(\frac{b^2-b_l^2}{b^2\epsilon^2}\right)m_g(\boldsymbol{F}\wedge\boldsymbol{l}), \end{aligned} \quad (2.31)$$

where $\boldsymbol{F} = (1/\log(1/\varepsilon))\,\boldsymbol{\sigma}_{\rm ext}\cdot\boldsymbol{b}$ (which we assume is $O(1)$ as $\varepsilon\to 0$; this is the distinguished limit). Note that we could add an arbitrary multiple of $\boldsymbol{l}$ to the right-

hand side of (2.31): such a term does not change the curve C, it merely corresponds to a different parametrisation of it.

2.2 Linear Stability Analysis

With (2.31), we can track the evolution of a rectilinear dislocation. As stated in the beginning of this chapter, superconducting vortices are similar to dislocations. In this section, we follow the idea in [50] and examine the helical stability of a dislocation line.

Note that, in this chapter, the Einstein summation convention is dropped temporarily. We use a subscript variable to denote 'differentiate with respect to this variable'.

We firstly consider the stability of a uniformly translating rectilinear dislocation. Without loss of generality, we choose the x_3 coordinate to be in the direction of the tangent, and denote it z for convenience. We still have one degree of freedom in orientating the coordinate system. We fix this by choosing the x_1 direction to be the projection of the Burgers vector in the plane normal to the dislocation, so that $b_1 \geq 0$, $b_2 = 0$, $b_3 \geq 0$. Then the solution of (2.31) corresponding to a uniformly translating rectilinear dislocation is

$$\boldsymbol{x}^{(0)} = m_g \begin{pmatrix} F_2 t \\ -\phi\left(\frac{b^2 - b_l^2}{b^2\epsilon^2}\right) F_1 t \\ z \end{pmatrix}. \tag{2.32}$$

For $b_1 > 0$, we perturb this solution by setting

$$\boldsymbol{x} = \boldsymbol{x}^{(0)} + \delta \begin{pmatrix} w_1 \\ w_2 \\ w_3 \end{pmatrix},$$

where $\delta \ll \epsilon^2$. Then related quantities in (2.31) can be expanded in terms of δ:

$$\boldsymbol{l} \sim \begin{pmatrix} 0 \\ 0 \\ 1 \end{pmatrix} + \delta \begin{pmatrix} w_{1,z} \\ w_{2,z} \\ 0 \end{pmatrix}; \qquad \kappa\boldsymbol{n} \sim \delta \begin{pmatrix} w_{1,zz} \\ w_{2,zz} \\ 0 \end{pmatrix}; \qquad \boldsymbol{n} \sim \frac{1}{\sqrt{w_{1,zz}^2 + w_{2,zz}^2}} \begin{pmatrix} w_{1,zz} \\ w_{2,zz} \\ 0 \end{pmatrix};$$

$$\boldsymbol{\rho}\cdot(\boldsymbol{F}\wedge\boldsymbol{l}) \sim F_2 + \delta\frac{F_1 b_3 - F_3 b_1}{b_1} w_{2,z}; \qquad \phi\left(\frac{b^2 - b_l^2}{b^2\epsilon^2}\right) \sim \phi\left(\frac{b_1^2}{b^2\epsilon^2}\right) - 2\delta\phi'\left(\frac{b_1^2}{b^2\epsilon^2}\right)\frac{b_1 b_3}{b^2\epsilon^2}.$$

Collecting the $\mathcal{O}(\delta)$ terms in the law of motion (2.31) gives the evolution of the perturbation as

$$\begin{aligned} w_{1,t} &= \frac{\mu m_g}{4\pi(1-\nu)} \cdot \left(b_3^2(1+\nu) + b_1^2(1-2\nu)w_{1,zz}^2\right) w_{1,zz} \\ &\quad - m_g\left((\phi-1)F_1 b_3/b_1 + F_3\right) w_{2,z}, \qquad (2.33) \\ w_{2,t} &= \frac{\mu m_g \phi}{4\pi(1-\nu)} \cdot \left(b_3^2(1+\nu) - b_1^2 \cdot \frac{(4\nu-1)w_{1,zz}^2 + w_{2,zz}^2}{w_{1,zz}^2 + w_{2,zz}^2}\right) w_{2,zz} \\ &\quad + m_g \phi F_3 w_{1,z} + \frac{2m_g \phi' b_1 b_3}{\epsilon^2 b^2} F_1 w_{1,z} + m_g(\phi-1)\frac{F_2 b_3}{b_1} w_{2,z}, \qquad (2.34) \\ w_{3,t} &= -m_g F_2 w_{1,z} + \phi m_g F_1 w_{2,z}, \qquad (2.35) \end{aligned}$$

where ϕ and ϕ' denote $\phi(b_1^2/(b^2\epsilon^2))$ and $\phi'(b_1^2/(b^2\epsilon^2))$, respectively. Equation (2.35) simply describes a change in parametrisation of the dislocation curve and we do not need to consider it further (in fact we could add a multiple of $\boldsymbol{l}$ to (2.31) to make $w_{3,t} = 0$ if we wished).

It is curious that, although we have linearised in δ and are performing a linear stability analysis, equation (2.34) is nonlinear. This is because the law of motion depends on the direction of the normal $\boldsymbol{n}$ and this is undefined for a rectilinear dislocation at $\delta = 0$. This complication does not arise for the analagous problem of a superconducting vortex, because there every normal vector is multiplied by the curvature, which is small. However, in the case of dislocations, the mobility depends directly on the normal vector (through the glide plane), so that $\mathbf{n}$ appears independently of the curvature.

To make progress we consider the limit in which $\epsilon \to 0$, that is, in which only dislocations which are close to screw can cross slip. The behaviour of the equations then depends crucially on how close to a pure screw the original dislocation is, that is, it depends on the size of b_1. We consider each distinguished limit in turn.

2.2.1 Perturbation to a Mixed Dislocation ($b_1 = \mathcal{O}(1)$)

In this case, $b_1^2/(\epsilon^2 b^2) \gg 1$, so that both ϕ and ϕ' are exponentially small. Thus equations (2.33) and (2.34) can be reduced to

$$\begin{aligned} w_{1,t} &= \frac{\mu m_g}{4\pi(1-\nu)}\left(b_3^2(1+\nu) + b_1^2(1-2\nu)\right) w_{1,zz} - m_g\left(F_3 - F_1\frac{b_3}{b_1}\right) w_{2,z}, \qquad (2.36) \\ w_{2,t} &= -m_g \frac{F_2 b_3}{b_1} w_{2,z}, \qquad (2.37) \end{aligned}$$

at leading order in ϵ. In this case, the glide plane is specified as the x-z plane, then zero initial data for w_2 leaves $w_2 \equiv 0$, so that the dislocation remains within the glide plane, while w_1 satisfies the diffusion equation

$$w_{1,t} = \frac{\mu m_g}{4\pi(1-\nu)} \left(b_3^2(1+\nu) + b_1^2(1-2\nu) \right) w_{1,zz}. \tag{2.38}$$

Since [34] $-1 < \nu < 1/2$, the diffusion coefficient in (2.38) is positive and the dislocation is stable; in this case the self-induced force causes the perturbation to decay.

2.2.2 Perturbation to an Almost-Screw Dislocation ($b_1 = \mathcal{O}(\epsilon)$)

We set $b_1 = \bar{b}_1 \epsilon$. Then $b_1^2/(\epsilon^2 b^2) = \bar{b}_1^2/b^2$ is $\mathcal{O}(1)$. Since

$$b_3 = b - \frac{\bar{b}_1}{2b}\epsilon^2 + O(\epsilon^4),$$

equations (2.33) and (2.34) respectively, can be rewritten as

$$\begin{aligned} w_{1,t} &= \frac{\mu m_g b^2(1+\nu)}{4\pi(1-\nu)} w_{1,zz} \\ &\quad - m_g \left((\phi - 1)(\bar{b}_1 \sigma_{11}\epsilon + b\sigma_{13}) \frac{b}{\bar{b}_1 \epsilon} + (\bar{b}_1 \sigma_{13}\epsilon + b\sigma_{33}) \right) w_{2,z} \qquad (2.39) \\ w_{2,t} &= \frac{\mu \phi m_g b^2(1+\nu)}{4\pi(1-\nu)} w_{2,zz} + m_g \phi (\bar{b}_1 \sigma_{13}\epsilon + b\sigma_{33}) w_{1,z} \\ &\quad + \frac{2 m_g \phi' \bar{b}_1}{b\epsilon} (\bar{b}_1 \sigma_{11}\epsilon + b\sigma_{13}) w_{1,z} + m_g(\phi - 1) \frac{b^2 \sigma_{23}}{\bar{b}_1 \epsilon} w_{2,z}, \qquad (2.40) \end{aligned}$$

where, in this regime, ϕ and ϕ' denote $\phi(\bar{b}_1^2/b^2)$ and $\phi'(\bar{b}_1^2/b^2)$, respectively.

Equations (2.39) and (2.40) are singularly perturbed since the coefficients of the second order derivatives are $\mathcal{O}(\epsilon)$ times those of the first order derivatives. We rescale by setting $t' = t/\epsilon^2$, $z' = z/\epsilon$, to give, at leading order,

$$w_{1,t'} = \frac{\mu m_g b^2(1+\nu)}{4\pi(1-\nu)} w_{1,z'z'} + m_g(1-\phi) \frac{b^2 \sigma_{13}}{\bar{b}_1} w_{2z'}, \tag{2.41}$$

$$w_{2,t'} = \frac{\mu m_g \phi b^2(1+\nu)}{4\pi(1-\nu)} w_{2,z'z'} + 2 m_g \phi'(s) \bar{b}_1 \sigma_{13} w_{1z'} + m_g(\phi - 1) \frac{b^2 \sigma_{23}}{\bar{b}_1} w_{2z'} \tag{2.42}$$

which we write as

$$\frac{\partial}{\partial t'} \begin{pmatrix} w_1 \\ w_2 \end{pmatrix} = \begin{pmatrix} c_1 & 0 \\ 0 & c_2 \end{pmatrix} \frac{\partial^2}{\partial z'^2} \begin{pmatrix} w_1 \\ w_2 \end{pmatrix} + \begin{pmatrix} 0 & a_{12} \\ a_{21} & a_{22} \end{pmatrix} \frac{\partial}{\partial z'} \begin{pmatrix} w_1 \\ w_2 \end{pmatrix}, \tag{2.43}$$

where

$$c_1 = \frac{\mu m_g b^2(1+\nu)}{4\pi(1-\nu)}, \quad c_2 = \frac{\mu m_g \phi b^2(1+\nu)}{4\pi(1-\nu)},$$

and

$$a_{12} = m_g(1-\phi)\frac{b^2\sigma_{13}}{\bar{b}_1}, \quad a_{21} = 2m_g\phi'(s)\bar{b}_1\sigma_{13}, \quad a_{22} = m_g(\phi-1)\frac{b^2\sigma_{23}}{\bar{b}_1}.$$

The solutions are of the form

$$w_1 = A_1 e^{\lambda' t'}\cos kz' + B_1 e^{\lambda' t'}\sin kz', \qquad w_2 = A_2 e^{\lambda' t'}\cos kz' + B_2 e^{\lambda' t'}\sin kz', \quad (2.44)$$

where

$$(A_1(\lambda' + c_1k^2) - a_{12}B_2k)\cos kz' + (B_1(\lambda' + c_1k^2) + a_{12}A_2k)\sin kz' = 0,$$

$$(A_2(\lambda'+c_1k^2) - a_{21}B_1k - a_{22}B_2k)\cos kz' + (B_2(\lambda'+c_2k^2) + a_{21}A_1k + a_{22}A_2k)\sin kz' = 0.$$

Equating coefficients of the trigonometric functions results in the systems of linear equations

$$\begin{pmatrix} \lambda'+c_1k^2 & 0 & 0 & -a_{12}k \\ 0 & a_{12}k & \lambda'+c_1k^2 & 0 \\ 0 & \lambda'+c_2k^2 & -a_{21}k & -a_{22}k \\ a_{21}k & a_{22}k & 0 & \lambda'+c_2k^2 \end{pmatrix} \begin{pmatrix} A_1 \\ A_2 \\ B_1 \\ B_2 \end{pmatrix} = \begin{pmatrix} 0 \\ 0 \\ 0 \\ 0 \end{pmatrix}. \quad (2.45)$$

The condition for the determinant of the matrix to vanish gives the dispersion relation between λ' and k. The cumbersome calculations are presented in Appendix A.4, with the result that

$$\Re(\lambda') = \frac{m_g bk}{2\sqrt{2}}\sqrt{\sqrt{(ckb)^4 + L^2 + 2(ckb)^2 Q} + (ckb)^2 - L} - \frac{m_g c_0 b^2(1+\phi)k^2}{2}, \quad (2.46)$$

where

$$L = (1-\phi)^2\frac{b^2\sigma_{23}^2}{\bar{b}_1^2} + 8(1-\phi)\phi'\sigma_{13}^2; \quad Q = (1-\phi)^2\frac{b^2\sigma_{23}^2}{\bar{b}_1^2} - 8(1-\phi)\phi'\sigma_{13}^2;$$

$$c_0 = \frac{\mu(1+\nu)}{4\pi(1-\nu)}; \quad c = c_0(1-\phi).$$

Here it is noted that two pairs of conjugate roots are the outcome by solving the fourth-order polynomial in Appendix A.4. Between the two values of $\Re(\lambda')$, we are only looking for one with a possibly positive value (this value effectively results in an unstable system). Then we are primarily interested in the maximum growth rate $\Re(\lambda')_{\max}$; if it is positive, then the system will be unstable. Note that since we are

working in a rescaled t and z, the wavelength of the perturbation on the original lengthscale is $\mathcal{O}(\epsilon)$, and the growth rate on the original timescale is $\lambda = \lambda'/\epsilon^2$.

We may reduce the number of parameters by setting

$$k = \frac{\sigma_{13}\hat{k}}{cb}, \quad \lambda' = \frac{m_g \sigma_{13}^2 \hat{\lambda}}{c_0}.$$

Then equation (2.46) can be written as

$$\Re(\hat{\lambda}) = \frac{\hat{k}}{2\sqrt{2}(1-\phi)} \sqrt{\sqrt{\hat{k}^4 + \hat{L}^2 + 2\hat{k}^2\hat{Q}} + \hat{k}^2 - \hat{L}} - \frac{(1+\phi)\hat{k}^2}{2(1-\phi)^2}, \tag{2.47}$$

where

$$\hat{L} = (1-\phi)^2 \frac{b^2}{\bar{b}_1^2}\frac{\sigma_{23}^2}{\sigma_{13}^2} + 8(1-\phi)\phi', \quad \hat{Q} = (1-\phi)^2 \frac{b^2}{\bar{b}_1^2}\frac{\sigma_{23}^2}{\sigma_{13}^2} - 8(1-\phi)\phi'.$$

The remaining parameters are $\bar{b}_1/b$, which measures the edge component of the Burgers vector, and the ratio of shear stresses σ_{23}/σ_{13} (recall that ϕ is a function of $\bar{b}_1/b$). Fig. 2.2 shows maximum $\Re(\hat{\lambda})_{\max}$ as a function of $\bar{b}_1/b$ and $\sigma_{23}^2/\sigma_{13}^2$.

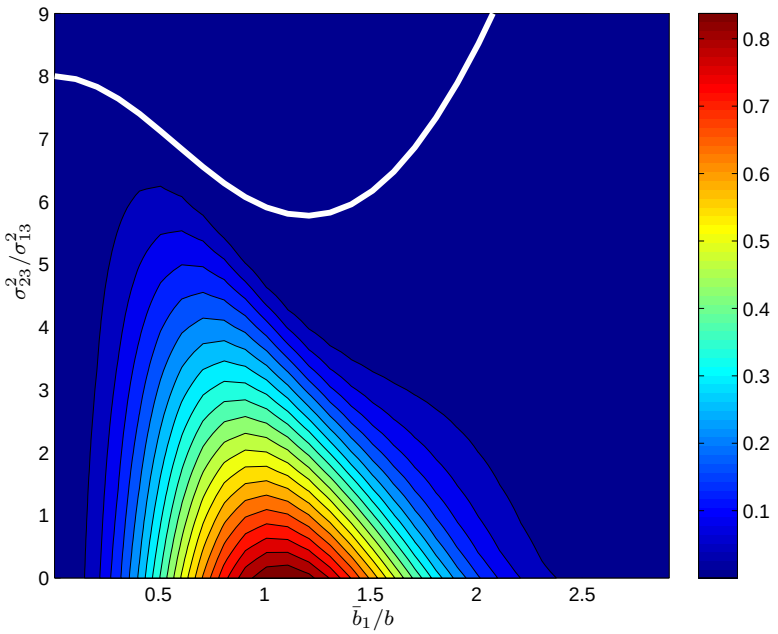


Figure 2.2: The rescaled maximum growth rate $\Re(\hat{\lambda})_{\max}$ as a function of $\bar{b}_1/b$ and $\sigma_{23}^2/\sigma_{13}^2$. The dislocation is unstable in the region below the solid white curve. The maximum growth rate is 0.18 and occurs for $\sigma_{23} = 0$, $\bar{b}_1/b \approx 0.981$ with a corresponding wavenumber $\hat{k} \approx 0.54$.

By analysing (2.47) we find that the dislocation is unstable if

$$\frac{\sigma_{23}^2}{\sigma_{13}^2} < -\frac{2\bar{b}_1^2(1+\phi)^2\phi'}{b^2(1-\phi)\phi}, \tag{2.48}$$

which is shown as the solid line in Fig. 2.2 (remember that $\phi' < 0$, so the right-hand side of (2.48) is positive). Note that the unstable region grows as $\bar{b}_1$ grows, which seems to contradict the fact that the dislocation is stable for b_1 of order one. However, as $\bar{b}_1$ grows the growth rate decays to zero exponentially and the wavenumber also tends zero, so that these (marginally) unstable modes match into the neutrally stable mode of the mixed dislocation.

The most unstable mode occurs when $\sigma_{23} = 0$, $\bar{b}_1/b \approx 0.981$ with a corresponding wavenumber $\hat{k} \approx 0.54$.

For the actual maximum growth rate, we need to scale back to (t, z) to obtain

$$\Re(\lambda)_{\max} = \frac{m_g\sigma_{13}^2\Re(\lambda')_{\max}}{c_0\epsilon^2}. \tag{2.49}$$

2.2.3 Perturbation to a Screw-Dominant Dislocation ($b_1 = \mathcal{O}(\epsilon^2)$)

We set $b_1 = \tilde{b}_1\epsilon^2$. Then

$$b_3 = b - \frac{\tilde{b}_1^2}{2b}\epsilon^4 + o(\epsilon^4), \qquad \phi\left(\frac{\tilde{b}_1^2\epsilon^2}{b^2}\right) = 1 + \frac{\tilde{b}_1^2}{b^2}\phi_0'\epsilon^2 + \mathcal{O}(\epsilon^4),$$

where $\phi_0' = \phi'(0)$. Incorporating these into (2.33) and (2.34) gives

$$\begin{aligned} w_{1,t} &= \frac{\mu m_g b^2(1+\nu)}{4\pi(1-\nu)}w_{1,zz} - m_g(\tilde{b}_1\sigma_{13}\phi_0' + b\sigma_{33})w_{2,z}, \\ w_{2,t} &= \frac{\mu m_g b^2(1+\nu)}{4\pi(1-\nu)}w_{2,zz} + m_g(b\sigma_{33} + 2\phi_0'\tilde{b}_1\sigma_{13})w_{1,z} + m_g\phi_0'\tilde{b}_1\sigma_{23}w_{2,z}. \end{aligned} \tag{2.50}$$

Similarly we write (2.50) as another linear PDE system:

$$\frac{\partial}{\partial t}\begin{pmatrix} w_1 \\ w_2 \end{pmatrix} = c_1\frac{\partial^2}{\partial z^2}\begin{pmatrix} w_1 \\ w_2 \end{pmatrix} + \begin{pmatrix} 0 & a_{12} \\ a_{21} & a_{22} \end{pmatrix}\frac{\partial}{\partial z}\begin{pmatrix} w_1 \\ w_2 \end{pmatrix}, \tag{2.51}$$

where

$$c_1 = \frac{\mu m_g b^2(1+\nu)}{4\pi(1-\nu)},$$

and

$$a_{12} = -m_g(\tilde{b}_1\sigma_{13}\phi_0' + b\sigma_{33}), \quad a_{21} = m_g(b\sigma_{33} + 2\phi_0'\tilde{b}_1\sigma_{13}), \quad a_{22} = m_g\phi_0'\tilde{b}_1\sigma_{23}.$$

Looking for solutions of the form (2.44) and equating coefficients as before gives

$$\begin{pmatrix} \lambda + c_1k^2 & 0 & 0 & -a_{12}k \\ 0 & a_{12}k & \lambda + c_1k^2 & 0 \\ 0 & \lambda + c_1k^2 & -a_{21}k & -a_{22}k \\ a_{21}k & a_{22}k & 0 & \lambda + c_1k^2 \end{pmatrix} \begin{pmatrix} A_1 \\ A_2 \\ B_1 \\ B_2 \end{pmatrix} = \begin{pmatrix} 0 \\ 0 \\ 0 \\ 0 \end{pmatrix}. \tag{2.52}$$

The detailed calculation of the dispersion relation is given in Appendix A.5. The result is that the dislocation is stable if and only if

$$\tilde{b}_1^2\sigma_{23}^2\phi_0'^2 - 4(\tilde{b}_1\sigma_{13}\phi_0' + b\sigma_{33})(2\tilde{b}_1\sigma_{13}\phi_0' + b\sigma_{33}) \geq 0. \tag{2.53}$$

The maximum growth rate and corresponding wavelength for the unstable case are

$$\Re(\lambda)_{\max} = \frac{m_g(4(\tilde{b}_1\sigma_{13}\phi_0' + b\sigma_{33})(2\tilde{b}_1\sigma_{13}\phi_0' + b\sigma_{33}) - \tilde{b}_1^2\sigma_{23}^2\phi_0'^2)}{16c_0b^2} \tag{2.54}$$

$$= \frac{m_g\sigma_{13}^2}{16c_0}\left(4\left(\frac{\tilde{b}_1}{b}\phi_0' + \frac{\sigma_{33}}{\sigma_{13}}\right)\left(2\frac{\tilde{b}_1}{b}\phi_0' + \frac{\sigma_{33}}{\sigma_{13}}\right) - \frac{\tilde{b}_1^2}{b^2}\frac{\sigma_{23}^2}{\sigma_{13}^2}\phi_0'^2\right), \tag{2.55}$$

$$k_{\max} = \frac{m_g\sqrt{4(\tilde{b}_1\sigma_{13}\phi_0' + b\sigma_{33})(2\tilde{b}_1\sigma_{13}\phi_0' + b\sigma_{33}) - \tilde{b}_1^2\sigma_{23}^2\phi_0'^2}}{4c_0b^2}, \tag{2.56}$$

where

$$c_0 = \frac{\mu(1+\nu)}{4\pi(1-\nu)}.$$

From (2.53) and (2.55) we see that, in this regime, the instability depends on not only on the shear stresses, but also on the normal stress σ_{33}; the key parameters are $\tilde{b}_1/b$, σ_{23}/σ_{13}, and σ_{33}/σ_{13}. We see from (2.55) that for large $\tilde{b}_1/b$ the dislocation is stable if and only if $\sigma_{23}/\sigma_{13} \geq \sqrt{8}$.

In the limit in which $\tilde{b}_1 \ll 1$, so that the dislocation is even closer to a pure screw, the dispersion relation can be written explicitly as

$$\Re(\lambda) = -m_g b\left(\sigma_{33}k + \frac{\mu b(1+\nu)k^2}{4\pi(1-\nu)}\right), \tag{2.57}$$

so that there is a band of unstable wavenumbers

$$k \in \begin{cases} \left(0, -\dfrac{2\pi(1-\nu)\sigma_{33}}{\mu b(1+\nu)}\right), & \sigma_{33} < 0; \\ \left(-\dfrac{2\pi(1-\nu)\sigma_{33}}{\mu b(1+\nu)}, 0\right), & \sigma_{33} > 0. \end{cases}$$

In this regime, the stability and growth rate depend only on the normal stress. We see that the dislocation is always unstable for small $\tilde{b}_1$ if $\sigma_{33} \neq 0$.

Fig. 2.3 depicts the maximum growth rate against $\tilde{b}_1$ for various combinations of applied stress. We see that even when the dislocation is unstable for small and large $\tilde{b}_1$ there may be a region of stability at moderate $\tilde{b}_1$ depending on the relative size and signs of σ_{13}, σ_{23} and σ_{33}.

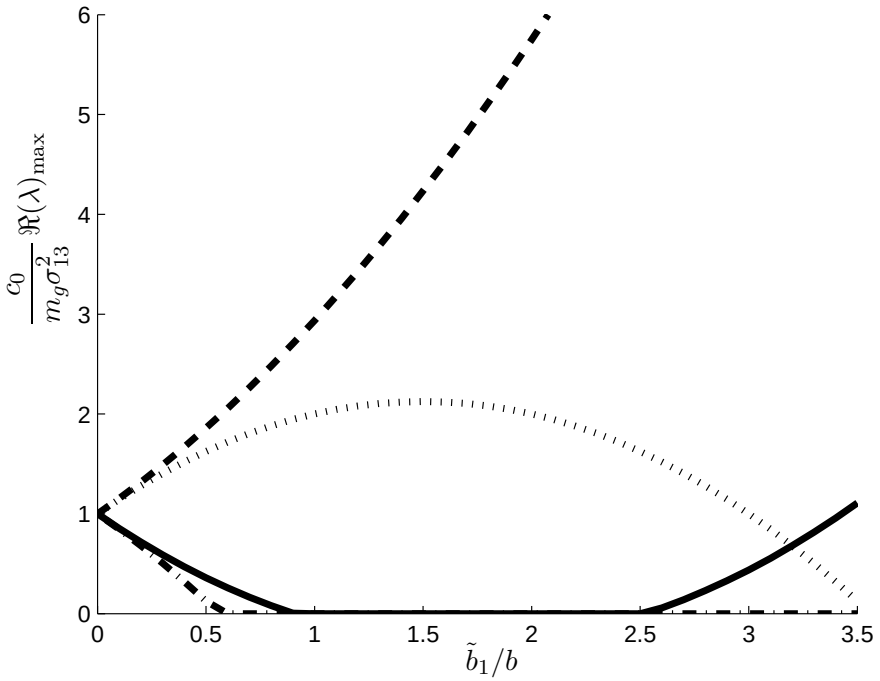


Figure 2.3: The maximum growth rate as a function of $\tilde{b}_1/b$. The solid curve corresponds to $\sigma_{23}/\sigma_{13} = 1$, $\sigma_{33}/\sigma_{13} = 2$; the dashed curve corresponds to $\sigma_{23}/\sigma_{13} = 1$, $\sigma_{33}/\sigma_{13} = -2$; the dotted curve corresponds to $\sigma_{23}/\sigma_{13} = 4$, $\sigma_{33}/\sigma_{13} = -2$; the dash-dotted curve corresponds to $\sigma_{23}/\sigma_{13} = 4$, $\sigma_{33}/\sigma_{13} = 2$. The dislocation is always unstable for $\tilde{b}_1$ small. For large $\tilde{b}_1$ it is stable if and only if $\sigma_{23}/\sigma_{13} \geq \sqrt{8}$. Even when the dislocation is unstable for small and large $\tilde{b}_1$ there may be a region of stability at moderate $\tilde{b}_1$ depending on the relative size and signs of σ_{13}, σ_{23} and σ_{33}.

2.2.4 A Uniformly Valid Dispersion Relation

We have derived two dispersion relations, depending on the size of b_1 with respect to ϵ. Here we use asymptotic matching to make sure that these two relations are consistent with each other, and to derive a uniformly valid maximum growth rate.

To pass from $b_1 \sim \mathcal{O}(\epsilon)$ to $b_1 \sim \mathcal{O}(\epsilon^2)$, we let $\bar{b}_1 \to 0$. Noting that

$$1 - \phi = -\phi_0' \frac{\bar{b}_1^2}{b^2} + o(\bar{b}_1^2),$$

we find that the condition for instability (2.48) becomes $\sigma_{23}^2 < 8\sigma_{13}^2$. When this is satisfied taking the limit $\bar{b}_1 \to 0$ in (2.49) and maximising over k (recalling that $\lambda = \lambda'/\epsilon^2$) gives

$$\Re(\lambda)_{\max} \sim \frac{m_g \bar{b}_1^2 (8\sigma_{13}^2 - \sigma_{23}^2)}{16 c_0 b^2 \epsilon^2}. \tag{2.58}$$

To pass from $b_1 = \mathcal{O}(\epsilon^2)$ to $b_1 = \mathcal{O}(\epsilon)$ we let $\tilde{b}_1 \to \infty$ in (2.54). As we have seen, this also gives instability only if $\sigma_{23}^2 < 8\sigma_{13}^2$, with a maximum growth rate given by (2.58).

Thus our dispersion relations match with each other as they should. We could now give a uniformly valid maximum growth rate by adding together our expressions in each region and subtracting the "overlap" expression (2.58) which has been double counted. However, it is easier to calculate a uniformly valid dispersion relation by determining the growth rate of perturbations in (2.39)-(2.40) without first expanding in powers of ϵ. Such an approach is useful for generating plots, but the result is too unwieldy to analyse analytically in the manner of §2.2.2 and §2.2.3.

Therefore, we can obtain the expression for the maximum growth rate $\Re(\lambda)_{\max}$ in the whole region as a function of $\bar{b}_1 = b_1/\epsilon$. In the inner region, where $b_1 \sim \mathcal{O}(\epsilon^2)$, we have

$$\Re(\lambda_{\text{in}})_{\max} = \begin{cases} 0 & 4\left(\frac{\bar{b}_1}{b}\phi_0' + \frac{\sigma_{33}}{\sigma_{13}}\epsilon\right)\left(\frac{2\bar{b}_1}{b}\phi_0' + \frac{\sigma_{33}}{\sigma_{13}}\epsilon\right) \le \left(\frac{\bar{b}_1\sigma_{23}}{b\sigma_{13}}\right)^2, \\ \frac{m_g\sigma_{13}^2}{16c_0\epsilon^2} \cdot \left(4\left(\frac{\bar{b}_1}{b}\phi_0' + \frac{\sigma_{33}}{\sigma_{13}}\epsilon\right)\left(\frac{2\bar{b}_1}{b}\phi_0' + \frac{\sigma_{33}}{\sigma_{13}}\epsilon\right) - \left(\frac{\bar{b}_1\sigma_{23}}{b\sigma_{13}}\right)^2\right), & \text{otherwise;} \end{cases} \tag{2.59}$$

in the outer region, where $b_1 \sim \mathcal{O}(\epsilon)$, we have

$$\Re(\lambda_{\text{out}})_{\max} = \frac{m_g c_0 \sigma_{13}^2 \hat{k}_{\max}}{2\epsilon^2(1-\phi)} \left(\sqrt{\frac{\sqrt{\hat{k}_{\max}^4 + \hat{L}^2 + 2\hat{k}_{\max}^2\hat{Q}} + \hat{k}_{\max}^2 - \hat{L}}{2}} - \frac{(1+\phi)\hat{k}_{\max}}{(1-\phi)} \right), \tag{2.60}$$

where $\hat{k}_{\max}$ maximise (2.47). In the overlapping region, the maximum growth rate denoted by $\Re(\lambda_{\text{mid}})$ is given in (2.58) when it is unstable. Thus a uniformly valid maximum growth rate can be expressed by

$$\Re(\lambda)_{\max} = \Re(\lambda_{\text{in}})_{\max} + \Re(\lambda_{\text{out}})_{\max} - \Re(\lambda_{\text{mid}})_{\max}. \tag{2.61}$$

Fig. 2.4 uses this uniformly valid dispersion relation to depict the maximum growth rate as a function of $\bar{b}_1$ on a log-log plot to cope with the vastly different growth rates for small and large $\bar{b}_1$.

We see that when the shear-driven instability of §2.2.2 is present it dominates, with a growth-rate which is orders of magnitude greater than the normal-stress-driven instability of §2.2.3.

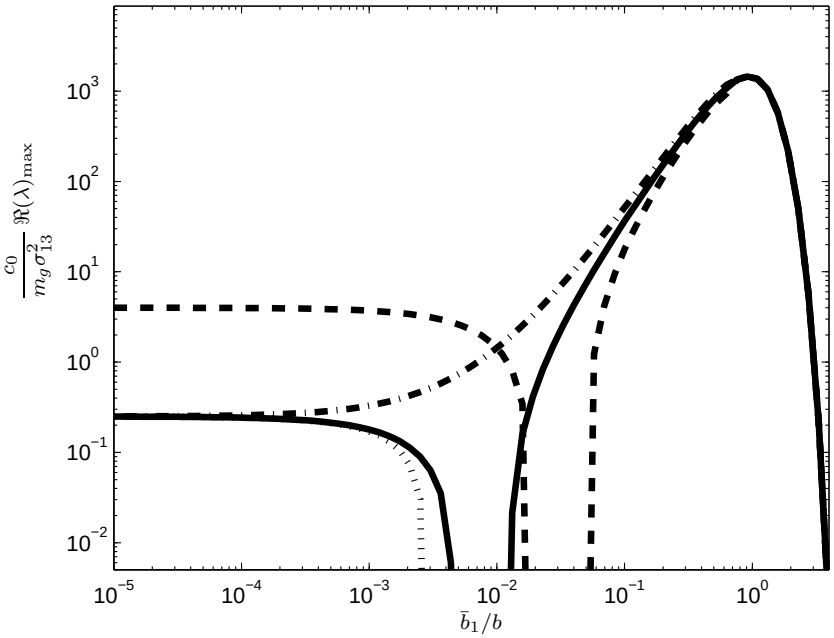


Figure 2.4: The maximum growth rate as a function of $\bar{b}_1$ for various combinations of applied stress. The solid curve corresponds to $\sigma_{23}/\sigma_{13} = 1$, $\sigma_{33}/\sigma_{13} = 4$; the dashed curve corresponds to $\sigma_{23}/\sigma_{13} = 4$, $\sigma_{33}/\sigma_{13} = 1$; the dotted curve corresponds to $\sigma_{23}/\sigma_{13} = 1$, $\sigma_{33}/\sigma_{13} = 1$; the dash-dotted curve corresponds to $\sigma_{23}/\sigma_{13} = -1$, $\sigma_{33}/\sigma_{13} = -1$. For all plots $\epsilon = 0.01$.

We may summarise the results of our stability calculations as follows.

(i) When $b_1 \sim \mathcal{O}(1)$, the dislocation is stable to any planar perturbation.

(ii) When $b_1 \sim \mathcal{O}(\epsilon)$, the dislocation is unstable if the shear-stress ratio σ_{23}/σ_{13} is less than a critical value which depends only on b_1. The wavelength of the most unstable mode is small ($\mathcal{O}(\epsilon)$), and the growth rate is large ($\mathcal{O}(\epsilon^{-2})$).

(iii) When $b_1 \sim \mathcal{O}(\epsilon^2)$,the dislocation is unstable whenever σ_{33} is non zero, for sufficiently small b_1. The wavelength and growth rate of this instability are $\mathcal{O}(1)$.

2.3 Nonlinear Evolution of the Instability

The linear stability analysis is useful for determining the stability of a rectilinear dislocation. However, to track the non-linear evolution of the instabilities we have found, we need to solve the evolution equation (2.31) numerically.

We discretise $\boldsymbol{x}$ and $\boldsymbol{v}$ in time and space. At the n-th time step we use a TVD Runge-Kunta method described in [36] to compute $\boldsymbol{x}^{n+1}$ from $\boldsymbol{x}^n$ and $\boldsymbol{v}^n$ via the following scheme:

$$\boldsymbol{x}^{n+1} = \boldsymbol{x}^n + \boldsymbol{v}^n \Delta t, \qquad \boldsymbol{x}^{n+2} = \boldsymbol{x}^{n+1} + \boldsymbol{v}^{n+1}\Delta t, \qquad \boldsymbol{x}^{n+1/2} = \frac{3}{4}\boldsymbol{x}^n + \frac{1}{4}\boldsymbol{x}^{n+2},$$

$$\boldsymbol{x}^{n+3/2} = \boldsymbol{x}^{n+1/2} + \boldsymbol{v}^{n+1/2}\Delta t, \qquad \boldsymbol{x}^{n+1} = \frac{1}{3}\boldsymbol{x}^n + \frac{2}{3}\boldsymbol{x}^{n+3/2};$$

all the other variables are updated in the sequence

$$\boldsymbol{x} \Rightarrow \boldsymbol{l} \Rightarrow \kappa\boldsymbol{n} \Rightarrow b_l, b_n \Rightarrow \boldsymbol{\rho} \Rightarrow \boldsymbol{v},$$

using the definitions

$$\boldsymbol{l} = \frac{\boldsymbol{x}_z}{|\boldsymbol{x}_z|}, \quad \boldsymbol{n} = \frac{\boldsymbol{l}_z}{|\boldsymbol{l}_z|}.$$

The derivatives of $\boldsymbol{x}$ at z_i are approximated by

$$\left.\frac{\partial \boldsymbol{x}}{\partial z}\right|_{z=z_i} = \frac{\boldsymbol{x}_{i+1} - \boldsymbol{x}_{i-1}}{2\Delta z}$$

and

$$\left.\frac{\partial^2 \boldsymbol{x}}{\partial z^2}\right|_{z=z_i} = \frac{\boldsymbol{x}_{i+1} + \boldsymbol{x}_{i-1} - 2\boldsymbol{x}_i}{\Delta z^2},$$

at z_i, where Δz is the spatial grid size.

We note the following three points. Firstly, we use the approximation that

$$\kappa\boldsymbol{n} = \frac{\partial \boldsymbol{l}}{\partial z} = \frac{1}{|\boldsymbol{x}_z|^2}\left(\boldsymbol{x}_{zz} - (\boldsymbol{l}\cdot\boldsymbol{x}_{zz})\boldsymbol{x}_{zz}\right),$$

to keep the truncation error $O(\Delta z^2)$. Secondly, we impose periodic boundary conditions on all variables except the z-component of displacement x_3, for which we impose

$$x_3(z_1) - x_3(z_2) = z_1 - z_2,$$

where z_1 and z_2 are the two end points. Finally we simply chose $\Delta t = 0.1\Delta x^2$, which was enough to ensure the numerical stability for the examples we considered.

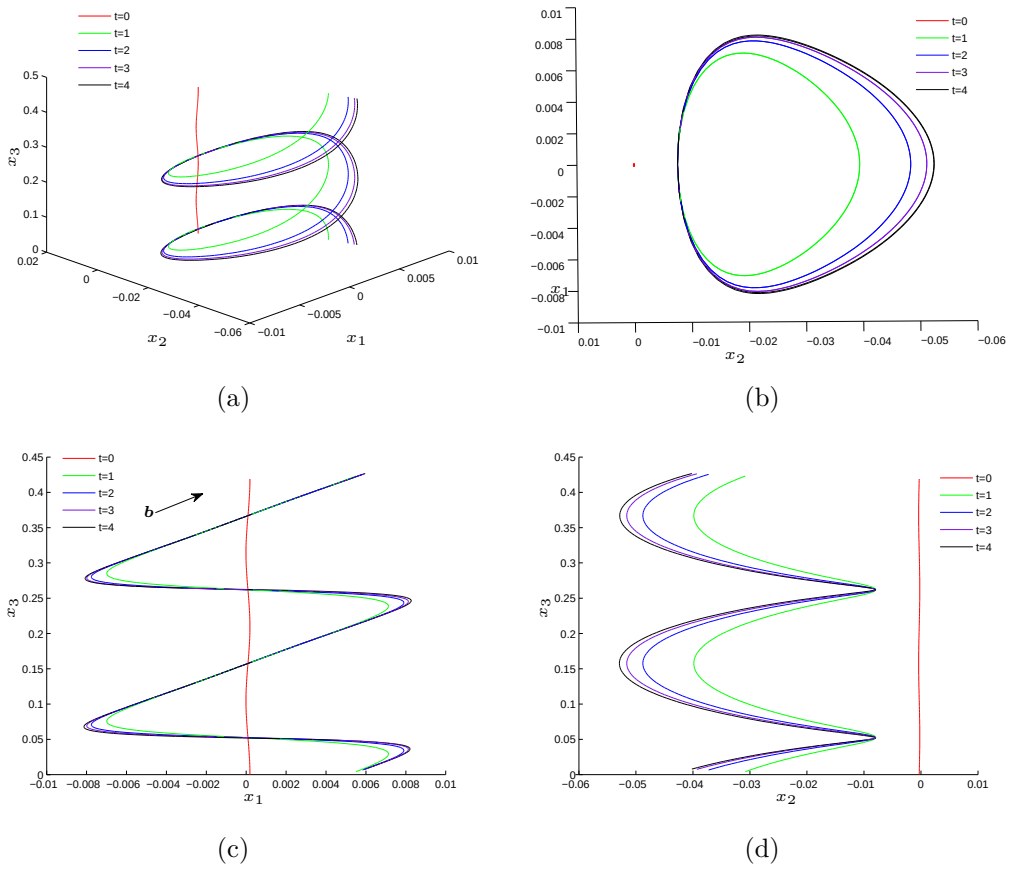


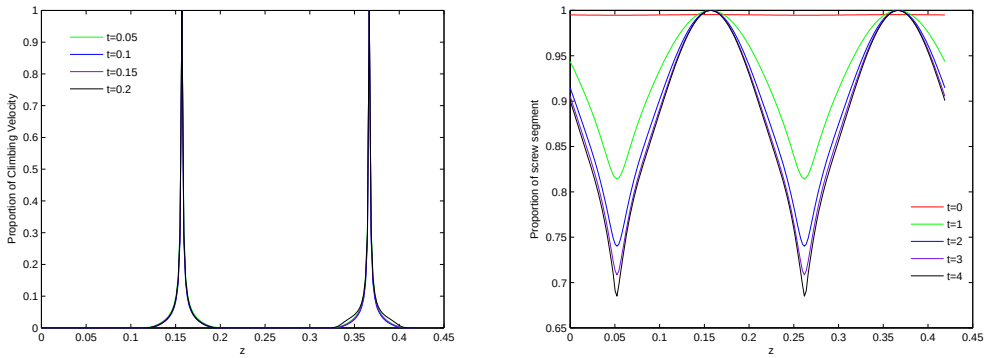
Figure 2.5: Non-linear evolution of a perturbed rectilinear dislocation. (a) three-dimensional view; (b) projection onto the x_1-x_2 plane; (c) projection onto the x_1-x_3 plane; (d) projection to the x_2-x_3 plane. The only nonzero component of the external stress is $\sigma_{13} = 1$.

2.3.1 Numerical Results

We begin by perturbing a dislocation in which $\boldsymbol{b} = (0.1, 0, 1)^T$ and the only nonzero external stress is $\sigma_{13} = 1$. We choose the wavenumber of the perturbation to be $k = 30$. For the simulations we choose $\Delta z = 0.0021$, and $\Delta t = 10^{-7}$.

Fig. 2.5 gives the evolution of the dislocation curve from various angles as well as its projection onto the coordinate planes. Fig. 2.5(b) depicts its projection to the x_1-x_2 plane, from which the expansion can be seen; Fig. 2.5(c) depicts its projection to the x_1-x_3 plane, from which the glide planes parallel to Burgers vector can be identified; Fig. 2.5(d) depicts its projection to the x_2-x_3 plane, from which we can see some parts in the dislocation curve pinned, while the other parts grow.

To try to understand this evolution we show in Fig. 2.6(a) the proportion of the



(a) (b)

Figure 2.6: The left plot gives the proportion of velocity in $\boldsymbol{\beta}$ (normal to the glide plane) direction against the spatial parameter z, showing that most parts of the dislocation do in-plane motion. The right plot depicts the proportion of screw segment at every point parameterized by z, showing that the edge components grow when evolving.

velocity in the direction normal to the glide plane $\boldsymbol{\beta}$ as a function of the spatial parameter z. We see that most parts of the dislocation are moving in the glide plane, with an exponentially small velocity in the cross-slip direction. Fig. 2.6(b) shows the proportion of the dislocation which is screw at every point, again parameterized by z. The parts which are close to pure screw are those which are cross slipping, as we would expect. Noting that initially the dislocation was almost screw, we see that the perturbation has evolved the dislocation into mixed-type dislocations undergoing in-plane motion for most of its length.

To check this, we can always find a plane M passing through the origin, parallel to the glide plane of a randomly chosen point from the dislocation curve. If the unit normal of M is $\boldsymbol{\beta}_0$, then the distance from every point $\boldsymbol{x}$ in the dislocation, to M can be written as follows

$$d = \boldsymbol{\beta}_0 \cdot \boldsymbol{x},$$

when the dislocation is evolving. From the fact that all points sharing the same d are planar, Fig. 2.7 shows that most parts of the dislocation will evolve to stay in a mutually parallel glide plane family after some time.

We can see from Fig. 2.5(b) that for the current parameter values the dislocation will reach a new non-rectilinear equilibrium, in which the "line tension" of the curved parts of the dislocation balances the external stress driving the expansion. This is

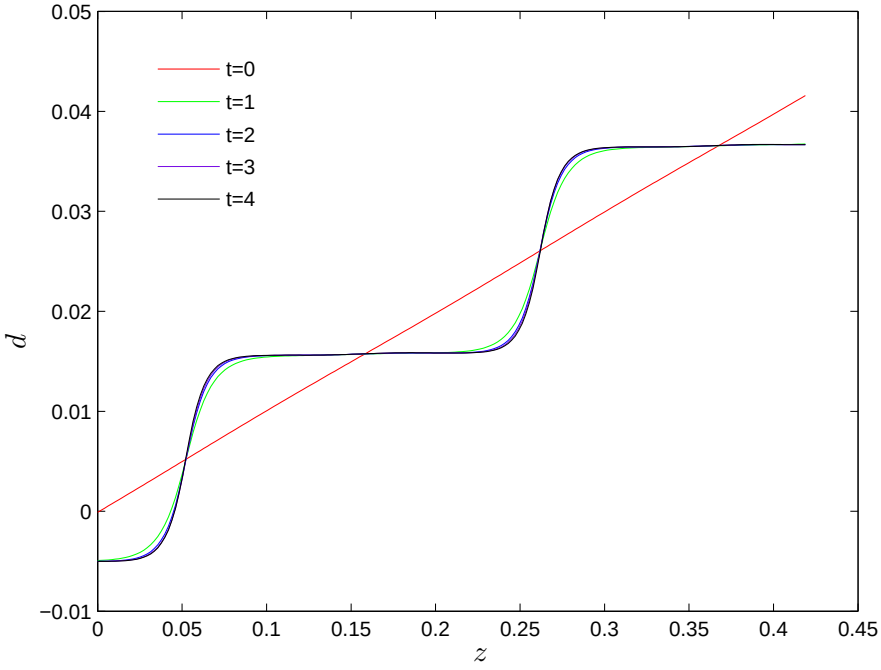


Figure 2.7: Glide plane family: dislocation segments sharing the same d reside in one glide plane. Most dislocation segments will evolve to a family of mutually parallel glide planes.

rather like the way forest interactions may pin a dislocation if the external stress is not too large.

When we increase the only non-vanishing component of the external stress to $\sigma_{13} = 5$, then the evolution behaves differently, as shown in Fig. 2.8 (for which we chose $k = 30$, $\Delta z = 2.0944 \times 10^{-4}$, $\Delta t = 5 \times 10^{-9}$). In this case the external stress is strong enough that no new equilibrium is found.

Fig. 2.8(a) shows the 3-D plot for the evolution. Fig. 2.8(b) shows the projection onto the x_1-x_2 plane, again showing the the expansion due to instability. Fig. 2.8(c) shows the projection onto the x_1-x_3 plane; the family of glide planes, which are all perpendicular to x_1-x_3 plane, can be identified. Fig. 2.8(d) shows the projection onto the x_2-x_3 plane; as before, some points of the dislocation are pinned in this projection.

After some time, the dislocation will move to a family of glide planes normal to $\boldsymbol{\beta} = (0.9950, 0, -0.0995)^T$ (as shown in Fig. 2.9(a)), and have some points pinned (when $z = 0.05$, 0.27 in Fig. 2.9(b)).

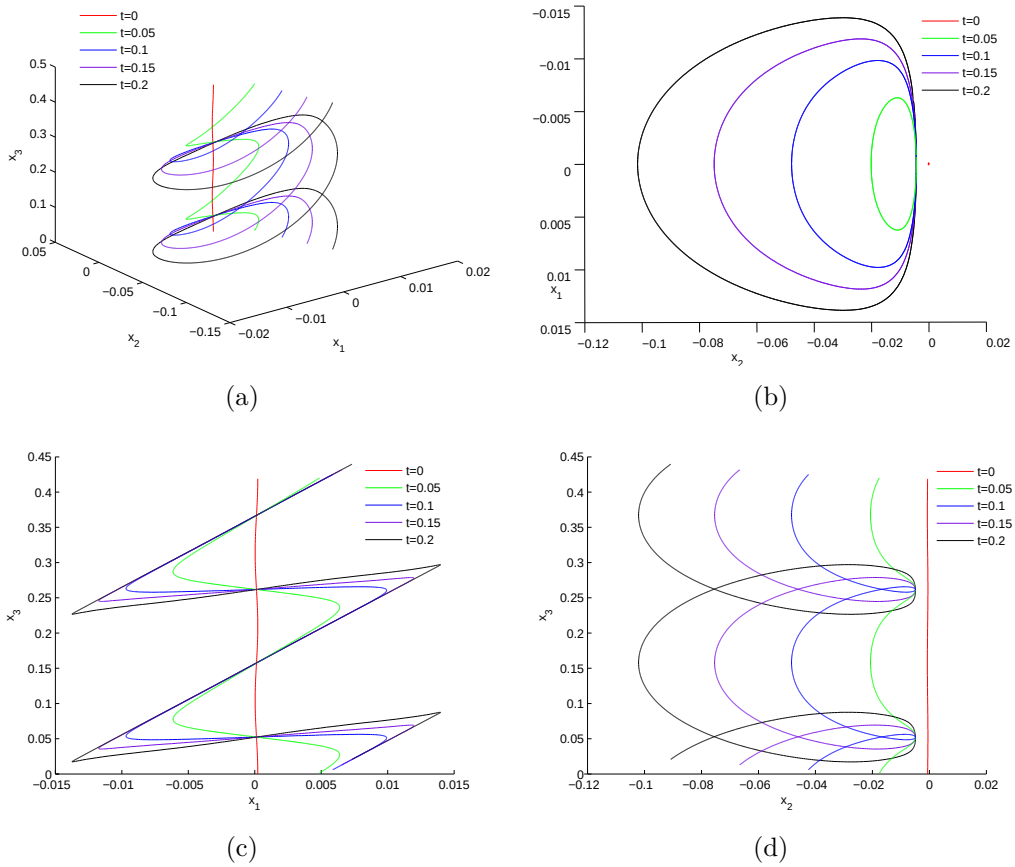


Figure 2.8: Evolution of the dislocation when $\sigma_{13} = 5$. (a) 3-D plot for the evolution; (b) projection onto the x_1-x_2 plane (c) projection onto the x_1-x_3 plane; (d) projection onto the x_2-x_3 plane.

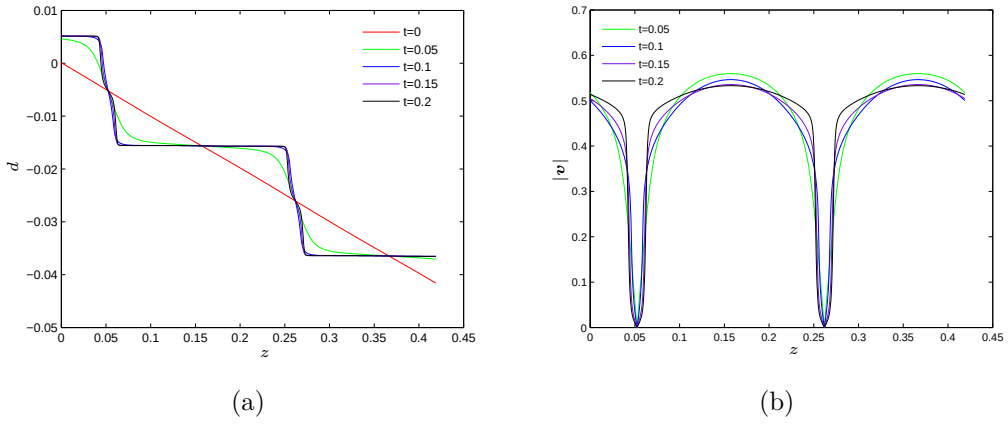


Figure 2.9: (a) shows that the dislocation will evolve to a family of glide planes; (b) draws the magnitude of the velocity at each point.

2.3.2 Discussion

While Fig. 2.5 and 2.8 are useful, they are not so easy to interpret. It is of some use to illustrate schematically the nonlinear evolution of the dislocation line, as in Fig. 2.10.

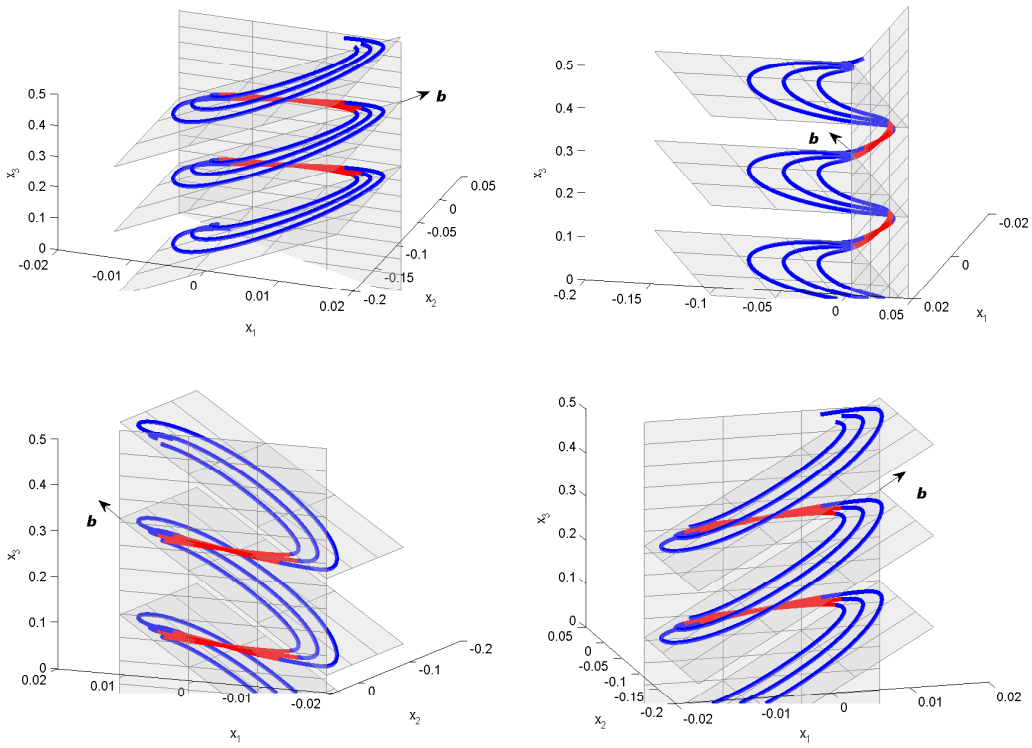


Figure 2.10: Schematic diagram of the nonlinear evolution.

After some time from the initial perturbation the dislocation line will comprise two sets of curves. The expanding blue curves lie in a family of parallel slip planes. They are joined by the red segments, which are straight lines lying in a different slip plane (with normal $(0, 1, 0)^T$), which is the glide plane of the original straight dislocation. Each of these joining red lines rotates around its central point (which doesn't move) and grows in length as the blue curves expand. Cross slip occurs only at the joins of the blue and red segments. The intersections of the two slip systems are, of course, parallel to the Burgers vector.

2.3.3 Implication for Non-Schmid Yield Criterion and Non-Associated Flow

With the schematic diagram in Fig. 2.10, we are enabled to check quantities related to experimental observation. The first one is the choice of $\boldsymbol{\beta}$. In our simulation, $\boldsymbol{\beta}$ is the consequence of the evolution. Whereas in practice, slip planes should be in the family that best resolve the applied stress. This resolved stress component τ^α, known as the Schmid stress, is defined in [59] as

$$\tau^\alpha = (\boldsymbol{\sigma}_{\text{ext}}\boldsymbol{b}^\alpha) \cdot \boldsymbol{\beta}^\alpha, \tag{2.62}$$

where $\boldsymbol{\beta}^\alpha$ and $\boldsymbol{b}^\alpha$ are the normal to the α-family slip planes and slip direction, respectively. Following this, we give our criterion for slip plane to be

$$\max_{\boldsymbol{\beta},\ |\boldsymbol{\beta}|=1} (\sigma_{\text{ext}}\boldsymbol{b}) \cdot \boldsymbol{\beta}, \qquad \text{s.t.} \quad \boldsymbol{\beta} \cdot \boldsymbol{b} = 0, \tag{2.63}$$

i.e. to maximise resolved stress subject to keeping the Burgers vector in slip plane.

It can be seen from Appendix A.6 that, in this context, where

$$\boldsymbol{b} = \begin{pmatrix} b_1 \\ 0 \\ b_3 \end{pmatrix}, \qquad \boldsymbol{\sigma}_{\text{ext}} = \begin{pmatrix} 0 & 0 & \sigma_{13} \\ 0 & 0 & \sigma_{23} \\ \sigma_{13} & \sigma_{23} & 0 \end{pmatrix},$$

the solution to (2.63) is

$$\boldsymbol{\beta} = \frac{1}{\sqrt{(1+s^2)((s^2+1)p^2 + (1-s^2)^2)}} \begin{pmatrix} 1-s^2 \\ p(1+s^2) \\ -s(1-s^2) \end{pmatrix}, \tag{2.64}$$

where $p = \sigma_{23}/\sigma_{13}$ and $s = b_1/b_3$. From (2.64), it can be seen that $\boldsymbol{\beta}$ is only a function of the slip direction and the shear ratio.

In the simulation, when $\boldsymbol{b} = (0.1, 0, 1)^T$, $\sigma_{13} = 5$ and $\sigma_{23} = 0$, we obtain $\boldsymbol{\beta} = (0.9950, 0, -0.0995)^T$, which agrees with the numerical results in page 58. Another numerical test was also conducted when $\boldsymbol{b} = (0.1, 0, 1)^T$, $\sigma_{13} = 5$ and $\sigma_{23} = 1$. From (2.64), we obtain $\boldsymbol{\beta} = (0.9751, 0.1990, -0.0975)^T$, which agrees well with the numerics ($\boldsymbol{\beta} = (0.9752, 0.1987, -0.0975)^T$). Thus we can conclude our law of motion automatically finds the best plane to accommodate the applied stress. Also, we obtain a way to estimate the active family of glide planes from (2.64).

2.3.4 Spacing and Orientation of Active Slip Planes

Another physical quantity can also be the outcome of our numerical simulation. We would expect the separation between the family of parallel slip planes to be the wavelength of the most unstable mode,

$$d = \frac{\mu(1+\nu)(1-\phi)b}{2(1-\nu)\sigma_{13}\hat{k}}, \tag{2.65}$$

where $\hat{k}$ maximises (2.47). Fig. 2.11 compares the numerics with the theoretical results.

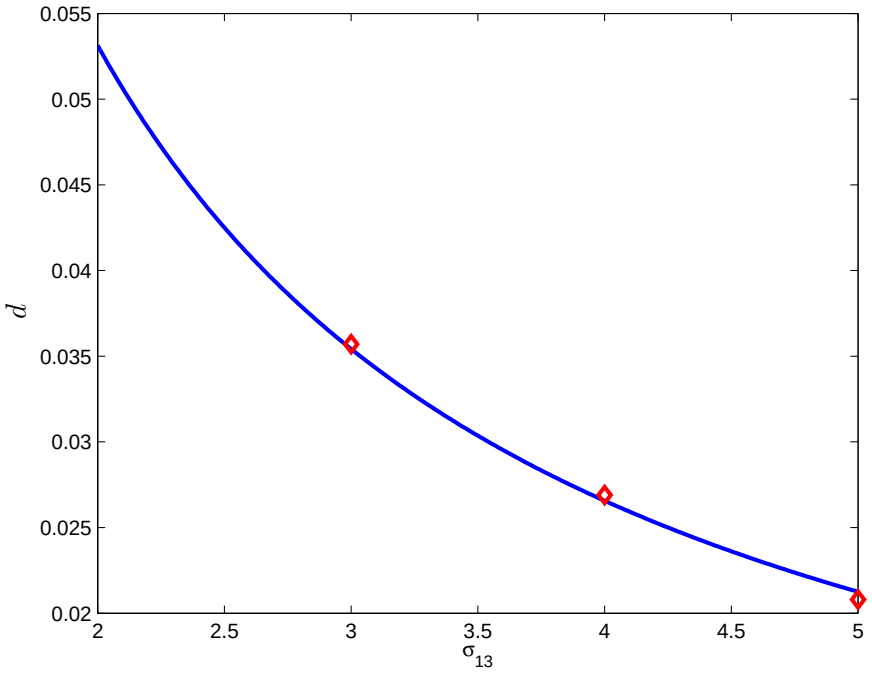


Figure 2.11: Comparison with the theoretical results: the curve is drawn from (2.65), the diamonds are from the simulation

2.4 Conclusion

In closing we make two further points. First, with respect to the experimental observations of Cahn [14] discussed further by Mott [42] related to bending of the slip traces, it is quite conceivable that when the loops on the cross-slip plane have expanded to a significant extent they would have produced extended close-to-screw segments

and if the loading orientation was such that the primary plane had some resolved shear stress on it, these screw segments could double cross-slip back onto the original plane producing a Frank-Read source mechanism.

Second, in the formulation of mesoscale plasticity models it is currently fashionable to introduce scalar dislocation densities with associated pde for their evolution. We believe that much like vortices in fluid dynamics and superconductivity, and as evidenced by the example considered in this chapter, a great deal of fundamental physics of dislocation motion is encoded in the conservation statement of topological charge carried by a line density, a statement which is quite different in content and implications than those that arise for scalar densities.

Chapter 3

Screw Segments

3.1 Introduction

As stated in Chapter 1, two factors are considered by experimentalists suspicious for the formation of PSBs. One is the motion of screw segments that connect edge dislocations from different veins through channels; the other is the collective behaviour of a large number of straight edge dislocations. In this chapter, we will mainly focus on formulating the motion of screw segments in channels. As shown in Fig. 3.1, although termed "screw segments", a screw segment is actually a segment of mixed dislocation connecting edge dislocations from different veins. When a cyclic load $\boldsymbol{\sigma}$ is applied to the specimen, these screw segments will move back and forth in channels and reshape themselves to accommodate the applied stress. The motion of a large number of such screw segments through channels will cause plastic flows. Although the exact mechanism of dislocation multiplication in the early stage of fatigue is still not well understood, the cross-slip motion of these segments is widely believed to be the key to dislocation nucleation. One possible explanation of such process is sketched in Fig. 3.2.

A screw segment moves in response to the cyclic applied stress in its primary slip plane as shown in Fig. 3.2(a). Since the tip of the segment is purely screw in character, it may initiate a cross-slip motion induced by some unspecified sources of stress. If such sources are strong enough, the screw segment will cross-slip to another slip plane as shown in Fig. 3.2(b). Thus the screw segment may move back to another slip plane, which is parallel to the original one as shown in Fig. 3.2(c) to create a double cross-slip configuration. As the cyclic load proceeds, the stress is reversed, which may trigger another cross-slip motion to bring the dislocation back to its original primary slip

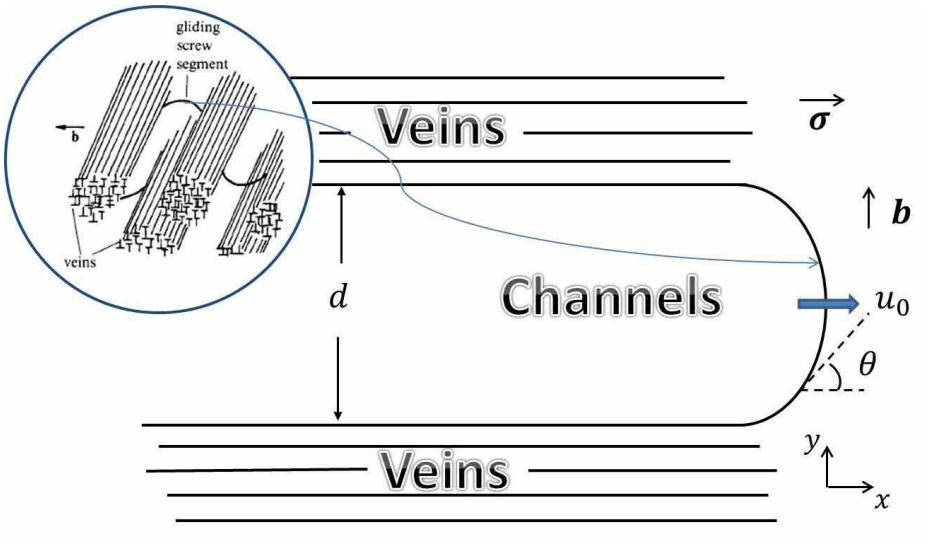


Figure 3.1: A screw segment is a mixed dislocation, which connects two edge dislocations from different veins. When an external stress $\boldsymbol{\sigma}$ is applied, it moves in the channels in response. Its motion can be formulated by travelling waves with a speed u_0. In this way, the evolution of the curve can be written as $(x(\theta)+u_0t, y(\theta))$, where θ is the angle between its tangent and x-axis. Here d is the width of the screw segment; $\boldsymbol{b}$ is the Burgers vector.

plane. According to the anisotropic nature of dislocations (most motion is restricted to the slip plane), the cross-slip-back motion does not follow the same path. Such irreversibility then leaves two prismatic loops in veins as shown in Fig.3.2(d).

The evolution of screw segments can be tracked by using an existing DD simulation codes. However, due to the complexity of the cross-slip mechanism, it is also practically meaningful to abstract formulae by making some realistic assumptions. Although not as accurate as the results from direct simulation, these formulae have simplified forms, so that engineers can combine them with other microstructural results to predict the material properties. Our goal in this chapter is to build models to approximately obtain formulae of quantities that govern the rate of dislocation multiplication. For this purpose, the chapter is arranged as follows. Firstly the travelling wave formulation of screw segments is given, followed by an investigation of the dislocation component that is able to cross-slip under an anti-plane stress. Then a criterion of dislocation nucleation is given by considering the net effect of the external and the self force. Finally, we give our estimation of the rate of dislocation multiplication.

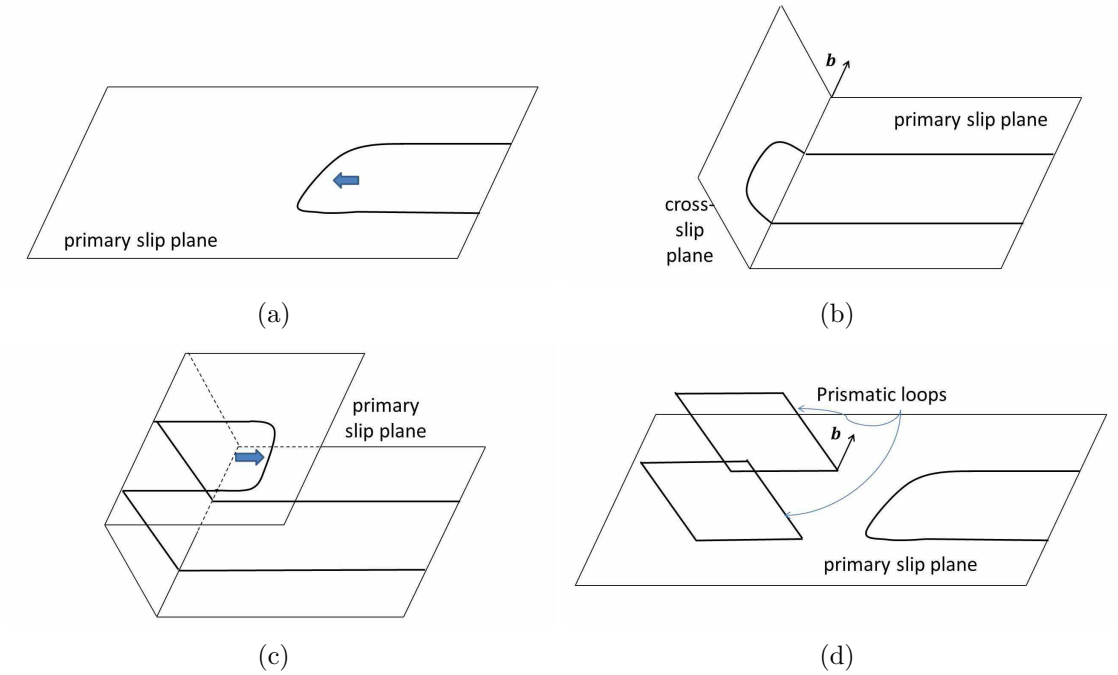


Figure 3.2: A proposed mechanism of dislocation multiplication in the early stage of fatigue: (a) A screw segment is moving in response to the cyclic applied stress in its primary slip plane. (b) Since the tip of the segment is purely a screw character, it may initiate a cross-slip motion induced by some unspecified sources. If such sources are strong enough, the screw segment will cross-slip to another slip plane. (c) The screw segment may move back to another slip plane, which is parallel to the original one to create a double cross-slip configuration. (d) As the cyclic load proceeds, the stress is reversed, which may trigger another cross-slip motion to bring the dislocation back to its original primary slip plane. According to the anisotropic nature of dislocations (most motion is restricted in their slip planes), the cross-slip-back motion does not follow the same path. Such irreversibility then leaves two prismatic loops in veins.

3.2 Travelling Wave Solutions to Screw Segments

As indicated above, the screw segments move through the channel in response to an applied stress. From the law of motion in Chapter 2, the stress that contributes to the dislocation motion, is the resolved component in the slip plane. In this chapter, for ease of notation, we use x, y and z as the mutually orthogonal spatial variables. The coordinate system is set up as shown in Fig. 3.1. The planes $z =$ constant form the primary slip system. The Burgers vector then becomes $\boldsymbol{b} = (0, b, 0)^T$. If we suppose the screw segment we are looking at to be in the $z = 0$ plane before it cross-slips, then the position of each point on the segment can be represented by $(x(\theta, t), y(\theta, t), 0)^T$, where θ is the angle between the dislocation tangent and x-axis as shown in Fig. 3.1.

Here $\theta \in [0, \pi]$, such that the screw segment joins two edge boundaries tangentially. Thus we obtain the applied force per unit length on the segment by the Peach-Koelher formula (1.13):

$$\boldsymbol{f}_{\mathrm{PK}} = (\boldsymbol{b} \cdot \boldsymbol{\sigma}) \wedge \boldsymbol{l} = \begin{pmatrix} -\sigma_{23} \sin\theta \\ \sigma_{23} \cos\theta \\ \sigma_{12} \sin\theta - \sigma_{22} \cos\theta \end{pmatrix}. \tag{3.1}$$

We find that the resolved stress component in this case is σ_{23}.

Here we first consider the planar motion of screw segments. Thus when there is no cross-slip motion, it is equivalent to set the applied stress to be

$$\boldsymbol{\sigma}_{\mathrm{ext}} = \begin{pmatrix} 0 & 0 & 0 \\ 0 & 0 & \sigma_{23} \\ 0 & \sigma_{23} & 0 \end{pmatrix}. \tag{3.2}$$

3.2.1 Governing Equations

Nondimensionlisation

We here nondimensionlise by setting

$$\hat{x} = \frac{x}{b}; \qquad \hat{y} = \frac{y}{b}; \qquad \hat{\boldsymbol{\sigma}} = \frac{\boldsymbol{\sigma}}{\mu}; \qquad \hat{\boldsymbol{v}} = \frac{\boldsymbol{v}}{m_g \mu}. \tag{3.3}$$

Without causing any confusion, we drop the hat of each dimensionless variables in the rest of the calculations in this chapter.

The Travelling Wave Formulation

Combining (3.3), we write the dimensionless version of the law of motion (2.13) to be

$$\boldsymbol{v} = \left((\gamma_1 b_n^2 + \gamma_2 b_l^2)\kappa \boldsymbol{n} + (\boldsymbol{b} \cdot \boldsymbol{\sigma}) \wedge \boldsymbol{l}\right) \boldsymbol{n} \otimes \boldsymbol{n} + \tilde{v}\boldsymbol{l}, \tag{3.4}$$

where

$$\gamma_1 = \frac{1 - 2\nu}{4\pi(1-\nu)}, \qquad \gamma_2 = \frac{1+\nu}{4\pi(1-\nu)} \tag{3.5}$$

and $\tilde{v}$ is an arbitrary velocity in tangential direction. Here, without loss of generality, σ_{23} is set to be negative, so that the force on the screw segment is positive in x direction.

Then we follow the idea in [45] to find the travelling wave solution to (3.4). Since the travelling wave does not change shape during the evolution and is restricted in x-y

plane, the screw segment can be described by $(x(\theta)+u_0 t, y(\theta))$, where u_0 is the wave speed, and the tangent at any point can then be written as

$$\boldsymbol{l} = \begin{pmatrix} \cos\theta \\ \sin\theta \end{pmatrix}. \tag{3.6}$$

It is noted that in the case of planar screw segments, all quantities are reduced to x-y space.

By the Frenet-Serret formulae, we have

$$\kappa \boldsymbol{n} = \frac{\mathrm{d}\boldsymbol{l}}{\mathrm{d}s} = \begin{pmatrix} -\sin\theta \\ \cos\theta \end{pmatrix} \cdot \frac{\mathrm{d}\theta}{\mathrm{d}s}, \tag{3.7}$$

where s is the arc length. Thus by comparison, we obtain

$$\kappa = \frac{\mathrm{d}\theta}{\mathrm{d}s}, \qquad \boldsymbol{n} = \begin{pmatrix} -\sin\theta \\ \cos\theta \end{pmatrix}. \tag{3.8}$$

The applied force on the segment has been computed in (3.1):

$$(\boldsymbol{b}\cdot\boldsymbol{\sigma}_{\mathrm{ext}}) \wedge \boldsymbol{l} = \sigma_{23} \begin{pmatrix} -\sin\theta \\ \cos\theta \end{pmatrix}. \tag{3.9}$$

Incorporating (3.6), (3.8) and (3.9) into (3.4), we have

$$\begin{pmatrix} u_0 \\ 0 \end{pmatrix} = \boldsymbol{v} = \left((\gamma_1 b_n^2 + \gamma_2 b_l^2) \cdot \frac{\mathrm{d}\theta}{\mathrm{d}s} + \sigma_{23} \right) \begin{pmatrix} -\sin\theta \\ \cos\theta \end{pmatrix} + \tilde{v} \begin{pmatrix} \cos\theta \\ \sin\theta \end{pmatrix}. \tag{3.10}$$

Taking inner product with $\boldsymbol{n}$ on both sides of (3.10) gives

$$-u_0 \sin\theta = (\gamma_1 \cos^2\theta + \gamma_2 \sin^2\theta) \cdot \frac{\mathrm{d}\theta}{\mathrm{d}s} + \sigma_{23}.$$

By rearranging, we obtain an ordinary differential equation for the travelling waves:

$$\frac{\mathrm{d}s}{\mathrm{d}\theta} = -\frac{(\gamma_1 \cos^2\theta + \gamma_2 \sin^2\theta)}{\sigma_{23} b + u_0 \sin\theta}. \tag{3.11}$$

Alternatively, in Cartesian coordinates, we have

$$\frac{\mathrm{d}x}{\mathrm{d}\theta} = \frac{\mathrm{d}s}{\mathrm{d}\theta} \cdot \cos\theta = -\frac{\left(\gamma_1 \cos^2\theta + \gamma_2 \sin^2\theta\right)\cos\theta}{\sigma_{23} + u_0 \sin\theta}; \tag{3.12}$$

$$\frac{\mathrm{d}y}{\mathrm{d}\theta} = \frac{\mathrm{d}s}{\mathrm{d}\theta} \cdot \sin\theta = -\frac{\left(\gamma_1 \cos^2\theta + \gamma_2 \sin^2\theta\right)\sin\theta}{\sigma_{23} + u_0 \sin\theta}. \tag{3.13}$$

For the ease of analysis, we can reduce the number of variables by setting

$$X = x\sigma_{23}, \qquad Y = y\sigma_{23}, \qquad U = \frac{u_0}{\sigma_{23}}. \tag{3.14}$$

Then (3.12) and (3.13) can be rewritten:

$$\frac{\mathrm{d}X}{\mathrm{d}\theta} = -\frac{\left(\gamma_1 \cos^2\theta + \gamma_2 \sin^2\theta\right)\cos\theta}{1 + U\sin\theta} \tag{3.15}$$

and

$$\frac{\mathrm{d}Y}{\mathrm{d}\theta} = -\frac{\left(\gamma_1 \cos^2\theta + \gamma_2 \sin^2\theta\right)\sin\theta}{1 + U\sin\theta}, \tag{3.16}$$

respectively.

Without loss of generality, we can set

$$X(\pi/2) = Y(\pi/2) = 0. \tag{3.17}$$

as the boundary conditions to (3.15) and (3.16).

3.2.2 Shapes of Screw Segments

Solutions to the Travelling Wave Equations

If solving (3.15) by integrating its right hand side with respect to θ, it can be observed that there are poles at $\sin\theta = -1/U$ when $U \leq -1$. Thus we will first discuss the case there are no poles, i.e. $U > -1$. In this scenario, the denominator stays positive for all $\theta \in [0, \pi]$, then we have

$$\begin{aligned}
X(\theta) &= -\int_{\pi/2}^{\theta} \frac{[\gamma_1 + (\gamma_2 - \gamma_1)\sin^2\theta']\cos\theta' \mathrm{d}\theta'}{1 + U\sin\theta'} \\
&= -\int_{1}^{\sin\theta} \frac{[\gamma_1 + (\gamma_2 - \gamma_1)\tau^2]\mathrm{d}\tau}{1 + U\tau} \\
&= -\frac{\gamma_2 - \gamma_1}{U}\int_{1}^{\sin\theta} \tau \mathrm{d}\tau + \frac{(\gamma_2 - \gamma_1)}{U^2}\int_{1}^{\sin\theta} \mathrm{d}\tau - \frac{(\gamma_2 - \gamma_1) + \gamma_1 U^2}{U^2}\int_{1}^{\sin\theta} \frac{\mathrm{d}\tau}{1 + U\tau} \\
&= \frac{\gamma_2 - \gamma_1}{2U}\cos^2\theta + \frac{(\gamma_2 - \gamma_1)}{U^2}(\sin\theta - 1) - \frac{(\gamma_2 - \gamma_1) + \gamma_1 U^2}{U^3}\ln\left(\frac{U\sin\theta + 1}{U + 1}\right).
\end{aligned} \tag{3.18}$$

Similarly, Y can also be computed by integrating (3.16) with respect to θ:

$$\begin{aligned} Y(\theta) &= -\int_{\pi/2}^{\theta} -\frac{[\gamma_1 + (\gamma_2 - \gamma_1)\sin^2\theta']\sin\theta' \mathrm{d}\theta'}{1 + U\sin\theta'} \\ &= -\frac{\gamma_2 - \gamma_1}{U}\int_{\pi/2}^{\theta} \sin^2\theta' \mathrm{d}\theta' + \frac{(\gamma_2 - \gamma_1)}{U^2}\int_{\pi/2}^{\theta} \sin\theta' \mathrm{d}\theta' \\ &\quad - \frac{(\gamma_2 - \gamma_1) + \gamma_1 U^2}{U^3}\int_{\pi/2}^{\theta} \mathrm{d}\theta' + \frac{(\gamma_2 - \gamma_1) + \gamma_1 U^2}{U^3}\int_{\pi/2}^{\theta} \frac{\mathrm{d}\theta'}{1 + U\sin\theta'}. \end{aligned} \tag{3.19}$$

It can be observed that from the last term of (3.19), $Y(\theta)$ depends on the sign of $(1 - U^2)$. When $U^2 < 1$,

$$\int_{\pi/2}^{\theta} \frac{\mathrm{d}\theta'}{1 + U\sin\theta'} = \frac{2}{\sqrt{1 - U^2}} \arctan\left(\frac{\sqrt{1 - U^2}\left(\tan\left(\frac{\theta}{2}\right) - 1\right)}{1 - U^2 + \left(\tan\left(\frac{\theta}{2}\right) + U\right)(1 + U)}\right); \tag{3.20}$$

when $U > 1$,

$$\int_{\pi/2}^{\theta} \frac{\mathrm{d}\theta'}{1 + U\sin\theta'} = \frac{1}{\sqrt{U^2 - 1}} \ln\left(\frac{\left(\sqrt{U^2 - 1} - \tan\left(\frac{\theta}{2}\right) - U\right)\left(\sqrt{U^2 - 1} + 1 + U\right)}{\left(\sqrt{U^2 - 1} + \tan\left(\frac{\theta}{2}\right) + U\right)\left(\sqrt{U^2 - 1} - 1 - U\right)}\right). \tag{3.21}$$

Hence the solutions to (3.15) and (3.16) should be collected into categories, depending on the value of U, as follows.

$\underline{U^2 < 1}$

Combining (3.18)-(3.20), we obtain

$$X(\theta) = \frac{\gamma_2 - \gamma_1}{2U}\cos^2\theta + \frac{(\gamma_2 - \gamma_1)}{U^2}(\sin\theta - 1) - \frac{(\gamma_2 - \gamma_1) + \gamma_1 U^2}{U^3} \ln\left(\frac{U\sin\theta + 1}{U + 1}\right), \tag{3.22}$$

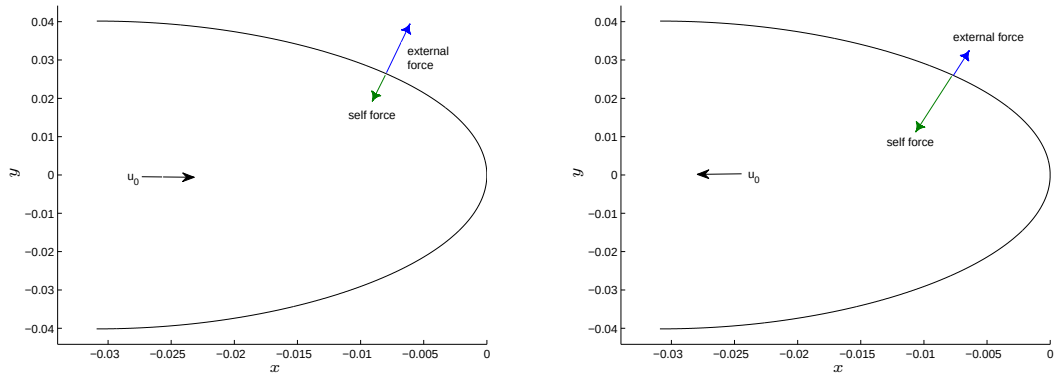
$$\begin{aligned} Y(\theta) = &-\frac{\gamma_2 + \gamma_1}{2U}\left(\theta - \frac{\pi}{2}\right) + \frac{\gamma_2 - \gamma_1}{4U}\sin 2\theta - \frac{(\gamma_2 - \gamma_1)}{U^2}\cos\theta - \frac{\gamma_2 - \gamma_1}{U^3}\left(\theta - \frac{\pi}{2}\right) \\ &+ \frac{2((\gamma_2 - \gamma_1) + \gamma_1 U^2)}{U^3\sqrt{1 - U^2}} \arctan\left(\frac{\sqrt{1 - U^2}\left(\tan\left(\frac{\theta}{2}\right) - 1\right)}{1 - U^2 + \left(\tan\left(\frac{\theta}{2}\right) + U\right)(1 + U)}\right). \end{aligned} \tag{3.23}$$

Using (3.14), we can express the screw segments in x-y coordinates by

$$x(\theta) = \frac{X(\theta)}{\sigma_{23}} \tag{3.24}$$

and

$$y(\theta) = \frac{Y(\theta)}{\sigma_{23}}. \tag{3.25}$$



(a) $-1 < U < 0$ (b) $0 < U < 1$

Figure 3.3: Schematic plots for screw segments when $U^2 < 1$: when $-1 < U < 0$, it is an external driven motion; when $0 < U < 1$, it is a self-driven motion. ν here is taken to be 0.3.

Schematic diagrams of the planar motion of screw segments when $U^2 < 1$ are shown in Fig. 3.3. If $-1 < U < 0$, the speed of the travelling wave u_0 is in the same direction as the external force. Thus it is an external-driven motion as shown in Fig. 3.3(a). On the other hand, if $0 < U < 1$, the self-force dominates the motion, so it is a self-driven motion as shown in Fig. 3.3(b). Additionally, $U = -1$ corresponds to the case when a straight screw dislocation is driven by an external stress.

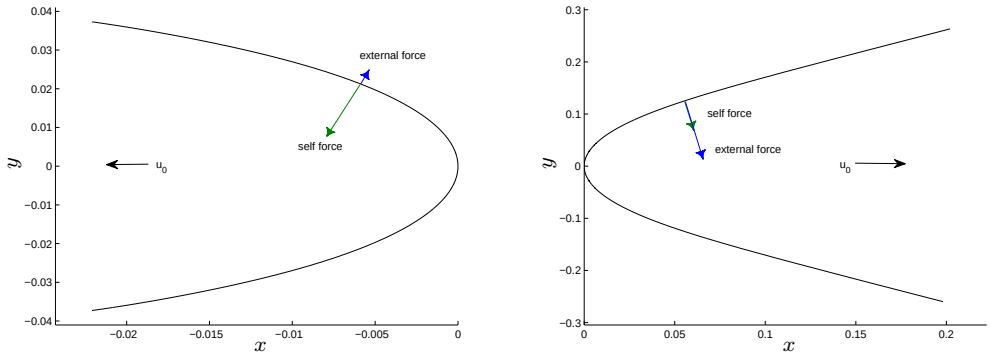
$\underline{U > 1}$

Similar analysis can be done to the case when $U > 1$. In this case we obtain

$$X(\theta) = \frac{\gamma_2 - \gamma_1}{2U}\cos^2\theta + \frac{\gamma_2 - \gamma_1}{U^2}(\sin\theta - 1) - \frac{\gamma_2 - \gamma_1 + \gamma_1 U^2}{U^3}\ln\left(\frac{U\sin\theta + 1}{U+1}\right), \quad (3.26)$$

$$\begin{aligned} Y(\theta) = &-\frac{\gamma_2 + \gamma_1}{2U}\left(\theta - \frac{\pi}{2}\right) + \frac{\gamma_2 - \gamma_1}{4U}\sin 2\theta - \frac{(\gamma_2 - \gamma_1)}{U^2}\cos\theta - \frac{\gamma_2 - \gamma_1}{U^3}\left(\theta - \frac{\pi}{2}\right) \\ &+ \frac{(\gamma_2 - \gamma_1) + \gamma_1 U^2}{U^3\sqrt{U^2-1}}\ln\left(\frac{\left(\tan\left(\frac{\theta}{2}\right) + U - \sqrt{U^2-1}\right)\left(1 + U + \sqrt{U^2-1}\right)}{\left(\tan\left(\frac{\theta}{2}\right) + U + \sqrt{U^2-1}\right)\left(1 + U - \sqrt{U^2-1}\right)}\right). \end{aligned} \quad (3.27)$$

The shape of a screw segment in this regime in the x-y plane is sketched in Fig. 3.4(a); the motion is of self-driven type.



(a) $U > 1$ (b) $U < -1$

Figure 3.4: The schematic diagrams for screw segments when $U^2 > 1$: when $U > 1$, it is self-driven motion; when $U < -1$, rather than joining tangentially to two edge dislocations in veins, the travelling wave will shoot to infinity at an angle $-\arcsin(1/U)$.

$\underline{U < -1}$

Finally, we consider the case when $U < -1$. Thus the poles are at $\theta = -\arcsin(1/U)$ or $\pi + \arcsin(1/U)$. To satisfy the boundary condition (3.17) that $\theta = \pi/2$ should be included in the computational domain, we require $\theta \in (-\arcsin(1/U), \pi + \arcsin(1/U))$. Therefore, we obtain

$$X(\theta) = \frac{\gamma_2 - \gamma_1}{2U}\cos^2\theta + \frac{\gamma_2 - \gamma_1}{U^2}(\sin\theta - 1) + \frac{\gamma_2 - \gamma_1 + \gamma_1 U^2}{U^3}\ln\left(\frac{U\sin\theta + 1}{U+1}\right), \quad (3.28)$$

$$\begin{aligned} Y(\theta) = &-\frac{\gamma_2 - \gamma_1}{2U}\left(\theta - \frac{\pi}{2}\right) + \frac{\gamma_2 - \gamma_1}{4U}\sin 2\theta - \frac{\gamma_2 - \gamma_1}{U^2}\cos\theta \\ &- \frac{\gamma_2 - \gamma_1 + \gamma_1 U^2}{U^3}\left(\theta - \frac{\pi}{2}\right) \\ &+ \frac{(\gamma_2 - \gamma_1) + \gamma_1 U^2}{U^3\sqrt{U^2-1}}\ln\left(\frac{\left(\tan(\theta/2) + U - \sqrt{U^2-1}\right)\left(1 + U + \sqrt{U^2-1}\right)}{\left(\tan(\theta/2) + U + \sqrt{U^2-1}\right)\left(1 + U - \sqrt{U^2-1}\right)}\right). \end{aligned} \quad (3.29)$$

The bound for θ suggests that, the screw segments in x-y plane, will asymptotically go to infinity at an angle of $-\arcsin(1/U)$ as shown in Fig. 3.4(b). This contradicts to the assumption that all screw segments should be connected to edge dislocations in veins tangentially, so this case is excluded in further discussion.

Conclusion

By using the travelling wave formulation, we obtain four families of solutions, classified by U. The results are summerised in Table 3.1.

Regime	U	θ	Type of motion
1	$(-1, 0)$	$[0, \pi]$	external-driven
2	$(0, 1)$	$[0, \pi]$	self-driven
3	$(1, +\infty)$	$[0, \pi]$	self-driven
4	$(-\infty, -1)$	$(-\arcsin(1/U), \pi + \arcsin(1/U))$	not confined to a strip

Table 3.1: Motion classified by U: when $-1 < U < 0$, motion is driven by the external force; when $U > 0$, the motion is driven by the self-force.

3.2.3 Relating Traveling Wave Solutions to Experiments

Width of Screw Segments

As seen above, the shapes of travelling waves depend on two parameters, u_0 and σ_{23}. From experimental point of view, however, the speed of screw segments u_0 cannot be easily measured. So it is sensible to replace u_0 by some parameters that are easily obtained from experiments. One candidate for such a parameter is the width of screw segments d (the width of the channel) in Fig. 3.1. Practically, it can be estimated from the averaged distance between neighbouring veins. By setting

$$D = d\sigma_{23},$$

we have

$$D = Y(\pi) - Y(0) \tag{3.30}$$

from the travelling wave solutions. Since $\sigma_{23} < 0$ as defined, D is also negative.

When $U^2 < 1$, combining (3.23) and (3.30) gives

$$D = -\frac{(\gamma_2 + \gamma_1)\pi}{2U} + \frac{2(\gamma_2 - \gamma_1)}{U^2} - \frac{(\gamma_2 - \gamma_1)\pi}{U^3} + \frac{4((\gamma_2 - \gamma_1) + \gamma_1 U^2)}{U^3\sqrt{1 - U^2}} \arctan\sqrt{\frac{1 - U}{1 + U}}. \tag{3.31}$$

Similarly, when $U > 1$, we have

$$\begin{aligned} D = &-\frac{(\gamma_2 + \gamma_1)\pi}{2U} + \frac{2(\gamma_2 - \gamma_1)}{U^2} - \frac{(\gamma_2 - \gamma_1)\pi}{U^3} \\ &+ \frac{2((\gamma_2 - \gamma_1) + \gamma_1 U^2)}{U^3\sqrt{U^2 - 1}} \ln\frac{1 + U + \sqrt{U^2 - 1}}{1 + U - \sqrt{U^2 - 1}}. \end{aligned} \tag{3.32}$$

In this way, we are enabled to obtain D as a function of U, with three singularities at $U = \pm 1$ and $U = 0$.

Removal of Singularities

In fact, two of the three singularities can be removed by asymptotic techniques.

Near $U = 1$, since

$$\lim_{U\to 1^+} \frac{1}{\sqrt{U^2-1}} \ln\left(\frac{1+U+\sqrt{U^2-1}}{1+U-\sqrt{U^2-1}}\right) = \lim_{U\to 1^+} \ln\left(1+\frac{2\sqrt{U^2-1}}{2-\sqrt{U^2-1}}\right) = 1,$$

we have the approximation by approaching $U = 1$ from the right side:

$$\lim_{U\to 1^+} D = \frac{1}{2}(\gamma_1 - 3\gamma_2)\pi + 4\gamma_2 - 2\gamma_1. \tag{3.33}$$

On the other hand, by using

$$\lim_{U\to 1^-} \frac{1}{\sqrt{1-U^2}} \arctan\sqrt{\frac{1-U}{1+U}} = \lim_{U\to 1^+} \frac{1}{1+U} = \frac{1}{2},$$

we can match the value of D at $U = 1$ from both sides by

$$\lim_{U\to 1^-} D = \frac{1}{2}(\gamma_1 - 3\gamma_2)\pi + 4\gamma_2 - 2\gamma_1 = \lim_{U\to 1^+} D. \tag{3.34}$$

Hence this singularity at $U = 1$ can be removed by defining

$$D|_{U=1} = -\frac{1}{2}(\gamma_1 - 3\gamma_2)\pi - 4\gamma_2 + 2\gamma_1.$$

Similarly, as $U \to 0$, we have the expansion that

$$\begin{aligned} &-\frac{4\left((\gamma_2-\gamma_1)+\gamma_1 U^2\right)}{U^3\sqrt{1-U^2}} \arctan\sqrt{\frac{1-U}{1+U}} \\ &\quad\sim -\frac{(\gamma_2-\gamma_1)\pi}{U^3} + \frac{2(\gamma_2-\gamma_1)}{U^2} - \frac{(\gamma_2+\gamma_1)\pi}{2U} + \frac{2}{3}(\gamma_1+2\gamma_2) + O(U). \end{aligned} \tag{3.35}$$

Plugging the above approximation into (3.31) shows that all singularities cancel. Hence we can regularise D as $U \to 0$ by defining

$$D|_{U=0} = -\frac{2}{3}(\gamma_1 + 2\gamma_2). \tag{3.36}$$

Therefore, the only singularity that cannot be removed, arises when $U \to -1$. We can, however, obtain the asymptotic behaviour of D from (3.31):

$$D \sim -\frac{\pi\gamma_2}{\sqrt{1+U}}, \tag{3.37}$$

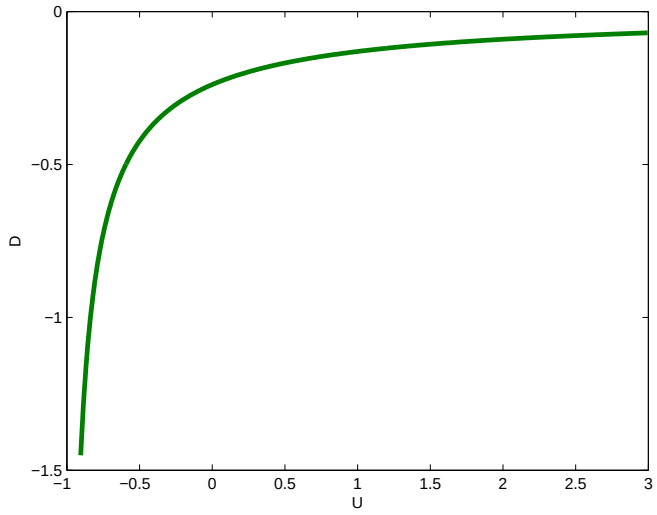


Figure 3.5: D is uniquely determined by U.

as $U \to -1$.

With the matching results above, we now plot D against U for $U > -1$, as shown in Fig. 3.5. A key observation can be made that D is uniquely determined by U. This one-to-one correspondence enables us to replace U in the expressions of $X(\theta)$ and $Y(\theta)$ by an implicit function of D. This suggests that the shapes of screw segments in the X-Y plane are solely determined by D. Or alternatively, given σ_{23} and d, the screw segment is then fixed.

Therefore, the shapes of screw segments are uniquely determined as follows. Given σ_{23} and d, U can be calculated from either (3.31) or (3.32). Then a planar travelling wave solution $(X(\theta), Y(\theta))$ can be worked out from travelling wave formulation. Finally, the formulae describing the segment shapes in x-y space can be obtained by $x = X/\sigma_{23}$ and $y = Y/\sigma_{23}$, respectively.

Moreover, it is noted that from Table 3.1, as U goes across 0, the type of motion is switched. In another word, as U turns negative, the screw segments start to flow driven by the external force. This shows that $U = 0$ is a critical value to the plastic flow in fatigue tests. Combining (3.5), (3.14) and (3.36), we obtain

$$\sigma_{23} d = -\frac{1}{2\pi(1-\nu)}, \tag{3.38}$$

in this case. The value in the right hand side of (3.38), as we will see later, is closely related to the saturation stress in the early stage of the fatigue test.

Comparison of Screw Segments

Thus we are able to make comparisons among screw segments under different experimental conditions. Fig. 3.6 compares the screw segments under various σ_{23} with d fixed. It can be observed that as σ_{23} increases, a screw segment will accommodate this applied stress by raising its proportion of screw components. From the law of

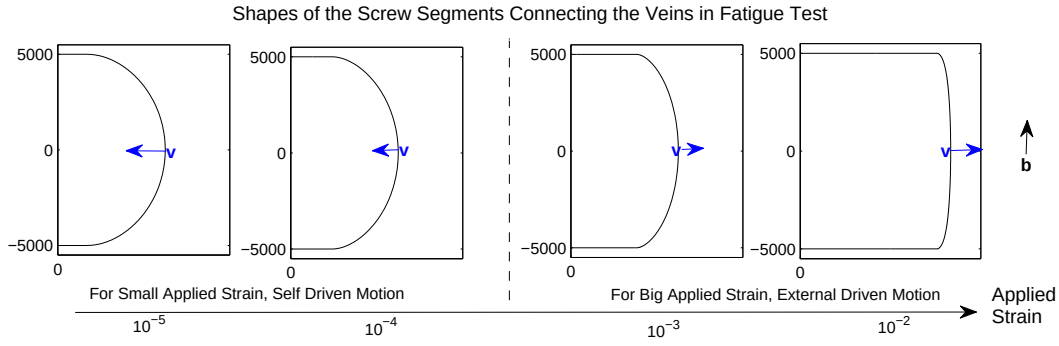


Figure 3.6: For fixed $d = 10^4$, the greater σ_{23} is, the more proportion of screw components a screw segment has.

motion, we know that a high proportion of screw components is more likely to initiate a cross-slip motion when an anti-plane stress is applied or it meets barriers. As mentioned in the beginning of this chapter, the cross-slip motion is believed to be the source of dislocation multiplication in the early stage of fatigue. The increase in the proportion of screw character induced by larger applied stress offers one reason to the experimental observation that the possibility of dislocation multiplication is enhanced with higher stain/stress amplitude.

3.3 Estimation of the Rate of Dislocation Multiplication

In the previous section, a model of travelling waves is proposed to track the in-plane propagation of screw segments. We have found that a larger stress gives rise to a higher proportion of screw characters, which may cross-slip to another glide plane if the segment feels an anti-plane stress by some unspecified source. In this section, the condition of the occurrence of the cross-slip motion will be discussed.

3.3.1 The Mechanism of Cross-Slip in Fatigue Test

When an anti plane stress, σ_{12} in this case, is applied to a screw segment, according to the law of motion in §2.1, the tip where the dislocation is almost screw can be pushed out of its primary slip plane, to initiate a cross-slip motion, as shown in Fig. 3.7. On the other hand, the remainder part of the dislocation, where screw is not dominant, will still be restricted to the primary slip plane. This process, therefore, creates a battle within the screw segment. Being dragged away from its slip plane, as shown in Fig. 3.7, the bow-out component will exert a self-stress $\boldsymbol{\sigma}_s$ to pull the cross-slip component back to its original glide plane. If this self force overcomes the external stress, the cross-slip will not occur.

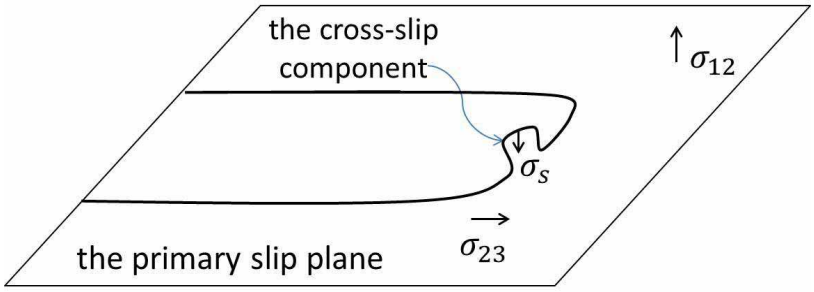


Figure 3.7: Mechanism of the initiation of a cross-slip motion: if applied an anti-plane stress σ_{12} by some unspecified sources, the tip of the screw segment will be pushed out of its glide plane. The cross slip component then will generate a self stress σ_s to impede the cross slip motion.

For a quantitative description for such a process, one way is to numerically solve the non-linear evolution under the law of motion. This approach, as seen in Chapter 2, is time consuming. Moreover, from numerical simulation, it is hard to summarise a formula indicating the mechanism of dislocation multiplication, from which the rate of dislocation multiplication can be estimated for engineers. Therefore, some simplifications have to be made to obtain a practically useful model to predict the dislocation multiplication via cross-slip motion in the early stage of metal fatigue.

3.3.2 Cross-Slip Components

From the law of motion introduced in §2.1, we know that the proportion of the screw character of a dislocation plays an important role on the possibility of its cross-slip motion (or climb). Recall from expression of the mobility tensor in (2.12), that the

weight function ϕ controls the extent to which the stress is resolved to its glide plane for a given dislocation orientation. To describe this extent mathematically, we can assign a value η_c, such that only dislocation components satisfying

$$\phi\left(\frac{b^2 - b_l^2}{b^2\epsilon}\right) > \eta_c, \tag{3.39}$$

have the ability to cross-slip.

For the case of screw segments, the screw tips are inclined to move in another slip plane under an applied anti-plane stress, while the remainder is restricted in the primary plane by a not-too-small edge character. For a screw segment $(x(\theta), y(\theta), 0)^T$ derived from the travelling wave formulation in the previous section, we obtain its screw and edge character as $\sin\theta$ and $\cos\theta$, respectively. Incorporating this with (3.39), we find that only dislocation components with $|\pi/2 - \theta| \leq \xi$, where

$$\xi = \arcsin\sqrt{\phi^{-1}(\eta_c)} \tag{3.40}$$

can move into another glide plane. Here we use the term "cross-slip component" to denote the dislocation part in a screw segment that is capable to cross-slip. In this case, the cross-slip component has the same expression $(x(\theta), y(\theta), 0)^T$ with its matrix screw segment, but with $\theta \in (\pi/2 - \xi, \pi/2 + \xi)$. Thus in Fig. 3.8, for a given width d of the screw segment, under various applied stress σ_{23}, screw segments and their cross-slip components are drawn. It can be seen that the proportion of the cross-slip component in width increases with a larger σ_{23}. Mathematically, this proportion can be captured by defining

$$p_c = \frac{D_c}{D}, \tag{3.41}$$

where

$$\begin{aligned} D_c &= Y\left(\frac{\pi}{2} + \xi\right) - Y\left(\frac{\pi}{2} - \xi\right) \\ &= -\frac{\gamma_1 + \gamma_2}{U} \cdot \xi - \frac{\gamma_2 - \gamma_1}{2U} \cdot \sin 2\xi + \frac{2(\gamma_2 - \gamma_1)}{U^2} \cdot \sin\xi - \frac{2(\gamma_2 - \gamma_1)}{U^3} \cdot \xi \\ &\quad + \frac{4((\gamma_2 - \gamma_1) + \gamma_1 U^2)}{U^3\sqrt{1 - U^2}} \cdot \arctan\left(\frac{\tan\frac{\xi}{2}\sqrt{1 - U^2}}{1 + U}\right), \end{aligned} \tag{3.42}$$

when $U < 1$;

$$\begin{aligned} D_c &= -\frac{\gamma_2 + \gamma_1}{U} \cdot \xi + \frac{\gamma_2 - \gamma_1}{2U}\sin 2\xi - \frac{2(\gamma_2 - \gamma_1)}{U^2}\sin\xi - \frac{2(\gamma_2 - \gamma_1)}{U^3} \cdot \xi \\ &\quad + \frac{2((\gamma_2 - \gamma_1) + \gamma_1 U^2)}{U^3\sqrt{U^2 - 1}} \ln\left(\frac{1 + U + \sqrt{U^2 - 1}\tan(\xi/2)}{1 + U - \sqrt{U^2 - 1}\tan(\xi/2)}\right), \end{aligned} \tag{3.43}$$

when $U > 1$; D is d/σ_{23} which is expressed in (3.31) and (3.32).

Fig. 3.9 depicts how p_c depends on σ_{23} under various ξ with d fixed.

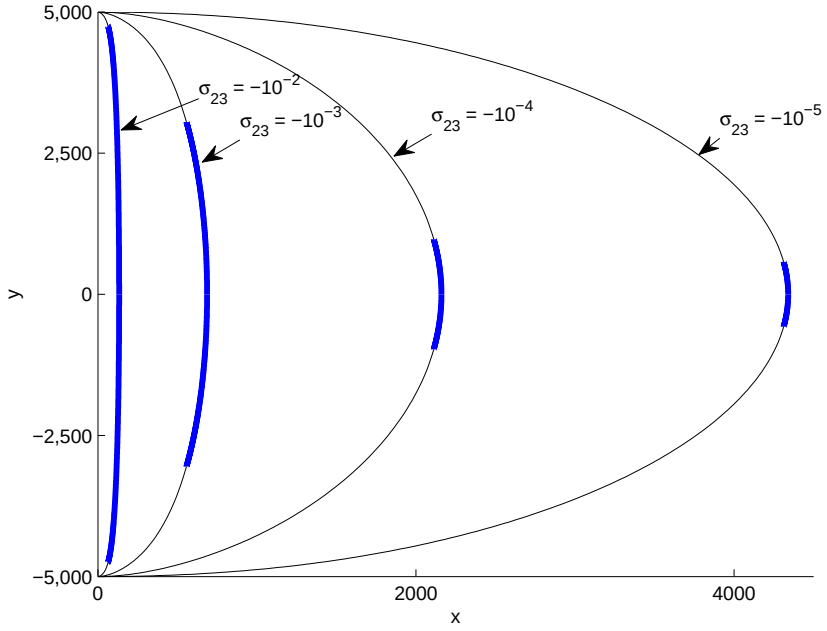


Figure 3.8: Cross-slip components under various σ_{23}: the thick blue curves are the cross-slip components, where d is fixed to be 10^4.

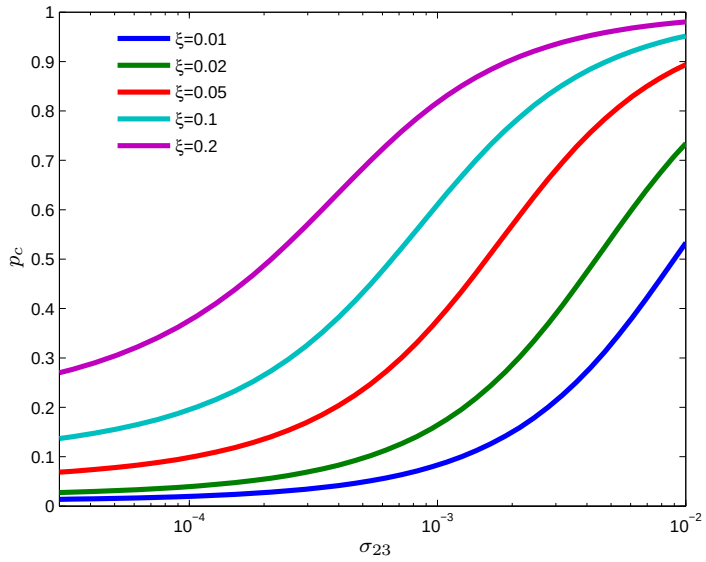


Figure 3.9: For fixed $d = 10^4$, the fraction of the width of the cross-slip component over that of its corresponding screw segment grows with an increasing σ_{23}. ξ is the critical cross-slip angle defined in (3.40).

3.3.3 Driving Forces on Cross-slip Components

Given d and σ_{23}, the shape of the screw segment and its cross-slip component can be calculated as above. When there is also a non-vanishing anti-plane stress component

σ_{12}, the cross-slip motion can be introduced. In this case, the applied stress becomes

$$\boldsymbol{\sigma}_{\text{ext}} = \begin{pmatrix} 0 & \sigma_{12} & 0 \\ \sigma_{12} & 0 & \sigma_{23} \\ 0 & \sigma_{23} & 0 \end{pmatrix}. \tag{3.44}$$

When it moves in the secondary slip plane, a self-stress will be generated to impede the cross-slip motion. Here, we will try to estimate this self-force. This σ_{12} can be generated by the applied stress or by all other dislocations. The procedure of how dislocation multiply themselves in the early stage of fatigue has been schematically introduced at the beginning of this chapter.

As shown in Fig. 3.10, being pushed by σ_{12}, the tip of the screw segment starts to

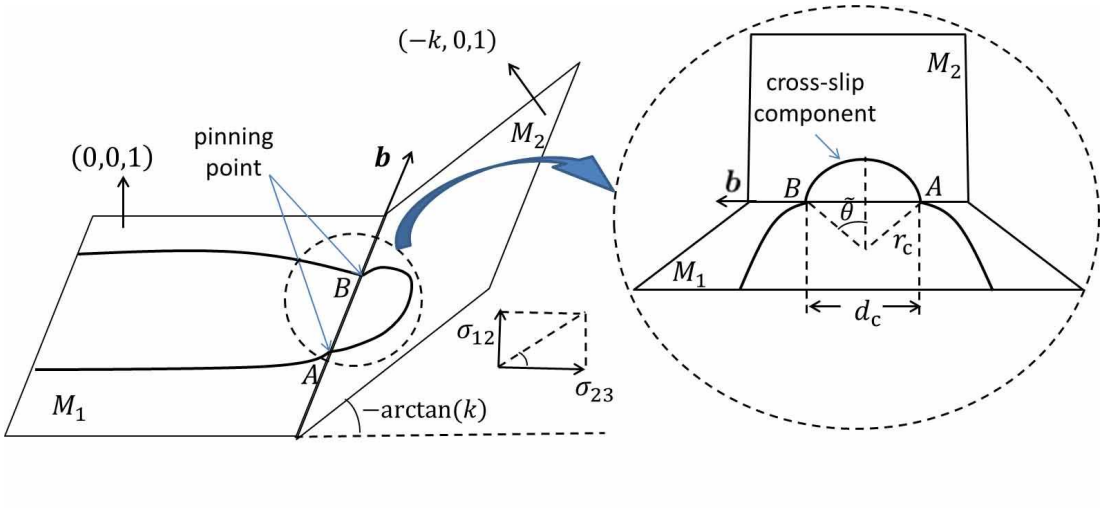


Figure 3.10: Cross-slip components: when applied an anti-plane stress component σ_{12} in addition to σ_{23}, the cross-slip component will start its motion in the plane that resolves both σ_{12} and σ_{23}. In this case, the new glide plan M_2 is normal to $(-k, 0, 1)$. For simplification, the cross-slip component is assumed to be in arc shape of radius cutting AB throughout the whole process.

move into a new slip plane M_2, which is set to be normal to

$$\boldsymbol{\beta}^c = \frac{1}{\sqrt{k^2+1}} \begin{pmatrix} -k \\ 0 \\ 1 \end{pmatrix}, \tag{3.45}$$

due to their dominant screw characters.

When the crystallography is considered, k can be chosen from a set of values that characterise all possible slip system; otherwise, from the law of motion from Chapter 2, the secondary slip plane is the best plane to resolve the applied stress, where

$k = \sigma_{12}/\sigma_{23}$. In either case, for any point on the cross-slip component with $\boldsymbol{l}^c$ and $\boldsymbol{n}^c$ as its tangent and normal, respectively, the applied force it experiences can be written by the Peach-Koelher formula in (1.13):

$$\boldsymbol{f}^c = (\boldsymbol{b} \cdot \boldsymbol{\sigma}_{\text{ext}}) \wedge \boldsymbol{l}^c = \begin{pmatrix} -\sigma_{23} l_2^c \\ \sigma_{23} l_1^c - \sigma_{12} l_3^c \\ \sigma_{12} l_2^c \end{pmatrix}.$$

Since $\boldsymbol{f}^c$ is perpendicular to $\boldsymbol{l}^c$ and the secondary slip plane is normal to $\boldsymbol{\beta}^c$, the force resolved in the secondary slip plane is in $\boldsymbol{n}^c$ with a magnitude of

$$\boldsymbol{f}^c \cdot \boldsymbol{n}^c = \sigma_{23}(l_1^c n_2^c - l_2^c n_1^c) + \sigma_{12}(l_2^c n_3^c - l_3^c n_2^c).$$

As we know $\boldsymbol{\beta}^c = \boldsymbol{l}^c \wedge \boldsymbol{n}^c$, we obtain the force resolved in M_2:

$$\boldsymbol{f}^c \cdot \boldsymbol{n}^c = \sigma_{12}\beta_1^c + \sigma_{23}\beta_3^c = \frac{\sigma_{23}(-k\beta_1^c + \beta_3^c)}{\sqrt{k^2+1}}. \tag{3.46}$$

3.3.4 Self-Forces on Cross-Slip Components

Dragged by this resolved force, the cross-slip component will bow-out into M_2 in Fig. 3.10, giving rise to a self-force $\boldsymbol{f}^s$ to impede its motion. As mentioned at the beginning of this chapter, some simplifications have to be made to estimate this $\boldsymbol{f}^s$. One approach is to follow the idea from Orowan mechanism in [35] to assume the cross-slip component evolves as a family of arc shapes which cut through AB in the secondary slip plane as shown in the right hand of Fig. 3.10. Thus each member of this family can be represented by the radius r_c of the circle, which the arc is from. One advantage of such simplification is that all quantities can be expressed explicitly. For example, the curvature then becomes $1/r_c$ and we also have

$$\boldsymbol{l}^c = \frac{1}{\sqrt{1+k^2}} \begin{pmatrix} \sin\tilde{\theta} \\ -\sqrt{1+k^2} \cdot \cos\tilde{\theta} \\ -k\sin\tilde{\theta} \end{pmatrix} \tag{3.47}$$

and

$$\boldsymbol{n}^c = \frac{1}{\sqrt{1+k^2}} \begin{pmatrix} \cos\tilde{\theta} \\ \sqrt{1+k^2} \cdot \sin\tilde{\theta} \\ -k\cos\tilde{\theta} \end{pmatrix}, \tag{3.48}$$

where $\tilde{\theta}$ is the parameter of the arc, with $\tilde{\theta} = 0$ at the screw tip as shown in the right hand of Fig. 3.10. Incorporating these geometric parameters into the expression for the self force derived in (2.30) gives

$$\boldsymbol{f}^s = \frac{\gamma_1 \sin^2\tilde{\theta} + \gamma_2 \cos^2\tilde{\theta}}{r_c} \cdot \boldsymbol{n}^c, \tag{3.49}$$

where γ_1 and γ_2 are defined the same as in (3.5).

3.3.5 A Criterion for the Completion of Cross-Slip Motion

With (3.46) and (3.49), we obtain the net force at the cross-slip component as $f\boldsymbol{n}^c$, where

$$f = \frac{\gamma_1 \sin^2\tilde{\theta} + \gamma_2 \cos^2\tilde{\theta}}{r_c} + \frac{(-k\beta_1^c + \beta_3^c)\sigma_{23}}{\sqrt{k^2+1}}. \tag{3.50}$$

Since $\boldsymbol{n}^c$ is defined to point in the same direction as the self-force, we can give the following criterion: when $f < 0$, the driving force exceeds the self-force so that the cross-slip motion will proceed, otherwise the self-force is big enough to stop the cross-slip motion.

Recalling the cross-slip arc always cuts AB in Fig. 3.10, which has a length of d_c, we have

$$r_c \geq \frac{d_c}{2}. \tag{3.51}$$

This indicates that the curvature has a maximum value:

$$\kappa_{\max} = 2/d_c. \tag{3.52}$$

Since $\gamma_2 > \gamma_1$, the maximum self-force can be obtained as $2\gamma_2/d_c$. Combining this with (3.50), we have

$$f \leq \frac{(-k\beta_1^c + \beta_3^c)\sigma_{23}}{\sqrt{k^2+1}} + \frac{2\gamma_2}{d_c}.$$

If the right hand side of the above inequality is negative, then $f < 0$ for all $\tilde{\theta}$. This actually suggests

$$\frac{(-k\beta_1^c + \beta_3^c)\sigma_{23}}{\sqrt{k^2+1}} + \frac{2\gamma_2}{d_c} < 0 \tag{3.53}$$

is a sufficient condition for the completion of the cross-slip motion. Rearranging (3.53) and using $D_c = d_c\sigma_{23}$, we have

$$D_c < -\frac{2\gamma_2\sqrt{k^2+1}}{-k\beta_1^c + \beta_3^c}. \tag{3.54}$$

This condition can be related to the experimental conditions as follows. From the experimental data, we can obtain the critical value for D_c:

$$D_c^* = -\frac{2\gamma_2\sqrt{k^2+1}}{k\tau + 1}.$$

Then the corresponding U_c^* can be obtained by solving an equation for U from (3.42) or (3.43):

$$D_c^* = -\frac{\gamma_1+\gamma_2}{U}\cdot\xi - \frac{\gamma_2-\gamma_1}{2U}\cdot\sin 2\xi + \frac{2(\gamma_2-\gamma_1)}{U^2}\cdot\sin\xi - \frac{2(\gamma_2-\gamma_1)}{U^3}\cdot\xi + \frac{4((\gamma_2-\gamma_1)+\gamma_1U^2)}{U^3\sqrt{1-U^2}}\cdot\arctan\left(\frac{\tan\frac{\xi}{2}\sqrt{1-U^2}}{1+U}\right), \quad -1<U<1;$$

$$D_c^* = -\frac{\gamma_2+\gamma_1}{U}\cdot\xi + \frac{\gamma_2-\gamma_1}{2U}\sin 2\xi - \frac{2(\gamma_2-\gamma_1)}{U^2}\sin\xi - \frac{2(\gamma_2-\gamma_1)}{U^3}\cdot\xi + \frac{2((\gamma_2-\gamma_1)+\gamma_1U^2)}{U^3\sqrt{U^2-1}}\ln\left(\frac{1+U+\sqrt{U^2-1}\tan(\xi/2)}{1+U-\sqrt{U^2-1}\tan(\xi/2)}\right), \quad U>1.$$

Finally, D^* can be calculated by incorporating U^* into the expression for $D = D(U)$ from (3.31) or (3.32).

Therefore, a criterion for the completion of the cross-slip motion becomes

$$\sigma_{23}d < D^*. \tag{3.55}$$

With this criterion, the space spanned by the two most crucial experimental parameters, σ_{23} and d can be separated by the curve $D^* = d\sigma_{23}$ which corresponds to the blue curve in Fig. 3.11. Only when (σ_{23}, d) is on the left hand of the curve, does the cross-slip occur. Within a cycle, the width of a channel is fixed. When σ_{23} is small, the screw segment will propagate in its primary slip plane as a travelling wave until the stress exceeds the critical value (correspondingly in Fig. 3.11, the arrow hits the curve). Then the cross-slip starts and part of the screw segment moves in the cross-slip plane. After reaching the stress amplitude resolved in the primary plane, denoted by $\sigma_{23}^{\max}$ (the blue curve in Fig. 3.11), σ_{23} is reversed. When σ_{23} is not big enough to keep the cross-slip motion (correspondingly in Fig. 3.11, the arrow hits the curve again), the cross-slip component will start their motion in a slip plane parallel to its original glide plane. As a cycle finishes, the number of the straight edge dislocations in veins doubles as shown in the beginning of this chapter in Fig.3.2(a)-(c). It should be noted that, the criterion given in (3.55) shows that the multiple of σ_{23} and d is a crucial quantity for the occurrence of cross-slip motion. It has a similar form to the Orowan description of dislocation passing obstacles detailed in [35].

3.4 Fitting Experimental Data into the Model

Here it is time to fit the experimental data into the model presented above. These data are all from the strain-control results in p.66-p.67, p.136 and p.147 of [2].

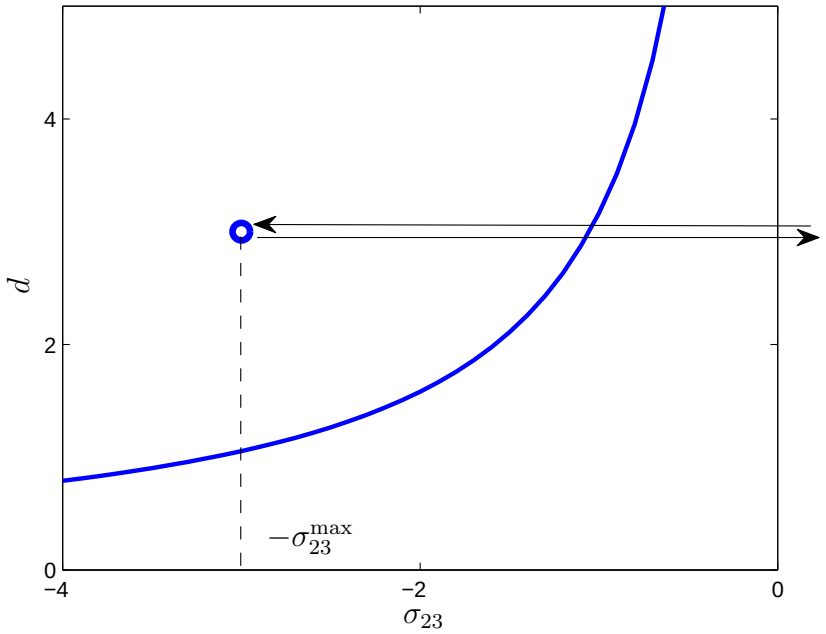


Figure 3.11: Cross-slip in a cycle: the space spanned two most crucial experimental parameters, σ_{23} and d can be separated by $D^* = d\sigma_{23}$ which corresponds to the blue curve. Only when (σ_{23}, d) is on the left hand of the curve, the cross-slip occurs. Within a cycle, the width of a channel is fixed. When σ_{23} is small, the screw segment will propagate in its primary slip plane as a travelling wave until the stress exceeds the critical value (when the arrow hits the curve). Then the cross-slip starts and part of the screw segment moves in the cross-slip plane. After reaching the stress amplitude resolved in the primary plane, denoted by $\sigma_{23}^{\max}$ (the blue curve), σ_{23} is reversed. When σ_{23} is not big enough to keep the cross-slip motion (when the arrow hits the curve again), the cross-slip component will start their motion in a slip plane parallel to its original glide plane.

3.4.1 Translation from the Crystallographic Notation to Cartesian System

In their experiments, the copper specimen is prepared to be in [541] oriented crystal, i.e. the applied load is along the [541] direction, where the crystallographic notation introduced in §1.1.1 is used. It can be found that the Burgers vector in the early stage of fatigue can be calculated as [101], and the primary slip plane is of face $(11\bar{1})$. In this case, the Schmid factor is 0.47. Once the Burgers vector is fixed, we need to decide the cross-slip plane. In order to implement our model, all these data have to be translated to fit the setting of the coordinates. This suggests x, y and z should be in the directions of $[1\bar{2}\bar{1}]$, [101] and $[\bar{1}\bar{1}1]$, respectively. Thus a vector expressed as

$[n_1 n_2 n_3]$ in the crystallographic system can be translated into $(m_1, m_2, m_3)^T$ in x-y-z by the linear transformation:

$$\begin{pmatrix} m_1 \\ m_2 \\ m_3 \end{pmatrix} = \frac{l}{\sqrt{6}} \begin{pmatrix} 1 & -2 & -1 \\ \sqrt{3} & 0 & \sqrt{3} \\ -\sqrt{2} & -\sqrt{2} & \sqrt{2} \end{pmatrix} \begin{pmatrix} n_1 \\ n_2 \\ n_3 \end{pmatrix}, \tag{3.56}$$

where l is the lattice spacing for copper.

3.4.2 Experimental Parameters

In order to implement our model, four experimental parameters are needed. They are the two shear applied stress components σ_{12} and σ_{23}; the width of channels d and the cross-slip angle ξ. Among these 4 parameters, stress components can be derived from the decomposition of the uniaxial stress; d can be measured as the average separation between veins by ECCI techniques (results can be found in p.136 and p.147); ξ is the maximum angle of dislocation that is away from a pure screw to cross-slip.

In their experiments for the fatigue tests, the shear modulus μ and the Poisson's ratio ν are 44GPa and 0.44, respectively. According to [52], the lattice spacing l is about 3.6147×10^{-4} microns, and the magnitude of the Burgers vector is about 2.556×10^{-4} microns. The plastic amplitude is about $\gamma \sim 2 \times 10^{-3}$.

If the crystallography is considered, the cross-slip plane in this scenario is fixed to be $(\bar{1}\bar{1}1)$. But it can be calculated that the resolved applied stress in this plane is 0. This suggests that the source of the anti-plane component σ_{12} could be either the interactions between screw segments or the image force near boundaries [18].

3.4.3 Comparisons with Experimental Data

The Saturation Stress

As from p.17 of [2], the saturation stress, which is, the stress amplitude measured at both ends of the specimen, has a constant value of about 28MPa. Such a saturation stress can be considered as the yield stress of the specimen. According to the flow rule in [9], the yield stress is the minimum stress to trigger the plastic flow, which corresponds to motions of a large number of screw segments driven by the external force in this context. From the travelling wave formulations, it can be seen that the

external driven dislocation motion starts when U turns negative. This suggests that $U = 0$ is the yield point of the specimen.

Recalling from (3.38), we know that in this case the dimensionless σ_{23} and d satisfy

$$\sigma_{23} d = -\frac{1}{2\pi(1-\nu)}. \tag{3.57}$$

Since d has been rescaled in (3.3) by the magnitude of the Burgers vector b, we can compute it by

$$d = \frac{d^{\text{mes}}}{b}, \tag{3.58}$$

where d^{mes} is the measured width of screw segments in the specimen. d^{mes} can be approximated by the distance between the neighbouring veins, whose experimental data can be found in p.136 of [2]. Similarly, since σ_{23} has been rescaled by the shear modulus μ, we can relate the saturation stress to σ_{23} by the Schmid factor λ:

$$\lambda \sigma^{\text{sat}} = -\mu \sigma_{23}. \tag{3.59}$$

Combining (3.57), (3.58) and (3.59) gives a formula for the saturation stress:

$$\sigma^{\text{sat}} = \frac{\mu b}{2\pi(1-\nu) d^{\text{mes}} \lambda}. \tag{3.60}$$

Again we list all the coefficients needed in (3.60): $\mu = 44\text{GPa}$; $\nu = 0.44$; $b = 2.556 \times 10^{-4}\mu\text{m}$; $\lambda = 0.47$. For d^{mes}, the averaging vein spacing d^{v} and averaging vein width w^{v} were both given in p.136 of [2]. Since d^{mes} is the average width of channels, it can be approximated by $d^{\text{mes}} = d^{\text{v}} - w^{\text{v}}$.

In table 3.2, a comparison between the measured saturation stresses and their computed values from (3.60) is given. It can be seen that they do not agree with each

Measured σ^{sat} (MPa)	w^{v} (μm)	d^{v} (μm)	Computed σ^{sat} (MPa)
8.8	0.68 ($\pm$0.2)	4.15 ($\pm$0.05)	1.9598
25.6	0.9 ($\pm$0.1)	2.4 ($\pm$0.05)	4.5337
28.2	1.03 ($\pm$0.1)	2.1 ($\pm$0.05)	5.3557
27.9	1.1 ($\pm$0.1)	1.9 ($\pm$0.05)	8.5008
27.8	1.11 ($\pm$0.1)	1.9 ($\pm$0.05)	8.6084

Table 3.2: Comparison to the measured saturation stress.

other quite well, and there are many possible reasons for this. One could be from the irregular shape of veins, which may greatly decrease the distance from a dislocation in one vein to its nearest opposite dislocation in another vein. Another explanation

could be that here we neglect the effect to a screw segment by other segments passing by. Actually, two opposite screw segments from neighbouring glide planes can lock themselves by forming screw dipoles. In this scenario, an extra external stress to break the screw dipole is required to trigger the external-driven motion of travelling waves, giving rise to an increase to the saturation stress computed in Table 3.2.

By rearranging (3.60), we can also give a criterion for the occurrence of the plastic flow between the applied stress at the two ends σ^{a} (MPa) and d^{mes} (μm) by

$$\sigma^{\mathrm{a}} d^{\mathrm{mes}} = \frac{\mu b}{2\pi(1-\nu)\lambda}. \tag{3.61}$$

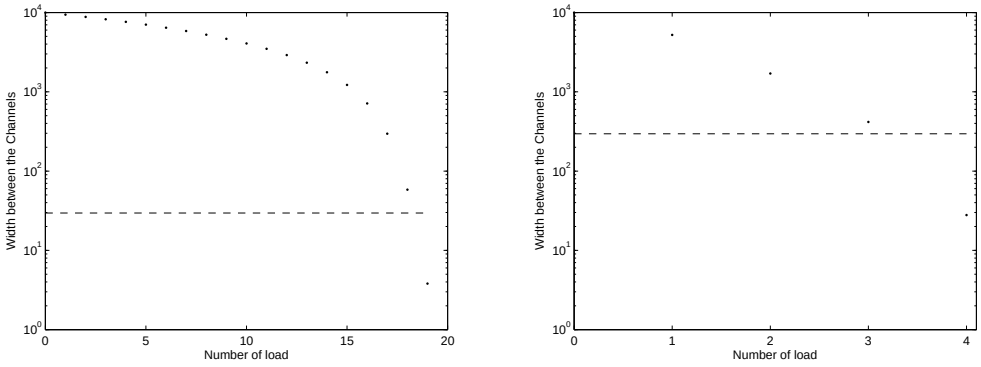
This suggests that the product of σ^{a} and d^{mes} is determinant in the early stage of the fatigue test.

A Model for the Rate of Dislocation Multiplication

At the end of this chapter, we give a model to roughly estimate the rate of dislocation multiplication. Without considering the crystallographic effect, as the cyclic load proceeds, screw segments are induced to cross-slip by the external stress σ_{12}. However, as from the above calculations, only screw segments which satisfy the cross-slip criterion in (3.55) can finish their cross-slip motion, resulting in dislocation multiplication. If starting with $d = 10^4$ and $k = 1$, the screw segment will cross-slip to generate a new segment with a width d_c as the cyclic load proceeds. If the new screw segment (with a width of d_c) still satisfies (3.55), it will become a possible matrix for further cross-slip. Such process will continue until (3.55) fails. In Fig. 3.12, for a given stress amplitude, the dots show the width of screw segment after n-th cycle of cross-slip motion derived from (3.55). It can be seen that the screw segment will keep cross-slipping until the dot falls below the dashed curve, which is the minimum distance required for the occurrence. Therefore, the number of cycles a screw is needed to be pinned in their primary slip plane is N, then $2(N-1)$ is the number of dislocations increased under such a process.

3.5 Conclusion

By applying the travelling wave formulation to the law of motion derived in the previous chapter, we have found the shapes of screw segments parameterised by the applied stress and the average separation between neighbouring veins. Then a criterion for



(a) $\gamma \sim 10^{-2}$ (b) $\gamma \sim 10^{-3}$

Figure 3.12: Dislocation multiplication under cyclic loads: for a given stress amplitude, the dots the width of screw segment after n-th cycle. of cross-slip motion derived from (3.55). It can be seen that the screw segment will keep cross-slipping until the dot falls below the dashed curve, which is the minimum distance required for the occurrence.

the occurrence of the cross-slip motion is proposed. With such a criterion, we are able to identify when the dislocation multiplication is stopped.

Although we finally get an estimation for the rate of dislocation multiplication, still the models proposed in this Chapter have some weakness. An essential drawback of the model is its lack of experimental or simulation support. Also, in order to seek an analytical formula for the criterion, some important mechanism may be neglected by making simplifications. However, the planar travelling wave formulation does offer us a way to capture the dislocation flow that arises in many mechanisms, for example finding the saturation stress. Furthermore, the criterion for the occurrence of the cross-slip motion may provide an approximation to finding the activated slip system in macroscopic plasticity.

Chapter 4

Homogenisation of One-Dimensional Monopole Arrays

In the previous chapter, the mechanism of dislocation multiplication in the early stage of metal fatigue was discussed. Experimental observations have shown that the newly generated edge dislocations dwell in veins and start to form PSBs when the stress reaches the saturation point [2]. So it is natural to look at the behaviour of a large number of straight edge dislocations, either in veins or PSBs. One main difficulty arising from the previous attempts recorded in literature, however, is that the number of dislocations is too large to calculate their evolution individually. To overcome this, we introduce a multiple-scale technique, to find the collective behaviour for these straight dislocations.

4.1 The Idea of Homogenisation of One-Dimensional Monopoles

4.1.1 Unstressed Single Pile-ups

A straight dislocation is translationally invariant along its tangent. Thus it is equivalent to study the behaviour of a point in a plane. These points, similar to electric charges, have signs depending on the direction of their tangents with respect to the Burgers vector.

As mentioned above, how dislocations distribute themselves is closely related to the behaviour of edge dislocations in veins or PSBs. The attempt to look for an equilibrium state for many straight dislocations dates back to 1951 in [20]. The modified

version of the configuration proposed in that paper is a one-dimensional array of monopoles, where a row of N straight dislocations, either edge or screw, of the same sign line up in the interval $(-1, 1)$ on the x-axis with a lock at either end. Here a 'lock' denotes a fixed dislocation monopole. When the system is in equilibrium under no applied stress, the position of the k-th dislocation, denoted by p_k, satisfies the condition that the net stress by all other dislocations, including the two locks at both ends should vanish. Mathematically, this gives

$$\sum_{i=0, i\neq k}^{N-1} \frac{1}{p_k - p_i} = 0. \tag{4.1}$$

Thus to understand how dislocations distribute themselves, one has to solve a linear system of $N-2$ equations (note that $p_0 = -1$ and $p_{N-1} = 1$ are the positions for the two locks). In real materials, N is very large, which raises the computational intensity. On the other hand, people are more interested in finding the density distribution at a continuous level, than the exact position of every single dislocation. In another word, people are more interested in understanding the density distribution of dislocations, which is defined by

$$\rho(x) = \lim_{\Delta x \to 0} \frac{n(x; \Delta x)}{2\Delta x}, \tag{4.2}$$

where $n(x; \Delta x)$ is the number of dislocations in the interval $[x - \Delta x, x + \Delta x]$.

One method to derive an equation for $\rho(x)$ was detailed in [33], where it is shown that the density distribution should satisfy the integral equation

$$\int_{-1}^{1} \frac{\rho(x')\mathrm{d}x'}{x - x'} = 0. \tag{4.3}$$

By using the Hilbert transformation and the fact that

$$\int_{-1}^{1} \rho(x)\mathrm{d}x = N,$$

we are thus able to homogenise the one-dimensional monopoles by writing down their density distribution:

$$\rho(x) = \frac{N}{\pi\sqrt{1 - x^2}}. \tag{4.4}$$

Nevertheless, the method proposed in [33] cannot be generalised to the homogenisation of dipoles. This is because the stress generated by a pair of equal and opposite dislocations is far less than by a monopole. Consequently, averaging a large number of dipoles appears equivalent to averaging nothing. To overcome this, in this and the

next chapter, a method using multiple scales is proposed. In the rest of this chapter, we will explain this method by deriving the equation for the density distribution of monopoles in the same form as (4.3). Then in the following chapter, we will apply the approach to homogenise a one-dimensional array of dipoles.

4.1.2 Quantities on Different Scales

The idea of the multiple-scale method is the following: by introducing an additional spatial variable on a smaller scale, we can track all quantities in two scales simultaneously. Then with the asymptotic expansions, the problem becomes solvable as an expansion in the ratio between the two scales.

Now we consider the same configuration of one-dimensional monopoles as in § 4.1.1, where we look at N monopoles in the interval $(-1, 1)$. If we set $\epsilon = 2/N$, we obtain two spatial scales, as illustrated in shown in Fig. 4.1. When the observation is

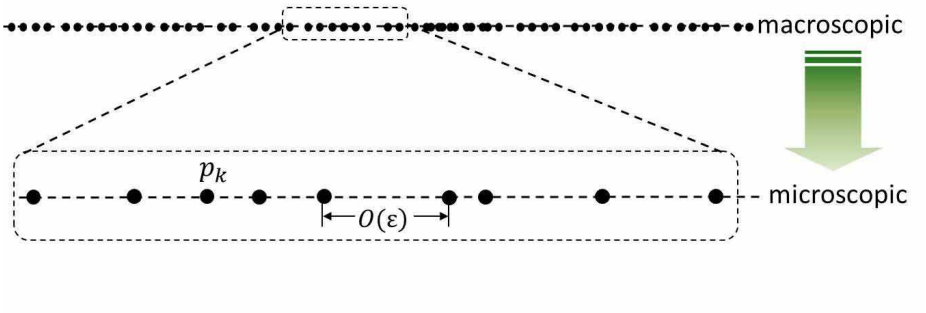


Figure 4.1: Quantities of different scales: when observation is made at a macroscopic level, say, $\mathcal{O}(1)$ by scale, the dislocations are so close to each other that they can be treated as continuously distributed. At this level, people are interested in the quantities, such as dislocation density. Isolated dislocations cannot be seen unless the observation is made at a microscopic level, i.e. $\mathcal{O}(\epsilon)$ by scale.

made at a macroscopic level, say, $\mathcal{O}(1)$ by scale, the dislocations are so close to each other that they can be treated as continuously distributed. At this level, people are interested in quantities, such as the dislocation density. Isolated dislocations cannot be seen unless the observation is made at a microscopic level, i.e. $\mathcal{O}(\epsilon)$ by scale. The density distribution in the macroscopic level is actually the consequence of the self-arrangement of all these isolated poles. As seen above, investigation of behaviour for all individual dislocations will give rise to a system of algebraic equations as in (4.1). A bridge is needed to pass the collective information from the small scale.

4.1.3 Introduction of the Fast Scale Variable

Such a bridge connecting the two scales can be built by defining a map B: $(-1,1) \to \mathbb{R}$, such that

$$B(p_k) = \epsilon k. \tag{4.5}$$

By interpolation (for example, by spline interpolation), $B(x)$ can be smoothly defined throughout $(-1,1)$. Then the domain $(-1,1)$ can be divided into N cells characterised by the dislocation within each. To be specific, we set the k-th cell occupies the interval $[B^{-1}(\epsilon k), B^{-1}(\epsilon(k+1)))$. In the $B(x)$ space, the cells are periodically lined up with a dislocation standing at the left boundary. Thus a fast-scale variable can be introduced by defining

$$X = \frac{B(x)}{\epsilon}. \tag{4.6}$$

The introduction of $B(x)$ enables us to investigate our problem in two scales. For any x, we can easily find that it belongs to the $\lfloor B(x)/\epsilon \rfloor$-th cell, where $\lfloor \cdot \rfloor$ denotes the integer part of. In another word, x belongs to the cell identified by the dislocation at

$$p_k = B^{-1}\left(\epsilon \left\lfloor \frac{B(x)}{\epsilon} \right\rfloor\right).$$

This suggests any function $f(x)$ in original coordinates can be written as $f(p_k, X)$. In each cell, the variation can be measured as a function of the small-scale variable X defined in (4.6), while the variation across cells is still described by the large-scale variable x. To avoid the ambiguity in variables, we introduce

$$\bar{x} = x \tag{4.7}$$

as the large-scale variable in the multiple-scale coordinates, while x is still the spatial variable in the original coordinate. Thus we are able to express any function $f(x)$ under the multiple-scale coordinates $(\bar{x}, X)$ as $f(\bar{x}, X)$.

The correlation between $\bar{x}$ and X is illustrated in Fig. 4.2. In the $(\bar{x}, X)$ space, the problem is actually being viewed along the curve $X = B(\bar{x})/\epsilon$. Such correlation suggests that the position in $(\bar{x}, X)$ space of any given point $x = x'$ cannot be assigned independently. From (4.7), we have $\bar{x} = x'$. Then its corresponding value in X can be obtained by using (4.6):

$$X' = \frac{B(x')}{\epsilon}. \tag{4.8}$$

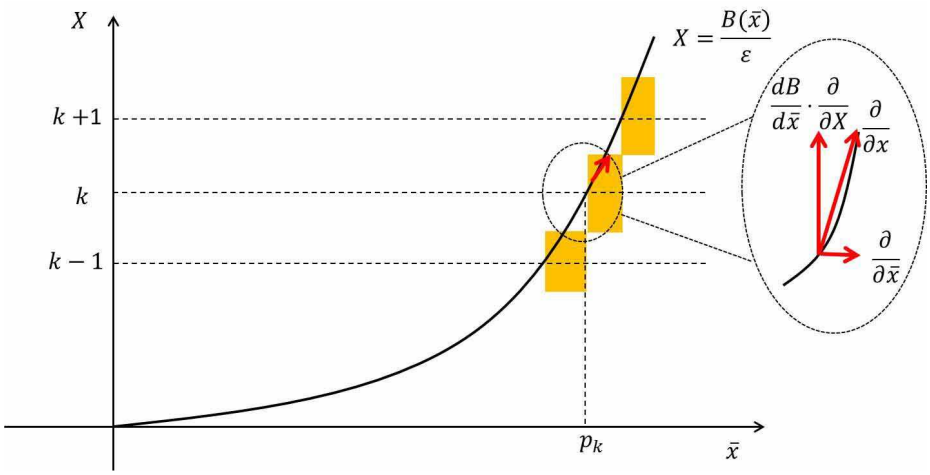


Figure 4.2: Correlation between $\bar{x}$ and x: in the $(\bar{x}, X)$ space, the problem is actually being looked at along the curve $X = B(\bar{x})/\epsilon$. In each cell, which is an orange box, the variation in $\bar{x}$ is at $\mathcal{O}(\epsilon)$ while that in X is $\mathcal{O}(1)$. The evolution in x can be expressed as a superposition of that in $\bar{x}$ and X as depicted in the right hand side. Since the derivatives with respect to $\bar{x}$ and X are not in the same scale, we can treat them independently throughout the calculation. However, as we will see later, when we evaluate at some specific point, the correlation between $\bar{x}$ and X has to be considered.

In the following calculations, we will also need to write the Dirac function in the multiple-scale forms. This can be achieved as follows:

$$\delta(x - x') = \frac{B'(x')}{\epsilon}\delta\left(\frac{B(x) - B(x')}{\epsilon}\right) = B'(x')\delta(X - X'(p_k)). \tag{4.9}$$

In each cell, which is an orange box in Fig. 4.2, the variation in $\bar{x}$ is of $\mathcal{O}(\epsilon)$ while that in X is $\mathcal{O}(1)$. When we consider the derivative of any function with respect to x, by using the chain rule that

$$\frac{\partial}{\partial x} = \frac{\partial}{\partial \bar{x}} + \frac{B'(\bar{x})}{\epsilon}\frac{\partial}{\partial X}, \tag{4.10}$$

we can decompose the derivative with respect to x into two derivatives with respect to $\bar{x}$ and X, respectively, as depicted in the right hand side of Fig. 4.2. (4.10) also shows that the evolution in the two variables are not in the same scale, which suggests that the asymptotic technique can be implemented. However, as we will see later, when we evaluate at some specific point in x, the correlation between $\bar{x}$ and X has to be considered. For example, when we approach p_k along x axis, we actually have

$$\lim_{x \to p_k} f(x) = \lim_{\bar{x} \to p_k, X \to k} f(\bar{x}, X),$$

in the multiple-scale form.

Before we proceed to introduce any detail in calculations, we need to mention that throughout the calculations, we will try to avoid evaluating precisely at p_k, because otherwise, we go back to solving the system of equations given at the beginning of this chapter. Instead, by defining

$$\zeta(\bar{x}) = \frac{B(\bar{x})}{\epsilon} - \left\lfloor \frac{B(\bar{x})}{\epsilon} \right\rfloor = \frac{B(\bar{x})}{\epsilon} - \frac{B(p_k)}{\epsilon}, \tag{4.11}$$

we are enabled to express p_k as a function of $\bar{x}$:

$$p_k = B^{-1}(B(\bar{x}) - \epsilon\zeta(\bar{x})). \tag{4.12}$$

It should be mentioned that, as a shift function, $\zeta(\bar{x})$ cannot be differentiated or expanded. As we will see from the calculations in the next section, we only need to evaluate $\zeta(\bar{x})$ at the position of monopoles, i.e.

$$\zeta(p_k) = 0. \tag{4.13}$$

4.1.4 Density Distribution

With the introduction of $B(\bar{x})$, the macroscopic density distribution can also be expressed under the regime of multiple scales. Recalling from (4.5), we have

$$n(x;\Delta x) = \left\lfloor \frac{B(x+\Delta x)}{\epsilon} \right\rfloor - \left\lfloor \frac{B(x-\Delta x)}{\epsilon} \right\rfloor.$$

Combining the definition of the density ρ in (4.2) and (4.12) gives

$$\begin{aligned} \rho(x) &\sim \frac{1}{2\Delta x}\left(\left\lfloor \frac{B(x+\Delta x)}{\epsilon} \right\rfloor - \left\lfloor \frac{B(x-\Delta x)}{\epsilon} \right\rfloor \right) \\ &\sim \frac{1}{\epsilon}\cdot\frac{B(x+\Delta x) - B(x-\Delta x)}{2\Delta x} - \frac{\zeta(x+\Delta x) - \zeta(x-\Delta x)}{\Delta x}\cdot, \end{aligned} \tag{4.14}$$

as $\Delta x \to 0$. If we rescale $\rho(x)$ by ϵ:

$$\hat{\rho}(x) = \epsilon\rho(x),$$

and still use $\rho(x)$ to denote the rescaled density, then (4.14) can be rewritten as

$$\rho(x) \sim \frac{B(x+\Delta x) - B(x-\Delta x)}{2\Delta x} + \mathcal{O}\left(\frac{\epsilon}{\Delta x}\right), \tag{4.15}$$

as $\Delta x \to 0$. Since ϵ is a microscopic quantity, it is still sensible to assume $\Delta x \gg \epsilon$. Therefore, by letting $\Delta x \to 0$ in (4.15), we have

$$\rho(x) \sim B'(x) + \mathcal{O}(\Delta x) + \mathcal{O}\left(\frac{\epsilon}{\Delta x}\right), \tag{4.16}$$

where $B'(x) = \mathrm{d}B/\mathrm{d}x$. This suggests that in the multiple-scale coordinates, the leading order density $\rho^{(0)}(\bar{x})$ satisfies

$$\rho^{(0)}(\bar{x}) = B'(\bar{x}). \tag{4.17}$$

Up to now, we have managed to introduce two spatial variables of different scales and the density distribution in the multiple-scale form. In the following sections, we will derive the equation for $B'(\bar{x})$ under the context of one-dimensional dislocation pile-ups.

4.2 Homogenisation of a Row of Screw Monopoles

The first example of implementing the multiple-scale technique is the homogenisation of one-dimensional unstressed screw monopoles. The configuration we consider here is a row of N positive screw dislocations distributed in the interval $(-1, 1) \times \{0\}$ in the x-y space, with each dislocation located at $(p_k, 0)$.

Here and in the next two chapters, we non-dimensionalise all spatial variables, such as x, y and b, by L, where L is the length scale that we are interested in. Typically, L is chosen to be 1 micron. According to experimental observations, the spacing between neighbouring dislocations d is about tens of nanometre ($\sim 10^{-8}$m). Thus ϵ is determined by $\epsilon = d/L \approx 0.01$.

4.2.1 Governing Equations

The stress field by a row of screw monopoles can be considered as a superposition of the stress fields by single straight screw dislocations. Thus referring to (1.26) in § 1.2.4, we solve an equation for the stress function $\varphi(x, y)$ which satisfies

$$\Delta\varphi = \epsilon^2 \sum_{k=0}^{N-1} \delta(x - p_k)\delta(y), \tag{4.18}$$

where φ has been rescaled by $\mu b/\epsilon^2$. Then the non-zero stress components can be computed by

$$\sigma_{13} = -\frac{\partial \varphi}{\partial y}, \qquad \sigma_{23} = \frac{\partial \varphi}{\partial x}. \tag{4.19}$$

If the system is in equilibrium, the net force on every single dislocation should vanish. Due to the singular nature of the stress components, we need to mathematically remove this singularity to write the force balance equation as

$$\lim_{x \to p_k, y \to 0} (\sigma_{13}(x, y) - \Sigma_{13}(x, y; p_k, 0)) = 0 \tag{4.20}$$

and

$$\lim_{x \to p_k, y \to 0} (\sigma_{23}(x, y) - \Sigma_{23}(x, y; p_k, 0)) = 0, \tag{4.21}$$

where

$$\Sigma_{13}(x, y; p_k, 0) = -\frac{\epsilon^2 y}{2\pi((x - p_k)^2 + y^2)} \tag{4.22}$$

and

$$\Sigma_{23}(x, y; p_k, 0) = \frac{\epsilon^2 (x - p_k)}{2\pi((x - p_k)^2 + y^2)}. \tag{4.23}$$

4.2.2 Expansions under the Multiple-Scale Coordinates

The difference in scales between $\bar{x}$ and X enables us to expand all quantities in terms of ϵ.

The Inner Region

When close to the monopole array, we are in the region where $y \sim \mathcal{O}(\epsilon)$. It is called the inner region as shown in Fig. 4.3. In the inner region, we need to rescale y by

$$Y = \frac{y}{\epsilon}. \tag{4.24}$$

Thus in the inner region, the stress function $\varphi(x, y)$ in (4.18) is defined to be a function of $\bar{x}$, X and Y: $\varphi_{\text{in}}(\bar{x}, X, Y)$. Replacing x' and $X'(p_k)$ in (4.9) by p_k and k, respectively, gives the δ-functions in the right hand side of (4.18):

$$\delta(x - p_k) = \frac{B'(p_k)}{\epsilon} \cdot \delta\left(X - k\right). \tag{4.25}$$

$\delta(y)$ can also be rewritten by

$$\delta(y) = \frac{1}{\epsilon} \cdot \delta\left(Y\right), \tag{4.26}$$

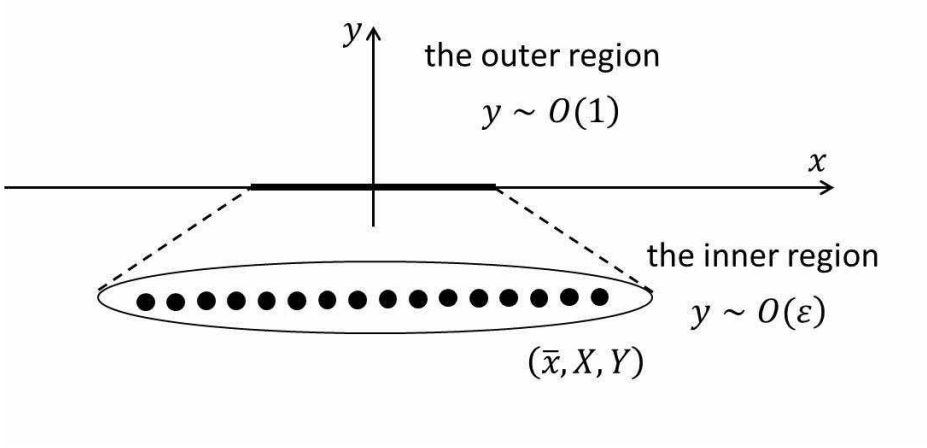


Figure 4.3: The inner and outer region: if the observation is made near the dislocation array, where $y \sim \mathcal{O}(\epsilon)$, we are in the inner region, where dislocations look discretely; if the observation is made away from the array, where $y \sim \mathcal{O}(1)$, we are in the outer region, where dislocations look continuously distributed.

in the inner region.

From (4.10) and the fact that

$$\frac{\partial}{\partial y} = \frac{1}{\epsilon} \cdot \frac{\partial}{\partial Y}, \tag{4.27}$$

(4.18) can be rewritten under the multiple-scale coordinates by

$$\left(\frac{\partial}{\partial \bar{x}} + \frac{B'(\bar{x})}{\epsilon} \cdot \frac{\partial}{\partial X} \right)^2 \varphi_{\text{in}} + \frac{1}{\epsilon^2} \cdot \frac{\partial^2 \varphi_{\text{in}}}{\partial Y^2} = \sum_{k=0}^{N-1} B'(p_k) \delta(X-k) \delta(Y). \tag{4.28}$$

As we mentioned above, p_k should also be approximated so that we can avoid solving the system of algebraic equations. This can be done by incorporating (4.12) with (4.28):

$$\left(\frac{\partial}{\partial \bar{x}} + \frac{B'(\bar{x})}{\epsilon} \cdot \frac{\partial}{\partial X} \right)^2 \varphi_{\text{in}} + \frac{1}{\epsilon^2} \cdot \frac{\partial^2 \varphi_{\text{in}}}{\partial Y^2} = \sum_{k=0}^{N-1} B'(B^{-1}(B(\bar{x}) - \epsilon\zeta(\bar{x}))) \cdot \delta(X-k) \delta(Y), \tag{4.29}$$

where $\zeta(\bar{x})$ in the right hand side is still a function of k.

From (4.29), it can be observed that the monopoles are periodically located in X, but their magnitudes $B'(\bar{x})$ vary from cell to cell. Since $B'(\bar{x})$ is slow varying in the nearby cell and decays like $1/x$ away from the k-th cell, it is sensible to assume that every quantity under the multiple-scale coordinates is periodic in X of period 1. As we will see in this and the following chapter, the error from imposing such periodicity does not come to effect before we find the equation for the density. This enables us to reduce the

computational domain to $\Omega = \{(\bar{x}, X, Y)| -1 < \bar{x} < 1, 0 \leq X < 1, -\infty < Y < \infty\}$. Or alternatively, we can define X by

$$X = \frac{B(x) - B(p_k)}{\epsilon}, \tag{4.30}$$

where x belongs to the cell characterised by p_k.

Therefore, it is equivalent to rewrite (4.29) as

$$\left(\frac{\partial}{\partial \bar{x}} + \frac{B'(\bar{x})}{\epsilon} \cdot \frac{\partial}{\partial X}\right)^2 \varphi_{\text{in}} + \frac{1}{\epsilon^2} \cdot \frac{\partial^2 \varphi_{\text{in}}}{\partial Y^2} = B'(B^{-1}(B(\bar{x}) - \epsilon\zeta(\bar{x}))) \cdot \delta(X)\delta(Y), \tag{4.31}$$

with X periodic in $[0, 1)$.

Once φ_{in} is obtained, the stress components in the inner region can be calculated by

$$\sigma_{13}^{\text{in}}(\bar{x}, X, Y) = -\frac{1}{\epsilon} \cdot \frac{\partial \varphi_{\text{in}}}{\partial Y} \tag{4.32}$$

and

$$\sigma_{23}^{\text{in}}(\bar{x}, X, Y) = \left(\frac{\partial \varphi_{\text{in}}}{\partial \bar{x}} + \frac{B'(\bar{x})}{\epsilon} \cdot \frac{\partial \varphi_{\text{in}}}{\partial X}\right), \tag{4.33}$$

respectively.

From (4.31), it can be seen that the leading order of the right hand side is $\mathcal{O}(1)$, which suggests that the stress component, by (4.32) and (4.33), starts from $\mathcal{O}(\epsilon)$. Thus we can assume

$$\sigma_{13}^{\text{in}}(\bar{x}, X, Y) \sim \epsilon\sigma_{13}^{\text{in}(1)}(\bar{x}, X, Y) + \epsilon^2\sigma_{13}^{\text{in}(2)}(\bar{x}, X, Y) + \epsilon^3\sigma_{13}^{\text{in}(3)}(\bar{x}, X, Y) + \cdots \tag{4.34}$$

and

$$\sigma_{23}^{\text{in}}(\bar{x}, X, Y) \sim \epsilon\sigma_{23}^{\text{in}(1)}(\bar{x}, X, Y) + \epsilon^2\sigma_{23}^{\text{in}(2)}(\bar{x}, X, Y) + \epsilon^3\sigma_{23}^{\text{in}(3)}(\bar{x}, X, Y) + \cdots . \tag{4.35}$$

To be systematic, $\varphi_{\text{in}}(\bar{x}, X, Y)$ should be expanded as

$$\varphi_{\text{in}}(\bar{x}, X, Y) \sim \epsilon\varphi_{\text{in}}^{(1)}(\bar{x}) + \epsilon^2\varphi_{\text{in}}^{(2)}(\bar{x}, X, Y) + \epsilon^3\varphi_{\text{in}}^{(3)}(\bar{x}, X, Y) + \cdots , \tag{4.36}$$

where $\varphi_{\text{in}}^{(1)}(\bar{x})$ is the carrier of the information from the applied stress. Then the problem can be considered sequentially by orders of ϵ.

Singularities due to a Screw Dislocation

Also we need to consider Σ_{13} and Σ_{23} in the force balance equations (4.20) and (4.21), respectively in the multiple-scale coordinates. To be systematic, we also define a stress potential $\Phi(\bar{x}, X, Y)$ satisfying

$$\left(\frac{\partial}{\partial \bar{x}} + \frac{B'(\bar{x})}{\epsilon} \cdot \frac{\partial}{\partial X}\right)^2 \Phi + \frac{1}{\epsilon^2} \cdot \frac{\partial^2 \Phi}{\partial Y^2} = B'(B^{-1}(B(\bar{x}) - \epsilon\zeta(\bar{x})))\delta(X)\delta(Y). \tag{4.37}$$

It should be mentioned that we are only interested in the singular behaviour of $\Phi(\bar{x}, X, Y)$, i.e. the case when $(X, Y) \to (0, 0)$. Then we obtain

$$\Sigma_{13}(x, y; p_k, 0) \triangleq \Sigma_{13}^{\text{in}}(\bar{x}, X, Y) = -\frac{1}{\epsilon} \cdot \frac{\partial \Phi}{\partial Y}$$

and

$$\Sigma_{23}(x, y; p_k, 0) \triangleq \Sigma_{23}^{\text{in}}(\bar{x}, X, Y) = \frac{\partial \Phi}{\partial \bar{x}} + \frac{B'}{\epsilon}\frac{\partial \Phi}{\partial X}.$$

Here we also need to assume that

$$\Phi(\bar{x}, X, Y) \sim \epsilon^2 \Phi^{(2)}(\bar{x}, X, Y) + \epsilon^3 \Phi^{(3)}(\bar{x}, X, Y) + \cdots; \tag{4.38}$$

$$\Sigma_{13}^{\text{in}}(\bar{x}, X, Y) \sim \epsilon \Sigma_{13}^{\text{in}(1)}(\bar{x}, X, Y) + \epsilon^2 \Sigma_{13}^{\text{in}(2)}(\bar{x}, X, Y) + \cdots; \tag{4.39}$$

$$\Sigma_{23}^{\text{in}}(\bar{x}, X, Y) \sim \epsilon \Sigma_{23}^{\text{in}(1)}(\bar{x}, X, Y) + \epsilon^2 \Sigma_{23}^{\text{in}(2)}(\bar{x}, X, Y) + \cdots. \tag{4.40}$$

Force Balance under the Multiple-Scale Coordinates

When we consider the force balance, we are required to evaluate the regular part of the stress component at $(p_k, 0)$ in the original x-y space. Correspondingly in the multiple-scale form, we need to consider the case when $(\bar{x}, X, Y) \to (p_k, 0, 0)$. By using the definition of Σ_{13}^{in} and Σ_{23}^{in}, we can rewrite the force balance equations (4.20) and (4.21) as

$$\lim_{(X,Y)\to(0,0)} \left(\sigma_{13}^{\text{in}}(p_k, X, Y) - \Sigma_{13}^{\text{in}}(p_k, X, Y)\right) = 0 \tag{4.41}$$

and

$$\lim_{(X,Y)\to(0,0)} \left(\sigma_{23}^{\text{in}}(p_k, X, Y) - \Sigma_{23}^{\text{in}}(p_k, X, Y)\right) = 0, \tag{4.42}$$

respectively.

The Outer Region

When away from the dislocation array, we are in a region where $y \sim \mathcal{O}(1)$, which is called the outer region. Since $y = 0$ is not included in this region, all δ-functions in the right hand side of (4.18) vanish. In this case, unlike in the inner region, y is kept as the vertical spatial variable, and the equation for the stress function, denoted by $\varphi_{\text{out}}(\bar{x}, y, X)$, becomes

$$\left(\left(\frac{\partial}{\partial \bar{x}} + \frac{B'(\bar{x})}{\epsilon} \cdot \frac{\partial}{\partial X} \right)^2 + \frac{\partial^2}{\partial y^2} \right) \varphi_{\text{out}}(\bar{x}, y, X) = 0. \tag{4.43}$$

Although our calculations will be made separately in both the inner and outer regions, they are still related. One physical intuition of such a link is the continuation of the stress components across the boundary layer between them. Mathematically, this provides the matching condition:

$$\lim_{y \to 0^{\pm}} \sigma_{13}^{\text{out}}(\bar{x}, y, X) = \lim_{Y \to \pm\infty} \sigma_{13}^{\text{in}}(\bar{x}, X, Y) \tag{4.44}$$

and

$$\lim_{y \to 0^{\pm}} \sigma_{23}^{\text{out}}(\bar{x}, y, X) = \lim_{Y \to \pm\infty} \sigma_{23}^{\text{in}}(\bar{x}, X, Y) \tag{4.45}$$

To be consistent, the expansions of φ_{out} and stress components in the outer region are set to be

$$\varphi_{\text{out}}(\bar{x}, y, X) \sim \epsilon \varphi_{\text{out}}^{(1)}(\bar{x}, y) + \epsilon^2 \varphi_{\text{out}}^{(2)}(\bar{x}, y, X) + \cdots ; \tag{4.46}$$

$$\sigma_{13}^{\text{out}}(\bar{x}, y, X) \sim \epsilon \sigma_{13}^{\text{out}(1)}(\bar{x}, y, X) + \epsilon^2 \sigma_{13}^{\text{out}(2)}(\bar{x}, y, X) + \cdots ; \tag{4.47}$$

$$\sigma_{23}^{\text{out}}(\bar{x}, y, X) \sim \epsilon \sigma_{23}^{\text{out}(1)}(\bar{x}, y, X) + \epsilon^2 \sigma_{23}^{\text{out}(2)}(\bar{x}, y, X) + \cdots . \tag{4.48}$$

4.2.3 The Leading Order

Once we have written all original equations under the multiple-scale coordinates, we can solve these equations by equating coefficients of power of ϵ sequentially. We will start our calculations from the leading order of the stress component, i.e. $\mathcal{O}(\epsilon)$.

The Inner Region

At $\mathcal{O}(\epsilon)$, the two non-zero stress components satisfy

$$\sigma_{13}^{\text{in}(1)}(\bar{x}, X, Y) = -\frac{\partial \varphi_{\text{in}}^{(2)}}{\partial Y} \tag{4.49}$$

and

$$\sigma_{23}^{\text{in}(1)}(\bar{x}, X, Y) = \frac{\partial \varphi_{\text{in}}^{(1)}}{\partial \bar{x}} + B'(\bar{x}) \cdot \frac{\partial \varphi_{\text{in}}^{(2)}}{\partial X}. \tag{4.50}$$

From now on, we can drop the input $\bar{x}$ for $B'(\bar{x})$ and $\zeta(\bar{x})$ without causing any ambiguity.

Then we need to solve an equation for the corresponding stress function $\varphi_{\text{in}}^{(2)}(\bar{x}, X, Y)$, which is the leading order equation of (4.31):

$$\left(B'^2 \cdot \frac{\partial^2}{\partial X^2} + \frac{\partial^2}{\partial Y^2}\right) \varphi_{\text{in}}^{(2)}(\bar{x}, X, Y) = B'\delta(X)\delta(Y), \tag{4.51}$$

with X is periodic in $[0, 1)$.

From Appendix A.7, we know that

$$\varphi_{\text{in}}^{(2)}(\bar{x}, X, Y) = \frac{1}{4\pi} \log\left(\cosh(2\pi B'Y) - \cos(2\pi X)\right) + c_{\text{in}}^{(2)}(\bar{x}) + Y h_{\text{in}}^{(2)}(\bar{x}), \tag{4.52}$$

where $c_{\text{in}}^{(2)}(\bar{x})$ and $h_{\text{in}}^{(2)}(\bar{x})$ are functions of $\bar{x}$ to be determined. Combining (4.52) with (4.49) and (4.50) gives

$$\sigma_{13}^{\text{in}(1)}(\bar{x}, X, Y) = -\frac{B' \sinh(2\pi B'Y)}{2(\cosh(2\pi B'Y) - \cos(2\pi X))} - h_{\text{in}}^{(2)}(x) \tag{4.53}$$

and

$$\sigma_{23}^{\text{in}(1)}(\bar{x}, X, Y) = \frac{B' \sin(2\pi X)}{2(\cosh(2\pi B'Y) - \cos(2\pi X))} + \frac{\mathrm{d}\varphi_{\text{in}}^{(1)}}{\mathrm{d}x}, \tag{4.54}$$

respectively.

Singularities

Similarly, the leading-order equation for Φ gives

$$\left(B'^2 \cdot \frac{\partial^2}{\partial X^2} + \frac{\partial^2}{\partial Y^2}\right) \Phi^{(2)}(\bar{x}, X, Y) = B'\delta(X)\delta(Y), \tag{4.55}$$

as $(X, Y) \to (0, 0)$, which suggests

$$\Phi^{(2)}(\bar{x}, X, Y) = \frac{1}{4\pi} \log\left(\alpha(\bar{x})\left(X^2 + (B'Y)^2\right)\right), \tag{4.56}$$

where $\alpha(\bar{x})$ is to be determined. Hence we obtain

$$\Sigma_{13}^{\text{in}(1)}(\bar{x}, X, Y) = -\frac{1}{\epsilon} \cdot \frac{\partial \Phi^{(2)}}{\partial Y} = -\frac{B'^2 Y}{2\pi(X^2 + (B'Y)^2)} \tag{4.57}$$

and

$$\Sigma_{23}^{\text{in}(1)}(\bar{x}, X, Y) = \frac{B'}{\epsilon} \cdot \frac{\partial \Phi^{(2)}}{\partial X} = \frac{B'X}{2\pi(X^2 + (B'Y)^2)}. \tag{4.58}$$

Force Balance

At $\mathcal{O}(\epsilon)$, the force balance equation (4.41) becomes

$$\lim_{X\to 0, Y\to 0} \left(\sigma_{13}^{\text{in}(1)}(p_k, X, Y) - \Sigma_{13}^{\text{in}(1)}(p_k, X, Y) \right) = 0. \tag{4.59}$$

Expanding (4.12) gives

$$p_k \sim \bar{x} - \frac{\epsilon\zeta}{B'} + \cdots, \tag{4.60}$$

which suggests that the shift $\zeta(\bar{x})$ is a higher order term. Therefore the leading order of the force balance equation (4.41) becomes

$$\lim_{X\to 0, Y\to 0} \left(\sigma_{13}^{\text{in}(1)}(\bar{x}, X, Y) - \Sigma_{13}^{\text{in}(1)}(\bar{x}, X, Y) \right) = 0. \tag{4.61}$$

To analyse the singular behaviour as $(X, Y) \to (0, 0)$, it is more convenient to express all quantities under a polar coordinate system where

$$X = r\cos\theta, \qquad Y = r\sin\theta/B'. \tag{4.62}$$

In this way, from (4.53) as $r \to 0$,

$$\sigma_{13}^{\text{in}(1)}(\bar{x}, X, Y) \sim -\frac{\sin\theta}{2\pi r} - h_{\text{in}}^{(2)}(\bar{x}) + \mathcal{O}(r). \tag{4.63}$$

Also, from (4.57), we can rewrite $\Sigma_{13}^{\text{in}(1)}(\bar{x}, X, Y)$ as

$$\Sigma_{13}^{\text{in}(1)}(\bar{x}, X, Y) = -\frac{\sin\theta}{2\pi r}. \tag{4.64}$$

Plugging (4.63) and (4.64) into (4.61) gives

$$h_{\text{in}}^{(2)}(\bar{x}) = 0,$$

which reduces the expression for $\varphi_{\text{in}}^{(2)}(\bar{x}, X, Y)$ in (4.52) to

$$\varphi_{\text{in}}^{(2)}(\bar{x}, X, Y) = \frac{1}{4\pi} \log\left(\cosh(2\pi B'Y) - \cos(2\pi X)\right) + c_{\text{in}}^{(2)}(\bar{x}). \tag{4.65}$$

Similarly the other force balance equation (4.42) becomes

$$\lim_{X\to 0, Y\to 0}\left(\sigma_{23}^{\text{in}(1)}(\bar{x}, X, Y) - \Sigma_{23}^{\text{in}(1)}(\bar{x}, X, Y)\right) = 0, \tag{4.66}$$

at $\mathcal{O}(\epsilon)$. The procedure can also be applied to (4.66) to obtain

$$\frac{\partial \varphi_{\text{in}}^{(1)}}{\partial \bar{x}} = 0.$$

Without loss of generality, we set

$$\varphi_{\text{in}}^{(1)}(\bar{x}) = 0.$$

The Outer Region

In the outer region, the leading-order equation of (4.43) is of $\mathcal{O}(1)$:

$$\frac{\partial^2 \varphi_{\text{out}}^{(2)}}{\partial X^2} = 0.$$

By using the periodicity in X, we can integrate the above equation to obtain $\partial \varphi_{\text{out}}^{(2)}/\partial X = 0$, which suggests $\varphi_{\text{out}}^{(2)}$ is independent of X.

At $\mathcal{O}(\epsilon)$, we have

$$\left(\frac{\partial^2}{\partial \bar{x}^2} + \frac{\partial^2}{\partial y^2}\right)\varphi_{\text{out}}^{(1)}(\bar{x}, y) + \frac{\partial^2 \varphi_{\text{out}}^{(3)}}{\partial X^2} = 0. \tag{4.67}$$

Again, integrating (4.67) with respect to X and using periodicity, we find that

$$\left(\frac{\partial^2}{\partial \bar{x}^2} + \frac{\partial^2}{\partial y^2}\right)\varphi_{\text{out}}^{(1)}(\bar{x}, y) = 0 \tag{4.68}$$

holds when being away from the slit $(-1, 1) \times \{0\}$. Then (4.67) is reduced to

$$\frac{\partial^2 \varphi_{\text{out}}^{(3)}}{\partial X^2} = 0.$$

Similarly as what we did to $\varphi_{\text{out}}^{(2)}$, we find $\varphi_{\text{out}}^{(3)}$ is also independent of X. Actually, we can use this method to prove that each order of φ_{out} is independent of X for all i. Physically, this shows that when away from the monopole arrays, dislocations look continuous, such that the change in the cell is hardly observed. The boundary conditions for $\varphi^{(1)}(\bar{x}, y)$ and its derivatives across the slit can be imposed by matching with the inner region:

$$\lim_{y\to 0^{\pm}} \varphi_{\text{out}}^{(1)}(\bar{x}, y) = 0; \tag{4.69}$$

$$\lim_{y\to 0^{\pm}} \frac{\partial \varphi_{\text{out}}^{(1)}}{\partial y} = -\lim_{y\to 0^{\pm}} \sigma_{13}^{\text{out}(1)}(\bar{x}, y) = -\lim_{Y\to\pm\infty} \sigma_{13}^{\text{in}(1)}(\bar{x}, X, Y) = \pm\frac{B'(\bar{x})}{2}; \tag{4.70}$$

$$\lim_{y\to 0^{\pm}} \frac{\partial \varphi_{\text{out}}^{(1)}}{\partial \bar{x}} = \lim_{y\to 0^{\pm}} \sigma_{23}^{\text{out}(1)}(\bar{x}, y) = -\lim_{Y\to\pm\infty} \sigma_{23}^{\text{in}(1)}(\bar{x}, X, Y) = 0. \tag{4.71}$$

From (4.70), it can be seen that the normal derivative across the slit is not continuous. If we treat $\varphi_{\text{out}}^{(1)}(x, y)$ as the real part of some holomorphic function $f(z)$, where $z = x + \mathrm{i}y$, by using the Plemelj formulae, we obtain

$$\varphi_{\text{out}}^{(1)}(\bar{x}, y) = \frac{1}{4\pi}\int_{-1}^{1} B'(x') \log\left((\bar{x} - x')^2 + y^2\right) \mathrm{d}x' + c(\bar{x}), \tag{4.72}$$

where $c(\bar{x})$ is some arbitrary function of $\bar{x}$. It can be checked that $\varphi_{\text{out}}^{(1)}$ in (4.72) satisfies the jump condition in (4.70).

To satisfy (4.71), we can take the derivative of (4.72) with respect to $\bar{x}$ to give

$$\sigma_{23}^{\text{out}(1)}(\bar{x}, y) = \frac{\partial \varphi_{\text{out}}^{(1)}}{\partial \bar{x}} = \frac{1}{2\pi}\fint_{-1}^{1} \frac{(\bar{x} - x')B'(x')\mathrm{d}x'}{(\bar{x} - x')^2 + y^2} + \frac{\mathrm{d}c}{\mathrm{d}\bar{x}},$$

where "$\fint$" denotes the Cauchy integral. Since there is no applied stress at infinity, $\mathrm{d}c/\mathrm{d}\bar{x}$ vanishes. Thus

$$\sigma_{23}^{\text{out}(1)}(\bar{x}, y) = \frac{1}{2\pi}\fint_{-1}^{1} \frac{(\bar{x} - x')B'(x')\mathrm{d}x'}{(\bar{x} - x')^2 + y^2}. \tag{4.73}$$

From the matching condition (4.71), we require

$$0 = \lim_{y\to 0} \sigma_{23}^{\text{out}(1)}(\bar{x}, y) = \fint_{-1}^{1} \frac{B'(x')\mathrm{d}x'}{\bar{x} - x'}. \tag{4.74}$$

Recalling from (4.17) that

$$\rho^{(0)}(\bar{x}) = B'(\bar{x}),$$

we finally reach an integral equation describing the leading order density distribution of the unstressed screw monopoles by

$$\fint_{-1}^{1} \frac{\rho^{(0)}(x')\mathrm{d}x'}{\bar{x} - x'} = 0. \tag{4.75}$$

This is in the same form as in (4.3) derived in §17.6 of [33]

4.3 Homogenisation of a Row of Edge Monopoles

The homogenisation of one dimensional edge monopoles follows the idea that is used in screw monopoles. However, for edge monopoles, it is more complicated. This is because the stress components by edge dislocations are related to solving an equation with the biharmonic operator.

The configuration we consider here is a row of positive dislocations distributed throughout the interval $(-1, 1)$ along the x-axis. The number of dislocations is set to be N, which is very large. Each dislocation is located at $(p_k, 0)$, where $k \in \mathbb{Z}$ and $0 \leq k < N$. Here $\epsilon = 2/N$, and the magnitude of the Burgers vector is of $\mathcal{O}(\epsilon^2)$, denoted by $b\epsilon^2$.

4.3.1 Governing Equations

For edge monopoles, referring to the equation of the stress function for a single edge dislocation in (1.34), we first need to solve an equation for the stress function, denoted by χ, as the superposition of stress function by individual dislocations:

$$\Delta^2 \chi(x, y) = 2\epsilon^2 \sum_{k=0}^{N-1} \delta\left(x - p_k\right) \delta'\left(y\right). \tag{4.76}$$

It is noted that compared to (1.34), χ has been rescaled by $-\mu b/((1-\nu)\epsilon^2)$. Then the stress components can be calculated by

$$\sigma_{11}(x, y) = -\frac{\partial^2 \chi}{\partial y^2}; \qquad \sigma_{12}(x, y) = \frac{\partial^2 \chi}{\partial x \partial y}; \qquad \sigma_{22}(x, y) = -\frac{\partial^2 \chi}{\partial x^2}. \tag{4.77}$$

If the system is in equilibrium, according to the law of motion, the resolved stress at each dislocation should vanish. In this scenario, the resolved stress component is σ_{12}. Then the force balance equation can be written by letting the regular part of the stress at every dislocation vanish:

$$\lim_{x \to p_k, y \to 0} \left(\sigma_{12}(x, y) - \Sigma_{12}(x, y; p_k, 0)\right) = 0, \tag{4.78}$$

where $\Sigma_{12}(x, y; p_k, 0)$ is the singular part of $\sigma_{12}(x, y)$ when we approach $(p_k, 0)$. To obtain it, we can define another stress potential $K(x, y; p_k, 0)$ satisfying

$$\Delta^2 K(x, y; p_k, 0) = 2\epsilon^2 \delta\left(x - p_k\right) \delta'\left(y\right). \tag{4.79}$$

Then we obtain

$$\Sigma_{12}(x, y; p_k, 0) = \frac{\partial^2 K(x, y; p_k, 0)}{\partial x \partial y} = \frac{\epsilon^2 (x - p_k)((x - p_k)^2 - y^2)}{((x - p_k)^2 + y^2)^2}. \tag{4.80}$$

To see the pile-ups of these monopoles, an external stress σ_{ext} is applied at infinity. To ensure the stress by monopoles is comparable to this applied stress, we can set the applied stress to be $\epsilon\sigma_{\text{ext}}$ with $\sigma_{\text{ext}} \sim \mathcal{O}(1)$. Therefore, we obtain another boundary condition for $\sigma_{12}(x, y)$[1]:

$$\lim_{x^2+y^2\to\infty} \sigma_{12}(x, y) = \epsilon\sigma_{\text{ext}}. \tag{4.81}$$

4.3.2 Expansions under the Multiple-Scale Coordinates

Introduction of Spatial Variables of Two Scales

Similar to the screw monopole case, a smooth function $B(x)$ is defined to map x to a space where monopoles are uniformly distributed. For any x, its corresponding p_k can be found by $p_k = \lfloor B(x)/\epsilon \rfloor$ and the fast variable X can be introduced by

$$X = \frac{B(x) - B(p_k)}{\epsilon}, \tag{4.82}$$

such that all functions are periodic in $X \in [0, 1)$.

The same as the case of screw monopoles, the large-scale variable is still defined by $\bar{x} = x$. Using the shift function $\zeta(\bar{x})$ defined in (4.12), we are able to represent p_k by

$$p_k = B^{-1}(B(\bar{x}) - \zeta(\bar{x})). \tag{4.83}$$

The Inner Region

In the inner region, where $y \sim \mathcal{O}(\epsilon)$, we rescale y by

$$Y = \frac{y}{\epsilon}. \tag{4.84}$$

Then by using the transformation of $\delta(x - p_k)$ in the case of screw monopoles and

$$\delta'(y) = \frac{1}{\epsilon^2} \cdot \delta'(Y),$$

we can rewrite the governing equation for the stress function, denoted by $\chi_{\text{in}}(\bar{x}, X, Y)$, can be rewritten as

$$\left(\left(\frac{\partial}{\partial \bar{x}} + \frac{B'}{\epsilon} \frac{\partial}{\partial X} \right)^2 + \frac{1}{\epsilon^2} \frac{\partial^2}{\partial Y^2} \right)^2 \chi_{\text{in}}(\bar{x}, X, Y) = \frac{2B'(B^{-1}(B(\bar{x}) - \epsilon\zeta(\bar{x})))}{\epsilon} \cdot \delta(X)\, \delta'(Y), \tag{4.85}$$

[1] Actually, the full problem can be decomposed to two sub-problems: the non-stress pile-ups and a uniform applied stress. The two sub-problems are connected in the force balance equations.

with periodic boundary condition in X.

Similar as in the case of screw monopoles, the expansion should be consistent with the order in the right hand side of (4.85). It can be observed that expansions of all stress components start from $\mathcal{O}(\epsilon)$, which require $\chi_{\text{in}}(\bar{x}, X, Y)$ be expanded as

$$\chi_{\text{in}}(\bar{x}, X, Y) \sim \epsilon c_{\text{in}}^{(1)}(\bar{x}) + \epsilon^2 h_{\text{in}}^{(2)}(\bar{x})Y + \epsilon^3 \chi_{\text{in}}^{(3)}(\bar{x}, X, Y) + \cdots, \tag{4.86}$$

where the functions of $c_{\text{in}}^{(1)}$ and $h_{\text{in}}^{(2)}$ are to pass the information from the applied stress in the outer region. Then we obtain

$$\begin{aligned}\sigma_{11}^{\text{in}}(\bar{x}, X, Y) &\sim \epsilon\sigma_{11}^{\text{in}(1)}(\bar{x}, X, Y) + \epsilon^2\sigma_{11}^{\text{in}(2)}(\bar{x}, X, Y) + \epsilon^3\sigma_{11}^{\text{in}(3)}(\bar{x}, X, Y) + \cdots \\ &\sim -\epsilon \cdot \frac{\partial^2 \chi_{\text{in}}^{(3)}}{\partial Y^2} - \epsilon^2 \cdot \frac{\partial^2 \chi_{\text{in}}^{(4)}}{\partial Y^2} + \cdots;\end{aligned} \tag{4.87}$$

$$\begin{aligned}\sigma_{12}^{\text{in}}(\bar{x}, X, Y) &\sim \epsilon\sigma_{12}^{\text{in}(1)}(\bar{x}, X, Y) + \epsilon^2\sigma_{12}^{\text{in}(2)}(\bar{x}, X, Y) + \epsilon^3\sigma_{12}^{\text{in}(3)}(\bar{x}, X, Y) + \cdots \\ &\sim \epsilon \cdot \left(\frac{\mathrm{d}h_{\text{in}}^{(2)}}{\mathrm{d}\bar{x}} + B'(\bar{x}) \cdot \frac{\partial^2 \chi_{\text{in}}^{(3)}}{\partial X \partial Y}\right) + \epsilon^2 \cdot \left(\frac{\partial^2 \chi_{\text{in}}^{(3)}}{\partial \bar{x} \partial Y} + B' \cdot \frac{\partial^2 \chi_{\text{in}}^{(4)}}{\partial X \partial Y}\right) + \cdots;\end{aligned} \tag{4.88}$$

$$\begin{aligned}\sigma_{22}^{\text{in}}(\bar{x}, X, Y) &\sim \epsilon\sigma_{22}^{\text{in}(1)}(\bar{x}, X, Y) + \epsilon^2\sigma_{22}^{\text{in}(2)}(\bar{x}, X, Y) + \epsilon^3\sigma_{22}^{\text{in}(3)}(\bar{x}, X, Y) + \cdots \\ &\sim -\epsilon \cdot \left(\frac{\mathrm{d}^2 c_{\text{in}}^{(1)}}{\mathrm{d}\bar{x}^2} + B'^2 \cdot \frac{\partial^2 \chi_{\text{in}}^{(3)}}{\partial X^2}\right) + \cdots.\end{aligned} \tag{4.89}$$

Singularities due to An Edge Dislocation

Also, a stress potential $K_{\text{in}}(\bar{x}, X, Y)$ is introduced to represent $K(x, y; p_k, 0)$ in (4.78) under the multiple-scale coordinates. Thus (4.79) can be rewritten as

$$\left(\left(\frac{\partial}{\partial \bar{x}} + \frac{B'}{\epsilon}\frac{\partial}{\partial X}\right)^2 + \frac{1}{\epsilon^2}\frac{\partial^2}{\partial Y^2}\right)^2 K_{\text{in}}(\bar{x}, X, Y) = \frac{2B'(B^{-1}(B(\bar{x}) - \epsilon\zeta(\bar{x})))}{\epsilon} \cdot \delta(X)\,\delta'(Y), \tag{4.90}$$

as $(\bar{x}, X, Y) \to (p_k, 0, 0)$. Then we can define the singular part of the shear stress in the inner region by

$$\Sigma_{12}^{\text{in}}(\bar{x}, X, Y) = \left(\frac{\partial}{\partial \bar{x}} + \frac{B'}{\epsilon}\frac{\partial}{\partial X}\right)\frac{\partial K_{\text{in}}}{\partial Y}. \tag{4.91}$$

Again we can assume the expansion that

$$K_{\text{in}}(\bar{x}, X, Y) \sim \epsilon^3 K_{\text{in}}^{(3)}(\bar{x}, X, Y) + \epsilon^4 K_{\text{in}}^{(4)}(\bar{x}, X, Y) + \cdots \tag{4.92}$$

and

$$\Sigma_{12}^{\text{in}}(\bar{x}, X, Y) \sim \epsilon\Sigma_{12}^{\text{in}(1)}(\bar{x}, X, Y) + \epsilon^2\Sigma_{12}^{\text{in}(2)}(\bar{x}, X, Y) + \cdots. \tag{4.93}$$

Force Balance Equations

Also under the multiple-scale coordinates, the force balance equation (4.78) can be rewritten as

$$\lim_{(X,Y)\to(0,0)} \left(\sigma_{12}^{\text{in}}(p_k, X, Y) - \Sigma_{12}^{\text{in}}(p_k, X, Y)\right) = 0. \tag{4.94}$$

The Outer Region

In the outer region, $y \sim \mathcal{O}(1)$. Like what happens in the case of screw monopoles, we assume the stress function χ_{out} is only a function of $\bar{x}$ and y. Thus we need to solve a biharmonic equation for $\chi_{\text{out}}(\bar{x}, y)$:

$$\left(\frac{\partial^2}{\partial \bar{x}^2} + \frac{\partial^2}{\partial y^2}\right)^2 \chi_{\text{out}}(\bar{x}, y) = 0. \tag{4.95}$$

With χ_{out} computed, the stress components can be calculated by

$$\sigma_{11}^{\text{out}}(\bar{x}, y) = -\frac{\partial^2 \chi_{\text{out}}}{\partial y^2}; \quad \sigma_{12}^{\text{out}}(\bar{x}, y) = \frac{\partial^2 \chi_{\text{out}}}{\partial \bar{x} \partial y}; \quad \sigma_{22}^{\text{out}}(\bar{x}, y) = -\frac{\partial^2 \chi_{\text{out}}}{\partial \bar{x}^2}. \tag{4.96}$$

We also have the boundary condition from σ_{12}^{out} by

$$\lim_{\bar{x}^2+y^2\to\infty} \sigma_{12}^{\text{out}}(\bar{x}, y) = \lim_{\bar{x}^2+y^2\to\infty} \frac{\partial^2 \chi_{\text{out}}}{\partial \bar{x} \partial y} = \epsilon \sigma_{\text{ext}}. \tag{4.97}$$

Assuming

$$\chi_{\text{out}}(\bar{x}, y) \sim \epsilon \chi_{\text{out}}^{(1)}(\bar{x}, y) + \epsilon^2 \chi_{\text{out}}^{(2)}(\bar{x}, y) + \cdots, \tag{4.98}$$

the corresponding stress components can be expanded by

$$\begin{aligned} \sigma_{11}^{\text{out}}(\bar{x}, y) &\sim \epsilon \sigma_{11}^{\text{out}(1)}(\bar{x}, y) + \epsilon^2 \sigma_{11}^{\text{out}(2)}(\bar{x}, y) + \epsilon^3 \sigma_{11}^{\text{out}(3)}(\bar{x}, y) + \cdots \\ &\sim -\epsilon \cdot \frac{\partial^2 \chi_{\text{out}}^{(1)}}{\partial y^2} - \epsilon^2 \cdot \frac{\partial^2 \chi_{\text{out}}^{(2)}}{\partial y^2} - \epsilon^3 \cdot \frac{\partial^2 \chi_{\text{out}}^{(3)}}{\partial y^2} + \cdots; \end{aligned} \tag{4.99}$$

$$\begin{aligned} \sigma_{12}^{\text{out}}(\bar{x}, y) &\sim \epsilon \sigma_{12}^{\text{out}(1)}(\bar{x}, y) + \epsilon^2 \sigma_{12}^{\text{out}(2)}(\bar{x}, y) + \epsilon^3 \sigma_{12}^{\text{out}(3)}(\bar{x}, y) + \cdots \\ &\sim \epsilon \cdot \frac{\partial^2 \chi_{\text{out}}^{(1)}}{\partial \bar{x} \partial y} + \epsilon^2 \cdot \frac{\partial^2 \chi_{\text{out}}^{(2)}}{\partial \bar{x} \partial y} + \epsilon^3 \cdot \frac{\partial^2 \chi_{\text{out}}^{(3)}}{\partial \bar{x} \partial y} + \cdots; \end{aligned} \tag{4.100}$$

$$\begin{aligned} \sigma_{22}^{\text{out}}(\bar{x}, y) &\sim \epsilon \sigma_{22}^{\text{out}(1)}(\bar{x}, y) + \epsilon^2 \sigma_{22}^{\text{out}(2)}(\bar{x}, y) + \epsilon^3 \sigma_{22}^{\text{out}(3)}(\bar{x}, y) + \cdots \\ &\sim -\epsilon \frac{\partial^2 \chi_{\text{out}}^{(1)}}{\partial \bar{x}^2} - \epsilon^2 \cdot \frac{\partial^2 \chi_{\text{out}}^{(2)}}{\partial \bar{x}^2} - \epsilon^3 \cdot \frac{\partial^2 \chi_{\text{out}}^{(3)}}{\partial \bar{x}^2} + \cdots. \end{aligned} \tag{4.101}$$

4.3.3 The Leading Order

The Inner Region

From the expansions above, all stress components start from $\mathcal{O}(\epsilon)$. At this order the stress components satisfy

$$\sigma_{11}^{\text{in}(1)} = -\frac{\partial^2 \chi_{\text{in}}^{(3)}}{\partial Y^2}; \tag{4.102}$$

$$\sigma_{12}^{\text{in}(1)} = \frac{\mathrm{d}h_{\text{in}}^{(2)}}{\mathrm{d}\bar{x}} + B'\frac{\partial^2 \chi_{\text{in}}^{(3)}}{\partial X \partial Y}; \tag{4.103}$$

$$\sigma_{22}^{\text{in}(1)} = -\frac{\mathrm{d}^2 c_{\text{in}}^{(1)}}{\mathrm{d}\bar{x}^2} - B'^2\frac{\partial^2 \chi_{\text{in}}^{(3)}}{\partial X^2}. \tag{4.104}$$

In order to calculate these components, we need to solve an equation for $\chi_{\text{in}}^{(3)}(\bar{x}, X, Y)$ from the leading order equation of (4.85)

$$\left((B')^2\frac{\partial^2}{\partial X^2} + \frac{\partial^2}{\partial Y^2}\right)^2 \chi_{\text{in}}^{(3)}(\bar{x}, X, Y) = 2B'\delta\left(X\right)\delta'\left(Y\right), \tag{4.105}$$

with $\chi_{\text{in}}^{(3)}(\bar{x}, X, Y)$ periodic in X.

Instead of finding the expression for $\chi_{\text{in}}^{(3)}(\bar{x}, X, Y)$ directly, we look for some $\tilde{G}(\bar{x}, X, Y)$, which satisfies

$$\left((B')^2\frac{\partial^2}{\partial X^2} + \frac{\partial^2}{\partial Y^2}\right)^2 \tilde{G}(\bar{x}, X, Y) = \delta(X)\delta'(Y), \tag{4.106}$$

with $\tilde{G}(\bar{x}, X, Y)$ periodic in X. It should be noted that all second derivatives of $\tilde{G}$ are bounded as $Y \to \infty$, since stress components are finite.

From § A.8, we know that all $\tilde{G}$ satisfying (4.106) have the form that

$$\tilde{G}(\bar{x}, X, Y) = G(\bar{x}, X, Y) + c(\bar{x}) + h(\bar{x})Y + \frac{a(\bar{x})Y^2}{2},$$

with $c(\bar{x})$, $h(\bar{x})$ and $a(\bar{x})$ to be determined, where

$$G = \frac{Y}{8\pi B'}\log\left(\cosh(2\pi B'Y) - \cos(2\pi X)\right). \tag{4.107}$$

Once $G(\bar{x}, X, Y)$ is computed, $\chi_{\text{in}}^{(3)}(\bar{x}, X, Y)$ can be calculated by

$$\chi_{\text{in}}^{(3)}(\bar{x}, X, Y) = 2B'G(\bar{x}, X, Y) + c_{\text{in}}^{(3)}(\bar{x}) + h_{\text{in}}^{(3)}(\bar{x})Y + \frac{a_{\text{in}}^{(3)}(\bar{x})Y^2}{2}, \tag{4.108}$$

Therefore, we have the expression for $\chi_{\rm in}^{(3)}(\bar{x}, X, Y)$:

$$\chi_{\rm in}^{(3)}(\bar{x}, X, Y) = \frac{Y}{4\pi}\log\left(\cosh(2\pi B'Y) - \cos(2\pi X)\right) + c_{\rm in}^{(3)}(\bar{x}) + h_{\rm in}^{(3)}(\bar{x})Y + \frac{a_{\rm in}^{(3)}(\bar{x})Y^2}{2}. \tag{4.109}$$

Hence by using (4.102), (4.103) and (4.104), we can compute the stress components at $\mathcal{O}(\epsilon)$ by

$$\begin{aligned}\sigma_{11}^{\rm in(1)}(\bar{x}, X, Y) &= -2B' \cdot \frac{\partial^2 G}{\partial Y^2}(\bar{x}, X, Y) - a_{\rm in}^{(3)}(\bar{x}) \\ &= -a_{\rm in}^{(3)}(\bar{x}) - \frac{B'\sinh(2\pi B'Y)}{\cosh(2\pi B'Y) - \cos(2\pi X)} - \frac{\pi B'^2 Y(1 - \cosh(2\pi B'Y)\cos(2\pi X))}{(\cosh(2\pi B'Y) - \cos(2\pi X))^2},\end{aligned} \tag{4.110}$$

$$\begin{aligned}\sigma_{12}^{\rm in(1)}(\bar{x}, X, Y) &= \frac{{\rm d}h_{\rm in}^{(2)}}{{\rm d}\bar{x}} + 2B'^2 \cdot \frac{\partial^2 G}{\partial X \partial Y}(\bar{x}, X, Y) \\ &= \frac{{\rm d}h_{\rm in}^{(2)}}{{\rm d}\bar{x}} + \frac{B'\sin(2\pi X)}{2(\cosh(2\pi B'Y) - \cos(2\pi X))} - \frac{\pi B'^2 Y \sin(2\pi X)\sinh(2\pi B'Y)}{(\cosh(2\pi B'Y) - \cos(2\pi X))^2}\end{aligned} \tag{4.111}$$

and

$$\begin{aligned}\sigma_{22}^{\rm in(1)}(\bar{x}, X, Y) &= \frac{{\rm d}^2 c_{\rm in}^{(1)}}{{\rm d}\bar{x}^2} - 2B'^3 \cdot \frac{\partial^2 G}{\partial X^2}(\bar{x}, X, Y) \\ &= -\frac{{\rm d}^2 c_{\rm in}^{(1)}}{{\rm d}x^2} + \frac{\pi B'^2 Y(1 - \cosh(2\pi B'Y)\cos(2\pi X))}{(\cosh(2\pi B'Y) - \cos(2\pi X))^2},\end{aligned} \tag{4.112}$$

respectively.

Singularities

Also, the leading order equation for $K_{\rm in}$ gives

$$\left(B'^2\frac{\partial^2}{\partial X^2} + \frac{\partial^2}{\partial Y^2}\right)^2 K_{\rm in}^{(3)}(\bar{x}, X, Y) = 2B'\delta(X)\delta'(Y), \tag{4.113}$$

which suggests that

$$K_{\rm in}^{(3)}(\bar{x}, X, Y) = \frac{Y}{4\pi}\log\left(\alpha(\bar{x})\left(X^2 + B'^2Y^2\right)\right). \tag{4.114}$$

Therefore, we have

$$\Sigma_{12}^{\rm in(1)}(\bar{x}, X, Y) = B'\frac{\partial^2 K_{\rm in}^{(3)}}{\partial X \partial Y} = \frac{B'X(X^2 - B'^2Y^2)}{2\pi(X^2 + B'^2Y^2)^2}. \tag{4.115}$$

Force Balance

As we know that

$$\sigma_{12}^{\mathrm{in}(1)}(B^{-1}(B(\bar{x})-\epsilon\zeta(\bar{x})),X,Y)\sim\sigma_{12}^{\mathrm{in}(1)}(\bar{x},X,Y)+\cdots$$

and

$$\Sigma_{12}^{\mathrm{in}(1)}(B^{-1}(B(\bar{x})-\epsilon\zeta(\bar{x})),X,Y)\sim\Sigma_{12}^{\mathrm{in}(1)}(\bar{x},X,Y)+\cdots,$$

the force balance equation at $\mathcal{O}(\epsilon)$ becomes

$$\lim_{(X,Y)\to(0,0)}\left(\sigma_{12}^{\mathrm{in}(1)}(\bar{x},X,Y)-\Sigma_{12}^{\mathrm{in}(1)}(\bar{x},X,Y)\right)=0. \tag{4.116}$$

Again, by analogy to the case of screw monopoles, it is more convenient to express $\sigma_{12}^{\mathrm{in}(1)}$ and $\Sigma_{12}^{(1)}$ in the polar system, when $(X,Y)\to(0,0)$, by setting

$$X=r\cos\theta,\qquad Y=r\sin\theta/B'. \tag{4.117}$$

Incorporating (4.117) with (4.111) and (4.115) gives

$$\sigma_{12}^{\mathrm{in}(1)}(\bar{x},X,Y)\sim\frac{B'\cos\theta\cos2\theta}{4\pi r}+\frac{\mathrm{d}h_{\mathrm{in}}^{(2)}}{\mathrm{d}\bar{x}}+\mathcal{O}(r)$$

and

$$\Sigma_{12}^{(1)}(\bar{x},X,Y;0,0)=\frac{B'\cos\theta\cos2\theta}{4\pi r},$$

as $r\to0$, respectively. Plugging them into the force balance equation (4.116), we find that the singularities cancel, giving rise to

$$\frac{\mathrm{d}h_{\mathrm{in}}^{(2)}}{\mathrm{d}\bar{x}}=0.$$

The Outer Region

In the outer region, the stress components at $\mathcal{O}(\epsilon)$ satisfy

$$\sigma_{11}^{\mathrm{out}(1)}=-\frac{\partial^2\chi_{\mathrm{out}}^{(1)}}{\partial y^2};\quad\sigma_{12}^{\mathrm{out}(1)}=\frac{\partial^2\chi_{\mathrm{out}}^{(1)}}{\partial\bar{x}\partial y};\quad\sigma_{22}^{\mathrm{out}(1)}=-\frac{\partial^2\chi_{\mathrm{out}}^{(1)}}{\partial\bar{x}^2}, \tag{4.118}$$

with $\chi_{\mathrm{out}}^{(1)}(\bar{x},y)$ satisfying

$$\left(\frac{\partial^2}{\partial\bar{x}^2}+\frac{\partial^2}{\partial y^2}\right)^2\chi_{\mathrm{out}}^{(1)}(\bar{x},y)=0. \tag{4.119}$$

The conditions as $y \to 0^{\pm}$ are from matching the stress with the inner region expressed in (4.110), (4.111) and (4.112):

$$\lim_{y\to 0^{\pm}} \frac{\partial^2 \chi_{\text{out}}^{(1)}}{\partial \bar{x}^2} = -\lim_{Y\to\pm\infty} \sigma_{22}^{\text{in}(1)}(\bar{x}, X, Y) = \frac{\mathrm{d}^2 c_{\text{in}}^{(1)}}{\mathrm{d}\bar{x}^2}; \tag{4.120}$$

$$\lim_{y\to 0^{\pm}} \frac{\partial^2 \chi_{\text{out}}^{(1)}}{\partial \bar{x}\partial y} = \lim_{Y\to\pm\infty} \sigma_{12}^{\text{in}(1)}(\bar{x}, X, Y) = 0; \tag{4.121}$$

and

$$\lim_{y\to 0^{\pm}} \frac{\partial^2 \chi_{\text{out}}^{(1)}}{\partial y^2} = -\lim_{Y\to\pm\infty} \sigma_{11}^{\text{in}(1)}(\bar{x}, X, Y) = a_{\text{in}}^{(3)}(\bar{x}) \mp B'(\bar{x}). \tag{4.122}$$

For simplicity, we just consider the case when $\mathrm{d}^2 c_{\text{in}}^{(1)}/\mathrm{d}\bar{x}^2$ and $a_{\text{in}}^{(3)}(\bar{x})$ both vanish. Such a simplification is sensible because $a_{\text{in}}^{(3)}$ and $\mathrm{d}^2 c_{\text{in}}^{(1)}/\mathrm{d}\bar{x}^2$ are both carriers of information from the applied stress in the outer region. In this case, the applied stress in the outer region σ_{11}^{ext} and σ_{22}^{ext} both vanish.

How we solve the equation for $\chi_{\text{out}}^{(1)}(\bar{x}, y)$ is detailed in § A.9. Replacing $g(x)$ by $-B'(\bar{x})$ in (A.28), we obtain an integral equation

$$⨍_{-1}^{1} \frac{B'(x')\mathrm{d}x'}{x - x'} = -\sigma_{\text{ext}}. \tag{4.123}$$

Here without causing any ambiguity, we can use x to replace $\bar{x}$ for the expression for density distribution $\rho^{(0)}(x) = B'(\bar{x})$. Thus an integral equation for the dislocation density can be obtained:

$$⨍_{-1}^{1} \frac{\rho^{(0)}(x')\mathrm{d}x'}{x - x'} = -\sigma_{\text{ext}}, \tag{4.124}$$

which agrees with the existing results compiled in Chapter 21 of [33].

4.4 Comparison of Results of Monopole Pile-ups among Various Method

4.4.1 Analytical Results

If we consider the non-stress pile up of monopoles, (4.124) becomes

$$⨍_{-1}^{1} \frac{\rho^{(0)}(x')\mathrm{d}x'}{x - x'} = 0. \tag{4.125}$$

Then the expression for the density can be obtained by using the Hilbert transformation:

$$\rho^{(0)}(x) = \frac{2}{\pi\sqrt{1-x^2}}. \tag{4.126}$$

The details can be found in [33]. We will compare this result with that from other methods.

4.4.2 Numerical Schemes

Numerical simulations have also been performed. In our computation, we look for the equilibrium state of N positive dislocations by iteratively solving the algebraic equations system (4.1) for each p_k.

Our simulation starts with N dislocations randomly positioned within the interval $(-1, 1)$, with a lock at each end. At i-th step, the k-th dislocation is moved by $f(p_k^i)\Delta t$, where $f(p_k^i)$ is the net force at the k-th dislocation. The loop continues until $|f(p_k^i)| < \eta$ for all k, and p_k is recorded as the equilibrium position for the k-th dislocation. Here we choose $\eta = 10^{-8}$.

Once $\{p_k | k \in \mathbb{Z}, 0 < k < N-1\}$ is obtained, the density can be computed in two approaches. One is to follow the definition of $\rho(x)$ in (4.2), by counting the number of dislocations within a small interval $(x-\Delta x, x+\Delta x)$, which we refer to the 'counting' method in the rest of this thesis. The other is from [24], that $2/(N(p_k - p_{k-1}))$ is also an approximation to the density distribution $\rho(p_k)$. It should be mentioned that the density obtained above by two methods have both been rescaled by ϵ for purpose of comparisons.

4.4.3 Comparison of Results

The results of dislocation density by the three methods are compared in Fig. 4.4. The grey bars are drawn by using the counting method within each small interval $(x-\Delta x, x+\Delta x)$; the black curve is drawn by the result in (4.126) from the multiple-scale calculation; the diamonds plot $2/(N(p_k - p_{k-1}))$ against p_k.

It can be seen that these three methods agree well. This validates our multiple-scale technique, as well as the numerical scheme. In the next chapter, the homogenisation of a row of dipoles will be discussed. Since there is no existing result for us to compare with, numerical simulations will offer some evidence to justify our results.

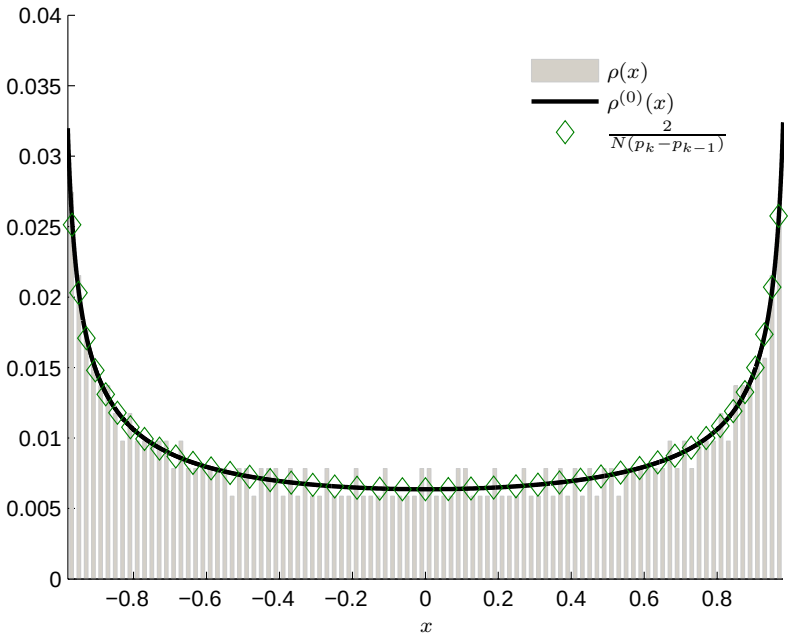


Figure 4.4: Comparison of densities obtained by different methods: The grey bars are drawn by the counting method within each small interval $(x-\Delta x, x+\Delta x)$; the curve is drawn by the result in (4.126) from the multiple-scale calculation; the diamonds depict $2/(N(p_k-p_{k-1}))$ against p_k. For the full problem, we use the numerical scheme in §4.4.2 with $N = 50$.

4.5 Conclusion

In this chapter, a method using multiple scales was presented, followed by two of its applications: the pile-up of a row of screw or edge monopoles. The multiple-scale technique was validated by comparing them with the existing results compiled in [33]. A numerical approach was also given and justified by being compared with the existing results.

In the next chapter, we will use these validated tools (the spatial multiple-scale method and the numerics) to investigate the collective behaviour of more mysterious one-dimensional array of dipoles.

Chapter 5

Homogenisation of One Dimensional Arrays of Dipoles

The multiple-scale technique introduced in the last chapter can be generalised to investigate a one-dimensional array of dipoles. Here 'dislocation dipoles' denote pairs of dislocations of opposite signs. It has been widely found that dislocation dipoles exist in materials more frequently than monopoles. In the scenario of the fatigue test, the number of dislocations is raised by double cross-slip or Frank-Read sources, through which dislocations are generated in pairs as discussed on p.9 to 10. However, as stated in Chapter 4, despite their practical importance, barely any theoretical results concerning the collective behaviour of dislocation dipoles can be found in literature compared to that of monopoles, which dates back to the early 1950s [20]. One main reason is that when we apply the traditional homogenisation method to dipoles, we get nothing. This can be explained from the formation of dipoles at an atomistic level as shown in Fig. 1.11. A pair of dislocations give rise to a column of interstitials or vacancies. Outside two dislocations are all perfect lattice. The consequence is that the stress in the outer region is diminished.

If we implement the multiple-scale technique introduced in Chapter 4 to dipoles, it will be seen later the leading-order equation in the outer region, where the density equation for monopoles was obtained, becomes trivial. So in order to get an equation for the density, one has to turn to higher orders. Unfortunately, like many other examples using asymptotic techniques, calculations at higher orders become very complicated.

In this chapter, we will present the multiple-scale calculations to one order higher than that for monopoles in order to obtain an equation describing the density. It will

be seen later that, in the case of dipoles, quantities have to be defined more precisely, so that the error from approximations is controlled at a higher order in ϵ.

5.1 Governing Equations

Here we consider two rows of dislocation monopoles with opposite signs as shown in Fig. 5.1. Each positive dislocation is located at $(p_k, 0)$, while its negative counterpart

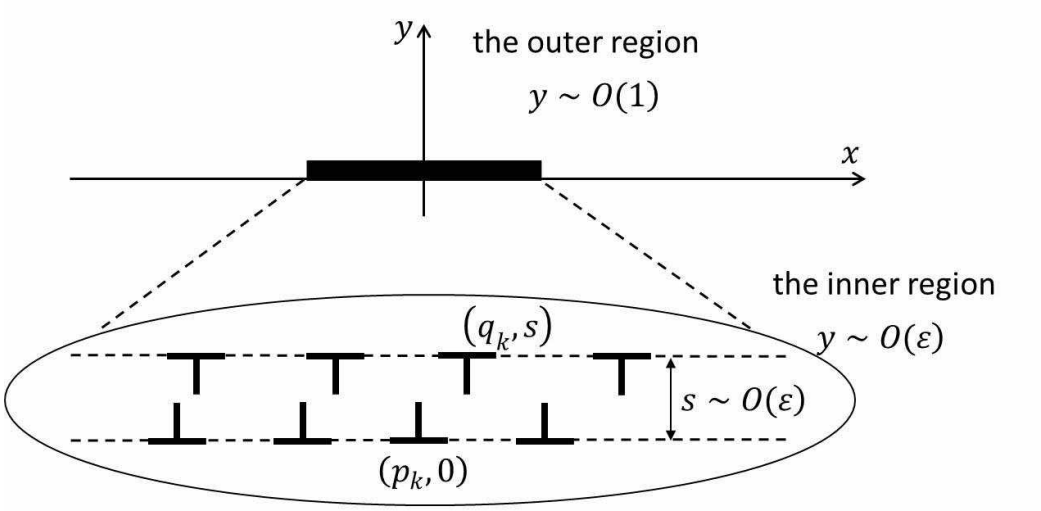


Figure 5.1: A row of dislocation pairs: it composes of two arrays of dislocation monopoles with opposite signs. The spacing between two glide planes is $s \sim \mathcal{O}(\epsilon)$. Each positive dislocation is located at $(p_k, 0)$, $k \in \mathbb{Z}$ and $0 \leq k < N$; each negative dislocation is located at (q_k, s).

is set to be at (q_k, s). The spacing between two glide planes s is set to satisfy $s \sim \mathcal{O}(\epsilon)$.

Similar as in the monopole case, firstly we write down an equation for the stress function $\chi(x, y)$ by superpositions of all dislocations:

$$\Delta^2 \chi(x, y) = 2\epsilon^2 \sum_{k=0}^{N} \left(\delta\left(x - p_k\right) \delta'\left(y\right) - \delta\left(x - q_k\right) \delta'\left(y - s\right) \right), \tag{5.1}$$

and the stress components then can be calculated by

$$\sigma_{11}(x, y) = -\frac{\partial^2 \chi}{\partial y^2}; \qquad \sigma_{12}(x, y) = \frac{\partial^2 \chi}{\partial x \partial y}; \qquad \sigma_{22}(x, y) = -\frac{\partial^2 \chi}{\partial x^2}. \tag{5.2}$$

Then the force-balance equations, in this scenario, are

$$\lim_{(x,y)\to(p_k,0)} \left(\sigma_{12}(x, y) - \Sigma_{12}(x, y; p_k, 0)\right) = 0 \tag{5.3}$$

and

$$\lim_{(x,y)\to(q_k,s)} (\sigma_{12}(x,y) + \Sigma_{12}(x,y;q_k,s)) = 0 \tag{5.4}$$

for all k, where

$$\Sigma_{12}(x,y;x',y') = \frac{\epsilon^2(x-x')((x-x')^2-(y-y')^2)}{2\pi((x-x')^2+(y-y')^2)^2}. \tag{5.5}$$

Or alternatively, we can define a stress potential $K(x,y;x',y')$ satisfying

$$\Delta^2 K(x,y;x',y') = 2\epsilon^2\delta(x-x')\delta'(y-y'), \tag{5.6}$$

and we obtain

$$\Sigma_{12}(x,y;x',y') = \frac{\partial^2 K(x,y;x',y')}{\partial x \partial y}.$$

It is noted that similar as the case of monopoles, the applied effect $\sigma_{\text{ext}}(x,y)$ is contained in σ_{12} by superposition. To be consistent with our calculations, we set this applied effect of $\mathcal{O}(\epsilon)$. Here there are two ways to choose $\sigma_{\text{ext}}(x,y)$. One is in consistency with the case in monopoles, we set $\sigma_{\text{ext}}(x,y) = \epsilon\sigma_e$. Alternatively, according to existing calculations, dislocation dipoles cannot be moved by external stress. They either change their mutual angle to accommodate or break down by the external force. However, they move in response to an applied 'stress gradient', where the applied stress varies linearly in y. Therefore, in order to see the 'pile-up' effect, we also need to include the effect from the stress gradient. Therefore, we can set

$$\sigma_{\text{ext}}(x,y) = \epsilon(\sigma_e + \phi y). \tag{5.7}$$

5.2 Multiple Scales and Relevant Expansions

5.2.1 Introduction of the Small-Scale Variable

In analogy to the case of monopoles, a map $B(x)$ is defined such that

$$B(p_k) = \epsilon k, \tag{5.8}$$

and B is interpolated to be meaningful over the interval $(-1,1)$. Again, the definition of $B(x)$ enables us to divide the domain $(-1,1)$ into N cells characterised by p_k. Then we introduce the fast-scale variable by

$$X = \frac{B(x) - B(p_k)}{\epsilon}. \tag{5.9}$$

In X space, everything is slowly varying from cell to cell, so that all quantities are assumed to be periodic in $X \in [0, 1)$. This suggests that the original spatial variable x can be expressed as a combination of variations across and within cells by

$$x = B^{-1}(B(p_k) + \epsilon X) \sim p_k + \frac{\epsilon X}{B'(p_k)} + \frac{\epsilon^2 B''(p_k) X^2}{2(B'(p_k))^3} + \cdots . \tag{5.10}$$

Also we define the large-scale variable by setting $\bar{x} = x$. In order to express p_k by a continuously varying variable, we introduce the shift variable

$$\zeta(\bar{x}) = \frac{B(\bar{x})}{\epsilon} - \left\lfloor \frac{B(\bar{x})}{\epsilon} \right\rfloor , \tag{5.11}$$

so that

$$p_k = B^{-1}(B(\bar{x}) - \epsilon\zeta(\bar{x})) \sim \bar{x} - \epsilon \cdot \frac{\zeta(\bar{x})}{B'(\bar{x})} + \cdots . \tag{5.12}$$

5.2.2 Targeting the Negative Dislocations with Multiple Scales

Coordinating the negative dislocations under the multiple-scale coordinates turns out to be one of the main barriers against generalising our method to dipoles. In this scenario, quantities have to be carefully defined concerning at least the following three aspects:

- How to express q_k in X space.
- How to approximate q_k in terms of the large-scale variable $\bar{x}$.
- How the singularity behaves as $x \to q_k$ at both scales.

The coordination of q_k will be accomplished through answering these three questions.

Since every cell is characterised by p_k, every variable originating from q_k should be a function of p_k. By using the fact that the difference between p_k and q_k is of $\mathcal{O}(\epsilon)$, we define

$$Q_k = Q(p_k) = \frac{B(q_k) - B(p_k)}{\epsilon}. \tag{5.13}$$

It should be mentioned that $Q(\bar{x})$ is defined for all $\bar{x}$. In the original x-space, Q is a piecewise function varying from cell to cell. In the multiple-scale form, we use a series of smooth functions to approximate this $Q(\bar{x})$, which gives rise to the expansion that

$$Q(\bar{x}) \sim Q^{(0)}(\bar{x}) + \epsilon Q^{(1)}(\bar{x}) + \cdots . \tag{5.14}$$

On the other hand, from (5.13), q_k can be approximated by

$$q_k = B^{-1}(B(p_k)+\epsilon Q(p_k)) \sim p_k + \frac{\epsilon Q^{(0)}(p_k)}{B'(p_k)} + \epsilon^2 \cdot \left(\frac{Q^{(1)}(p_k)}{B'(p_k)} + \frac{B''(p_k){Q^{(0)}}^2(p_k)}{2(B'(p_k))^3} \right) + \cdots . \tag{5.15}$$

Incorporating (5.15) with (5.12) gives how q_k is expressed by a function of the macroscopic variable $\bar{x}$:

$$q_k \sim \bar{x} + \frac{\epsilon}{B'(\bar{x})} \left(Q^{(0)}(\bar{x}) - \zeta(\bar{x}) \right) + \cdots . \tag{5.16}$$

At a macroscopic level, as we approach q_k, we should have $\bar{x} \to q_k$. According to the definition of $\zeta(\bar{x})$ in (5.11), the shift at q_k in the multiple-scale coordinates satisfies

$$\zeta(q_k) = \frac{B(q_k)}{\epsilon} - \left\lfloor \frac{B(q_k)}{\epsilon} \right\rfloor = \frac{B(q_k) - B(p_k)}{\epsilon} = Q(p_k). \tag{5.17}$$

Therefore as $x \to q_k$, in the multiple-scale coordinates, we should have

$$\bar{x} \to q_k \tag{5.18}$$

and

$$X \to Q_k \sim Q^{(0)}(\bar{x}) + \epsilon \cdot \left(Q^{(1)}(\bar{x}) - \frac{\zeta(\bar{x})}{B'(\bar{x})} \cdot \frac{\mathrm{d}Q^{(0)}}{\mathrm{d}\bar{x}} \right) + \cdots . \tag{5.19}$$

5.2.3 The Inner Region

Analogously to the monopole case, our calculations will be discussed in two regions. The first one is the inner region, where $y \sim \mathcal{O}(\epsilon)$, as shown in Fig. 5.1. In this case, we need to rescale y and s by

$$Y = \frac{y}{\epsilon}, \qquad S = \frac{s}{\epsilon},$$

respectively.

Expansions

The equation for the stress function in the inner region under the multiple-scale regime, denoted by $\chi_{\text{in}}(\bar{x}, X, Y)$, becomes

$$\begin{aligned} \left(\left(\frac{\partial}{\partial \bar{x}} + \frac{B'}{\epsilon} \frac{\partial}{\partial X} \right)^2 + \frac{1}{\epsilon^2} \cdot \frac{\partial^2}{\partial Y^2} \right)^2 \chi_{\text{in}}(\bar{x}, X, Y) &= \frac{B'(B^{-1}(B(\bar{x}) - \epsilon\zeta(\bar{x})))}{\epsilon} \cdot \delta(X)\, \delta'(Y) \\ - \frac{B'(B^{-1}(B(\bar{x}) - \epsilon(\zeta(\bar{x}) + Q_k)))}{\epsilon} &\cdot \delta(X - Q_k)\, \delta'(Y - S). \end{aligned} \tag{5.20}$$

Note that in this case, the dependence of Q_k on k may destroy the periodicity in X. As we will see later, the non-periodicity from Q_k can be avoided by implementing some techniques depending on the expression of $Q^{(0)}$. Therefore, we still set $\chi_{\text{in}}(\bar{x}, X, Y)$ to be periodic in $X \in [0, 1)$ beforehand.

As in the case of monopoles, $\chi_{\text{in}}(\bar{x}, X, Y)$ is assumed to have the expansion

$$\chi_{\text{in}}(\bar{x}, X, Y) \sim \epsilon^2 h_{\text{in}}^{(2)} Y + \epsilon^3 \chi_{\text{in}}^{(3)}(\bar{x}, X, Y) + \epsilon^4 \chi_{\text{in}}^{(4)}(\bar{x}, X, Y) + \cdots, \tag{5.21}$$

and the expansions for stress components are

$$\sigma_{11}^{\text{in}}(\bar{x}, X, Y) \sim \epsilon \sigma_{11}^{\text{in}(1)}(\bar{x}, X, Y) + \epsilon^2 \sigma_{11}^{\text{in}(2)}(\bar{x}, X, Y) + \cdots; \tag{5.22}$$

$$\sigma_{12}^{\text{in}}(\bar{x}, X, Y) \sim \epsilon \sigma_{12}^{\text{in}(1)}(\bar{x}, X, Y) + \epsilon^2 \sigma_{12}^{\text{in}(2)}(\bar{x}, X, Y) + \cdots; \tag{5.23}$$

$$\sigma_{22}^{\text{in}}(\bar{x}, X, Y) \sim \epsilon \sigma_{22}^{\text{in}(1)}(\bar{x}, X, Y) + \epsilon^2 \sigma_{22}^{\text{in}(2)}(\bar{x}, X, Y) + \cdots. \tag{5.24}$$

Singularities due to a Single Dislocation

In the case of dipoles, we need to consider the singularity at both p_k and q_k. Or generally, we consider the singularity caused by a dislocation located at $(x, y) = (x', y')$ in the original space. We can solve an equation for the stress potential $K(x, y; x', y')$, which satisfies (5.6). As from the previous chapter, we know that the dislocation is correspondingly put at $(\bar{x}, X, Y) = (x', X', Y')$ in the multiple-scale form, where

$$X' = \frac{B(x') - B(p_k)}{\epsilon}, \qquad Y' = \frac{y'}{\epsilon}.$$

Thus if we denote $K(x, y; x', y')$ by $K_{\text{in}}(\bar{x}, X, Y; X', Y')$ in the multiple-scale form, then combining (4.9) and (5.6) gives an equation for $K_{\text{in}}(\bar{x}, X, Y; X', Y')$:

$$\begin{aligned} &\left(\left(\frac{\partial}{\partial \bar{x}} + \frac{B'}{\epsilon} \frac{\partial}{\partial X} \right)^2 + \frac{1}{\epsilon^2} \cdot \frac{\partial^2}{\partial Y^2} \right)^2 K_{\text{in}}(\bar{x}, X, Y; X', Y') = \\ &\qquad \frac{2B'(B^{-1}(B(p_k) + \epsilon X'(p_k)))}{\epsilon^3} \cdot \delta(X - X') \delta'(Y - Y'). \end{aligned} \tag{5.25}$$

Thus the singular part of the shear stress at $(\bar{x}, X', Y')$ in the multiple-scale coordinates denoted by $\Sigma_{12}^{\text{in}}(\bar{x}, X - X', Y - Y')$ becomes

$$\Sigma_{12}^{\text{in}}(\bar{x}, X - X', Y - Y') = \left(\frac{\partial}{\partial \bar{x}} + \frac{B'}{\epsilon} \cdot \frac{\partial}{\partial X} \right) K_{\text{in}}(\bar{x}, X, Y; X', Y'). \tag{5.26}$$

At p_k, we have $\bar{x} = p_k$, $X'(p_k) = 0$ and $Y' = 0$; at q_k, we have $\bar{x} = q_k$, $X'(p_k) = Q_k$ and $Y' = S$.

Here, we also assume the expansion that

$$K_{\text{in}}(\bar{x}, X, Y) \sim \epsilon^3 K_{\text{in}}^{(3)}(\bar{x}, X, Y) + \epsilon^4 K_{\text{in}}^{(4)}(\bar{x}, X, Y) + \cdots ; \tag{5.27}$$

and

$$\Sigma_{12}^{\text{in}}(\bar{x}, X - X', Y - Y') \sim \epsilon \Sigma_{12}^{\text{in}(1)}(\bar{x}, X - X', Y - Y') + \cdots . \tag{5.28}$$

5.2.4 Force-Balance Equations

The force-balance equations (5.3) and (5.4) can be rewritten by

$$\lim_{(X,Y)\to(0,0)} (\sigma_{12}^{\text{in}}(p_k, X, Y) - \Sigma_{12}^{\text{in}}(p_k, X, Y)) = 0 \tag{5.29}$$

and

$$\lim_{(X,Y)\to(Q_k,S)} (\sigma_{12}^{\text{in}}(q_k, X, Y) + \Sigma_{12}^{\text{in}}(q_k, X - Q_k, Y - S)) = 0, \tag{5.30}$$

in the multiple-scale form, respectively.

5.2.5 The Outer Region

In the outer region, where $y \sim \mathcal{O}(1)$, the equation for $\chi_{\text{out}}(\bar{x}, y)$ becomes

$$\left(\left(\frac{\partial}{\partial \bar{x}} + \frac{B'}{\epsilon} \frac{\partial}{\partial X} \right)^2 + \frac{\partial^2}{\partial y^2} \right)^2 \chi_{\text{out}}(\bar{x}, y) = 0. \tag{5.31}$$

Expanding

$$\chi_{\text{out}}(\bar{x}, y) \sim \epsilon \chi_{\text{out}}^{(1)}(\bar{x}, y) + \epsilon^2 \chi_{\text{out}}^{(2)}(\bar{x}, y) + \epsilon^3 \chi_{\text{out}}^{(3)}(\bar{x}, y) + \cdots , \tag{5.32}$$

we have

$$\sigma_{11}^{\text{out}}(\bar{x}, y) \sim \epsilon \sigma_{11}^{\text{out}(1)}(\bar{x}, y) + \epsilon^2 \sigma_{11}^{\text{out}(2)}(\bar{x}, y) + \cdots ; \tag{5.33}$$

$$\sigma_{12}^{\text{out}}(\bar{x}, y) \sim \epsilon \sigma_{12}^{\text{out}(1)}(\bar{x}, y) + \epsilon^2 \sigma_{12}^{\text{out}(2)}(\bar{x}, y) + \cdots ; \tag{5.34}$$

$$\sigma_{22}^{\text{out}}(\bar{x}, y) \sim \epsilon \sigma_{22}^{\text{out}(1)}(\bar{x}, y) + \epsilon^2 \sigma_{22}^{\text{out}(2)}(\bar{x}, y) + \cdots . \tag{5.35}$$

5.3 The Leading Order

5.3.1 The Inner Region

Equations for the Shear Stress

The leading-order equation for χ_{in} is of $\mathcal{O}(\epsilon)$:

$$\left(B'^2\frac{\partial^2}{\partial X^2}+\frac{\partial^2}{\partial Y^2}\right)^2\chi_{\text{in}}^{(3)}=2B'\cdot\left(\delta\left(X\right)\delta'\left(Y\right)-\delta\left(X-Q^{(0)}\right)\delta'\left(Y-S\right)\right), \quad (5.36)$$

with X of period 1. The same as the case of edge monopoles, we know that the solution to (5.36) satisfies

$$\chi_{\text{in}}^{(3)}(\bar{x},X,Y)=2B'\cdot(G(\bar{x},X,Y)-G(x,X-Q^{(0)},Y-S)))+c_{\text{in}}^{(3)}+h_{\text{in}}^{(3)}Y+\frac{Y^2a_{\text{in}}^{(3)}}{2} \quad (5.37)$$

where $c_{\text{in}}^{(3)}$, $h_{\text{in}}^{(3)}$, $a_{\text{in}}^{(3)}$ are all functions of $\bar{x}$ to be determined;

$$G(\bar{x},X,Y)=\frac{Y}{8\pi B'}\log\left(\cosh(2\pi B'Y)-\cos(2\pi X)\right), \quad (5.38)$$

as derived in §A.7.

Therefore, all non-zero stress components in the inner region can be calculated by

$$\begin{aligned}\sigma_{11}^{\text{in}(1)}&=-\frac{\partial^2\chi_{\text{in}}^{(3)}}{\partial Y^2}\\&=-\frac{B'\sinh(2\pi B'Y)}{\cosh(2\pi B'Y)-\cos(2\pi X)}+\frac{B'\sinh(2\pi B'(x)(Y-S))}{\cosh(2\pi B'(x)(Y-S))-\cos(2\pi(X-Q^{(0)}))}\\&\quad-\frac{\pi B'^2Y(1-\cosh(2\pi B'Y)\cos(2\pi X))}{(\cosh(2\pi B'Y)-\cos(2\pi X))^2}\\&\quad+\frac{\pi B'^2(Y-S)(1-\cosh(2\pi B'(x)(Y-S))\cos(2\pi(X-Q^{(0)})))}{(\cosh(2\pi B'(x)(Y-S))-\cos(2\pi(X-Q^{(0)})))^2}-a_{\text{in}}^{(3)}(\bar{x});\end{aligned} \quad (5.39)$$

$$\begin{aligned}\sigma_{12}^{\text{in}(1)}&=B'\frac{\partial^2\chi_{\text{in}}^{(3)}}{\partial X\partial Y}+\frac{\partial^2\chi_{\text{in}}^{(2)}}{\partial\bar{x}\partial Y}\\&=\frac{B'\sin(2\pi X)}{2(\cosh(2\pi B'Y)-\cos(2\pi X))}-\frac{B'\sin(2\pi(X-Q^{(0)}))}{2(\cosh(2\pi B'(x)(Y-S))-\cos(2\pi(X-Q^{(0)})))}\\&\quad-\frac{\pi B'^2Y\sin(2\pi X)\sinh(2\pi B'Y)}{(\cosh(2\pi B'Y)-\cos(2\pi X))^2}\\&\quad+\frac{\pi B'^2(Y-S)\sin(2\pi(X-Q^{(0)}))\sinh(2\pi B'(x)(Y-S))}{(\cosh(2\pi B'(x)(Y-S))-\cos(2\pi(X-Q^{(0)})))^2}+\frac{\mathrm{d}h_{\text{in}}^{(2)}}{\mathrm{d}\bar{x}};\end{aligned} \quad (5.40)$$

$$\begin{aligned}\sigma_{22}^{\text{in}(1)} &= -B'^2\frac{\partial^2\chi_{\text{in}}^{(3)}}{\partial X^2}\\ &= \frac{\pi B'^2 Y(1-\cosh(2\pi B'Y)\cos(2\pi X))}{(\cosh(2\pi B'Y)-\cos(2\pi X))^2}\\ &\quad - \frac{\pi B'^2(Y-S)(1-\cosh(2\pi B'(x)(Y-S))\cos(2\pi(X-Q^{(0)})))}{(\cosh(2\pi B'(x)(Y-S))-\cos(2\pi(X-Q^{(0)})))^2}.\end{aligned} \tag{5.41}$$

Singularities

The $\mathcal{O}(\epsilon)$ equation for $K(\bar{x}, X, Y; X', Y')$ satisfies

$$\left(B'^2\cdot\frac{\partial^2}{\partial X^2}+\frac{\partial^2}{\partial Y^2}\right)^2 K_{\text{in}}^{(3)}(\bar{x}, X, Y; X', Y') = 2B'\cdot\delta(X-X')\delta(Y-Y'), \tag{5.42}$$

which gives

$$K_{\text{in}}^{(3)}(\bar{x}, X, Y; X', Y') = \frac{Y}{4\pi}\cdot\log\left(\alpha(\bar{x})\left(X^2+(B'Y)^2\right)\right). \tag{5.43}$$

Thus at p_k, we combine with (5.26) to obtain

$$\Sigma_{12}^{\text{in}(1)}(p_k, X, Y) = B'(p_k)\cdot\frac{\partial^2 K_{\text{in}}^{(3)}(\bar{x}, X, Y; 0, 0)}{\partial X\partial Y} = \frac{B'(p_k)}{2\pi}\cdot\frac{X(X^2-(B'(p_k))^2Y^2)}{(X^2+(B'(p_k))^2Y^2)^2}. \tag{5.44}$$

Similarly, we have

$$\Sigma_{12}^{\text{in}(1)}(q_k, X-Q_k, Y-S) = \frac{B'(q_k)}{2\pi}\cdot\frac{(X-Q_k)((X-Q_k)^2-(B'(q_k))^2(Y-S)^2)}{((X-Q_k)^2+(B'(q_k))^2(Y-S)^2)^2}. \tag{5.45}$$

5.3.2 Force Balance

With $\sigma_{12}^{\text{in}(1)}$ and $\Sigma_{12}^{\text{in}(1)}$ obtained above, we now consider the force-balance equations. From (5.29), we see that the force-balance at p_k of $\mathcal{O}(\epsilon)$ satisfies

$$\sigma_{12}^{\text{in}(1)}(p_k, X, Y) - \Sigma_{12}^{\text{in}(1)}(p_k, X, Y) = 0, \tag{5.46}$$

as $(X, Y)\to(0, 0)$ and

$$\sigma_{12}^{\text{in}(1)}(q_k, X, Y) - \Sigma_{12}^{\text{in}(1)}(q_k, X-Q_k, Y-S) = 0, \tag{5.47}$$

as $(X, Y)\to(Q_k, S)$.

Force Balance at p_k

It should be noted that

$$\begin{aligned}\sigma_{12}^{\mathrm{in}(1)}(p_k,X,Y) &= \sigma_{12}^{\mathrm{in}(1)}(B^{-1}(B(\bar{x})-\epsilon\zeta(\bar{x})),X,Y)\\ &\sim \sigma_{12}^{\mathrm{in}(1)}(\bar{x},X,Y)-\frac{\epsilon\zeta}{B'}\cdot\frac{\partial\sigma_{12}^{\mathrm{in}(1)}}{\partial\bar{x}}(\bar{x},X,Y)+\cdots\end{aligned} \tag{5.48}$$

and

$$\begin{aligned}\Sigma_{12}^{\mathrm{in}(1)}(p_k,X,Y) &= \Sigma_{12}^{\mathrm{in}(1)}(B^{-1}(B(\bar{x})-\epsilon\zeta(\bar{x})),X,Y)\\ &\sim \Sigma_{12}^{\mathrm{in}(1)}(\bar{x},X,Y)-\frac{\epsilon\zeta}{B'}\cdot\frac{\partial\Sigma_{12}^{\mathrm{in}(1)}}{\partial\bar{x}}(\bar{x},X,Y)+\cdots.\end{aligned} \tag{5.49}$$

Thus the equation (5.46), up to $\mathcal{O}(\epsilon)$ becomes

$$\lim_{(X,Y)\to(0,0)}\Big(\sigma_{12}^{\mathrm{in}(1)}(\bar{x},X,Y)-\Sigma_{12}^{\mathrm{in}(1)}(\bar{x},X,Y)\Big)=0, \tag{5.50}$$

which holds for all $\bar{x}$.

Similar to in the case of monopoles, it is more convenient to express all variables in the polar system. Thus if we define

$$X=r_1\cos\theta,\qquad Y=\frac{r_1\sin\theta}{B'}, \tag{5.51}$$

by using (5.40) and (5.44), we obtain

$$\sigma_{12}^{\mathrm{in}(1)}(\bar{x},X,Y)\sim\frac{B'\cos\theta\cos2\theta}{2\pi r_1}-2B'^2\frac{\partial^2G}{\partial X\partial Y}(\bar{x},-Q^{(0)},-S),$$

and

$$\Sigma_{12}^{\mathrm{in}(1)}(\bar{x},X,Y)\sim\frac{B'\cos\theta\cos2\theta}{2\pi r_1}$$

respectively, as $(X,Y)\to(0,0)$. Incorporating these expressions with (5.50) implies

$$-2B'^2\frac{\partial^2G}{\partial X\partial Y}(\bar{x},-Q^{(0)},-S)+\frac{\mathrm{d}h_{\mathrm{in}}^{(2)}}{\mathrm{d}\bar{x}}=0.$$

Noting that

$$\frac{\partial^2G}{\partial X\partial Y}(\bar{x},Q^{(0)},S)=-\frac{\partial^2G}{\partial X\partial Y}(\bar{x},-Q^{(0)},-S),$$

we have

$$2B'^2\frac{\partial^2G}{\partial X\partial Y}(\bar{x},Q^{(0)},S)+\frac{\mathrm{d}h_{\mathrm{in}}^{(2)}}{\mathrm{d}\bar{x}}=0. \tag{5.52}$$

Therefore, we obtain an equation from the force-balance at p_k:

$$\frac{B'\sin(2\pi Q^{(0)})}{2(\cosh(2\pi B'S)-\cos(2\pi Q^{(0)}))}-\frac{\pi B'^2S\sin(2\pi Q^{(0)})\sinh(2\pi B'S)}{(\cosh(2\pi B'S)-\cos(2\pi Q^{(0)}))^2}+\frac{\mathrm{d}h_{\mathrm{in}}^{(2)}}{\mathrm{d}\bar{x}}=0. \tag{5.53}$$

Force Balance at q_k

The force-balance at q_k can be treated similarly, but it is more complicated since this time Q is now a function of $\bar{x}$. Hence we have

$$\begin{aligned}\Sigma_{12}^{\mathrm{in}(1)}(q_k, X-Q_k, Y-S) &= \Sigma_{12}^{\mathrm{in}(1)}\left(\bar{x}+\frac{\epsilon(Q^{(0)}-\zeta)}{B'}+\cdots, X-Q^{(0)}+\cdots, Y-S\right)\\ &\sim \Sigma_{12}^{\mathrm{in}(1)}(\bar{x}, X-Q^{(0)}(\bar{x}), Y-S)\\ &\quad -\frac{\epsilon(\zeta-Q^{(0)}(\bar{x}))}{B'}\cdot\frac{\partial\Sigma_{12}^{\mathrm{in}(1)}}{\partial\bar{x}}(\bar{x}, X-Q(\bar{x}), Y-S)\\ &\quad +\frac{\epsilon\zeta}{B'}\frac{\mathrm{d}Q}{\mathrm{d}\bar{x}}\cdot\frac{\partial\Sigma_{12}^{\mathrm{in}(1)}}{\partial X}(\bar{x}, X-Q(\bar{x}), Y-S)+\cdots.\end{aligned} \tag{5.54}$$

Here we emphasise that the notation $\partial\Sigma_{12}^{\mathrm{in}(1)}/\partial\bar{x}(\bar{x}, X-Q(\bar{x}), Y-S)$ denotes taking derivative of $\Sigma_{12}^{\mathrm{in}(1)}(\bar{x}, a, b)$ with respect to its first entry then evaluating at $a = X - Q(\bar{x})$ and $b = Y - S$, i.e.

$$\frac{\partial\Sigma_{12}^{\mathrm{in}(1)}}{\partial\bar{x}}(\bar{x}, X-Q(\bar{x}), Y-S) = \left.\frac{\partial\Sigma_{12}^{\mathrm{in}(1)}(\bar{x}, a, b)}{\partial\bar{x}}\right|_{a=X-Q(\bar{x}), b=Y-S}. \tag{5.55}$$

In contrast, we also introduce a notation $\mathrm{d}\Sigma_{12}^{(1)}/\mathrm{d}\bar{x}(\bar{x}, X-Q(\bar{x}), Y-S)$ to denote the total derivative of $\Sigma_{12}^{\mathrm{in}(1)}(\bar{x}, X-Q^{(0)}(\bar{x}), Y-S)$ with respective to $\bar{x}$, i.e.

$$\frac{\mathrm{d}\Sigma_{12}^{\mathrm{in}(1)}}{\mathrm{d}\bar{x}}(\bar{x}, X-Q(\bar{x}), Y-S) = \frac{\partial\Sigma_{12}^{\mathrm{in}(1)}}{\partial\bar{x}}(\bar{x}, X-Q(\bar{x}), Y-S) - \frac{\mathrm{d}Q}{\mathrm{d}\bar{x}}\cdot\frac{\partial\Sigma_{12}^{\mathrm{in}(1)}}{\partial X}(\bar{x}, X-Q(\bar{x}), Y-S). \tag{5.56}$$

Combining (5.48) and (5.56) gives

$$\lim_{(X,Y)\to(Q(\bar{x}),S)}\left(\sigma_{12}^{\mathrm{in}(1)}(\bar{x}, X, Y)+\Sigma_{12}^{\mathrm{in}(1)}(\bar{x}, X-Q(\bar{x}), Y-S)\right)=0. \tag{5.57}$$

Recalling the expansion for Q_k in (5.13), we finally get the other force-balance equation of $\mathcal{O}(\epsilon)$

$$\lim_{(X,Y)\to(Q^{(0)}(\bar{x}),S)}\left(\sigma_{12}^{\mathrm{in}(1)}(\bar{x}, X, Y)+\Sigma_{12}^{\mathrm{in}(1)}(\bar{x}, X-Q^{(0)}(\bar{x}), Y-S)\right)=0. \tag{5.58}$$

If we set

$$X = Q^{(0)} + r_2\cos\theta, \qquad Y = S + \frac{r_2\sin\theta}{B'}, \tag{5.59}$$

by using (5.40) and (5.45), we obtain

$$\sigma_{12}^{\mathrm{in}(1)}(\bar{x}, X-Q^{(0)}, Y-S) \sim -\frac{B'\cos\theta\cos 2\theta}{2\pi r_2} + 2B'^2\frac{\partial^2 G}{\partial X\partial Y}(\bar{x}, Q^{(0)}, S),$$

and

$$\Sigma_{12}^{\text{in}(1)}(\bar{x}, X, Y) \sim \frac{B' \cos\theta \cos 2\theta}{2\pi r_2}$$

respectively, as $(X, Y) \to (Q^{(0)}, S)$. Incorporating these expressions with (5.57) implies

$$2B'^2 \frac{\partial^2 G}{\partial X \partial Y}(\bar{x}, Q^{(0)}, S) + \frac{\mathrm{d}h_{\text{in}}^{(2)}}{\mathrm{d}\bar{x}} = 0. \tag{5.60}$$

This is the same equation as (5.52).

5.3.3 The Outer Region

To match with the stress from the inner region, the equation for the stress function $\chi_{\text{out}}(\bar{x}, y)$ should be viewed at $\mathcal{O}(\epsilon)$:

$$\left(\frac{\partial^2}{\partial \bar{x}^2} + \frac{\partial^2}{\partial y^2}\right)^2 \chi_{\text{out}}^{(1)}(\bar{x}, y) = 0, \tag{5.61}$$

away from $y = 0$. Near the slit $y = 0$, the boundary conditions are approached by stress components from the inner region:

$$\lim_{y\to 0^{\pm}} \frac{\partial^2 \chi_{\text{out}}^{(1)}}{\partial \bar{x}^2} = -\lim_{y\to 0^{\pm}} \sigma_{22}^{\text{out}(1)} = -\lim_{Y\to\pm\infty} \sigma_{22}^{\text{in}(1)} = \frac{\mathrm{d}^2 c_{\text{in}}^{(1)}}{\mathrm{d}\bar{x}^2}; \tag{5.62}$$

$$\lim_{y\to 0^{\pm}} \frac{\partial^2 \chi_{\text{out}}^{(1)}}{\partial \bar{x} \partial y} = \lim_{y\to 0^{\pm}} \sigma_{12}^{\text{out}(1)} = \lim_{Y\to\pm\infty} \sigma_{12}^{\text{in}(1)} = \frac{\mathrm{d}h_{\text{in}}^{(2)}}{\mathrm{d}\bar{x}}; \tag{5.63}$$

$$\lim_{y\to 0^{\pm}} \frac{\partial^2 \chi_{\text{out}}^{(1)}}{\partial y^2} = -\lim_{y\to 0^{\pm}} \sigma_{11}^{\text{out}(1)} = -\lim_{Y\to\pm\infty} \sigma_{11}^{\text{in}(1)} = a_{\text{in}}^{(3)}(\bar{x}). \tag{5.64}$$

It can be seen from (5.62) to (5.64) that all second derivatives of $\chi_{\text{out}}^{(1)}$ are continuous across $y = 0$. Following the same argument in §4.3.3, all these second derivatives will be constants in the outer region, providing all its third derivatives are continuous across $y = 0$. It will be seen from the next order stress components from the inner region that, such condition of continuity holds. Therefore, these constant second derivatives, i.e. stress components should be the same as the applied stress at infinity. Since we are only interested in σ_{12}, we assume that the only non-zero applied stress is $\lim_{x^2+y^2\to\infty} \sigma_{12}(x, y) = \sigma_{\text{ext}}$. This suggests that

$$\frac{\mathrm{d}h_{\text{in}}^{(2)}}{\mathrm{d}\bar{x}} = \sigma_{\text{ext}}. \tag{5.65}$$

5.3.4 Equilibria

Incorporating (5.65) into (5.53) gives the equation for $Q^{(0)}$:

$$\frac{B'\sin(2\pi Q^{(0)})}{2(\cosh(2\pi B'S)-\cos(2\pi Q^{(0)}))}-\frac{\pi B'^2 S\sin(2\pi Q^{(0)})\sinh(2\pi B'S)}{(\cosh(2\pi B'S)-\cos(2\pi Q^{(0)}))^2}+\sigma_{\text{ext}}=0. \quad (5.66)$$

Now for simplicity, we set $\sigma_{\text{ext}}=0$, then we have three possible solutions $Q^{(0)}=0$, $Q^{(0)}=1/2$ and

$$Q^{(0)}(\bar{x})=\frac{1}{2\pi}\cos^{-1}\left(\cosh(2\pi B'(\bar{x})S)-2\pi B'(\bar{x})S\sinh(2\pi B'(\bar{x})S)\right). \quad (5.67)$$

Sequentially, we name the equilibrium states characterised by these $Q^{(0)}$ of equilibrium Type I, II and III, respectively. From (5.67), it can also be observed that $Q^{(0)}$ does not exist for all S and B'. If the input of the arccos function is less than -1, then $Q^{(0)}$ does not exist and the system only have two possible equilibrium states.

It should be mentioned that not all these equilibrium states are stable. We will investigate them in more detail in §5.6, where, in particular, their stability will be determined. First we proceed to higher order in the asymptotic expansions in order to obtain an equation for the density. However, we note that we will later discover

- Type I is always unstable;
- Type II is conditionally stable;
- Type III is stable but does not always exist.

In the next two sections, we will look for an equation for the density in the stable cases, i.e. Type II and III.

As we discussed above, the expression of $Q^{(0)}(\bar{x})$ may ruin the periodicity in X. But here we have found that for Type I and II, $Q^{(0)}$ is a constant, so that the periodicity is preserved. On the other hand, the slowly-varying nature of $Q^{(0)}(\bar{x})$ may be troublesome. As we will see later, we can use the case when s is very small to represent equilibrium of Type III, and it is proved to work well by comparing with the simulations presented in §5.5.

5.4 The First Order

5.4.1 The Inner Region

Equations for the Shear Stress

At $\mathcal{O}(\epsilon^2)$, we need to solve an equation for $\chi_{\text{in}}^{(4)}(\bar{x}, X, Y)$:

$$\left(B'^2\frac{\partial^2}{\partial X^2}+\frac{\partial^2}{\partial Y^2}\right)^2\chi_{\text{in}}^{(4)}=2B'\cdot\left(Q^{(1)}+\zeta\frac{\mathrm{d}Q^{(0)}}{\mathrm{d}\bar{x}}\right)\delta'(X-Q^{(0)})\delta'(Y-S)-\frac{\partial\mathcal{L}\chi_{\text{in}}^{(3)}}{\partial X}$$
$$-\frac{2B''\zeta}{B'}\cdot\big(\delta(X)\delta'(Y)-\delta(X-Q^{(0)})\delta'(Y-S)\big)-\frac{2B''Q^{(0)}}{B'}\cdot\delta(X-Q^{(0)})\delta'(Y-S), \tag{5.68}$$

with X periodic, where $\mathcal{L}$ is defined by

$$\mathcal{L}=6B'^2B''\frac{\partial^2}{\partial X^2}+4B'^3\frac{\partial^3}{\partial\bar{x}\partial X^2}+4B'\frac{\partial^3}{\partial\bar{x}\partial Y^2}+2B''\frac{\partial^2}{\partial Y^2}. \tag{5.69}$$

Again by using the property of G defining in (5.38), we have

$$\chi_{\text{in}}^{(4)}=2B'\cdot\left(Q^{(1)}+\zeta\cdot\frac{\mathrm{d}Q^{(0)}}{\mathrm{d}\bar{x}}\right)\cdot\frac{\partial G}{\partial X}(\bar{x},X-Q^{(0)},Y-S)+\chi_F(\bar{x},X,Y)$$
$$-\frac{B''\zeta\chi_{\text{in}}^{(3)}}{B'^2}-\frac{2B''Q^{(0)}}{B'}G(\bar{x},X-Q^{(0)},Y-S)+c_{\text{in}}^{(4)}(\bar{x})+h_{\text{in}}^{(4)}(\bar{x})Y+\frac{a_{\text{in}}^{(4)}Y^2}{2}. \tag{5.70}$$

where

$$\left(B'^2\frac{\partial^2}{\partial X^2}+\frac{\partial^2}{\partial Y^2}\right)^2\chi_F(\bar{x},X,Y)=-\frac{\partial\mathcal{L}\chi_{\text{in}}^{(3)}}{\partial X}. \tag{5.71}$$

Finding the expression for χ_F is similar as solving for $G(\bar{x}, X, Y)$ as detailed in §A.10, and we obtain

$$\chi_F=-\frac{B''Y^3\sin(2\pi X)}{4(\cosh(2\pi B'Y)-\cos(2\pi X))}+\frac{B''\cdot(Y-S)^3\sin(2\pi(X-Q^{(0)}))}{4(\cosh(2\pi(Y-S)B')-\cos(2\pi(X-Q^{(0)}))}. \tag{5.72}$$

By plugging in, we have the expression for the stress components at $\mathcal{O}(\epsilon^2)$:

$$\sigma_{12}^{\text{in}(2)}=\frac{\partial^2\chi_{\text{in}}^{(3)}}{\partial\bar{x}\partial Y}+B'\frac{\partial^2\chi_{\text{in}}^{(4)}}{\partial X\partial Y}$$
$$=2B'^2\cdot\left(Q^{(1)}+\zeta\frac{\mathrm{d}Q^{(0)}}{\mathrm{d}\bar{x}}\right)\cdot\frac{\partial^3G}{\partial X^2\partial Y}(\bar{x},X-Q^{(0)},Y-S)+B'\cdot\frac{\partial^2\chi_F}{\partial X\partial Y}$$
$$-2B''Q^{(0)}\frac{\partial^2G}{\partial X\partial Y}(\bar{x},X-Q^{(0)},Y-S)-\frac{B''\zeta}{B'}\cdot\frac{\partial^2\chi_{\text{in}}^{(3)}}{\partial X\partial Y}+\frac{\partial^2\chi_{\text{in}}^{(3)}}{\partial\bar{x}\partial Y}+\phi Y. \tag{5.73}$$

It can be easily checked that all first derivative of $\sigma_{11}^{\text{in}(2)}$, $\sigma_{12}^{\text{in}(2)}$ and $\sigma_{22}^{\text{in}(2)}$ with respect to X or Y meet the condition of continuity mentioned in §5.4.3. Thus all arguments in it are validated.

With (5.73), we can proceed to the force-balance equations at $\mathcal{O}(\epsilon^2)$ to search for an equation describing the density.

Singularities

To get the singularities of $\mathcal{O}(\epsilon^2)$, we need to solve an equation for $K_{\text{in}}^{(4)}(\bar{x}, X, Y; X', Y')$:

$$\left(B'^2\frac{\partial^2}{\partial X^2}+\frac{\partial^2}{\partial Y^2}\right)^2 K_{\text{in}}^{(4)} = -\frac{2B''\cdot(\zeta-X')}{B'}\cdot\delta(X-X')\delta(Y-Y') - \frac{\partial\mathcal{L}K_{\text{in}}^{(3)}}{\partial X}, \quad (5.74)$$

where $\mathcal{L}$ is defined the same as (5.69). If we define $K_F(\bar{x}, X, Y; X', Y')$, such that

$$\begin{aligned}\left(B'^2\frac{\partial^2}{\partial X^2}+\frac{\partial^2}{\partial Y^2}\right)^2 K_F &= -\frac{\partial\mathcal{L}K_{\text{in}}^{(3)}}{\partial X}\\ &= \frac{24B''B'^2\cdot(X-X')(Y-Y')((X-X')^2-B'^2(Y-Y')^2)}{\pi((X-X')^2+B'^2(Y-Y')^2)^3},\end{aligned} \quad (5.75)$$

by using the separation of variables in the polar coordinates, we obtain

$$K_F(\bar{x}, X, Y; X', Y') = \frac{B''\cdot(X-X')(Y-Y')((X-X')^2-B'^2(Y-Y')^2)}{8\pi B'^2\cdot((X-X')^2+B'^2(Y-Y')^2)}. \quad (5.76)$$

Thus

$$\begin{aligned}K_{\text{in}}^{(4)}(\bar{x}, X, Y; X', Y') &= -\frac{B''\cdot(\zeta-X')(Y-Y')}{4\pi B'^2}\cdot\log\left((X-X')^2+B'^2(Y-Y')^2\right)\\ &= K_F(\bar{x}, X, Y; X', Y') + \beta(\bar{x})(X-X')(Y-Y'),\end{aligned} \quad (5.77)$$

where $\beta(\bar{x})$ is to be determined.

Therefore, at p_k, replacing (X', Y') by $(0, 0)$ gives the singular part of the shear stress as

$$\begin{aligned}\Sigma_{12}^{\text{in}(2)}(\bar{x}, X, Y) &= B'\frac{\partial^2 K_{\text{in}}^{(4)}(\bar{x}, X, Y; 0, 0)}{\partial X\partial Y} + \frac{\partial^2 K_{\text{in}}^{(3)}(\bar{x}, X, Y; 0, 0)}{\partial\bar{x}\partial Y}\\ &= -\frac{\zeta B''\cdot X(X^2-B'^2Y^2)}{2\pi B'\cdot(X^2+B'^2Y^2)} + \frac{\mathrm{d}\alpha}{\mathrm{d}\bar{x}}\cdot\frac{1}{4\pi\alpha} + B'\beta\\ &\quad + \frac{B''\cdot(X^6+21B'^2X^4Y^2+7B'^4X^2Y^4+3B'^6Y^6)}{8\pi B'\cdot(X^2+B'^2Y^2)^3},\end{aligned} \quad (5.78)$$

where α is the arbitrary function of $\bar{x}$ in (5.43).

The next step is to determine α and β. Since we know that, in the original coordinate, a dislocation at $(p_k, 0)$ corresponds to

$$K = \frac{\epsilon^2 y}{4\pi} \log((x - p_k)^2 + y^2).$$

Recalling that

$$x = B^{-1}(B(p_k) - \epsilon X) \sim p_k + \frac{\epsilon X}{B'(p_k)} + \frac{\epsilon^2 X^2 B''(p_k)}{2(B'(p_k))^3} + \cdots,$$

we have

$$K \sim \frac{\epsilon Y}{4\pi} \log(\epsilon^2) + \frac{\epsilon Y}{4\pi} \left(\frac{X^2}{B'(p_k)^2} + Y^2 \right) + \frac{\epsilon X^3 Y B''(p_k)}{4\pi (B'(p_k))^2 (X^2 + (B'(p_k) Y)^2)} + \cdots.$$

Replacing p_k by $B^{-1}(B(\bar{x}) - \epsilon\zeta(\bar{x}))$, we find that the stress satisfies

$$\begin{aligned} \Sigma_{12} &= B' \frac{\partial^2 K}{\partial X \partial Y} + \frac{\partial^2 K}{\partial \bar{x} \partial Y} \\ &\sim \left(\epsilon B' - \frac{\epsilon^2 \zeta B''}{B'} \right) \cdot \frac{X(X^2 - B'^2 Y^2)}{2\pi (X^2 + B'^2 Y^2)^2} - \frac{\epsilon^2 B'' \cdot (X^6 - 6X^4 B'^2 Y^2 + X^2 B'^4 Y^4)}{4\pi B' \cdot (X^2 + (B'Y)^2)^3} + \cdots. \end{aligned}$$

A comparison between this Σ_{12} and $\epsilon \Sigma_{12}^{\mathrm{in}(1)} + \epsilon^2 \Sigma_{12}^{\mathrm{in}(2)}$ shows that

$$\frac{\mathrm{d}\alpha}{\mathrm{d}\bar{x}} \cdot \frac{1}{4\pi\alpha} + B'\beta = -\frac{3B''}{8\pi B'}. \tag{5.79}$$

Therefore, we find that

$$\begin{aligned} \Sigma_{12}^{\mathrm{in}(2)}(\bar{x}, X, Y) = &-\frac{\zeta B'' \cdot X(X^2 - B'^2 Y^2)}{2\pi B' \cdot (X^2 + B'^2 Y^2)} - \frac{3B''}{8\pi B'} \\ &+ \frac{B'' \cdot (X^6 + 21 B'^2 X^4 Y^2 + 7 B'^4 X^2 Y^4 + 3 B'^6 Y^6)}{8\pi B' \cdot (X^2 + B'^2 Y^2)^3}. \end{aligned} \tag{5.80}$$

If we replace (X', Y') by (Q_k, S) in (5.77), we can also obtain

$$\begin{aligned} \Sigma_{12}^{\mathrm{in}(2)}(\bar{x}, X - Q_k, Y - S) &= B' \frac{\partial^2 K_{\mathrm{in}}^{(4)}(\bar{x}, X, Y; Q_k, S)}{\partial X \partial Y} + \frac{\mathrm{d}}{\mathrm{d}\bar{x}} \frac{\partial K_{\mathrm{in}}^{(3)}(\bar{x}, X, Y; Q_k, S)}{\partial Y} \\ &= -\left(\frac{(\zeta - Q_k) B''}{B'} + B' \frac{\mathrm{d}Q_k}{\mathrm{d}\bar{x}} \right) \cdot \frac{\hat{X}(\hat{X}^2 - B'^2 \hat{Y}^2)}{2\pi (\hat{X}^2 + B'^2 \hat{Y}^2)} - \frac{3B''}{8\pi B'} \\ &\quad + \frac{B'' \cdot (\hat{X}^6 + 21 B'^2 \hat{X}^4 \hat{Y}^2 + 7 B'^4 \hat{X}^2 \hat{Y}^4 + 3 B'^6 \hat{Y}^6)}{8\pi B' \cdot (\hat{X}^2 + B'^2 \hat{Y}^2)^3}, \end{aligned} \tag{5.81}$$

where $\hat{X} = X - Q_k$ and $\hat{Y} = Y - S$.

5.4.2 Force Balance

Force Balance at p_k

Combining (5.48) and (5.49), we can rewrite the force-balance equation at p_k of $\mathcal{O}(\epsilon^2)$ from (5.29) by

$$\begin{aligned} 0 = -\frac{\zeta}{B'} \cdot \lim_{(X,Y)\to(0,0)} \left(\frac{\partial \sigma_{12}^{\mathrm{in}(1)}}{\partial \bar{x}}(\bar{x}, X, Y) - \frac{\partial \Sigma_{12}^{\mathrm{in}(1)}}{\partial \bar{x}}(\bar{x}, X, Y) \right) \\ + \lim_{(X,Y)\to(0,0)} \left(\sigma_{12}^{\mathrm{in}(2)}(p_k, X, Y) - \Sigma_{12}^{\mathrm{in}(2)}(p_k, X, Y) \right). \end{aligned} \tag{5.82}$$

As $(X, Y) \to (0, 0)$, combining the polar transformation in (5.51) and the expression that

$$\sigma_{12}^{\mathrm{in}(1)}(\bar{x}, X, Y) = 2B' \cdot \left(\frac{\partial^2 G}{\partial X \partial Y}(\bar{x}, X, Y) - \frac{\partial^2 G}{\partial X \partial Y}(\bar{x}, X - Q^{(0)}(\bar{x}), Y - S) \right),$$

we obtain

$$\frac{\partial \sigma_{12}^{\mathrm{in}(1)}}{\partial \bar{x}} \sim \frac{B'' \cos\theta \cos 4\theta}{2\pi r_1} + 4B'B'' \cdot \frac{\partial^2 G}{\partial X \partial Y}(\bar{x}, Q^{(0)}, S) + 2B'^2 \cdot \frac{\mathrm{d}}{\mathrm{d}\bar{x}} \left(\frac{\partial^2 G}{\partial X \partial Y}(\bar{x}, Q^{(0)}, S) \right). \tag{5.83}$$

From the force-balance in the last order, we know that

$$\frac{\partial^2 G}{\partial X \partial Y}(\bar{x}, Q^{(0)}, S) = 0,$$

which reduces (5.83) to

$$\frac{\partial \sigma_{12}^{\mathrm{in}(1)}}{\partial \bar{x}} \sim \frac{B'' \cos\theta \cos 4\theta}{2\pi r_1},$$

as $r_1 \to 0$. From (5.44), we also find

$$\frac{\partial \Sigma_{12}^{\mathrm{in}(1)}}{\partial \bar{x}} \sim \frac{B'' \cos\theta \cos 4\theta}{2\pi r_1}.$$

Thus the singular part of $\partial \sigma_{12}^{\mathrm{in}(1)} / \partial \bar{x}$ cancels with that of $\partial \Sigma_{12}^{\mathrm{in}(1)} / \partial \bar{x}$ as they should, giving rise to

$$\lim_{(X,Y)\to(0,0)} \left(\frac{\partial \sigma_{12}^{\mathrm{in}(1)}}{\partial \bar{x}}(\bar{x}, X, Y) - \frac{\partial \Sigma_{12}^{\mathrm{in}(1)}}{\partial \bar{x}}(\bar{x}, X, Y) \right) = 0.$$

Recalling from (4.13) that $\zeta(p_k) = 0$, then we replace p_k by $B^{-1}(B(\bar{x}) - \epsilon\zeta(\bar{x}))$ to write down

$$\begin{aligned}\sigma_{12}^{\mathrm{in}(2)}(p_k, X, Y) \sim\ & 2B'^2 Q^{(1)} \cdot \frac{\partial^3 G}{\partial X^2 \partial Y}(\bar{x}, X - Q^{(0)}, Y - S) + B' \cdot \frac{\partial^2 \chi_F}{\partial X \partial Y}(\bar{x}, X, Y) \\ & - 2B'' Q^{(0)} \cdot \frac{\partial^2 G}{\partial X \partial Y}(\bar{x}, X - Q^{(0)}, Y - S) + \frac{\partial^2 \chi_{\mathrm{in}}^{(3)}}{\partial \bar{x} \partial Y}(\bar{x}, X, Y) + \phi Y.\end{aligned} \tag{5.84}$$

Again $(X, Y) \to (0, 0)$, the third term of (5.84) vanishes, and the force-balance equation (5.82) finally becomes

$$\lim_{X \to 0, Y \to 0} \left(\frac{\partial^2 \chi_{\mathrm{in}}^{(3)}}{\partial \bar{x} \partial Y} + B' \frac{\partial^2 \chi_F}{\partial X \partial Y} - \Sigma_{12}^{\mathrm{in}(2)} \right) + 2B'^2 Q^{(1)} \cdot \frac{\partial^3 G}{\partial X^2 \partial Y}(\bar{x}, Q^{(0)}, S) = 0, \tag{5.85}$$

where the first three terms in (5.85) are all functions of $\bar{x}$, X and Y.

force-balance at q_k

The force-balance equation at q_k is more complicated than that at p_k, because the expansion of Q_k and its derivative with respect to $\bar{x}$ should both be considered. Thus the $\mathcal{O}(\epsilon^2)$ equation of (5.30) can be rewritten by

$$\begin{aligned}0 = & \frac{Q^{(0)} - \zeta}{B'} \cdot \lim_{(X,Y) \to (Q_k, S)} \left(\frac{\mathrm{d}\sigma_{12}^{\mathrm{in}(1)}}{\mathrm{d}\bar{x}}(\bar{x}, X, Y) + \frac{\mathrm{d}\Sigma_{12}^{\mathrm{in}(1)}}{\mathrm{d}\bar{x}}(\bar{x}, X - Q_k, Y - S) \right) \\ & + Q^{(1)}(p_k) \cdot \lim_{(X,Y) \to (Q_k, S)} \left(\frac{\partial \sigma_{12}^{\mathrm{in}(1)}}{\partial X}(\bar{x}, X, Y) + \frac{\partial \Sigma_{12}^{\mathrm{in}(1)}}{\partial X}(\bar{x}, X - Q_k, Y - S) \right) \\ & + \lim_{(X,Y) \to (Q_k, S)} \left(\sigma_{12}^{\mathrm{in}(2)}(q_k, X, Y) + \Sigma_{12}^{\mathrm{in}(2)}(q_k, X - Q_k, Y - S) \right).\end{aligned} \tag{5.86}$$

Then similarly as for p_k, we replace q_k in (5.86) by $B^{-1}(B(\bar{x}) - \epsilon(\zeta - Q_k/B'))$ to find an equation at $\mathcal{O}(\epsilon^2)$, which ideally is independent of q_k. For the first part in the right hand side of (5.86), it is asymptotically equivalent to write

$$\begin{aligned}& \lim_{(X,Y) \to (Q^{(0)}, S)} \left(\frac{\mathrm{d}\sigma_{12}^{\mathrm{in}(1)}}{\mathrm{d}\bar{x}}(\bar{x}, X, Y) + \frac{\mathrm{d}\Sigma_{12}^{\mathrm{in}(1)}}{\mathrm{d}\bar{x}}(\bar{x}, X - Q^{(0)}, Y - S) \right) \\ \sim & \lim_{(X,Y) \to (Q^{(0)}, S)} \left(\frac{\partial \sigma_{12}^{\mathrm{in}(1)}}{\partial \bar{x}}(\bar{x}, X, Y) + \frac{\partial \Sigma_{12}^{\mathrm{in}(1)}}{\partial \bar{x}}(\bar{x}, X - Q^{(0)}, Y - S) \right) \\ & + \frac{\mathrm{d}Q^{(0)}}{\mathrm{d}\bar{x}} \cdot \lim_{(X,Y) \to (Q^{(0)}, S)} \left(2B'^2 \frac{\partial^3 G}{\partial X^2 \partial Y}(\bar{x}, X - Q^{(0)}, Y - S) - \frac{\partial \Sigma_{12}^{\mathrm{in}(1)}}{\partial X}(\bar{x}, X - Q^{(0)}, Y - S) \right)\end{aligned} \tag{5.87}$$

Again, by using the polar transformation in (5.59), we have

$$\frac{\partial \sigma_{12}^{\mathrm{in}(1)}}{\partial \bar{x}} \sim -\frac{B'' \cos\theta \cos 4\theta}{2\pi r_2} + 2B'^2 \cdot \frac{\partial^3 G}{\partial \bar{x} \partial X \partial Y}(\bar{x}, Q^{(0)}, S) = -\frac{B'' \cos\theta \cos 4\theta}{2\pi r_2}; \quad (5.88)$$

$$\frac{\partial \Sigma_{12}^{\mathrm{in}(1)}}{\partial \bar{x}} \sim \frac{B'' \cos\theta \cos 4\theta}{2\pi r_2}; \quad (5.89)$$

$$\frac{\partial^3 G}{\partial X^2 \partial Y}(\bar{x}, X - Q^{(0)}, Y - S) \sim -\frac{\cos 4\theta}{4\pi B' r_2^2} - \frac{\pi}{12B'}; \quad (5.90)$$

$$\frac{\partial \Sigma_{12}^{\mathrm{in}(1)}}{\partial X}(\bar{x}, X - Q^{(0)}, Y - S) \sim -\frac{B' \cos 4\theta}{2\pi r_2^2}, \quad (5.91)$$

as $(X, Y) \to (Q^{(0)}, S)$. Incorporating above expressions into (5.87) gives

$$\lim_{(X,Y)\to(Q_k,S)} \left(\frac{\mathrm{d}\sigma_{12}^{\mathrm{in}(1)}}{\mathrm{d}\bar{x}} + \frac{\mathrm{d}\Sigma_{12}^{\mathrm{in}(1)}}{\mathrm{d}\bar{x}}(\bar{x}, X - Q^{(0)}, Y - S) \right) \sim -\frac{\pi B'}{6} \cdot \frac{\mathrm{d}Q^{(0)}}{\mathrm{d}\bar{x}}. \quad (5.92)$$

From (5.90) and (5.91), we also find that the second term of (5.86) satisfies

$$\begin{aligned} &\lim_{(X,Y)\to(Q_k,S)} \left(\frac{\partial \sigma_{12}^{\mathrm{in}(1)}}{\partial X}(\bar{x}, X, Y) + \frac{\partial \Sigma_{12}^{\mathrm{in}(1)}}{\partial X}(\bar{x}, X - Q_k, Y - S) \right) \\ &\sim 2B'^2 \frac{\partial^3 G}{\partial X^2 \partial Y}(\bar{x}, Q^{(0)}, S) + \frac{\pi B'}{6} \end{aligned} \quad (5.93)$$

Incorporating (5.92) and (5.93) into (5.86) gives the other force-balance equation of $\mathcal{O}(\epsilon^2)$:

$$\begin{aligned} &Q^{(1)} \cdot \left(2B'^2 \frac{\partial^3 G}{\partial X^2 \partial Y}(\bar{x}, Q^{(0)}, S) + \frac{\pi B'}{6} \right) + \frac{\pi}{6} \cdot \frac{\mathrm{d}Q^{(0)}}{\mathrm{d}\bar{x}} \left(\zeta - Q^{(0)} \right) \\ &\quad + \lim_{(X,Y)\to(Q^{(0)},S)} \left(\sigma_{12}^{\mathrm{in}(2)}(q_k, X, Y) + \Sigma_{12}^{\mathrm{in}(2)}(q_k, X - Q^{(0)}, Y - S) \right) = 0. \end{aligned} \quad (5.94)$$

Up to now, we transform the two force-balance equations (5.29) and (5.30) of $\mathcal{O}(\epsilon^2)$ into (5.85) and (5.94), respectively. In the next two sections, we will look for an equation for density of the two types of equilibria by evaluating these equations.

5.4.3 Equilibria of Type II

An Equation for the Density

First, we consider equilibria of Type II, where $Q^{(0)} = 1/2$. In that case, all terms multiplied by $\mathrm{d}Q^{(0)}/\mathrm{d}\bar{x}$ vanish. Then the force-balance equations (5.85) and (5.94)

become

$$\lim_{(X,Y)\to(0,0)}\left(\frac{\partial^2\chi_{\rm in}^{(3)}}{\partial\bar{x}\partial Y}+B'\frac{\partial^2\chi_F}{\partial X\partial Y}-\Sigma_{12}^{\rm in(2)}\right)+2B'^2Q^{(1)}\cdot\frac{\partial^3 G}{\partial X^2\partial Y}(\bar{x},1/2,S)=0 \quad (5.95)$$

and

$$\begin{aligned}&Q^{(1)}\cdot\left(2B'^2\frac{\partial^3 G}{\partial X^2\partial Y}(\bar{x},1/2,S)-\frac{\pi B'}{6}\right)\\&+\lim_{(X,Y)\to(Q^{(0)},S)}\left(\sigma_{12}^{\rm in(2)}(q_k,X,Y)+\Sigma_{12}^{\rm in(2)}(q_k,X-Q^{(0)},Y-S)\right)=0,\end{aligned} \quad (5.96)$$

respectively.

Since

$$\begin{aligned}\frac{\partial^3 G(\bar{x},1/2,S)}{\partial X^2\partial Y} &= \frac{\pi\mathrm{sech}^2(\pi SB')}{4B'}\left(-1+2\pi SB'\tanh(\pi SB')\right);\\ \frac{\partial^2\chi_F(\bar{x},X,Y)}{\partial X\partial Y} &= \frac{B''}{16\pi B'^2}\cdot(-2+3\cos 2\theta-\cos 6\theta)\\ &\quad+\frac{B''\pi S^3\mathrm{sech}^2(\pi SB')}{4\pi B'}\left(-3+2\pi^2 SB'\tanh(\pi SB')\right);\\ \frac{\partial^2\chi_{\rm in}^{(3)}(\bar{x},X,Y)}{\partial\bar{x}\partial Y} &= \frac{B''}{8\pi B'}\left(3-2\cos 2\theta-\cos 4\theta\right)\\ &\quad-\frac{SB''\mathrm{sech}^2(\pi SB')(\pi SB'+\sinh(2\pi SB'))}{2}+\frac{\mathrm{d}h_{\rm in}^{(3)}}{\mathrm{d}x};\\ \Sigma_{12}^{\rm in(2)}(p_k,X,Y) &= -\frac{B''}{16\pi B'}\left(\cos 2\theta+2\cos 4\theta+\cos 6\theta\right),\end{aligned}$$

as $(X,Y)\to(0,0)$, we can reduce (5.95) to

$$\begin{aligned}0=&\frac{\pi Q^{(1)}B'\mathrm{sech}^2(\pi SB')}{2}\left(-1+2\pi SB'\tanh(\pi SB')\right)+\frac{B''}{4\pi B'}+\frac{\mathrm{d}h_{\rm in}^{(3)}}{\mathrm{d}x}\\&+\frac{\pi S^3B'B''}{4}\mathrm{sech}^2(\pi SB')\left(-3+2\pi^2 SB'\tanh(\pi SB')\right)\\&-\frac{SB''\mathrm{sech}^2(\pi SB')(\pi SB'+\sinh(2\pi SB'))}{2}.\end{aligned} \quad (5.97)$$

On the other hand, by using (5.73) and (5.81), we have

$$\begin{aligned}\sigma_{12}^{\mathrm{in}(2)}(q_k,X,Y) \sim\ & 2B'^2Q^{(1)}\cdot\frac{\partial^3 G}{\partial X^2\partial Y}(\bar{x},X-1/2,Y-S)+B'\frac{\partial^2\chi_F}{\partial X\partial Y}+\frac{\partial^2\chi_{\mathrm{in}}^{(3)}}{\partial\bar{x}\partial Y}\\ &-2B''Q^{(0)}\cdot\frac{\partial^2 G}{\partial X\partial Y}(\bar{x},X-1/2,Y-S)+\phi S\\ \sim\ & -Q^{(1)}\cdot\left(\frac{B'\cos 4\theta}{2\pi r_2^2}+\frac{\pi B'}{6}\right)-\frac{B''}{16\pi B'^2}\cdot(-2+3\cos 2\theta-\cos 6\theta)\\ &-\frac{B''\pi S^3\mathrm{sech}^2(\pi SB')}{4\pi B'}\left(-3+2\pi^2 SB'\tanh(\pi SB')\right)\\ &-\frac{B''}{8\pi B'}(3-2\cos 2\theta-\cos 4\theta)\\ &+\frac{SB''\mathrm{sech}^2(\pi SB')(\pi SB'+\sinh(2\pi SB'))}{2}+\phi S-\frac{B''\cos\theta\cos 2\theta}{4\pi B' r_2}\end{aligned} \tag{5.98}$$

and

$$\Sigma_{12}^{\mathrm{in}(2)}(q_k,X-Q^{(0)},Y-S)\sim\frac{B''}{B'}\cdot\frac{\cos\theta\cos 2\theta}{4\pi r_2}-\frac{B''}{16\pi B'}\cdot(\cos 2\theta+2\cos 4\theta+\cos 6\theta)\,, \tag{5.99}$$

as $(X,Y)\to(Q^{(0)},S)$.

Incorporating (5.98) and (5.99) into (5.96) gives the other force-balance equation:

$$\begin{aligned}0=\ & \frac{\pi Q^{(1)}B'\mathrm{sech}^2(\pi SB')}{2}(-1+2\pi SB'\tanh(\pi SB'))\\ &-\frac{B''}{4\pi B'}-\frac{\pi S^2B'B''}{4}\mathrm{sech}(\pi SB')\left(-3+2\pi^2SB'\tanh(\pi SB')\right)\\ &+\frac{SB''\mathrm{sech}^2(\pi SB')(\pi SB'+\sinh(2\pi SB'))}{2}+\frac{\mathrm{d}h_{\mathrm{in}}^{(3)}}{\mathrm{d}x}+S\frac{\mathrm{d}a_{\mathrm{in}}^{(3)}}{\mathrm{d}\bar{x}}.\end{aligned} \tag{5.100}$$

Thus subtracting the two force-balance equations gives

$$\begin{aligned}&\frac{B''}{2\pi B'}+\frac{\pi S^2B''B'}{2}\mathrm{sech}^2(\pi SB')\left(-3+2\pi^2SB'\tanh(\pi SB')\right)\\ &\qquad -SB''\mathrm{sech}^2(\pi SB')(\pi SB'+\sinh(2\pi SB'))=S\frac{\mathrm{d}a_{\mathrm{in}}^{(3)}}{\mathrm{d}\bar{x}}.\end{aligned} \tag{5.101}$$

It should be mentioned that $\mathrm{d}a_{\mathrm{in}}^{(3)}/\mathrm{d}\bar{x}$ passes the information of the applied stress gradient. Here we set it to be ϕ to agree with (5.7).

Integrating (5.101) with respect to $\bar{x}$ and replacing B' by ρ enables us to obtain the equation for the density:

$$-\frac{\log\rho}{2\pi}+\frac{\log\cosh(\pi\rho S)}{2\pi}+\frac{\pi\rho^2S^2}{2\cosh^2(\pi\rho S)}+\frac{3S\rho\tanh(\pi\rho S)}{2}=C-S\phi\bar{x}, \tag{5.102}$$

where C is a constant to be determined by the total number of dipoles.

5.4.4 Pile-up of Dipoles with Super Small Gap Between Slip Planes

Now we consider the equilibria of Type III, when $\mathrm{d}Q^{(0)}/\mathrm{d}\bar{x}$ does not vanish. However, as discussed above, the slow varying nature of $Q^{(0)}$ may destroy our assumption of the periodicity in X. Therefore, we consider the case when the gap between slip planes s is very small.

Equilibrium Condition for a Dipole Pair

Before applying the method of multiple scales, we first consider the equilibrium condition for a dipole pair. If we consider the stress at any dislocation in a row of dipoles, from the law of motion of a single dislocation, we find that three sources may contribute to its motion:

- σ_{12}^{l} - stress by its opposite character in the cell;
- σ_{12}^{g} - stress by all other dislocations;
- σ_{ext} - applied stress or stress gradient.

Now, let us consider two rows of dislocations, where the spacing between the two slip planes s tends to 0, as shown in Fig. 5.2. In this case, the two glide planes are so close

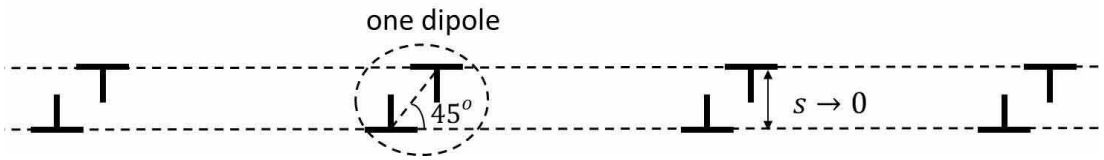


Figure 5.2: Dipoles with super small gap between slip planes.

to each other that σ_{12}^{l} becomes dominant. The consequence is that the dislocations will form in pairs and display an angle of 45° to accommodate this local stress, if there is no applied stress.

This suggests that the two dislocation in the k-th cell can be assumed to be at $(p_k, 0)$ and $(p+s+f_k(s), s)$, respectively, where $\lim_{s\to 0} f_k(s)/s = 0$. For equilibria, we require

$$\sigma_{12}^{g}(p_k, 0) + \frac{\epsilon^2(s + f_k(s))((s + f_k(s))^2 - s^2)}{2\pi((s + f_k(s))^2 + s^2)^2} = 0 \tag{5.103}$$

and

$$\sigma_{12}^g(p_k + s + f_k(s), s) + \frac{\epsilon^2(s + f_k(s))((s + f_k(s))^2 - s^2)}{2\pi((s + f_k(s))^2 + s^2)^2} + \phi s = 0. \tag{5.104}$$

By subtraction, we have

$$\sigma_{12}^g(p_k + s + f_k(s), s) - \sigma_{12}^g(p_k, 0) + \phi s = 0.$$

Letting $s \to 0$, we asymptotically obtain the condition for the equilibrium state of a row of dipoles:

$$\frac{\partial \sigma_{12}^g}{\partial x}(p_k, 0) + \frac{\partial \sigma_{12}^g}{\partial y}(p_k, 0) + \phi = 0, \tag{5.105}$$

which holds for every integer $k \in [1, N-1]$. From (5.105), it can be seen that, with such a simplifying process, we only need to solve a system of algebraic equations for p_k. This leads us back to Chapter 4, where we use our multiple-scale technique to solve for the density of monopole pile-ups. If we can appropriately express the stress σ_{12}^g by all other dipoles as a function only of p_k, then the multiple-scale method can then be implemented.

Governing Equations

In order to implement the multiple-scale technique, we need to relate σ_{12}^g to some stress function. As from Fig. 5.2, it is reasonable to assume in this case s is much smaller than the size of each cell. Thus, the two dislocations in one cell can be treated as an object and it exerts a shear stress of

$$\sigma_{12}^d(x, y) = \sigma(x - p_k, y) - \sigma(x - p_k - s - f_k(s), y - s), \tag{5.106}$$

where

$$\sigma(a, b) = \frac{\epsilon^2 a(a^2 - b^2)}{2\pi(a^2 + b^2)^2}.$$

As $s \to 0$, we have

$$\sigma_{12}^d(x, y) \sim s \cdot \left(\frac{\partial \sigma}{\partial a}(x - p_k, y) + \frac{\partial \sigma}{\partial b}(x - p_k, y) \right).$$

To be systematic with the previous discussion, we still use $S = s/\epsilon$. Thus we can introduce a stress function χ satisfying

$$\Delta^2 \chi(x, y) = 2\epsilon^3 S \sum_{k=0}^{N} \delta(x - p_k)\delta'(y), \tag{5.107}$$

such that

$$\sigma_{12}(x,y) = \frac{\partial^2 \chi}{\partial x \partial y}. \tag{5.108}$$

Analogously to the previous cases, another stress potential $K(x,y;p_k,0)$ yielding

$$\Delta^2 K(x,y) = 2\epsilon^3 S\delta(x-p_k)\delta'(y), \tag{5.109}$$

is also introduced, in order to calculate the singular behaviour of σ_{12} by

$$\Sigma_{12}(x,y;p_k,0) = \frac{\partial^2 K}{\partial x \partial y}. \tag{5.110}$$

Then we are enabled to say

$$\sigma_{12}^g = \left(\frac{\partial}{\partial x} + \frac{\partial}{\partial y}\right)(\sigma_{12} - \Sigma_{12}), \tag{5.111}$$

and the force-balance equation (5.105) becomes

$$\phi + \lim_{x\to p_k, y\to 0}\left(\frac{\partial}{\partial x} + \frac{\partial}{\partial y}\right)\left(\sigma_{12}^d(x,y) - \Sigma_{12}^d(x,y)\right) = 0, \tag{5.112}$$

Expansions in the Multiple-Scale Form

Following the same procedure, we can introduce variables of two scales by

$$\bar{x} = x, \qquad X = \frac{B(x) - B(p_k)}{\epsilon}.$$

Also, we can assume the expansion that

$$\chi(x,y) \triangleq \chi_{\text{in}}(\bar{x},X,Y) \sim \epsilon^4 \chi_{\text{in}}^{(4)}(\bar{x},X,Y) + \epsilon^5 \chi_{\text{in}}^{(5)}(\bar{x},X,Y) + \cdots; \tag{5.113}$$

$$K(x,y;p_k,0) \triangleq K_{\text{in}}(\bar{x},X,Y) \sim \epsilon^4 K_{\text{in}}^{(4)}(\bar{x},X,Y) + \epsilon^5 K_{\text{in}}^{(5)}(\bar{x},X,Y) + \cdots; \tag{5.114}$$

$$\sigma_{12}(x,y) \triangleq \sigma_{12}^{\text{in}}(\bar{x},X,Y) \sim \epsilon^2 \sigma_{12}^{\text{in}(2)}(\bar{x},X,Y) + \epsilon^3 \sigma_{12}^{\text{in}(3)}(\bar{x},X,Y) + \cdots; \tag{5.115}$$

$$\Sigma_{12}(x,y;p_k,0) \triangleq \Sigma_{12}^{\text{in}}(\bar{x},X,Y) \sim \epsilon^2 \Sigma_{12}^{\text{in}(2)}(\bar{x},X,Y) + \epsilon^3 \Sigma_{12}^{\text{in}(3)}(\bar{x},X,Y) + \cdots. \tag{5.116}$$

Then the stress potential in the multiple-scale form satisfies

$$\left(\left(\frac{\partial}{\partial \bar{x}} + \frac{B'}{\epsilon}\frac{\partial}{\partial X}\right)^2 + \frac{1}{\epsilon^2}\frac{\partial}{\partial Y}\right)^2 \chi_{\text{in}}(\bar{x},X,Y) = 2SB'(p_k)\delta(X)\delta'(Y) \tag{5.117}$$

and

$$\left(\left(\frac{\partial}{\partial \bar{x}} + \frac{B'}{\epsilon}\frac{\partial}{\partial X}\right)^2 + \frac{1}{\epsilon^2}\frac{\partial}{\partial Y}\right)^2 K_{\text{in}}(\bar{x},X,Y) = 2SB'(p_k)\delta(X)\delta'(Y). \tag{5.118}$$

The force-balance equation (5.112) then becomes

$$\phi + \lim_{(X,Y)\to(0,0)}\left(\frac{\partial}{\partial \bar{x}} + \frac{B'}{\epsilon}\frac{\partial}{\partial X} + \frac{1}{\epsilon}\frac{\partial}{\partial Y}\right)^2 (\Sigma_{12}^{\text{in}}(\bar{x},X,Y) - \Sigma_{12}^{\text{in}}(\bar{x},X,Y)) = 0. \tag{5.119}$$

The Leading Order

The leading order equation for χ_{in} is

$$\left(B'^2\frac{\partial^2}{\partial X^2}+\frac{\partial^2}{\partial Y^2}\right)^2\chi_{\text{in}}^{(4)}(\bar{x},X,Y)=2SB'\delta(X)\delta'(Y), \tag{5.120}$$

which suggests

$$\chi_{\text{in}}^{(4)}(\bar{x},X,Y)=2SB'G(\bar{x},X,Y), \tag{5.121}$$

where

$$G=\frac{Y}{8\pi B'}\log\left(\cosh(2\pi B'Y)-\cos(2\pi X)\right).$$

Therefore, we have

$$\sigma_{12}^{\text{in}(2)}(\bar{x},X,Y)=2SB'^2\frac{\partial^2 G}{\partial X\partial Y}(\bar{x},X,Y). \tag{5.122}$$

On the other hand, we also need to consider the leading order equation for K_{in}:

$$\left(B'^2\frac{\partial^2}{\partial X^2}+\frac{\partial^2}{\partial Y^2}\right)^2K_{\text{in}}^{(4)}(\bar{x},X,Y)=2SB'\delta(X)\delta'(Y), \tag{5.123}$$

which suggests

$$\Sigma_{12}^{\text{in}(2)}(\bar{x},X,Y)=\frac{SB'}{2\pi}\cdot\frac{X(X^2-Y^2)}{(X^2+B'^2Y^2)^2}. \tag{5.124}$$

At the leading order, the force-balance equation

$$\lim_{(X,Y)\to(0,0)}\left(B'\frac{\partial}{\partial X}+\frac{\partial}{\partial Y}\right)^2\left(\sigma_{12}^{\text{in}(2)}(\bar{x},X,Y)-\Sigma_{12}^{\text{in}(2)}(\bar{x},X,Y)\right)=0. \tag{5.125}$$

Unsurprisingly, by combining (5.122) and (5.124), we find that (5.125) holds for every $\bar{x}$.

The First Order

At the next order, we need to solve

$$\left(B'^2\frac{\partial^2}{\partial X^2}+\frac{\partial^2}{\partial Y^2}\right)^2\chi_{\text{in}}^{(5)}(\bar{x},X,Y)=-\frac{\partial\mathcal{L}\chi_{\text{in}}^{(4)}}{\partial X}+\frac{2\zeta SB''}{B'}\delta(X)\delta'(Y), \tag{5.126}$$

which gives

$$\chi_{\text{in}}^{(5)}(\bar{x},X,Y)=-\frac{SB''Y^3\sin(2\pi X)}{4\pi(\cosh(2\pi B'Y)-\cos(2\pi X))}+\frac{2\zeta SB''}{B'}\cdot G(\bar{x},X,Y). \tag{5.127}$$

Therefore, we have

$$\sigma_{12}^{\text{in}(3)}(\bar{x}, X, Y) = B' \frac{\partial^2 \chi_{\text{in}}^{(5)}}{\partial X \partial Y} + \frac{\partial^2 \chi_{\text{in}}^{(4)}}{\partial \bar{x} \partial Y}. \tag{5.128}$$

Similarly, it can be calculated that

$$\Sigma_{12}^{\text{in}(3)}(\bar{x}, X, Y) = -\frac{SB'' \cdot (X^6 - 6X^4(B'Y)^2 + X^2(B'Y)^4)}{4\pi B' \cdot (X^2 + (B'Y)^2)^3} + \frac{\zeta SB'' X(X^2 - Y^2)}{2\pi(X^2 + Y^2)^2}. \tag{5.129}$$

At the first order, the force-balance equation becomes

$$\begin{aligned} &\lim_{X\to 0, Y\to 0} \left(B'' \frac{\partial}{\partial X} + 2B' \frac{\partial^2}{\partial \bar{x} \partial X} + 2 \frac{\partial^2}{\partial \bar{x} \partial Y} \right) \left(\sigma_{12}^{\text{in}(2)}(\bar{x}, X, Y) - \Sigma_{12}^{\text{in}(2)}(\bar{x}, X, Y) \right) \\ &\quad + \lim_{X\to 0, Y\to 0} \left(B' \frac{\partial}{\partial X} + \frac{\partial}{\partial Y} \right)^2 \left(\sigma_{12}^{\text{in}(3)}(p_k, X, Y) - \Sigma_{12}^{\text{in}(3)}(p_k, X, Y) \right) + \phi = 0. \end{aligned} \tag{5.130}$$

Incorporating (5.122), (5.124), (5.128) and (5.129) into (5.130) gives an equation for the density:

$$\pi S B' B'' + \phi = 0. \tag{5.131}$$

This suggests that

$$\rho(\bar{x}) = \sqrt{\frac{2(C - \phi \bar{x})}{S}}, \tag{5.132}$$

where C is some constant to be determined.

5.4.5 Summary

To summarise, by using the multiple-scale technique, we are enabled to obtain an equation for the macroscopic density ρ of two types of equilibria: (5.102) for equilibrium Type II and (5.132) for a super small s. Although we cannot get an equation for ρ for a general problem of Type III due to the break down of periodicity in X, we may see from numerics later, that it is reasonable to estimate the density distribution by the equation (5.132) derived from the case of a super small s for the general problem of Type III.

5.5 Numerical Results

5.5.1 Numerical Scheme

Numerical tests are also conducted to compare with results from the multiple-scale analysis. We start with N pairs of dislocations within the interval $[L_1, L_2]$. The spacing between two glide planes is set to be s. Throughout the simulation, a system of algebraic equations for p_k and q_k satisfying

$$\sum_{i=0, i\neq k}^{N-1} \frac{1}{2\pi(p_k - p_i)} - \sum_{i=0}^{N-1} \frac{(p_k - q_i)((p_k - q_i)^2 - s^2)}{2\pi((p_k - q_i)^2 + s^2)^2} + \sigma_{\text{ext}} = 0 \tag{5.133}$$

and

$$-\sum_{i=0, i\neq k}^{N-1} \frac{1}{2\pi(q_k - q_i)} + \sum_{i=0}^{N-1} \frac{(q_k - p_i)((q_k - p_i)^2 - s^2)}{2\pi((q_k - p_i)^2 + s^2)^2} + \sigma_{\text{ext}} + \phi S = 0, \tag{5.134}$$

respectively, are iteratively solved for all integer k that $1 \leq k \leq N-1$. At each end, a pair of vertically aligned dislocation pair are locked, i.e. $p_0 = q_0 = L_1$ and $p_{N-1} = q_{N-1} = L_2$. The computation stops until the shear stress on each dislocation is less than a critical value σ_c.

5.5.2 Unstressed Dipolar Distribution

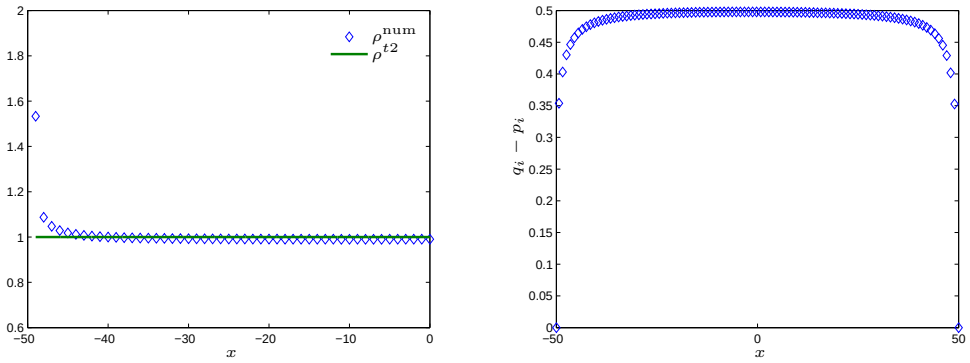
5.5.3 Equilibria of Type II

If we set $N = 101$, $s = 0.5$, $L_1 = -50$ and $L_2 = 50$, then we run the simulation until the net stress at every dislocation is less than $\sigma_c = 10^{-4}$. In Fig. 5.3, we compared the results from numerics with that the multiple-scale technique. Here, for simplification of notation, we use ρ^{num} to denote the density computed by numerics, i.e.

$$\rho^{\text{num}}(p_k) = \frac{1}{p_k - p_{k-1}}, \tag{5.135}$$

for all integer $k \in (1, N-1]$. ρ^{t2} and ρ^{t3} denote the density calculated from (5.102) of Type II and (5.132) of Type III, respectively.

From Fig. 5.3(a), we see that most dislocation pairs are uniformly distributed apart from those few near the lock. Near the lock, a boundary layer, where dislocation dipoles have to be treated discretely, should be considered. As in [60], in Fig. 5.3(b),



(a) density (b) local pattern

Figure 5.3: Comparison of unstressed dipole distribution of Type II between results from the multiple-scale method and numerics: (a) $\rho^{\mathrm{num}} = 1/(p_k - p_{k-1})$, while the green curve is the density predicted by the method using multiple scales, which suggests $\rho^{t2} = N/(L_2 - L_1)$. (b) The diamonds are the horizon spacing within dislocation pairs. their corresponding theoretical values by the method of multiple scales are all $1/2$. Throughout the simulation, $N = 101$, $s = 0.5$, $L_1 = -50$ and $L_2 = 50$.

the horizontal spacing within dislocation pairs is also drawn. For Equilibria Type II, the theoretical result is $1/2$. It can be seen that all dislocation pairs behave as predicted when away from two locks.

In Fig. 5.4, the dipolar arrangement from the above simulation is also depicted.

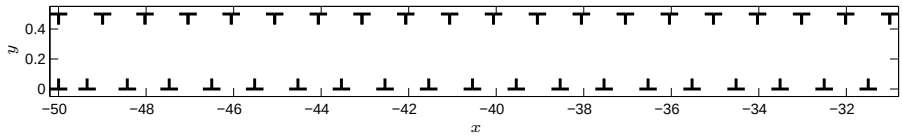
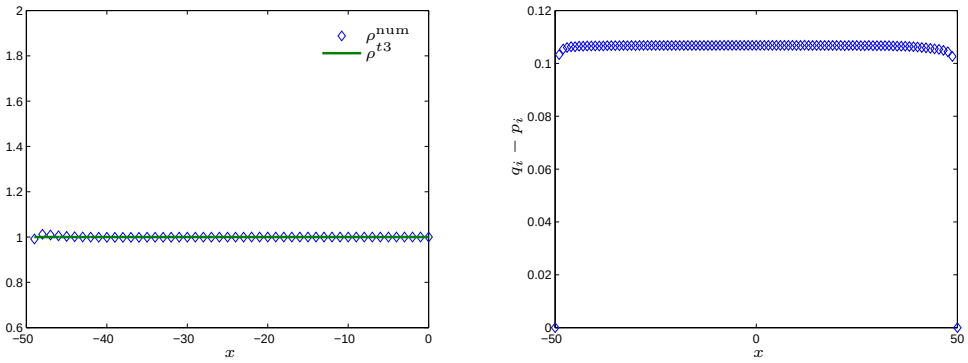


Figure 5.4: Dipolar arrangement of Type II: $N = 101$, $s = 0.5$.

Equilibria of Type III

If we narrow the gap between two slip planes to be $s = 0.1$ and start our simulation still with 101 pairs of dislocations within $(-50, 50)$, a numerical equilibrium of Type III is then obtained. Similarly as the case of Type II, we compare between numerical and theoretical results of the density ρ, as well as $q_i - p_i$ as shown in Fig. 5.5. It should be mentioned that from Fig. 5.5(b), away from the lock, $q_i - p_i$ is almost the same as $s = 0.1$. This suggests that they are 45° dipoles. The dipolar arrangement in this



(a) density (b) local pattern

Figure 5.5: Comparison between numerical and theoretical results of density as well as $q_i - p_i$ of Type III: $N = 101$, $s = 0.1$ $L_1 = -50$ and $L_2 = 50$.

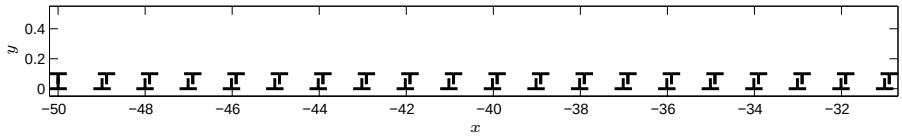


Figure 5.6: Dipole arrangement of Type III: $N = 101$, $s = 0.1$

case is also depicted in Fig. 5.6. It can be seen that every dislocation is attached one with the opposite sign to form dipoles, and they are observed uniformly distributed

By comparison, we conclude that the results from the method of multiple-scales, agree well with the numerical simulations for the case of unstressed dipole distribution.

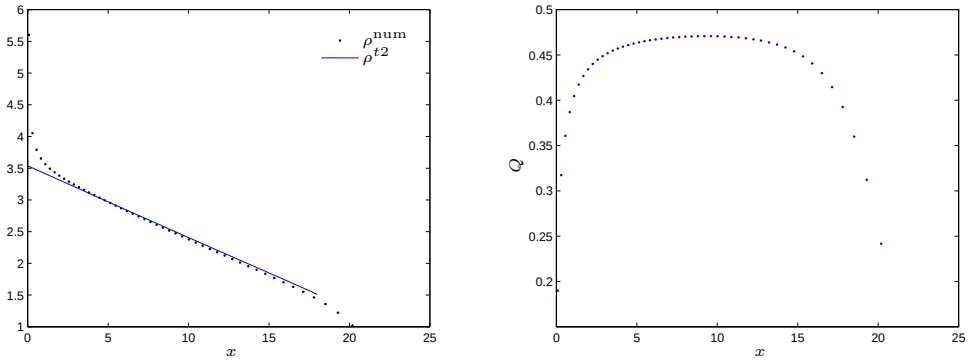
5.5.4 Pile-up of Dipoles Against Stress Gradient

Equilibria of Type II

Now we proceed to test the theoretical results with numerics for the case when there is applied stress gradient.

In this case, we start with 50 pair of dislocations within the interval $[0, 50]$. According to the theoretical results, when the separation s is big enough, there will only be equilibria of Type II. Here we choose $s = 0.5$ and the the stress gradient $\phi = 0.2$, which pushes all dipoles towards to $x = 0$. Thus in this case, we only need to fix the position of a pair of vertically aligned dislocations at $p_0 = q_0 = 0$. The programme will be stopped when $\sigma_c < 10^{-6}$.

In Fig. 5.7, the density distribution and the local pattern of this case are drawn. Again, the two results agree well away from the lock.

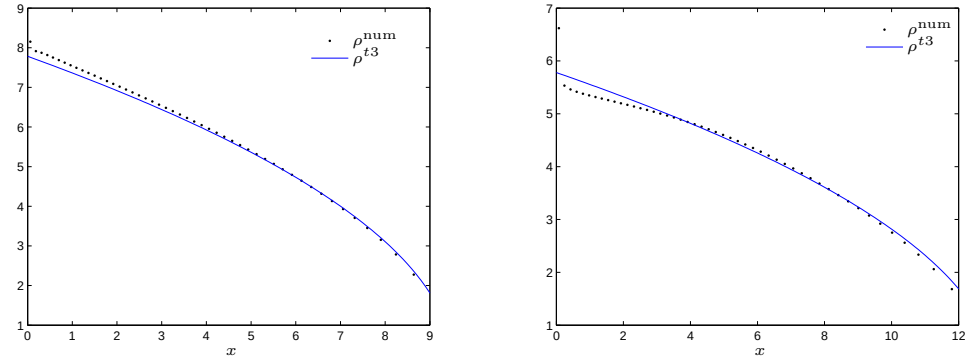


(a) density (b) local pattern

Figure 5.7: Dipole Pile-up Against Stress Gradient of Type II: $s = 0.2$, $\phi = 0.2$, N = 50.

Equilibria of Type III

Similarly, the numerical tests have also been conducted for Type III. In order to find the equilibria in this scenario, we need to use small s and the results are shown in Fig. 5.8 for $s = 0.02$ and 0.05.



(a) $s = 0.02$ (b) $s = 0.05$

Figure 5.8: Dipole Pile-up Against Stress Gradient of Type III: $\phi = 0.2$, N = 50.

Equilibria of Mixed Type

From above, we have numerically found two regimes of equilibria according to different value of s. Generally speaking, when the gap between slip planes is large, it is equilibrium of Type II. As the gap narrows, the system translates to Type III. Such fact qualitatively suggests that a bifurcation of equilibrium states exists and Type III is more stable than Type II.

To find the bifurcation point, we consider the expression for $Q^{(0)}$ in (5.67)

$$Q^{(0)} = \frac{1}{2\pi} \cos^{-1} \left(\cosh(2\pi\rho S) - 2\pi\rho S \sinh(2\pi\rho S) \right).$$

Since the cosine function cannot be less than -1, we require

$$\cosh(2\pi\rho S) - 2\pi\rho S \sinh(2\pi\rho S) \geq -1, \tag{5.136}$$

for the existence of Type III. This suggests the product of ρ and S must be less than some critical value, i.e.

$$\rho S \leq A, \tag{5.137}$$

where A can be obtained as 0.2456 by numerically solving (5.136) with the equal sign.

Therefore, we conclude that, when $\rho > A/S$, it is of Type II, otherwise, it is of Type III. For some s, such transition can be actually visualised as the dipole pile-up of mixed type. An example is shown in Fig. 5.9, when $s = 0.08$. From it, it can be seen that near the lock, it is of Type II. As ρ decreases such that (5.137) holds, the system shift to Type III. The horizontal dash-dot line is where $\rho s = 0.2456$. The results by the method of multiple scales agree well with numerics for both cases.

Thus although we did not give the equation describing the density for the full problem of Type III, by comparison with numerics, we find that the case when s is small in § 5.4.4 is a good alternative to the full problem.

5.6 Analysis of Uniformly Distributed Dipoles

In previous sections, we managed to obtain equations for the density for a row of dipoles. However, more analysis is needed to explain their properties, such as the transition between different types of equilibria. The main difficulty for the analysis here lies in the complexity in the expression for ρ.

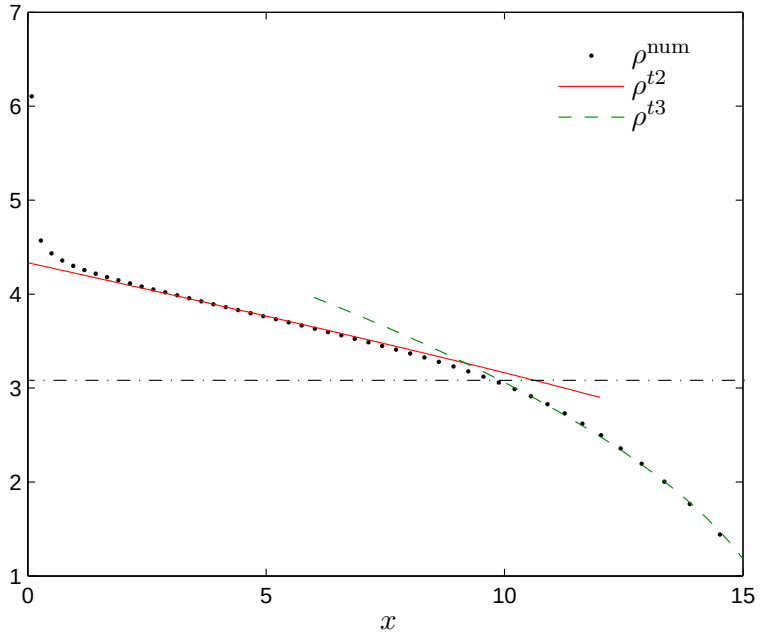


Figure 5.9: Dipole pile-up against stress gradient of mixed type: near the lock, it is of Type II. As ρ decreases such that (5.137) holds, the system shift to Type III. The horizontal dash-dot line is where $\rho s = 0.2456$. Here $S = 0.08$ and $\phi = 0.2$.

In the end of this chapter, we will spend some pages on the analysis of the simplest case: uniformly distributed dipoles, which will provides some guides for the dipole distributions throughout the two-dimensional space in the next chapter.

From the above discussion, we know that without an applied stress gradient, dislocation dipoles are periodically distributed. By revisiting the equation for $Q^{(0)}$ in (5.66), we find that in this case ρ, Q and S satisfy

$$\frac{\sin(2\pi Q)}{2(\cosh(2\pi\rho S) - \cos(2\pi Q^{(0)}))} - \frac{\pi\rho S \sin(2\pi Q)\sinh(2\pi\rho S)}{(\cosh(2\pi\rho S) - \cos(2\pi Q))^2} + \sigma_{\text{ext}} = 0. \qquad (5.138)$$

If the number of dislocations and the length of the interval are known, we can work out ρ as an external coefficient. Therefore, we are enabled to find all equilibrium states, i.e. (Q, S) for any given ρ and σ_{ext}. The results are compiled in Fig. 5.10. When $\rho = 1$, the solid curves are sets of (Q, S) such that the system is in equilibrium under an external stress σ_{ext}, which are correspondingly indicated on the curve. The diamonds denote (Q, S) for some specific numerically calculated equilibrium states of the full problem under $\sigma_{12}^{\text{ext}} = 0.1$ or 0.01. It can be seen that all diamonds lie almost on top of their corresponding equilibrium contours. Also we can see that for

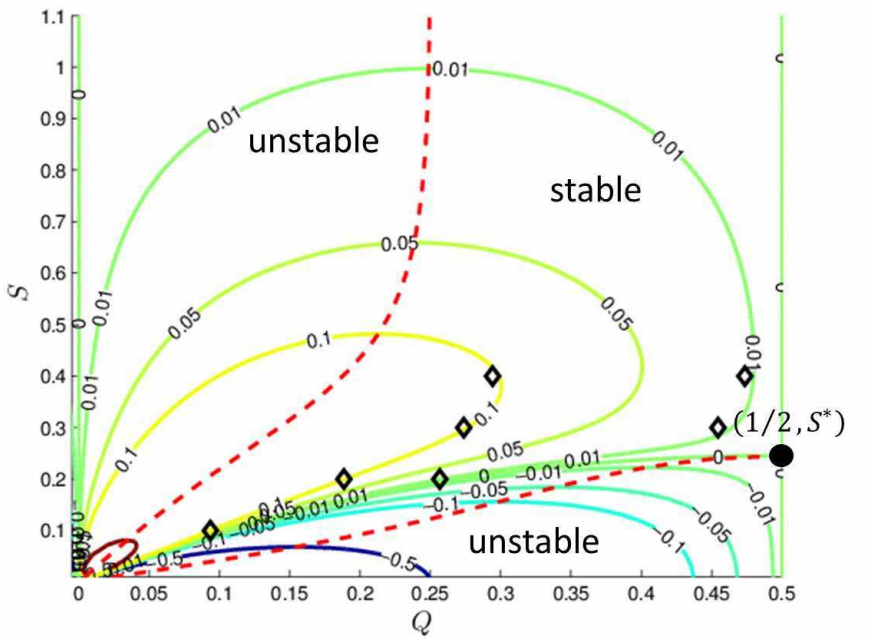


Figure 5.10: Uniformly distributed dipoles: the solid curves are sets of (Q, S) such that the system is in equilibrium under an external stress σ_{ext}, which are correspondingly indicated on the curve. The diamonds denote (Q, S) for some specific equilibrium states. We can also see that for a given σ_{ext}, there exists a maximum S_c, such that all $S \leq S_c$. Finally, the two dashed curves are the boundaries between stable and unstable regions. Here ρ is set to be 1.

a given σ_{ext}, there exists a maximum S_c, such that all $S \leq S_c$. In Fig. 5.10, this S_c is attained at the top of each contour characterised by σ_{ext}. Mathematically, (Q_c, S_c) can be found by taking derivatives with respect to Q on both sides of (5.138), then letting $\mathrm{d}S/\mathrm{d}Q$ vanish. Physically, S_c is the minimum separation between slip planes for σ_{ext} to break dipoles. In Fig. 5.11, S_c is plotted against σ_{ext} for different densities. If we connect all possible (Q_c, S_c) by dashed curves as in Fig. 5.10, we find that all equilibrium states obtained by numerics lie between the two curves.

From Fig. 5.10, it can also be seen that increasing σ_{ext} decreases S_c such that $S > S_c$. In this case, σ_{ext} will break the dislocation dipoles, giving rise to pile-ups of monopoles at both ends as shown in Fig. 5.12. It can be observed that these monopoles will exert a stress field to counter σ_{ext}, such that dislocations in the middle will recombine to form new dipoles.

As a special case, when there is no applied stress, we can see the three types of equilibria from Fig. 5.10: $Q = 0$, $1/2$ or $Q(S)$, respectively. When $Q = 0$, it is in the unstable region, so Type I is always unstable. When $Q = 1/2$, it can be observed that

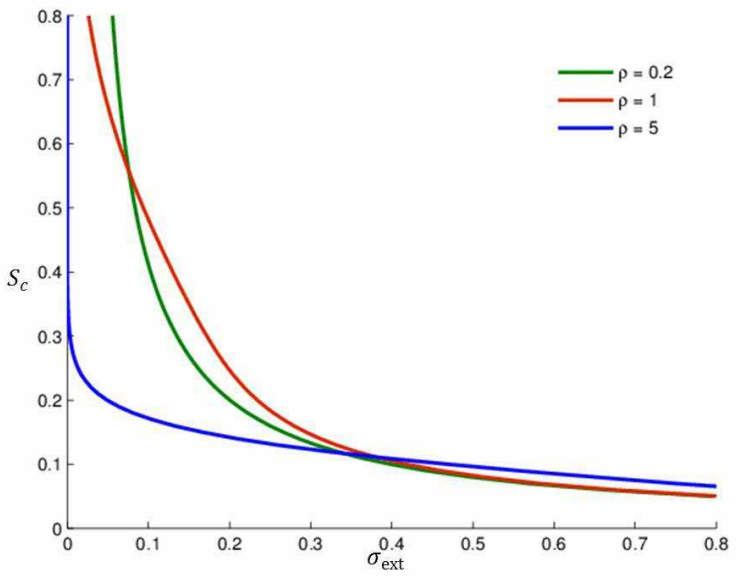


Figure 5.11: The maximum spacing S_c to retain dipoles under σ_{ext}.

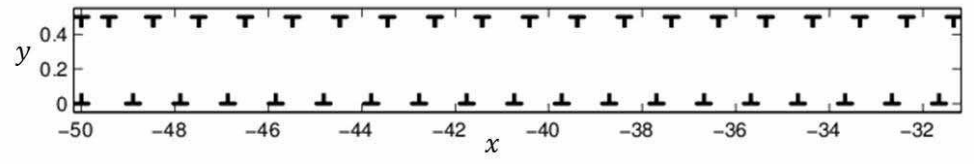


Figure 5.12: When the external stress σ_{ext} is too large, the dislocations will recombine to form new dipoles, giving rise to the pile-ups of monopoles at both ends. Here in the simulation, $S = 0.4$ and $\sigma_{\text{ext}} = 0.4$.

the system is stable only if the gap between slip planes S is greater than some critical value S^* indicated in Fig. 5.10. If $S < S^*$, the third type of equilibrium occurs as the only stable configuration. Therefore, the row of dipoles undergo a natural transition in types of equilibria as S goes across S^* to attain a stable configuration. As we will see in the next chapter, such transition also exists for two-dimensional periodic lattices, which is crucial to explaining the transition from veins to PSBs in the early stage of fatigue tests. From numerics, $S^* = 0.2445$.

5.7 Conclusion

In this chapter, we generalised the method of multiple scales developped in Chapter 4 to investigate the homogenisation of a row of dislocation dipoles. Two regimes of equilibria have been found, and an equation for densities in each case was derived. A

comparison with numerics validates our theoretical results. In the end of this chapter, a row of uniformly distributed dipoles is also discussed.

As from the beginning of this chapter, dislocation dipoles can be considered equivalent to vacancy or interstitial loops. Thus an investigation of the collective behaviours throughout the two-dimensional space can be realistically important, in this scenario, the formation of PSBs. In the next chapter, we will generalise the idea implemented to uniformly distributed dipoles to the examination of dipoles in two-dimensional space, and give our explanation of the transition from veins to PSBs.

Chapter 6

Two-Dimensional Dipole Patterns and Stability Analysis

6.1 Introduction

In the last two chapters, the collective behaviour of a row of dislocation monopoles or dipoles were studied by the multiple-scale technique. In theory, this technique can be generalised to investigate two-dimensional dipole arrays. Practically, such generalisation, however, can not be easily achieved, since it requires far more complicated calculations than that of the one-dimensional case, which has already shown to be troublesome in Chapter 4 and 5. However, because of the important role two dimensional dipole arrays play in veins or PSBs, we still need to find some approaches to analyse them.

In this chapter, as an initial attempt for finding the collective behaviour of dipoles in two-dimensional space, we study the 2D rectangular lattice, where edge dipoles are uniformly distributed in rectangular cells. Recalling from Chapter 5, under a constant stress, the leading order of the density ρ is constant when the system is in equilibrium. From this point of view, uniform lattices can be regarded as a good resemblance to actual configurations inside materials.

The rectangular lattice we study here is shown schematically in Fig. 6.1. X-Y space is divided into identical rectangular cells in each of which there is a dipole pair with a Burgers vector $\boldsymbol{b} = (b, 0)^T$. Here every rectangle is of size $\alpha \times \beta$, and the mutual horizontal and vertical separation within each dislocation pair are defined to be Q

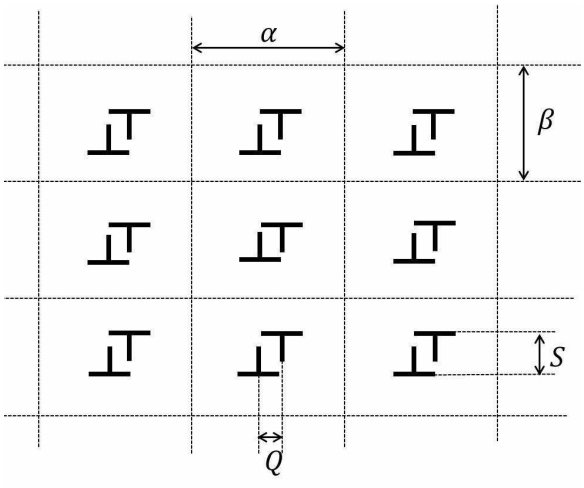


Figure 6.1: Rectangular Lattice: the infinite region is divided by identical rectangle of size $\alpha \times \beta$. In each lattice, there two dislocations of opposite signs. Their mutual horizontal and vertical spacing are set to be Q and S, respectively.

and S, respectively. Without loss of generality, we set

$$0 \leq Q \leq \alpha/2$$

and

$$0 < S \leq \beta/2.$$

Such a configuration guarantees the periodicity of cells in both X and Y directions, with periods α and β, respectively. Therefore, the evaluation of the stress components can be confined to one particular cell.

This chapter is arranged as follows. The study of the simplest case, where each cell is a unit square, will first be presented, followed by the investigation of the distribution of dipoles in any rectangular lattice. Based on results from a linear stability analysis of the lattice, an interpretation of the mechanism of the formation of PSBs will be given. Finally, a comparison with experimental results will be made.

6.2 Unit Square Lattice

To start with the simplest case, we consider dipoles in unit square lattices, where α and β are both set to be 1. Suppose all positive dislocations are located at (n, k), then their negative counterparts are at $(Q+n, S+k)$, where $n, k \in \mathbb{Z}$. Thus the total shear

stress component exerted by all dislocations at (X, Y), denoted by $\sigma_{12}^t(X, Y)$ can be expressed as superpositions of the stress component from every single dislocation:

$$\begin{aligned}\sigma_{12}^t(X,Y) = &\frac{1}{2\pi}\sum_{n,k\in\mathbb{Z}}\frac{(X-n)((X-n)^2-(Y-k)^2)}{((X-n)^2+(Y-k)^2)^2}\\ &-\frac{1}{2\pi}\sum_{n,k\in\mathbb{Z}}\frac{(X-n-Q)((X-n-Q)^2-(Y-k-S)^2)}{((X-n-Q)^2+(Y-k-S)^2)^2},\end{aligned} \tag{6.1}$$

where similarly as in Chapter 4 and 5, σ_{12}^t has been rescaled by $\mu b/(1-\nu)$.

6.2.1 Equilibria

Force-Balance Equations

When the system is in equilibrium, the net shear stress component σ_{12} from all other dislocations should vanish, giving rise to two force balance equations:

$$\lim_{(X,Y)\to(0,0)}\left(\sigma_{12}^t(X,Y)-\frac{X(X^2-Y^2)}{2\pi(X^2+Y^2)^2}\right)=0 \tag{6.2}$$

and

$$\lim_{(X,Y)\to(Q,S)}\left(\sigma_{12}^t(X,Y)-\frac{(X-Q)((X-Q)^2-(Y-S)^2)}{2\pi((X-Q)^2+(Y-S)^2)^2}\right)=0. \tag{6.3}$$

Then for any given S, we are looking for Q such that the force balance equations above hold.

Incorporating (6.2) or (6.3) with (6.1) gives a same equation for Q and S:

$$\frac{1}{2\pi}\sum_{n\neq 0}\sum_{k\in\mathbb{Z}}\frac{n(n^2-k^2)}{(n^2+k^2)^2}-\frac{1}{2\pi}\sum_{n,k\in\mathbb{Z}}\frac{(n-Q)((n-Q)^2-(k-S)^2)}{((n-Q)^2+(k-S)^2)^2}=0. \tag{6.4}$$

If we put the convergence aside, the first series in (6.4) vanishes due to the symmetry in n. Physically this suggests that the shear stress by a dislocation at (n, k) on one at $(0, 0)$ cancels exactly with a dislocation of the same sign at $(-n, k)$. By this mean, (6.4) can be reduced to

$$\sum_{n,k\in\mathbb{Z}}\frac{(Q-n)((Q-n)^2-(S-m)^2)}{((Q-n)^2+(S-m)^2)^2}=0, \tag{6.5}$$

where Q is the unknown for any given S. Once (Q, S) is computed, the local pattern of dipoles can be predicted.

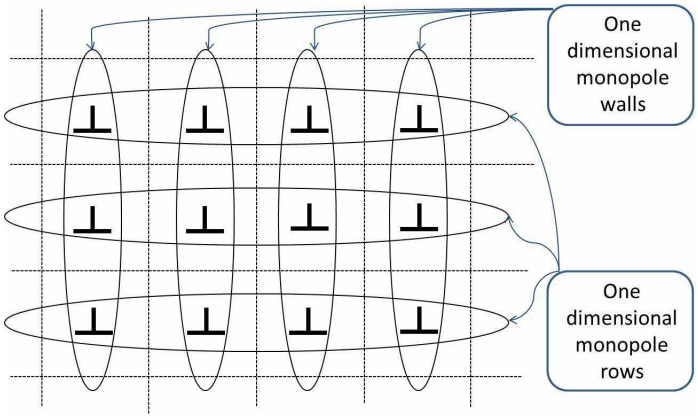


Figure 6.2: Two dimensional monopoles: solving (6.7) is equivalent to finding the zero contour of $\sigma_{12}^{+}(X,Y)$ defined in (6.6). There are two ways to estimate $\sigma_{12}^{+}(X,Y)$. One way is to treat these monopoles as a collection of one-dimensional walls, then σ_{12}^{+} can be estimated as a sum of shear stress by these walls. The other way, vice versa, is to estimate σ_{12}^{+} by a sum of stress component by monopole rows.

Stress by Monopoles in Periodic Lattices

Instead of solving (6.5) directly, we turn to considering the implication from its left hand side. If we consider infinite number of monopoles in periodic lattice as shown in Fig. 6.2, the total shear stress by these positive monopoles can be written by

$$\sigma_{12}^{+}(X,Y) \sim \frac{1}{2\pi} \sum_{n,k\in\mathbb{Z}} \frac{(X-n)((X-n)^2-(Y-k)^2)}{((X-n)^2+(Y-k)^2)^2}. \tag{6.6}$$

A comparison between (6.6) and (6.5) implies finding (Q,S) from (6.5) is equivalent to finding the zero contour of $\sigma_{12}^{+}(X,Y)$.

There are two ways to estimate $\sigma_{12}^{+}(X,Y)$. One way is to treat these monopoles as a collection of one-dimensional walls as shown in Fig. 6.2, then σ_{12}^{+} can be estimated as a sum of shear stress by these walls. The other way is to estimate σ_{12}^{+} by an infinite sum of stress component by monopole rows as diagrammed in Fig 6.2. The two approaches will not make a big difference in this case. But as we will see in the next section, the accuracy of the estimation does depend on the choice of approach.

Here, we use the latter approach mentioned above by treating monopoles as a sum of monopole rows. Then the k-th row can be regarded as one dimensional monopoles discussed in Chapter 4. By replacing Y and B' in (4.111) by $Y-k$ and 1, respectively,

we have

$$\sigma_{12}^{x}(X,Y;k)=\frac{\sin(2\pi X)}{2(\cosh(2\pi(Y-k))-\cos(2\pi X))}-\frac{\pi(Y-k)\sin(2\pi X)\sinh(2\pi(Y-k))}{(\cosh(2\pi(Y-k))-\cos(2\pi X))^{2}}, \tag{6.7}$$

where $\sigma_{12}^{x}(X,Y;k)$ denotes the shear stress component by all dislocations in the k-th glide plane. Then (6.6) becomes

$$\sigma_{12}^{+}(X,Y)\sim\sum_{k\in\mathbb{Z}}\sigma_{12}^{x}(X,Y;k).$$

It can be observed that $\sigma_{12}^{x}(X,Y;k)$ decays exponentially with k. From §A.11, we know that

$$\left|\sigma_{12}^{+}(X,Y)-\sum_{k=-k_0}^{k_0}\sigma_{12}^{x}(X,Y;k)\right|<\frac{e^{-\pi k_0}(k_0+5)}{(1-e^{-\pi})^{2}}. \tag{6.8}$$

From (6.8), it can be seen that the truncation error also decays exponentially with k_0 increasing.

It can be checked that when $k_0=4$, the difference between σ_{12}^{+} and $\sum_{k=-k_0}^{k_0}\sigma_{12}^{x}(X,Y;k)$ is already less than 10^{-5}. Thus it is sensible to approximate σ_{12}^{+} by

$$\sigma_{12}^{x}(X,Y)=\sum_{k=-4}^{4}\sigma_{12}^{x}(X,Y;k). \tag{6.9}$$

Alternatively, σ_{12}^{+} can also be estimated by summing dislocation walls. By using the DiGamma function, the shear stress component of the n-th wall can be calculated by

$$\sigma_{12}^{y}(X,Y;n)=-\frac{\pi(X-n)(1-\cosh(2\pi(X-n))\cos(2\pi Y))}{(\cosh(2\pi(X-n))-\cos(2\pi Y))^{2}}. \tag{6.10}$$

This suggests that σ_{12}^{+} can also be approximated by

$$\sigma_{12}^{+}(X,Y)\approx\sum_{n=-4}^{4}\sigma_{12}^{y}(X,Y;n)=-\pi\sum_{n=-4}^{4}\left(\frac{(X-n)(1-\cosh(2\pi(X-n))\cos(2\pi Y))}{(\cosh(2\pi(X-n))-\cos(2\pi Y))^{2}}\right). \tag{6.11}$$

Types of Equilibria

As the approximation of σ_{12}^{+} is obtained, we are looking for its zero contour to find Q and S. Mathematically, this requires that (Q,S) satisfy $\{(Q,S)|\sigma_{12}^{x}(Q,S)=0\}$. Although we are still unable to explicitly calculate Q and S, we can use numerics to find the zero contour of σ_{12}^{x} in (6.9) as shown in Fig. 6.3.

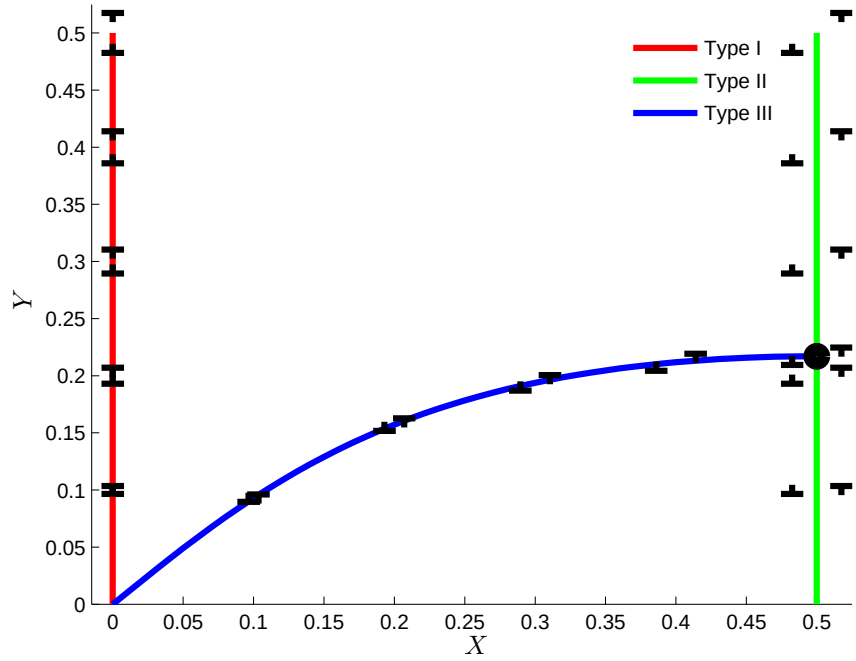
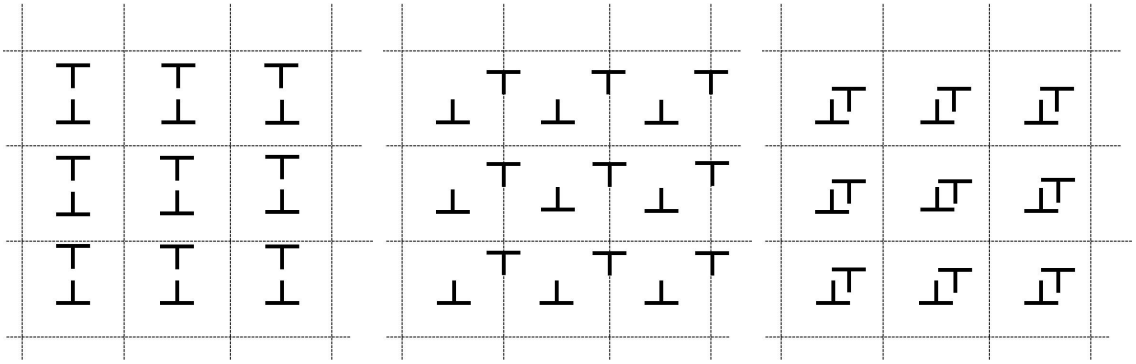


Figure 6.3: Zero contour of σ_{12}^{+}: three types of equilibrium can be spotted. Type I and II correspond to the cases when Q is 0 and 1/2, respectively. These two types of equilibria exist regardless the value of S; Type III exists only when the mutual spacing between glide planes of dipoles is less than a critical value S^*, marked as the black dot. In this case, $S^* = 0.2170$. Also, the lattice patterns of some equilibrium states are sketched on top of their corresponding (Q, S).

It can be seen that the same as in the case of one dimensional array of monopoles, there exist three types of equilibria. When Q is 0 or 1/2, regardless the value of S, the system is always in equilibrium. However, if S is less than some critical value S^*, which corresponds to the black dot in Fig. 6.3, there exists another type of equilibria. In the case of unit lattices, $S^* = 0.2170$. For a better understanding of what this contour means, the dipolar pattern for particular equilibrium states are also drawn on top of their corresponding (Q, S).

To summerise, by finding the zero contour of σ_{12}^{+}, we obtain three types of lattice pattern in equilibrium. As sketched in Fig. 6.4, they are

- Type I: $Q = 0$, one is aligned with its opposite counterpart;
- Type II: $Q = 1/2$, one lies halfway between its two opposite neighbours;
- Type III: $S < S^*$, one is coupled with its opposite counterpart.



(a) Type I (b) Type II (c) Type III

Figure 6.4: Equilibrium pattern in two-dimensional unit lattice.

6.2.2 Stability Analysis

The next question is whether these three types of equilibria are stable or not. To answer this question, we apply the stability analysis to the equilibrium states obtained above by examining the restoring force of dislocations after being perturbed. The idea of the stability analysis here can be illustrated by referring to Fig. 6.5.

In Fig. 6.5, a set of periodically distributed positive monopoles exert a stress field such that $\sigma_{12}^{+}(X,Y) > 0$ in the green regions and $\sigma_{12}^{+}(X,Y) < 0$ in the white regions. To find equilibrium state, we simply need to put a set of periodically distributed negative monopoles at positions where $\sigma_{12}^{+}(X,Y) = 0$. Correspondingly in Fig. 6.5, they are the boundaries that separate a green and a white region.

To find the stability, we give these force-free negative monopoles a small displacement δX, then see how they respond to this perturbation. If they go back to their original equilibrium positions, the configuration is stable, otherwise not. From the Peach-Koelher force defined in (1.13), the horizontal force a negative dislocation at (X,Y) feels is $-\sigma_{12}^{+}(X,Y)$. Therefore, when dropped in a green region, these negative monopoles will be pushed to the left and otherwise to the right. From this angle, only equilibrium states that correspond to boundaries with white region on the left in Fig. 6.5 are stable.

Then a comparison between Fig. 6.3 and 6.5 suggests that Type I is always unstable; Type II is stable when $S > S^{*}$; Type III is always stable.

Mathematically, this restoring force can be found by the variational method. It can

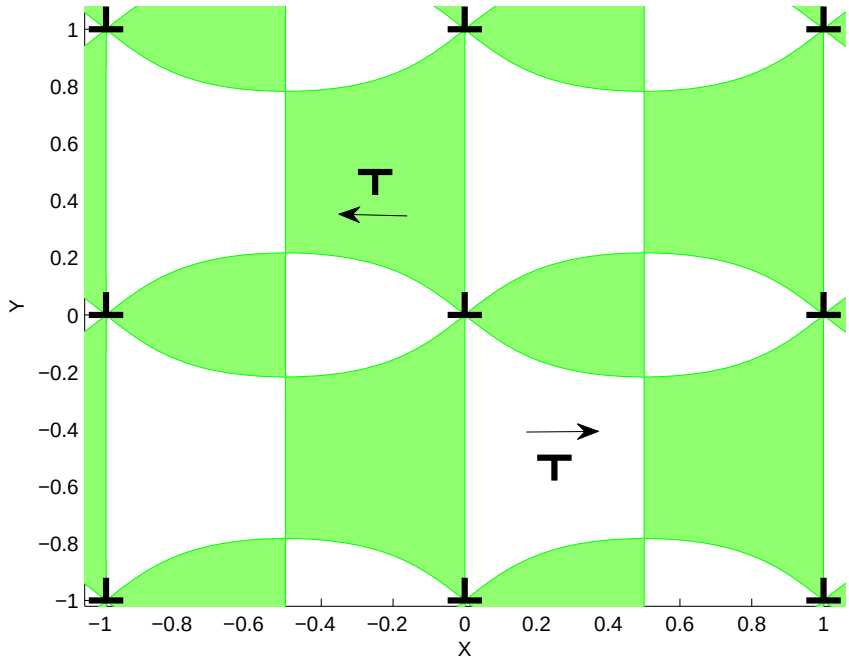


Figure 6.5: Idea of the stability analysis to equilibrium states: A set of periodically distributed positive monopoles exert a stress field such that $\sigma_{12}^{+}(X,Y) > 0$ in the green regions and $\sigma_{12}^{+}(X,Y) < 0$ in the white regions. The equilibrium states correspond to the boundaries that separate a green and a white region. A negative dislocation in this system will be pushed to the left in green regions and to the right in white regions This suggests that only equilibrium states that correspond to boundaries with white region on the left are stable.

be calculated that

$$-\sigma_{12}^{+}(Q+\delta X, S) \sim f_r(Q,S)\cdot\delta X + \mathcal{O}(\delta^2), \tag{6.12}$$

where

$$f_r(Q,S) = -\left.\frac{\mathrm{d}\sigma_{12}^{+}(X,S)}{\mathrm{d}X}\right|_{X=Q}. \tag{6.13}$$

If $f_r(Q,S) < 0$, the restoring force is always pushing the dislocation back to its equilibrium state. In another word, the equilibrium state is stable if and only if $f_r(Q,S) < 0$. Actually, the value of $f_r(Q,S)$ can be considered as a metric of the stability of the system. The stronger a negative $f_r(Q,S)$ is, the more stable the system is.

From (6.9), we obtain

$$
\begin{aligned}
f_r(Q,S) &= -\left.\frac{\partial \sigma_{12}^{+}(X,S)}{\partial X}\right|_{X=Q} = -\sum_{k=-4}^{4}\left.\frac{\partial \sigma_{12}^{x}(X,S;k)}{\partial X}\right|_{X=Q} \\
&= \sum_{k=-4}^{4}\left(\frac{\pi(1-\cosh(2\pi(S-k))\cos(2\pi Q))}{(\cosh(2\pi(S-k))-\cos(2\pi Q))^2} + \frac{2\pi^2(S-k)\cos(2\pi Q)\sinh(2\pi(S-k))}{(\cosh(2\pi(S-k))-\cos(2\pi Q))^2}\right) \\
&\quad - \sum_{k=-4}^{4}\frac{4\pi^2(S-k)\sin^2(2\pi Q)\sinh(2\pi(S-k))}{(\cosh(2\pi(S-k))-\cos(2\pi Q))^3}.
\end{aligned}
\tag{6.14}
$$

For a given equilibrium type, Q is either a constant (Type I and II) or a function of S. Thus we can write $f_r(Q,S)$ as a function of S under all cases by $f_r(0,S)$, $f_r(1/2,S)$ or $f_r(Q(S),S)$. In Fig. 6.6, how f_r depends on S are plotted for all the three types. The messages conveyed from Fig. 6.6 are listed below, which are consistent with

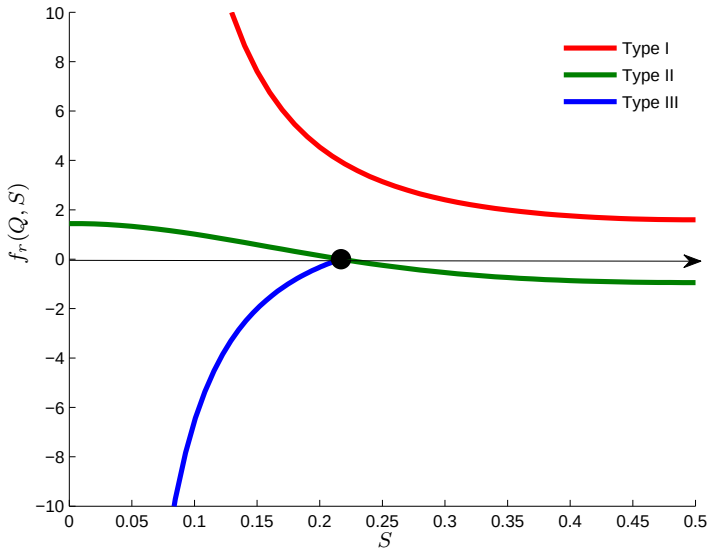


Figure 6.6: Stabilities for the equilibria in unit lattices: for Type I, it is always unstable. For Type II, it is conditionally stable. The most stable configuration of this type arises when $S = 0.5$. When $S < S^*$(the black dot), Type III occurs. In this case, a dislocation will be coupled with one of its neighbouring opposite counterpart to form a pair of dipole. Another key observation can be made from Fig. 6.6 is that for any given S, there exists only one stable state. When $S > S^*$, it is of Type II; when $S < S^*$, the stable system bifurcates to Type III.

our qualitative analysis above: The equilibrium of Type I is always unstable. The equilibrium of Type II is conditionally stable. The most stable configuration of this

type arises when $S = 0.5$. In this case, dislocations form the infinite Taylor lattice discussed in [43], which has a similar appearance as in Fig. 6.4(b). The shear stress field of Taylor lattice in one cell is drawn in Fig. 6.7(a). When $S < S^*$, Type III occurs. In this case, a dislocation will be coupled with its neighbouring opposite counterpart to form a pair of dipole. If we plot the shear stress field in a cell for Type III, we will see that the stress field is more localised compared to Type II, as shown in Fig. 6.7(b). Another key observation can be made from Fig. 6.6 is that for any given S, there exists only one stable state. When $S > S^*$, it is of Type II; when $S < S^*$, the stable state bifurcates to Type III.

Summary

The equilibrium states obtained above have great similarities to dipoles in veins or PSBs. In veins as depicted in Fig. 1.13, these dipoles spread and may behave like the Taylor lattices. In PSB walls depicted in Fig. 1.14, dipoles are more localised and may behave like equilibria of Type III. From this point of view, the transition from veins to PSBs may be interpreted as the result of the geometrical instability.

6.3 Rectangular Lattices

The analysis of dipoles in unit square lattices can be generalised to investigate dipoles in rectangular lattices. As shown in Fig. 6.1, in this scenario, each cell now becomes a rectangle of $\alpha \times \beta$, with positive and negative dislocations situated at $(\alpha n, \beta k)$ and $(Q + \alpha n, S + \beta k)$, respectively, for all n, $k \in \mathbb{Z}$. Thus the dislocation density satisfies

$$\rho \propto \frac{1}{\alpha\beta}. \tag{6.15}$$

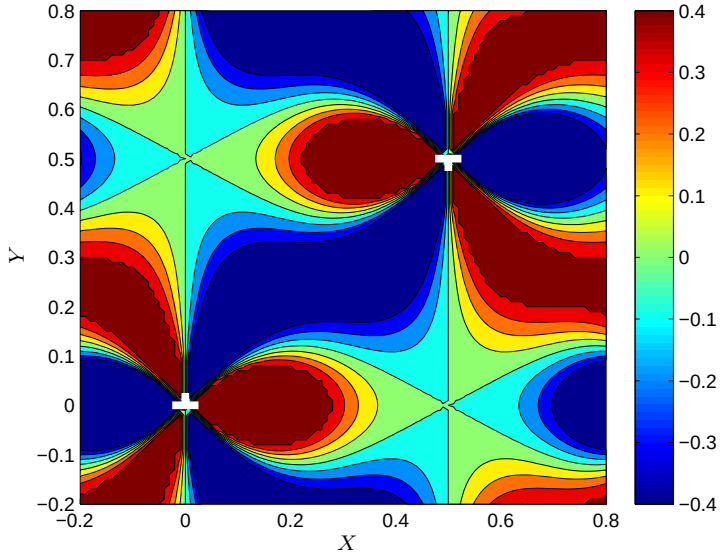
The total shear stress σ_{12}^t by all dislocations becomes

$$\sigma_{12}^t(X, Y; \alpha, \beta) = \sigma_{12}^+(X, Y; \alpha; \beta) - \sigma_{12}^+(X - Q, Y - S; \alpha; \beta), \tag{6.16}$$

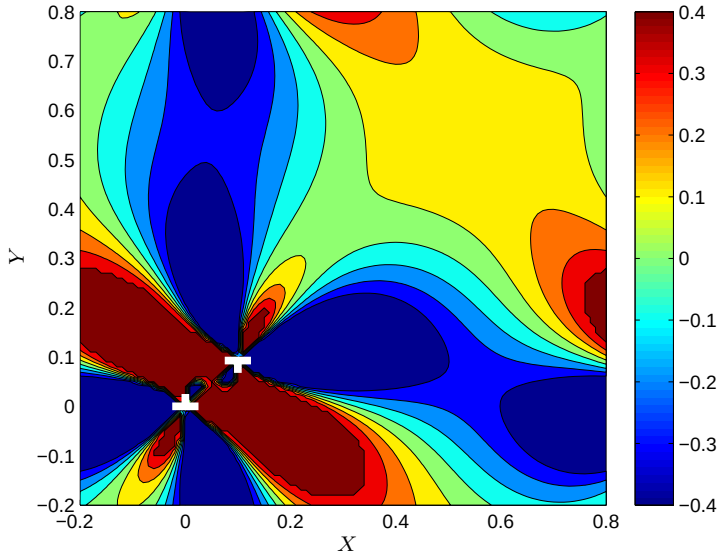
where

$$\sigma_{12}^+(X, Y; \alpha, \beta) = \sum_{n,k\in\mathbb{Z}} \frac{(X - \alpha n)((X - \alpha n)^2 - (Y - \beta k)^2)}{((X - \alpha n)^2 + (Y - \beta k)^2)^2} \tag{6.17}$$

and $0 \leq Q < \alpha$ and $0 < S < \beta$.



(a) Type II



(b) Type III

Figure 6.7: Shear stress field by two dimensional dipoles in one cell: in the first plot, the stress is exerted by the Taylor Lattice of equilibrium Type II, where two dislocations are at $(0, 0)$ and $(1/2, 1/2)$, respectively; in the second plot, the dislocations are located at $(0, 0)$ and $(0.1, 0.1)$. The shear stress is localised between two dislocations, which gives rise to a stress free region away from the dipole.

6.3.1 Equilibria

Analogously to the case of unit lattice, we are looking for Q and S, such that (6.16) vanishes. Since in periodic rectangular lattices, a dislocation cannot feel the net force

by all other dislocations with the same sign due to symmetry. Thus searching for (Q, S) is equivalent to finding the zero contour of $\sigma_{12}^{+}(X, Y; \alpha, \beta)$ in the X-Y plane.

Before doing any calculation, we firstly define $\hat{X} = X/\alpha$ and $\hat{Y} = Y/\beta$. Thus both $\hat{X}$ and $\hat{Y}$ have the period of 1.

To approximate $\sigma_{12}^{+}(X, Y; \alpha, \beta)$, we have two approaches.: to sum firstly over n then truncate by k or the other way round. It was mentioned in the case of the unit lattice that the two methods should give similar estimations to σ_{12}^{+}. Whereas in rectangular lattices, as we will see later, they have different convergent rates.

If we use the former approach, we can rewrite σ_{12}^{+} in (6.17) by

$$\sigma_{12}^{+} \sim \frac{1}{\alpha} \sum_{n,k\in\mathbb{Z}} \frac{\left(\hat{X}-n\right)\left(\left(\hat{X}-n\right)^2 - \left(\frac{\hat{Y}-k}{\lambda}\right)^2\right)}{\left(\left(\hat{X}-n\right)^2 + \left(\frac{\hat{Y}-k}{\lambda}\right)^2\right)^2}, \tag{6.18}$$

where λ is defined to be the edge ratio:

$$\lambda = \frac{\alpha}{\beta}. \tag{6.19}$$

A comparison of (6.18) with (6.6) suggests that $\sigma_{12}^{+}(X, Y; \alpha, \beta)$ can be approximated by

$$\sigma_{12}^{+} \approx \hat{\sigma}_{12}^{x}(\hat{X}, \hat{Y}; \alpha, \lambda) = \sum_{k=-4}^{4} \hat{\sigma}_{12}^{x}(\hat{X}, \hat{Y}; \alpha, \lambda; k), \tag{6.20}$$

where

$$\begin{aligned}\hat{\sigma}_{12}^{x}(\hat{X}, \hat{Y}; \alpha, \lambda; k) \triangleq \frac{1}{\alpha}\sin\left(2\pi\hat{X}\right) \times \\ \frac{\lambda\left(\cosh\left(\frac{2\pi(\hat{Y}-k)}{\lambda}\right) - \cos\left(2\pi\hat{X}\right)\right) - 2\pi(\hat{Y}-k)\sinh\left(\frac{2\pi(\hat{Y}-k)}{\lambda}\right)}{2\lambda\left(\cosh\left(\frac{2\pi(\hat{Y}-k)}{\lambda}\right) - \cos\left(2\pi\hat{X}\right)\right)^2}.\end{aligned} \tag{6.21}$$

It should be noted that $\hat{\sigma}_{12}^{x}(\hat{X}, \hat{Y}; \alpha, \lambda; k)$ still decays exponentially with k. Nevertheless, a large λ may dramatically weaken the rate of the decay, resulting in a big truncating error. To avoid this, we can estimate σ_{12}^{+} by firstly summing over k then truncate over n. In this scenario, we can rewrite σ_{12}^{+} by

$$\sigma_{12}^{+} \sim \frac{1}{\beta} \sum_{n,k\in\mathbb{Z}} \frac{\lambda\left(\hat{X}-n\right)\left(\lambda^2\left(\hat{X}-n\right)^2 - \left(\hat{Y}-k\right)^2\right)}{\left(\lambda^2\left(\hat{X}-n\right)^2 + \left(\hat{Y}-k\right)^2\right)^2}. \tag{6.22}$$

By replacing $X - n$ in (6.11) by $\lambda\left(\hat{X} - n\right)$, we obtain another estimation to σ_{12}^{+} by

$$\sigma_{12}^{+}(X, Y; \alpha, \beta) \approx \hat{\sigma}_{12}^{y}(\hat{X}, \hat{Y}; \beta, \lambda) = \sum_{n=-4}^{4} \hat{\sigma}_{12}^{y}(\hat{X}, \hat{Y}; \beta, \lambda; n), \tag{6.23}$$

where

$$\hat{\sigma}_{12}^{y}(\hat{X}, \hat{Y}; \beta, \lambda; n) \triangleq -\frac{\pi\lambda^2(\hat{X} - n)(1 - \cosh(2\pi\lambda(\hat{X} - n))\cos(2\pi\hat{Y}))}{\beta(\cosh(2\pi\lambda(\hat{X} - n)) - \cos(2\pi\hat{Y}))^2}. \tag{6.24}$$

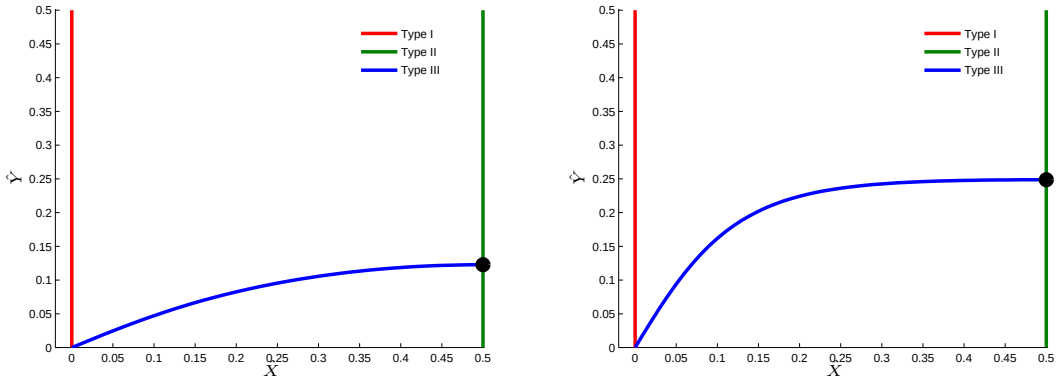
In this case, a large λ may accelerate the convergent rate if we use (6.23).

Therefore, we can approximate a new $\sigma_{12}^{+}(X, Y; \alpha, \beta)$ by

$$\sigma_{12}^{+}(X, Y, \alpha, \beta) = \begin{cases} \hat{\sigma}_{12}^{x}(X/\alpha, Y/\beta, \alpha, \lambda), & \lambda \leq 1; \\ \hat{\sigma}_{12}^{y}(X/\alpha, Y/\beta, \beta, \lambda), & \lambda > 1. \end{cases} \tag{6.25}$$

Practically, a large λ corresponds to the situation when the horizontal spacing is greater than vertical spacing. Thus it is sensible to treat the configuration as the sum of monopole walls, i.e. mathematically, sum first over k then truncate over n.

It can be observed from (6.18) and (6.22) that the zero-contour of σ_{12}^{+} in $\hat{X}$-$\hat{Y}$ space only depends on the value of λ. Thus we look for $(\hat{Q}, \hat{S})$ from the zero contour of $\hat{\sigma}_{12}^{x}(\hat{X}, \hat{Y}, \alpha, \lambda)$ or $\hat{\sigma}_{12}^{y}(\hat{X}, \hat{Y}, \beta, \lambda)$, such that $(\alpha\hat{Q}, \beta\hat{S})$ is an equilibrium position for the negative monopole. By using Matlab, we still find three types of equilibria under various λ: $\hat{Q} = 0$, $\hat{Q} = 1/2$ and $\hat{Q} = \hat{Q}(\hat{S})$. In Fig. 6.8, the zero contours of σ_{12}^{+} are plotted for λ being 0.5 and 2.



(a) $\lambda = 0.5$ (b) $\lambda = 2$

Figure 6.8: Zero-contour of σ_{12}^{+} in $\hat{X}$-$\hat{Y}$ space: still three types of equilibria can be observed.

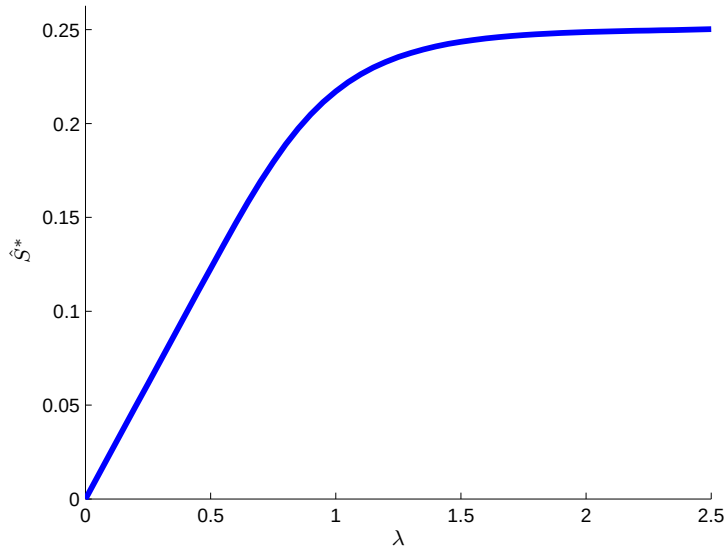


Figure 6.9: $\hat{S}^*$ against λ: $\hat{S}^*$ has an upper limit of 0.25. On the other hand, as $\lambda \to 0$, the system is equivalent to the case of one-dimensional array of dipoles. The slope at the origin is the critical value S^*.

For a given λ, there exists a maximum $\hat{S}^*(\lambda)$, only below which, the equilibrium of Type III occurs. In Fig. 6.9, $\hat{S}^*(\lambda)$ against λ is drawn. It is seen that $\hat{S}^*$ has an upper limit at 0.25. On the other hand, if we let $\lambda \to 0$ in Fig. 6.9, we have $\beta \to \infty$, which suggests that the rows of dipoles are well separated. Thus $\lambda \to 0$ should take us back to the case of one-dimensional array of dipoles. The critical value S^* in this scenario can be calculated by

$$S^* = \lim_{\beta \to \infty} \hat{S}^* \beta = \lim_{\lambda \to 0} \frac{\hat{S}^*}{\lambda}.$$

This suggests that in the plot of $\hat{S}^*$ against λ, as $\lambda \to 0$, $\hat{S}^* \to 0$, but the slope at the origin corresponds to the critical value S^* of the one-dimensional array of dipoles. It can be computed here that the slope is 0.2456, which is the same as the S^* from one-dimensional array of dipoles of p.146.

6.3.2 Stability Analysis

Stability of Three Types of Equilibria

As we did for unit square lattices, we then perform the linear stability analysis to the equilibrium states in rectangular lattices. Here, we still use the 'restoring force' of a

system defined by

$$f_r(Q,S;\alpha.\beta) = -\left.\frac{\partial\sigma_{12}^{+}(X,S;\alpha,\beta)}{\partial X}\right|_{X=Q} \tag{6.26}$$

as a metric of the stability.

By using (6.20) and (6.23), we obtain

$$\begin{aligned}\frac{\partial\hat{\sigma}_{12}^{x}(X/\alpha,\hat{S};\alpha,\lambda)}{\partial X} &= -\frac{\pi}{\alpha^2}\sum_{k=-4}^{4}\frac{2\pi(\hat{S}-k)\sinh\left(\frac{2\pi(\hat{S}-k)}{\lambda}\right)\cos\left(\frac{2\pi X}{\alpha}\right)}{\lambda\left(\cosh\left(\frac{2\pi(\hat{S}-k)}{\lambda}\right)-\cos\left(\frac{2\pi X}{\alpha}\right)\right)^2}\\ &+\frac{\pi}{\alpha^2}\sum_{k=-4}^{4}\left(\frac{\cosh\left(\frac{2\pi(\hat{S}-k)}{\lambda}\right)\cos\left(\frac{2\pi X}{\alpha}\right)-1}{\left(\cosh\left(\frac{2\pi(\hat{S}-k)}{\lambda}\right)-\cos\left(\frac{2\pi X}{\alpha}\right)\right)^2}+\frac{4\pi(\hat{S}-k)\sinh\left(\frac{2\pi(\hat{S}-k)}{\lambda}\right)\sin^2\left(\frac{2\pi X}{\alpha}\right)}{\lambda\left(\cosh\left(\frac{2\pi(\hat{S}-k)}{\lambda}\right)-\cos\left(\frac{2\pi X}{\alpha}\right)\right)^3}\right),\end{aligned} \tag{6.27}$$

and

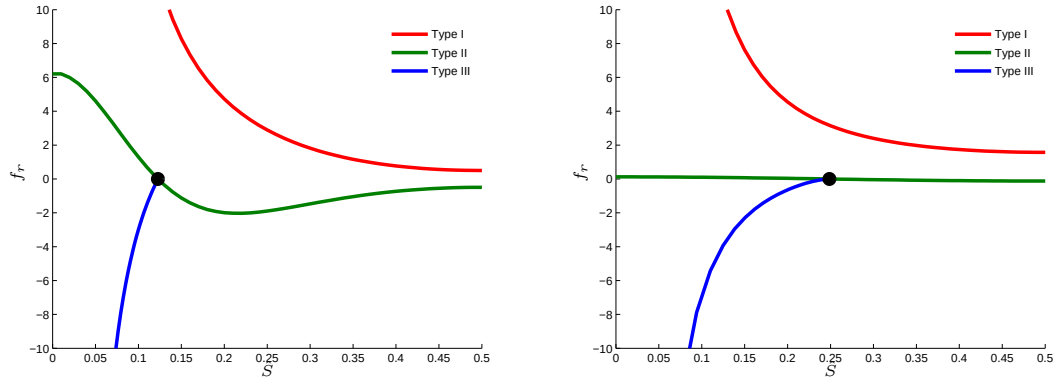
$$\begin{aligned}\frac{\partial\hat{\sigma}_{12}^{y}(X/\alpha,\hat{S};\beta,\lambda)}{\partial X} &= -\frac{\pi\lambda}{\beta}\sum_{k=-4}^{4}\frac{1-\cosh\left(2\pi\lambda\left(\frac{X}{\alpha}-k\right)\right)\cos\left(2\pi\hat{S}\right)}{\left(\cosh\left(2\pi\lambda\left(\frac{X}{\alpha}-k\right)\right)-\cos\left(2\pi\hat{S}\right)\right)^2}\\ &+\frac{2\pi^2\lambda^2}{\beta}\sum_{k=-4}^{4}\frac{\left(\frac{X}{\alpha}-k\right)\sinh\left(2\pi\lambda\left(\frac{X}{\alpha}-k\right)\right)\cos\left(2\pi\hat{S}\right)}{\left(\cosh\left(2\pi\lambda\left(\frac{X}{\alpha}-k\right)\right)-\cos\left(2\pi\hat{S}\right)\right)^2}\\ &+\frac{4\pi^2\lambda^2}{\beta}\sum_{k=-4}^{4}\frac{\left(\frac{X}{\alpha}-k\right)\left(1-\cosh\left(2\pi\lambda\left(\frac{X}{\alpha}-k\right)\right)\cos\left(2\pi\hat{S}\right)\right)\sinh\left(2\pi\lambda\left(\frac{X}{\alpha}-k\right)\right)}{\left(\cosh\left(2\pi\lambda\left(\frac{X}{\alpha}-k\right)\right)-\cos\left(2\pi\hat{S}\right)\right)^3},\end{aligned} \tag{6.28}$$

respectively. Then the restoring force f_r is calculated by

$$f_r(Q,S;\alpha,\beta) = \begin{cases} -\left.\dfrac{\partial\hat{\sigma}_{12}^{x}(X/\alpha,\hat{S};\alpha,\lambda)}{\partial X}\right|_{X=Q}, & \lambda\le 1;\\ -\left.\dfrac{\partial\hat{\sigma}_{12}^{y}(X/\alpha,\hat{S};\beta,\lambda)}{\partial X}\right|_{X=Q}, & \lambda>1. \end{cases} \tag{6.29}$$

Again, given an equilibrium type, Q can be expressed as a function of S or a constant, thus f_r against $\hat{S}$ can be plotted in Fig. 6.10. Unsurprisingly, the results of stability are the same as that in unit lattices:

- For Type I, it is always unstable;
- For Type II, it is stable when $\hat{S} > \hat{S}^*(\lambda)$;
- For Type III, it only exists when $\hat{S} \le \hat{S}^*(\lambda)$ and it is stable.



(a) $\lambda = 0.5$ (b) $\lambda = 2$

Figure 6.10: Stability in rectangular lattices.

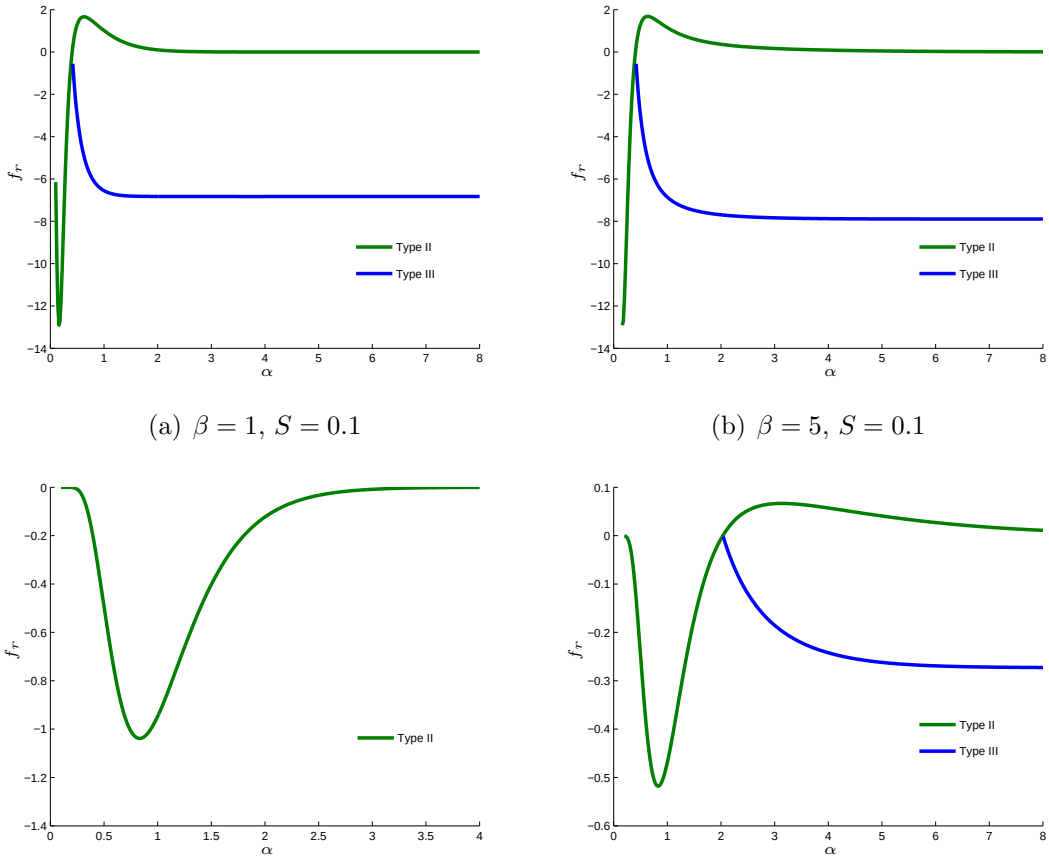
Stability of Equilibria Among All Rectangular Lattices

For a given pair of α and β, (Q, S) or $(\hat{Q}, \hat{S})$ can be calculated to identify the position of negative monopoles. The most striking observation is that there exists a bifurcation of stability in equilibrium types, which may be related to the transition from veins to PSBs. Recalling from Chapter 3, we know that the dislocation density in veins increases in the early stage of the fatigue test. Correspondingly in this model, it suggests that the cyclic loads multiply dislocations, resulting in a variation in cell structures (α and β). From this point of view, it is also sensible to compare the stability of equilibrium states among all rectangular lattices.

To quantify the 'comparison of stability', we still use $f_r(\hat{Q}, \hat{S}, \alpha, \beta)$ as our metric. Here we say System A is more stable than system B if f_r of A is less than that of B. Since $\hat{Q}$ can be expressed as a function of $\hat{S}$, α and β, depending on the type, for a specimen, the equilibrium state can be determined by $\hat{S}$, α and β.

Since these three parameters are still too many to do analysis, we start with the case when β and $\hat{S}$ are both fixed. In Fig. 6.11, how f_r behaves against α are drawn under different combinations of β and S. It can be seen that the bifurcation in equilibrium types takes places when $f_r = 0$ in (a), (b) and (d). It can also be observed that, f_r decreases with α. This suggests that these dipoles are trying to expel each other until their mutual force is unable to move them. This spacing should be linked with the spacing between rungs of PSBs.

Although the comparison of stability here may not have practical meaning, it does send a signal that the variation of cell structure induced by the density change in-



(a) $\beta = 1$, $S = 0.1$

(b) $\beta = 5$, $S = 0.1$

(c) $\beta = 1$, $S = 0.5$

(d) $\beta = 5$, $S = 0.5$

Figure 6.11: Comparison of stability under different combinations of β and S.

troduces instability of Type II. And the system will stabilise themselves by naturally adopting equilibrium of Type III.

6.4 Mechanism of the Formation of PSBs

Following the analogy of the natural transition from Type II to III with the formation of PSBs, we will give our explanation on the mechanism of the initiation of PSBs.

6.4.1 Evolution of Parameters under the Cyclic Loads

The dependence of f_r on (S, α, β) enables us to produce a manifold in S-α-β-f_r space. In the early stage of the fatigue test, the cyclic loads create paths on this manifold. A simplified example of this idea is shown in Fig. 6.12. Suppose S is a constant, then

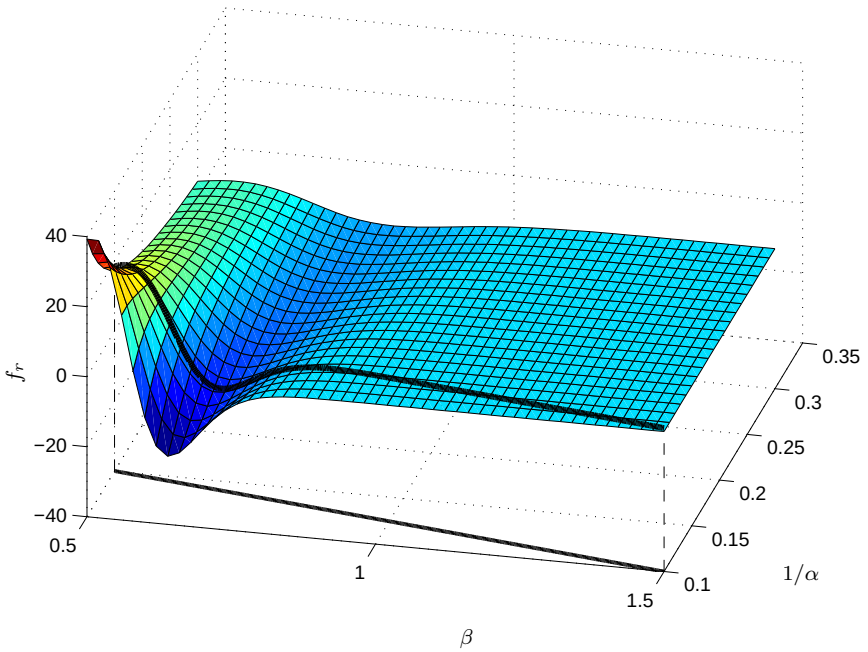


Figure 6.12: A simplified example of how dislocation multiplication influence the lattice stability: suppose S is a constant, then a surface can be drawn for f_r in $1/\alpha$-β space. Each point in the surface, satisfies $f_r = f_r(Q, S, \alpha, \beta)$. As the cyclic load proceeds, a paths in the parameter space is chosen by the process of dislocation multiplication. Then how f_r varies with the process can be identified on the surface.

a surface can be drawn for f_r in $1/\alpha$-β space. Each point in the surface, satisfies $f_r = f_r(Q, S, \alpha, \beta)$. As the cyclic load proceeds, a paths in the parameter space is chosen by the process of dislocation multiplication. Then how f_r varies with the process can be identified on the surface.

In another word, S, α and β all evolve with the dislocation multiplication which has been discussed in Chapter 3. If we assume it always has uniform density in veins or PSBs, then we can track the stability of the system by the following step:

$$\text{dislocation multiplication} \Rightarrow (S, \alpha, \beta) \Rightarrow f_r \Rightarrow \text{stability}$$

How (S, α, β) is determined by dislocation multiplication was discussed in Chapter 3. Qualitatively speaking, S and β should both decrease to accommodate newly generated edge characters. Here we assume that S and β drop in constant rates:

$$S = S_0 - u_S t \tag{6.30}$$

and

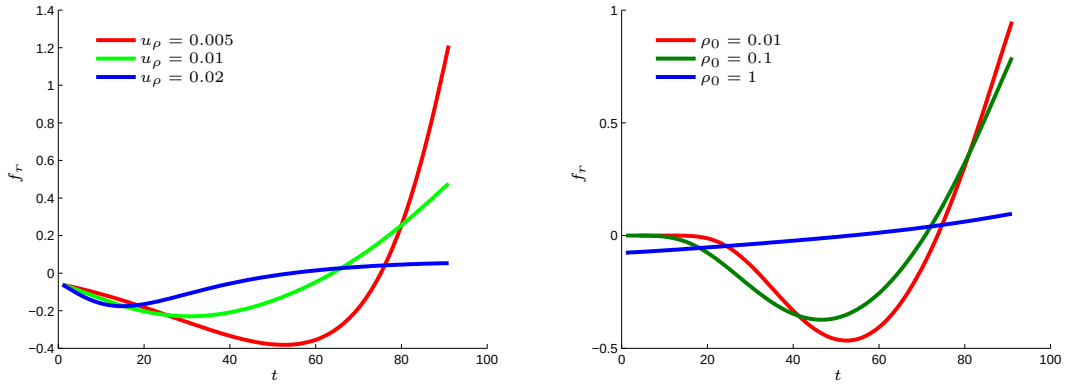
$$\beta = \beta_0 - u_\beta t. \tag{6.31}$$

The variation of α can be recorded via the dislocation density ρ. Without loss of generality, we refer to (6.15) to set $\rho = 1/(\alpha\beta)$. Here ρ is also assumed to grow in a constant rate u_ρ:

$$\rho = \rho_0 + u_\rho t, \tag{6.32}$$

where u_ρ should be an outcome from Chapter 3.

Therefore, all parameters can be expressed as a function given time t. Thus the evolution of f_r of Type II can be tracked. Such evolution is diagrammed in Fig. 6.13.



(a) (b)

Figure 6.13: Evolution into the instability as cyclic loads proceed: in (a), we start with $\rho_0 = 1$, and draw the evolution under different u_ρ; in (b), we start with different ρ_0, and draw the evolution under $u_\rho = 0.01$. Here, $\beta = 3 - 0.02t$ and $S = 1 - 0.01t$.

In both plots, we choose $\beta = 3 - 0.02t$ and $S = 1 - 0.01t$. In Fig. 6.13(a), we start with $\rho_0 = 1$, and draw the evolution under different u_ρ; in Fig. 6.13(a), we start with different ρ_0, and draw the evolution under $u_\rho = 0.01$. A key observation can be made that as the density increases with t, f_r becomes positive, giving rise to the instability of Type II. As this happens, dislocations start to form dipoles and the whole system becomes of Type III.

6.4.2 Formation of Dipole Walls

Based on these discussions, we give our explanation on the formation of PSBs in the early stage of the fatigue test as illustrated in Fig. 6.14.

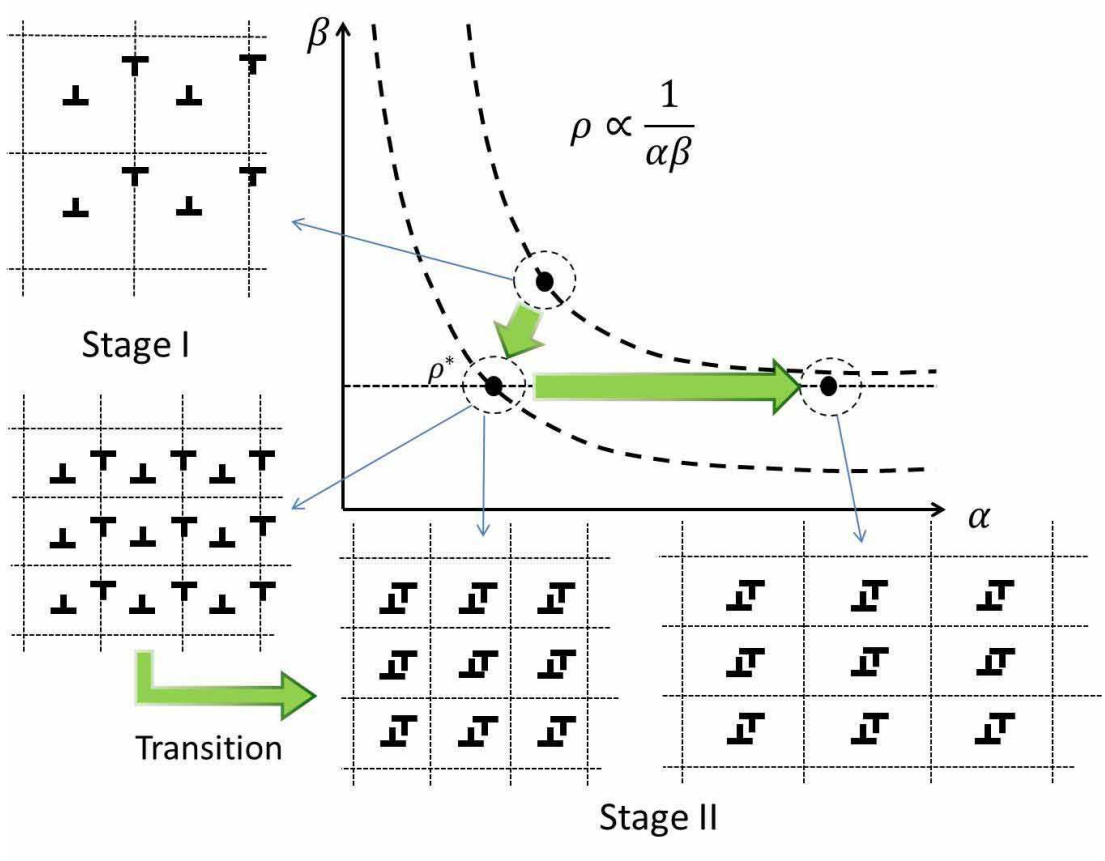


Figure 6.14: Mechanism of the formation of PSBs: In stage I, dislocations are sparsely distributed in veins of equilibrium Type II. As the cyclic loads proceed, the dislocations are multiplied. The result is a gradual reduction of β and S, accompanying with an increased density ρ. Such process raise the value of f_r, giving rise to a weakening of the stability of Type II. When the density rises to a critical value ρ^*, f_r reaches 0. Positive dislocations start to lock with negative dislocations to form dipole, and the system transits to equilibrium of Type III. In stage II, further dislocation multiplication will result in the cancelation of dislocations, leaving a row of dipole walls.

In stage I, dislocations are sparsely distributed in veins of equilibrium Type II. As the cyclic loads proceed, the dislocations are multiplied. The result is that a gradual reduction of β and S, accompanying with an increased density ρ. Such process raise the value of f_r, giving rise to a weakening of the stability of Type II. When the density rises to a critical value ρ^*, f_r reaches 0. Positive dislocations start to lock with negative dislocations to form dipole, and the system transits to equilibrium of Type III. In stage II, further dislocation multiplication will result in the cancelation of dislocations, leaving a row of dipole walls. The wall structure proposed here coincides with the results calculated by Neumann [43].

It should be mentioned that the mechanism of the formation of dipole walls proposed in stage II is still uncertain. As we will discuss in the next chapter, many other possible mechanisms of the formation of PSBs are also possible.

6.5 Comparisons to Experimental Data

Finally, we are going to compare our results with experimental data. Fig 6.15 is a diagram of the experimentally observed parameters of PSBs from Page 14 of [2].

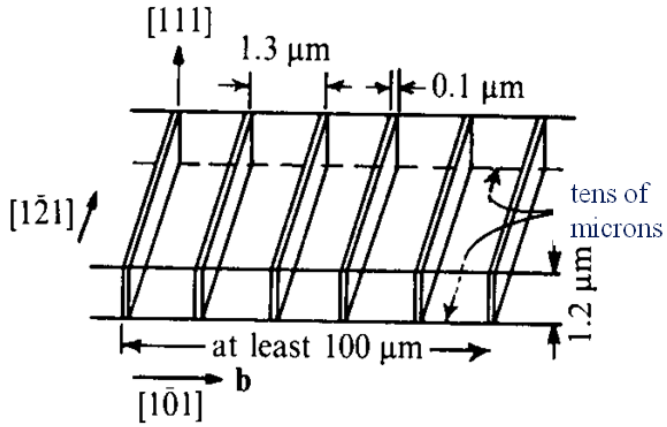


Figure 6.15: Parameters of PSBs.

To fit into our model, the rung spacing can be translated into α, which is 1.3μm. According to [6], the height of a vacancy dipole is $\sim$ 4nm. Therefore, $S = 4$nm. As we know, if $\alpha \gg \beta$, then the dipole will be stablised at 45°, i.e. $Q = S$. Here, we take $Q = S = 4$nm, and it can be seen later that this assumption is sensible. β can be calculated by using the fact that the dipole density in walls is $\sim 3 \times 10^{15}\text{m}^2$ [8]. We know that number of dislocations in one wall is

$$3 \times 10^{15}\text{m}^2 \times 4\text{nm} \times 1.2\mu\text{m} \approx 14.$$

This suggests there are about 14 cells along one rung, which is 1.2μm in height. Thus we have

$$\beta = \frac{1.2\mu\text{m}}{14} \approx 80\text{nm}.$$

It can be checked α is much larger than β in this scenario. Therefore, we give our prediction of the PSB configuration as shown in Fig. 6.16.

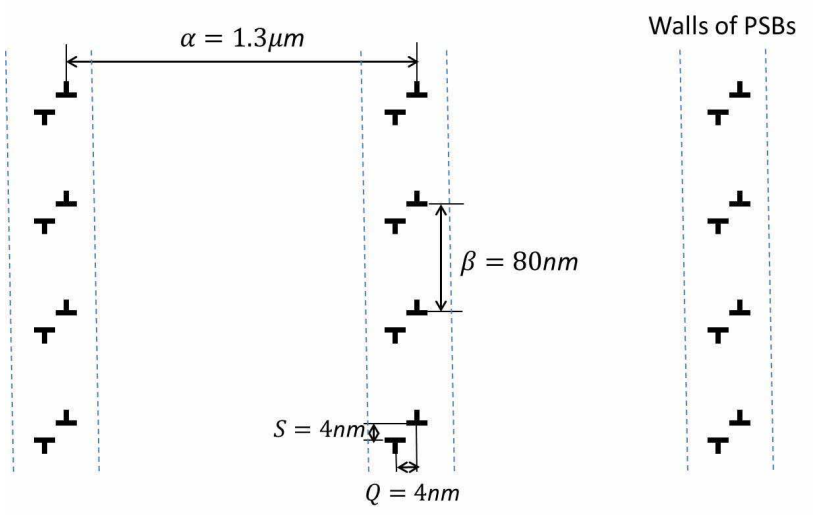


Figure 6.16: PSB configuration predicted from our model.

6.6 Conclusion

In this chapter, we have discussed the equilibrium states of dislocation dipoles throughout two-dimensional rectangular lattices. From the stability analysis, we found a natural instability existing in equilibria of Type II, which will transit the system to a more stable configuration of Type III. Based on these results, we attribute the formation of PSBs as the consequence of such instability induced by cyclic loads, followed by an interpretation of the rungs of PSBs as dipole walls. A comparison with the experimental data gives the configuration of PSBs from our model.

The dipole wall structure we discuss here may not be the actual configuration in materials, as many other structures have been raised to interpret PSBs. However, the geometric instability discussed in this chapter, does offer us some insights on the reason for the collapse of the channel-vein structures.

Chapter 7

Conclusions and Future Work

7.1 Conclusion

If the diagram in Fig. 1.17, which is redrawn as Fig. 7.1, is visited again now, I hope the points highlighted in it get consolidated. To understand the formation of PSBs

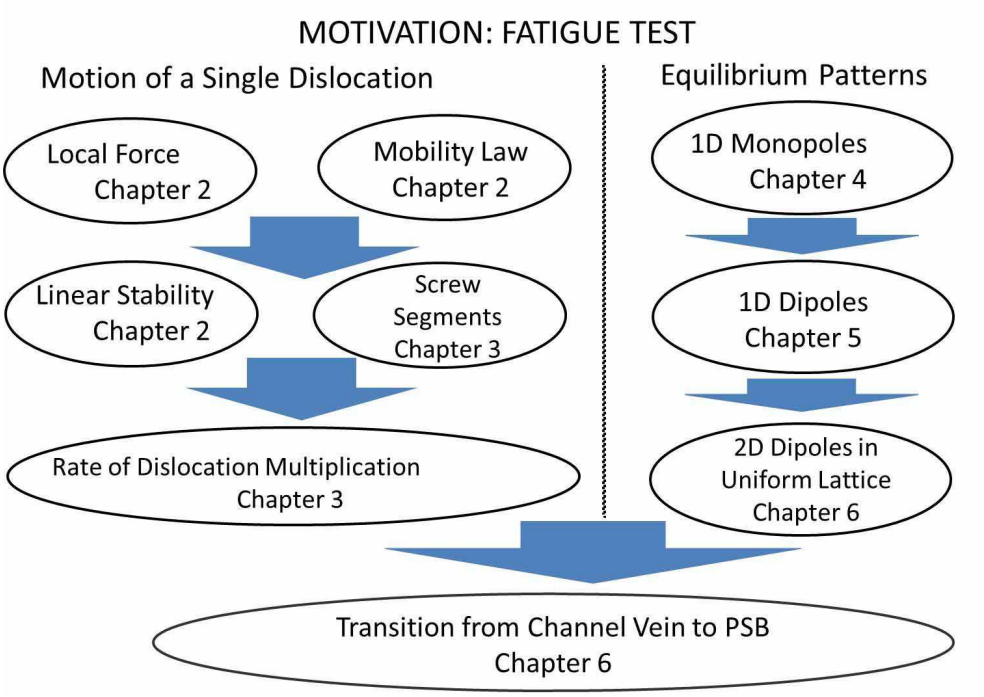


Figure 7.1: Outline of the thesis.

in the early stage of fatigue test, we consider the problem from two angles: motions of isolated dislocations and equilibria of a large number of straight dislocations.

The motion of curved dislocations are commonly regarded responsible for dislocation multiplication by acting as double cross-slip sources. In Chapter 2, a mobility law was proposed by smoothing the discrepant abilities to climb (or cross-slip) between edge and screw characters. This law of motion gives rise to the instability of almost screw dislocations, which were numerically justified afterwards. Further in Chapter 3, the screw segments connecting edge characters from different veins were also discussed. By using the travelling wave formulation, we have found a greater applied stress/strain increases the proportion of screw characters of screw characters, which are inclined to cross-slip under an anti-plane stress. Finally in this piece of work, a criterion for cross-slips were given aiming to estimate the rate of dislocation multiplications with an easy formula.

On the other hand, dislocation macroscopic density were also studied and a method using multiple scales was developed. Such a technique was firstly tested to the understanding of the collective behaviour of a row of dislocation monopoles in Chapter 4. Then the idea is generalised to the study of the pile-up of a row of dipoles against stress gradient in Chapter 5. Based on these observations, we further investigate the equilibrium pattern of dipoles and their stabilities in two-dimensional rectangular lattices.

Integrating all attempts mentioned above, we give our interpretation of the transition from veins to PSBs: the cyclic loads multiply dislocations through cross-slips, then a higher density triggers the system to stablise themselves by bifurcating from equilibria of Type II (vein structure) to Type III (dipole walls).

7.2 Further Work

With regard to the future work, extensions from results introduced in this thesis can be made from at least the following three aspects.

7.2.1 The Mechanism of Cross-slip Motions

The travelling wave formulation, along with the law of motion provides convincing results on properties of planar screw segments. However, we are still unable to track the path of screw segments under cyclic loads. In order to see the possible formation

of prismatic loops depicted in Fig. 3.2, several ingredients have to be added to the model.

Firstly the mechanism of the initiation of cross-slip motions is still not well-understood. For Fcc, this may involve partial dislocations and stacking faults (Chapter 10 of [33]). In this case, a term representing the anisotropy has to be added to the law of motion for screw characters.

The second possible change follows the previous one. As shown in Chapter 2, our law of motion will automatically pick up the best plane to resolve the stress as the primary slip plane. This property helps to avoid the time-consuming searching for glide planes, but the downside is that for some metals, FCC especially, the activated slip system is only from a finite set of planes. In this scenario, the crystallography has to be taken into consideration.

Also, a better numerical scheme will be helpful. The programme can be utilised either by adopting more stable temporal scheme (compared to the Runge-Kutta method in our simulation) or by an effective approach to redistribute nodes through the evolutions.

7.2.2 Density Distribution of Dipoles Throughout Two Dimensional Space

The second possible extension of the current work will be more from the angle of mathematics. The multiple-scale techniques we developed has proved to work fine to homogenise a row of dipoles. In theory this method can be generalised to investigate the two-dimensional dipolar distribution. However, due to the complexity and limitation of time, we did not have time to carefully consider such a generalisation.

Nevertheless, the successful implementation to the case of a row of dipoles boost the confidence of applying this technique to two-dimensional dipoles. Mathematically, if successful, this will be a continuation of the pioneering work by Head et al. on two-dimensional monopoles [30]. Practically, an equation describing density distribution may reveal some other ways of considering the formation of PSBs, such as the instability of the density distribution.

7.2.3 Elements in Walls of PSBs

In our models, we proposed that PSBs consist of dipole walls. But generally speaking, the elements in rungs of PSBs are still unknown experimentally. Moreover, results from our model do not coincide with the experimental data abstracted from Fig. 6.15. In our model, the horizontal spacing within a pair of dipole is calculated as 4nm, which should equal to the width of rungs of PSBs. Yet the experimental data shows that it is about 100nm. Such a big difference could be a matter of resolution. Or PSB rungs do not consist of exactly a column of dipoles. In the literature, there exist some other suggestions for the configuration of PSB walls. One is that the rung consists of multi-poles. These multi-poles discussed in [43] share the properties of dipoles but are more stable. Another possible configuration can be from [18] and [19], where PSBs consist of a series of prismatic loops. This suggestion, somehow does not contradict our model, based on our description of dipoles at an atomistic level in Fig. 1.11.

Since the lack of experimental evidence of PSB configuration, more work is needed to justify our proposal. One possible direction can be a comparison of the energy of a prismatic loop by atomic computation and that of a dipole to see the inter-relation of the two objects.

Appendix A

A.1 Derivation of (1.17)

The incompatibility tensor may be written in a more convenient form as follows ([17])

$$\begin{aligned}\eta_{ij} &= -\varepsilon_{ikl}\varepsilon_{jmn}e_{ln,km}\\ &= -\varepsilon_{ikl}\varepsilon_{jmn}(\varepsilon_{npr}\varepsilon_{rql}+\delta_{pq}\delta_{ln})\\ &= -(\delta_{jp}\delta_{mr}-\delta_{jr}\delta_{mp})(\delta_{ir}\delta_{kq}-\delta_{iq}\delta_{kr})e_{pq,km}-(\delta_{ij}\delta_{km}-\delta_{im}\delta_{kj})e_{pp,km}\\ &= e_{ij,kk}+e_{kk,ij}-(e_{ik,jk}+e_{jk,ik})+(e_{kl,kl}-e_{kk,ll})\delta_{ij}.\end{aligned}$$

A.2 Proof of $\boldsymbol{\chi}$ satisfying (1.49)

Again we follow [17] to prove that (1.49) always holds. Suppose we found a solution χ'_{ij} of (1.45) that does not yield (1.49). Then another function

$$\boldsymbol{\chi} = \boldsymbol{\chi'} + \frac{1}{2}(\nabla\boldsymbol{\phi} + (\nabla\boldsymbol{\phi})^T), \tag{A.1}$$

for some function, will then give the same value of $\boldsymbol{\sigma}$, from the face that

$$\nabla^T \wedge \nabla(\nabla\phi + (\nabla\phi)^T) = \mathbf{0}.$$

Now if (1.49) must hold for $\boldsymbol{\chi}$, then

$$\nabla\cdot\boldsymbol{\chi} + \frac{1}{2}(\nabla^2\boldsymbol{\phi} + \nabla(\nabla\cdot\boldsymbol{\phi})) = \vec{0},$$

from which we can obtain

$$\phi_i = -\frac{1}{8\pi}\int_{\mathbb{R}^3}\left(\chi'_{kl,l'}(\boldsymbol{x'})X_{,ik} - 2\chi'_{il,l'}(\boldsymbol{x'})X_{,kk}\right)\mathrm{d}V',$$

where $X = |\boldsymbol{x}-\boldsymbol{x'}|$. Since χ'_{ij} is known, we can calculate ϕ_i. We can then use to find a function $\boldsymbol{\chi}$ which satisfies (1.49).

A.3 Derivation of equation (2.26)

If the unit vector in the x_i direction is denoted by $\boldsymbol{e}_i$, then we have

$$\begin{aligned}
[\mathrm{d}\boldsymbol{q}\cdot(\boldsymbol{b}\wedge\nabla'(\boldsymbol{z}\otimes\boldsymbol{z}))]_{i,j} &= 2\left((\boldsymbol{z}\cdot\boldsymbol{e}_i)(\boldsymbol{b}\wedge\boldsymbol{e}_j)\cdot\mathrm{d}\boldsymbol{q}\right)^S \\
&= 2\left((\boldsymbol{z}\cdot\boldsymbol{e}_i)(b_n\boldsymbol{n}+b_m\boldsymbol{m}+b_l\boldsymbol{l})\wedge(n_j\boldsymbol{n}+m_j\boldsymbol{m}+t_j\boldsymbol{l})\cdot(\varepsilon\boldsymbol{l}+\varepsilon^2\boldsymbol{n}\kappa l)\mathrm{d}l\right)^S \\
&= 2\mathrm{d}l\left(z_i\left(\varepsilon(b_nm_j-b_mn_j)+\varepsilon^2\kappa l(b_mt_j-b_lm_j)\right)\right)^S \\
&= 2(\varepsilon b_n-\varepsilon^2b_l\kappa l)\mathrm{d}l(z_im_j)^S-2\varepsilon b_m\mathrm{d}l(z_in_j)^S+2\varepsilon^2b_m\kappa l\mathrm{d}l(z_it_j)^S,
\end{aligned}$$

where ^{S} denotes the symmetric part and n_j, m_j, t_j and z_j are the j-th entries of the corresponding vectors. The final line is (2.26) in component form.

A.4 Derivation of equation (2.46)

For there to exist non-zero solutions of the linear system (2.45) the determinant of the matrix must vanish, so that

$$(\lambda+c_1k^2)^2(\lambda+c_2k^2)^2+2a_{12}a_{21}(\lambda+c_1k^2)(\lambda+c_2k^2)k^2+a_{22}^2(\lambda+c_1k^2)k^2+a_{12}^2a_{21}^2k^4=0.$$

Completing the square gives

$$\left((\lambda+c_1k^2)(\lambda+c_2k^2)+a_{12}a_{21}k^2\right)^2+a_{22}k^2(\lambda+c_1k^2)^2=0, \tag{A.2}$$

so that

$$(\lambda+c_1k^2)(\lambda+c_2k^2)+a_{12}a_{21}k^2=\mp\mathrm{i}a_{22}k(\lambda+c_1k^2),$$

where $\mathrm{i}^2=-1$. Now collecting powers of λ gives

$$\lambda^2+\left((c_1+c_2)k^2\pm\mathrm{i}a_{22}k\right)\lambda+c_1c_2k^4+a_{12}a_{21}k^2\pm\mathrm{i}a_{22}c_1k^3=0.$$

The solutions for λ are therefore

$$\lambda=\frac{1}{2}\left(-(c_1+c_2)k^2\mp\mathrm{i}a_{22}k\pm\sqrt{\Delta}\right), \tag{A.3}$$

where

$$\Delta=(c_1-c_2)^2k^4-(a_{22}^2+4a_{12}a_{21})k^2\pm2\mathrm{i}a_{22}(c_2-c_1)k^3. \tag{A.4}$$

Now observing that, for real x and y,

$$(x+\mathrm{i}y)^{1/2}=\frac{1}{\sqrt{2}}\left(\sqrt{\sqrt{x^2+y^2}+x}+\mathrm{i}\sqrt{\sqrt{x^2+y^2}-x}\right), \tag{A.5}$$

we find that the real part of λ is given by

$$\begin{aligned}\mathrm{Re}(\lambda) &= -\frac{(c_1+c_2)k^2}{2} \\ &\quad \pm\frac{k}{2\sqrt{2}}\Bigg(\sqrt{(c_1-c_2)^4k^4+2(c_1-c_2)^2(a_{22}^2-4a_{12}a_{21})k^2+(a_{22}^2+4a_{12}a_{21})^2} \\ &\qquad\qquad +(c_1-c_2)^2k^2-(a_{22}^2+4a_{12}a_{21})\Bigg)^{1/2}.\end{aligned}$$

Substituting for c_1, c_2, a_{12}, a_{21} and a_{22} leads to (2.46).

A.5 Derivation of the dispersion relation of (2.53)

The slightly simpler system of (2.52) means that we can determine the stability criterion and maximal growth rate explicitly. From it, we can obtain a quartic equation for λ as

$$(\lambda+c_1k^2)^4+(a_{22}^2+2a_{12}a_{21})k^2(\lambda+c_1k^2)^2+a_{12}^2a_{21}^2k^4=0.$$

By using $\Gamma=(\lambda+c_1k^2)^2/k^2$, we can reduce the quartic equation the quadratic

$$\Gamma^2+(a_{22}^2+2a_{12}a_{21})\Gamma+a_{12}^2a_{21}^2=0. \tag{A.6}$$

If $\Delta=a_{22}^2+4a_{12}a_{21}$ is positive then the discriminant of (A.6) is positive, so the two roots of (A.6) are real. Since $a_{12}^2a_{21}^2>0$ and

$$a_{22}^2+2a_{12}a_{21}=\frac{1}{2}\left(a_{22}^2+4a_{12}a_{21}\right)+\frac{a_{22}^2}{2}>0,$$

both roots must be negative. Then the real part of λ is $-c_1k^2$, so the dislocation is stable.

If $\Delta<0$, then we can express the 2 roots of (A.6) by

$$\Gamma_\pm=\frac{-(a_{22}^2+2a_{12}a_{21})\pm\mathrm{i}\sqrt{-a_{22}^2(a_{22}^2+4a_{12}a_{21})}}{2}.$$

Using (A.5) we then find

$$\Re(\lambda)=-c_1k^2+\frac{k}{2}\sqrt{-a_{22}^2-4a_{12}a_{21}}. \tag{A.7}$$

Maximising over k we obtain

$$\Re(\lambda)_{\max}=-\frac{(a_{22}^2+4a_{12}a_{21})}{16c_1}.$$

Substituting for c_1, a_{12}, a_{21} and a_{22} gives the results quoted in (2.53).

A.6 Derivation of (2.64)

We are looking for a unit vector $\boldsymbol{\beta}$ to maximise

$$(\sigma_{\text{ext}}\boldsymbol{b}) \cdot \boldsymbol{\beta} \tag{A.8}$$

subjected to

$$\boldsymbol{\beta} \cdot \boldsymbol{b} = 0. \tag{A.9}$$

For our computation, $\boldsymbol{b} = (b_1, 0, b_3)^T$ and the two nonzero components of $\boldsymbol{\sigma}_{\text{ext}}$ are σ_{13} and σ_{23}. Thus from (A.9), we obtain

$$\beta_3 = -s\beta_1, \tag{A.10}$$

where $s = b_1/b_3$. Since $\boldsymbol{\beta}$ is a unit vector, combining (A.10) gives

$$s^2\beta_1^2 + \beta_2^2 = 1,$$

which implies that trigonometric functions can be used:

$$\beta_1 = \frac{\cos\theta}{s}, \qquad \beta_2 = \sin\theta. \tag{A.11}$$

Incorporating (A.10) and (A.11) with (A.8) gives

$$(\sigma_{\text{ext}}\boldsymbol{b}) \cdot \boldsymbol{\beta} = \frac{\sigma_{13}}{1+s^2}\left(p\sqrt{1+s^2}\sin\theta + (1-s^2)\cos\theta\right), \tag{A.12}$$

where $p = \sigma_{23}/\sigma_{13}$. We know the right hand side of (A.12) is maximised, when

$$\theta = \frac{\pi}{2} - \arctan\left(\frac{1-s^2}{p(1+s^2)}\right). \tag{A.13}$$

Plugging this θ into (A.10) and (A.11) gives (2.64).

A.7 Proof of (4.52)

Here, we are solving an equation for $G(x, X, Y)$ with X periodic:

$$\left((B'(x))^2 \cdot \frac{\partial^2}{\partial X^2} + \frac{\partial^2}{\partial Y^2}\right) G(x, X, Y) = \delta(X)\delta(Y). \tag{A.14}$$

As mentioned before, the left hand side of the above equation is in the similar form as the Laplacian operator for any fixed x. Actually, by defining

$$\tilde{X} = X, \qquad \tilde{Y} = B'(x)Y, \tag{A.15}$$

we can transform (A.14) into

$$\left(\frac{\partial^2}{\partial\tilde{X}^2}+\frac{\partial^2}{\partial\tilde{Y}^2}\right)\tilde{G}(x,\tilde{X},\tilde{Y})=\frac{1}{B'(x)}\cdot\delta(\tilde{X})\delta(\tilde{Y}), \tag{A.16}$$

with $\bar{X}$ periodic of 1, where $\tilde{G}(x,\tilde{X},\tilde{Y})=G(x,X,Y)$. The δ-function in the right hand side of (A.16) suggests that, when $(\tilde{X},\tilde{Y})\to(0,0)$, we should have

$$\tilde{G}(x,\tilde{X},\tilde{Y})\sim\frac{1}{4\pi B'(x)}\log\left(\tilde{X}^2+\tilde{Y}^2\right).$$

Hence, if transformed back to the (x,X,Y) coordinates, $G(x,X,Y)$ should has the approximation that

$$G(x,X,Y)\sim\frac{1}{4\pi B'(x)}\log\left(X^2+B'(x)Y^2\right),$$

as $(X,Y)\to(0,0)$.

Furthermore, to preserve periodicity for $G(x,X,Y)$, we can assume placing an image dislocation at each $(X,Y)=(k,0)$, $k\in\mathbb{Z}$, $k\neq 0$. Then $G(x,X,Y)$ should be expressed as combination of stress function by all dislocations (image or real):

$$G(x,X,Y)\sim\frac{1}{4\pi B'}\sum_{k\in\mathbb{Z}}\log\left((X-k)^2+B'^2Y^2\right). \tag{A.17}$$

This way of summation ensures the periodicity in the dislocation source. However, the above series does not converge. To obtain a convergent series, we take the derivative of (A.17) with respect to Y on its both sides and interchange the sum and derivative:

$$\begin{aligned}\frac{\partial G}{\partial Y}&\sim\frac{1}{2\pi}\sum_{k\in\mathbb{Z}}\frac{B'Y}{(X-k)^2+B'^2Y^2}\\&=-\frac{\mathrm{i}}{4\pi}\left(\Psi^{(0)}(1-\bar{Z})-\Psi^{(0)}(1-Z)+\Psi^{(0)}(Z)-\Psi^{(0)}(\bar{Z})\right)\\&=\frac{\mathrm{i}(\cot\pi Z-\cot\pi\bar{Z})}{4}\\&=\frac{\sinh(2\pi B'Y)}{2(\cosh(2\pi B'Y)-\cos 2\pi X)},\end{aligned} \tag{A.18}$$

where $\Psi^{(0)}$ is the diGamma function (detailed in [1]);

$$Z=X+\mathrm{i}Y;$$

$\bar{Z}$ is Z's conjugate. Integrating (A.18) with respect to Y gives

$$G(x,X,Y)=\frac{1}{4\pi B'}\log\left(\cosh(2\pi B'Y)-\cos(2\pi X)\right). \tag{A.19}$$

It can be checked that $G(x, X, Y)$ is one solution to (A.14). All solutions to (A.14) should have the form that

$$\hat{G}(x, X, Y) = G(x, X, Y) + g_1(x) + Y g_2(x), \tag{A.20}$$

where g_1 and g_2 are both arbitrary functions of x.

By using (A.20), we know that

$$\varphi^{(2)}_{\text{in}}(x, X, Y) = \frac{1}{4\pi} \log \left(\cosh(2\pi B'Y) - \cos(2\pi X)\right) + c^{(2)}_{\text{in}}(x) + Y h^{(2)}_{\text{in}}(x),$$

which gives (4.52).

A.8 Proof of (4.107)

We are looking for the solution of an equation of $G(x, X, Y)$:

$$\left((B')^2 \cdot \frac{\partial^2}{\partial X^2} + \frac{\partial^2}{\partial Y^2}\right)^2 G(x, X, Y) = \delta(X)\delta'(Y),$$

with $G(x, X, Y)$ periodic in X and all its second derivatives bounded. Similar as in Appendix 1, if we change the coordinates by

$$\tilde{X} = X, \qquad \tilde{Y} = B'Y,$$

The equation is transformed to

$$\left(\frac{\partial^2}{\partial \tilde{X}^2} + \frac{\partial^2}{\partial \tilde{Y}^2}\right)^2 \tilde{G}(x, \tilde{X}, \tilde{Y}) = \frac{1}{(B')^2} \cdot \delta(\tilde{X})\delta'(\tilde{Y}),$$

where $\tilde{G}(x, \tilde{X}, \tilde{Y}) = G(x, X, Y)$. It is well known that the local behaviour of the Green's function of a biharmonic equation should be like

$$\frac{(\tilde{X}^2 + \tilde{Y}^2)}{8\pi} \log\left(\tilde{X}^2 + \tilde{Y}^2\right),$$

as $(\tilde{X}, \tilde{Y}) \to (0, 0)$. Then taking derivative with respect to $\tilde{Y}$ and multiplied by the coefficient $1/(B')^2$ gives the local behaviour of $\tilde{G}(x, \tilde{X}, \tilde{Y})$

$$\tilde{G}(x, \tilde{X}, \tilde{Y}) \sim \frac{\tilde{Y}}{4\pi(B')^2} \log\left(\tilde{X}^2 + \tilde{Y}^2\right),$$

as $(\tilde{X}, \tilde{Y}) \to (0, 0)$. In the (x, X, Y) space, we have

$$G(x, X, Y) \sim \frac{Y}{4\pi B'} \log\left(X^2 + (B')^2 Y^2\right),$$

near the origin.

To preserve periodicity, we assume the expression for $G(x, X, Y)$ in terms of a divergent series:

$$G(x, X, Y) \sim \frac{Y}{4\pi B'} \sum_{k\in\mathbb{Z}} \log\left((X-k)^2 + (B')^2 Y^2\right).$$

Differentiating the above series with respect to Y twice, we have

$$\begin{aligned}
\frac{\partial^2 G}{\partial Y^2} &= \frac{B'Y}{2\pi} \sum_{k\in\mathbb{Z}} \frac{3(X-k)^2 + B'^2Y^2}{((X-k)^2 + B'^2Y^2)^2} \\
&= \frac{\mathrm{i}B'}{4\pi}\left(\psi^{(0)}(-Z) + \psi^{(0)}(1+\bar{Z}) - \psi^{(0)}(-\bar{Z}) - \psi^{(0)}(1+Z)\right) \\
&\quad + \frac{B'^2Y}{8\pi}\left(\psi^{(1)}(-Z) + \psi^{(1)}(1+\bar{Z}) + \psi^{(1)}(-\bar{Z}) + \psi^{(1)}(1+Z)\right) \\
&= \frac{\mathrm{i}B'}{4\pi}\left(\cot(\pi\bar{Z}) + \cot(\pi Z)\right) + \frac{\pi B'^2(Y-\eta)}{8}\left(\csc^2(\pi Z) + \csc^2(\pi\bar{Z})\right) \\
&= \frac{B'\sinh(2\pi B'Y)}{2(\cosh(2\pi B'Y) - \cos(2\pi X))} + \frac{\pi B'^2 Y(1 - \cosh(2\pi B'Y)\cos(2\pi X))}{2(\cosh(2\pi B'Y) - \cos(2\pi X))^2},
\end{aligned} \tag{A.21}$$

where

$$Z = X + \mathrm{i}B'Y.$$

Integrating the (A.21) with respect to Y twice gives one expression for $G(x, X, Y)$

$$G(x, X, Y) = \frac{Y}{8\pi B'} \log\left(\cosh(2\pi B'Y) - \cos(2\pi X)\right).$$

It can be checked that $G(x, X, Y)$ is an solution to (4.106). Moreover, we know that any solution of (4.106) should have the form that

$$G(x, X, Y) + f_1(x) + f_2(x)Y.$$

A.9 Derivation of (4.123)

If we are given an equation for u yielding

$$\Delta^2 u = 0, \qquad \text{in } y \neq 0, \tag{A.22}$$

with all its second derivatives vanishing at infinity. Across the x axis, we have the jump condition:

$$\lim_{y\to 0^{\pm}} \frac{\partial^2 u}{\partial x^2} = 0; \tag{A.23}$$

$$\lim_{y\to 0^{\pm}} \frac{\partial^2 u}{\partial x \partial y} = 0; \tag{A.24}$$

$$\lim_{y\to 0^{\pm}} \frac{\partial^2 u}{\partial y^2} = \pm g(x). \tag{A.25}$$

Firstly, by combining (A.23) and (A.25), we write down an equation for Δu:

$$\begin{cases} \Delta\left(\Delta u\right) = 0; \\ \lim\limits_{y\to 0^{\pm}} \Delta u = \pm g(x); \\ \lim\limits_{|\boldsymbol{x}|\to\infty} \Delta u = 0. \end{cases} \tag{A.26}$$

By using the plemelj formulae, we obtain

$$\Delta u = \frac{1}{\pi}\int_{-K}^{K} \frac{g(x')y\mathrm{d}x'}{(x-x')^2+y^2}. \tag{A.27}$$

This suggests that

$$u = \frac{1}{4\pi}\int_{-1}^{1} y\log((x-x')^2+y^2)g(x')\mathrm{d}x' + a + bx + cy + dxy,$$

where a, b, c and d are all constants.

Then we have

$$\frac{\partial^2 u}{\partial x \partial y} = \frac{1}{\pi}\int_{-1}^{1} \frac{(x-x')((x-x')^2-y^2)g(x')\mathrm{d}x'}{((x-x')^2+y^2)^2} + d.$$

Since the applied stress at infinity is σ_{ext}, then we have $d = \sigma_{\text{ext}}$.

By using the matching condition (A.24), we finally have

$$\frac{1}{2\pi}\int_{-1}^{1} \frac{g(x')\mathrm{d}x'}{x-x'} + \sigma_{\text{ext}} = 0, \tag{A.28}$$

which is (4.123) if we replace $g(x')$ by $B'(x')$.

A.10 The Calculation of χ_F

We are trying to solve (5.71)

$$\left(B'^2\frac{\partial^2}{\partial X^2} + \frac{\partial^2}{\partial Y^2}\right)^2 \chi_F = -\frac{\partial \mathcal{L}\chi_{\text{in}}^{(3)}}{\partial X},$$

with periodic boundary condition in X.

Because near singularities $\chi_{\text{in}}^{(3)}$ behaves the same as $K^{(3)}$ in (5.43). Then from (5.74), we know when approaching the singularities, for example $(X,Y)\to(0,0)$, χ_F should behave like K_F in (5.76):

$$\chi_F \sim \frac{B''(x)XY(X^2-B'(x)^2Y^2)}{8\pi B'^2\left(X^2+B'(x)^2Y^2\right)}. \tag{A.29}$$

Then we have

$$\frac{\partial^2\chi_F}{\partial X^2}Y \sim \frac{B''(x)(X^6+9X^4B'^2Y^2-9X^2B'^4Y^4-B'^6Y^6)}{8\pi B'^2\left(X^2+B'^2Y^2\right)^3}. \tag{A.30}$$

Hence we assume

$$\frac{\partial^2\chi_F}{\partial X\partial Y} \sim \sum_{k=-\infty}^{\infty}\left(\frac{\partial^2 K_F}{\partial X\partial Y}(x,X-k,Y)-\frac{\partial^2 K_F}{\partial X\partial Y}(x,X-Q^{(0)}-k,Y-S)\right),$$

to preserve periodicity.

This can be computed term by term

$$\sum_{k=-\infty}^{\infty}\frac{B'^2(X-k)^4Y^2}{((X-k)^2+B'^2Y^2)^3} = \frac{3\mathrm{i}B'Y}{16}\mathcal{A}+\frac{5B'^2Y^2}{16}\mathcal{B}+\frac{\mathrm{i}B'^3Y^3}{16}\mathcal{C},$$

where

$$\begin{aligned}
\mathcal{A} &= \Psi^{(0)}(-X-\mathrm{i}B'Y)+\Psi^{(0)}(1+X-\mathrm{i}B'Y)\\
&\quad -\Psi^{(0)}(-X+\mathrm{i}B'Y)-\Psi^{(0)}(1+X+\mathrm{i}B'Y)\\
&= -\frac{2\mathrm{i}\pi\sinh(2\pi B'Y)}{\cosh(2\pi B'Y)-\cos(2\pi X)};\\
\mathcal{B} &= \Psi^{(1)}(-X-\mathrm{i}B'Y)+\Psi^{(1)}(1+X-\mathrm{i}B'Y)+\Psi^{(1)}(-X+\mathrm{i}B'Y)\\
&\quad +\Psi^{(1)}(1+X+\mathrm{i}B'Y)\\
&= \frac{4\pi^2(1-\cosh(2\pi B'Y)\cos(2\pi X))}{(\cosh(2\pi B'Y)-\cos(2\pi X))^2};\\
\mathcal{C} &= -\Psi^{(2)}(-X-\mathrm{i}B'Y)-\Psi^{(2)}(1+X-\mathrm{i}B'Y)\\
&\quad +\Psi^{(2)}(-X+\mathrm{i}B'Y)+\Psi^{(2)}(1+X+\mathrm{i}B'Y)\\
&= \frac{4\mathrm{i}\pi^3\sinh(2\pi B'Y)(1-\cos(4\pi X)-2\cosh(2\pi B'Y)\cos(2\pi X))}{(\cosh(2\pi B'Y)-\cos(2\pi X))^3},
\end{aligned}$$

where $\Psi^{(i)}$ are the PolyGamma functions.

Also

$$\sum_{k=-\infty}^{\infty}\frac{B'^2(X-k)^4Y^2}{((X-k)^2+B'^2Y^2)^3} = \frac{\mathrm{i}B'Y}{16}\mathcal{A}-\frac{B'^2Y^2}{16}\mathcal{B}-\frac{\mathrm{i}B'^3Y^3}{16}\mathcal{C};$$

$$\sum_{k=-\infty}^{\infty}\frac{B'^2(X-k)^4Y^2}{((X-k)^2+B'^2Y^2)^3}=\frac{3\mathrm{i}B'Y}{16}\mathcal{A}-\frac{3B'^2Y^2}{16}\mathcal{B}+\frac{\mathrm{i}B'^3Y^3}{16}\mathcal{C}.$$

Due to divergence, the sum of

$$\mathcal{H}:=\sum_{k=-\infty}^{\infty}\frac{(X-k)^6}{((X-k)^2+B'^2Y^2)^3}$$

is more complicated. Since

$$\frac{\partial\mathcal{H}}{\partial Y}\sim-\sum_{k=-\infty}^{\infty}\frac{6B'^2(X-k)^6Y}{((X-k)^2+B'^2Y^2)^4},$$

we have

$$\begin{aligned}\mathcal{H}&\sim-6B'^2\int Y\sum_{k=-\infty}^{\infty}\frac{(X-k)^6Y}{((X-k)^2+B'^2Y^2)^4}\mathrm{d}Y\\&\sim-\frac{15\mathrm{i}B'Y}{16}\mathcal{A}-\frac{3B'^2Y^2}{4}\mathcal{B}-\frac{\mathrm{i}B'^3Y^3}{16}\mathcal{C}.\end{aligned}$$

Then we obtain

$$\begin{aligned}\frac{\partial^2G_F}{\partial X\partial Y}&\sim\sum_{k=-\infty}^{\infty}\frac{(X-k)^6+9B'^2(X-k)^4Y^2-9B'^4(X-k)^2Y^4-Y^6}{((X-k)^2+B'^2Y^2)^3}\\&\sim3B'^2Y^2\mathcal{B}+\mathrm{i}B'^3Y^3\mathcal{C}.\end{aligned}\tag{A.31}$$

Integrating the above identity with respect to X and Y sequentially, gives

$$G_F=-Y^3B'^2\left(\cot(\pi(X+\mathrm{i}B'Y)+\cot(\pi(X-\mathrm{i}B'Y))\right)=-\frac{2\pi Y^3B'^2\sin(2\pi X)}{\cosh(2\pi B'Y)-\cos(2\pi X)}.\tag{A.32}$$

Therefore,

$$\begin{aligned}\chi_F&=\frac{B''}{8\pi B'^2}\left(G_F(x,X,Y)-G_F(x,X-Q^{(0)},Y-S)\right)\\&=-\frac{B''Y^3\sin(2\pi X)}{4\pi(\cosh(2\pi B'Y)-\cos(2\pi X))}+\frac{B''(Y-S)^3\sin(2\pi(X-Q^{(0)}))}{4\pi(\cosh(2\pi B'(Y-S))-\cos(2\pi(X-Q^{(0)}))}.\end{aligned}\tag{A.33}$$

The next step is to check whether χ_F in (A.33) is the solution for (5.71). Firstly, we can integrate (A.33) with respect to X to obtain

$$I_F=\int G_F(x,X,Y)\mathrm{d}Y=-B'^2Y^3\log\left(\cosh(2\pi B'Y)-\cos(2\pi X)\right).\tag{A.34}$$

Then it can be checked that

$$\begin{aligned}\tilde{\nabla} I_F &= -\frac{48\pi B'^3 \sinh(2\pi B'Y)}{\cosh(2\pi B'Y)-\cos(2\pi X)} - \frac{96\pi^2 Y B'^4(1-\cosh(2\pi B'Y)\cos(2\pi X))}{(\cosh(2\pi B'Y)-\cos(2\pi X))^2} \\ &= -96\pi B'^3\left(\frac{\partial^2 G}{\partial Y^2} - B'^2\frac{\partial^2 G}{\partial X^2}\right).\end{aligned}$$

Finally, combining (5.71) gives

$$\left(B'^2\frac{\partial^2}{\partial X^2}+\frac{\partial^2}{\partial Y^2}\right)^2 \chi_F = -\frac{\partial \mathcal{L}\chi_{\text{in}}^{(3)}}{\partial X}.$$

A.11 Proof of (6.8)

From (6.6) and (6.7), the difference between $\tilde{\sigma}_{12}$ and σ_{12}^+ can be expressed by

$$|\tilde{\sigma}_{12}-\sigma_{12}^+| = \sum_{k=k_0}^{\infty}\left|\frac{\sin(2\pi X)}{\cosh(2\pi(Y-k))-\cos(2\pi X)} - \frac{2\pi(Y-k)\sin(2\pi X)\sinh(2\pi(Y-k))}{(\cosh(2\pi(Y-k))-\cos(2\pi X))^2}\right|.$$

By using

$$\begin{aligned}\cosh(2\pi(Y-k))-\cos(2\pi X) &\geq \cosh(2\pi(k-1/2))-1 \\ &\geq \frac{e^{2\pi(k-1/2)}}{2}-1 > \frac{e^{3\pi k/2}}{2}\end{aligned}$$

and

$$(Y-k)\sinh(2\pi(Y-k)) \leq \frac{2k-1}{4}\cdot e^{2\pi k},$$

we can do the estimation that

$$\begin{aligned}|\tilde{\sigma}_{12}-\sigma_{12}^+| &\leq \sum_{k=k_0}^{\infty}\left|\frac{\sin(2\pi X)}{\cosh(2\pi(Y-k))-\cos(2\pi X)} - \frac{2\pi(Y-k)\sin(2\pi X)\sinh(2\pi(Y-k))}{(\cosh(2\pi(Y-k))-\cos(2\pi X))^2}\right| \\ &\leq 2e^{-3\pi/4}\sum_{k=k_0}^{\infty}e^{-3\pi k/2} + 4\pi e^{-\pi}\sum_{k=k_0}^{\infty}ke^{-\pi k} + 2\pi e^{-\pi}\sum_{k=k_0}^{\infty}e^{-\pi k}\end{aligned}$$

for any $k_0 \geq 1$.

Since

$$\begin{aligned}\sum_{k=k_0}^{\infty}ke^{-\pi k} &= -\frac{1}{\pi}\sum_{k=k_0}^{\infty}\frac{\mathrm{d}e^{-\pi kt}}{\mathrm{d}t}\bigg|_{t=1} \\ &= -\frac{1}{\pi}\frac{\mathrm{d}}{\mathrm{d}t}\left(\frac{e^{-\pi k_0 t}}{1-e^{-\pi t}}\right)\bigg|_{t=1} = \frac{k_0 e^{-k_0\pi}}{1-e^{-\pi}} + \frac{e^{-(k_0+1)\pi}}{(1-e^{-\pi})^2},\end{aligned}$$

we have

$$|\tilde{\sigma}_{12} - \sigma_{12}^{+}| \leq \frac{2e^{-3\pi/4} \cdot e^{-3\pi k_0/2}}{1 - e^{-3\pi/2}} + \frac{k_0 e^{-(\pi+1)k_0}}{1 - e^{-\pi}} + \frac{e^{-(k_0+2)\pi}}{(1 - e^{-\pi})^2} + \frac{2e^{-(k_0+1)\pi}}{(1 - e^{-\pi})^2}$$
$$\leq \frac{(k_0 + 5)e^{-(k_0+1)\pi}}{(1 - e^{-\pi})^2},$$

which agrees with (6.8).

Bibliography

[1] M. Abramowitz and I. Stegun. *Handbook of Mathematical Functions with Formulas, Graphs, and Mathematical Tables*. Denvor, 1964.

[2] J. Ahmed. *A Study of Fatigue in Single Crystal Copper using Electron Channelling Contrast Imaging*. DPhil thesis, University of Oxford, 1998.

[3] J. Ahmed, A. J. Wilkinson, and S. G. Roberts. Electron channelling contrast imaging characterization of dislocation structures associated with extrusion and intrusion systems and fatigue cracks in copper single crystals. *Philosophical Magazine a-Physics of Condensed Matter Structure Defects and Mechanical Properties*, 81(6):1473–1488, 2001.

[4] M. Ainsworth and J. Oden. *A posteriori error estimation in finite element analysis*. Wiley, New York, 2000.

[5] O. Alvarez, P. Hoch, Y. Le Bouar, and R. Monneau. Dislocation dynamics: Short-time existence and uniqueness of the solution. *Archive for Rational Mechanics and Analysis*, 181(3):449–504, 2006.

[6] J. G. Antonopoulos, L. M. Brown, and A. T. Winter. Vacancy dipoles in fatigued copper. *Philosophical Magazine*, 34(4):549–563, 1976.

[7] M. Arndt and M. Luskin. Analysis of a force-based quasicontinuum approximation. *Math. Model. Numer. Anal.*, 42:113–139, 2008.

[8] Z. S. Basinski and S. J. Basinski. Fundamental-aspects of low amplitude cyclic deformation in face-centered cubic-crystals. *Progress in Materials Science*, 36:89–148, 1992.

[9] J. L. Bassani. Plastic-flow of crystals. *Advances in Applied Mechanics, Vol 30*, 30:191–258, 1994.

[10] P. Biler, G. Karch, and R. Moneau. Nonlinear diffusion of dislocation density and self-similar solutions. *Commun. Maths. Phy.*, 196:71–96, 2010.

[11] V. Bulatov and W. Cai. *Computer simulations of dislocations*. Oxford University Press, 2006.

[12] J. Burgers. Some considerations of the field of stress connected with dislocations. *Proc. Kon. Ned. Acad. Wet.*, 47:239–325, 1939.

[13] S. Cacace and A. Garroni. A multi-phase transition model for dislocations with interfacial microstructure. *Interfaces and Free Boundaries*, 11(2):291–316, 2009.

[14] R. Cahn. Slip and polygonization in aluminium. *J. Inst. Met.*, 79:129–158, 1951.

[15] J. Chang, W. Cai, V. Bulatov, and S. Yip. Dislocation motion in bcc metals by molecular dynamics. *Mater. Sci. and Eng. A*, 309-310:160–163, 2001.

[16] S. J. Chapman and G. Richardson. Motion of vortices in type-Ii superconductors. *Siam Journal on Applied Mathematics*, 55(5):1275–1296, 1995.

[17] A. de Wit. The continuum theory of stationary dislocations. *Solid State Phys.*, 10:249–292, 1960.

[18] C. Depres, C. F. Robertson, and M. C. Fivel. Low-strain fatigue in aisi 316l steel surface grains: a three-dimensional discrete dislocation dynamics modelling of the early cycles - 1. dislocation microstructures and mechanical behaviour. *Philosophical Magazine*, 84(22):2257–2275, 2004.

[19] C. Depres, C. F. Robertson, and M. C. Fivel. Low-strain fatigue in 316l steel surface grains: a three dimension discrete dislocation dynamics modelling of the early cycles. part 2: Persistent slip markings and micro-crack nucleation. *Philosophical Magazine*, 86(1):79–97, 2006.

[20] J. D. Eshelby, F. C. Frank, and F. R. N. Nabarro. The equilibrium of linear arrays of dislocations. *Philosophical Magazine*, 42(327), 1951.

[21] U. Essmann, U. Goesele, and H. Mughrabi. A model of extrusions and intrusions in fatigued metals - i. point-defect production and the growth of extrusions,. *Phil. Mag. A*, 44:405–426, 1981.

[22] S. Frederekson and K. Jacobsen. Density functional theory studies of screw dislocation core structures in bcc metals. *Philo. Mag.*, 83:365–375, 2003.

[23] J. Grosskreutz and H. Mghrabi. *Constitutive equations in plasticity.* Cambridge, Massachusetts: MIT Press, 1975.

[24] C. L. Hall, S. J. Chapman, and J. R. Ockendon. Asymptotic analysis of a system of algebraic equations arising in dislocation theory. *Siam Journal on Applied Mathematics*, 70(7):2729–2749, 2010.

[25] A. Head and N. Louat. The distribution of dislocations in linear arrays. *Aust.J.Physics*, 8:1–7, 1955.

[26] A. K. Head. Dislocation group dynamics .1. similarity solutions of body problem. *Philosophical Magazine*, 26(1):43–53, 1972.

[27] A. K. Head. Dislocation group dynamics .2. general solutions of body problem. *Philosophical Magazine*, 26(1):55–63, 1972.

[28] A. K. Head. Dislocation group-dynamics .6. release of a pile-up. *Philosophical Magazine*, 27(3):531–539, 1973.

[29] A. K. Head, S. D. Howison, J. R. Ockendon, and S. P. Tighe. An equilibrium-theory of dislocation continua. *Siam Review*, 35(4):580–609, 1993.

[30] A. K. Head, S. D. Howison, J. R. Ockendon, J. B. Titchener, and P. Wilmott. A continuum model for two-dimensional dislocation distributions. *Philosophical Magazine a-Physics of Condensed Matter Structure Defects and Mechanical Properties*, 55(5):617–629, 1987.

[31] A. K. Head and W. W. Wood. Dislocation group-dynamics .4. general solutions of continuum approximation. *Philosophical Magazine*, 27(3):505–517, 1973.

[32] A. K. Head and W. W. Wood. Dislocation group-dynamics .5. equilibrium revisited. *Philosophical Magazine*, 27(3):519–530, 1973.

[33] J. Hirth and J. Lothe. *Theories of Dislocations.* Krieger, 1982.

[34] P. Howell, C. Kozyreff, and J. Ockendon. *Applied solid mechanics,.* Cambridge University Press, 2009.

[35] D. Hull and D. Bacon. *Introduction to Dislocations.* Elsevier Ltd., 2011.

[36] G. Jiang and D. Peng. Weighed ENO schemes for Hamilton-Jacobi equations. *SIAM J. Sci. Comp.*, 21(6):2126–2143, 2000.

[37] W. Johnston and J. Gilman. Dislocation velocities, dislocation densities and plastic flow in lithium fluoride crystals. *J. Appl. Phys.*, 30:129–144, 1959.

[38] M. Kanninen and A. Rosenfield. Dynamics of dislocation pile-up formation. *Phil. Mag.*, 20:569–587, 1969.

[39] M. Koslowski, A. M. Cuitino, and M. Ortiz. A phase-field theory of dislocation dynamics, strain hardening and hysteresis in ductile single crystals. *Journal of the Mechanics and Physics of Solids*, 50(12):2597–2635, 2002.

[40] E. Kroener. Kontinnuumstheorie der bersetzungen und eigenspannungen. *Springer, Berlin*, 1958.

[41] J. Li. Petch relation and grain boundary sources. *Z. Phys.*, 135:239–247, 1953.

[42] N. Mott. The mechanical properties of metals. *Proc. Phys. Soc. B*, 64:729–742, 1951.

[43] P. Neumann. Low-energy dislocation configurations - a possible key to the understanding of fatigue. *Materials Science and Engineering*, 81(1-2):465–475, 1986.

[44] H. Ockendon and J. R. Ockendon. Dynamic dislocation pile-ups. *Philosophical Magazine a-Physics of Condensed Matter Structure Defects and Mechanical Properties*, 47(5):707–719, 1983.

[45] J. Ockendon, S. Howison, A. Lacey, and A. Movchan. *Applied Partial Differential Equations*. Oxford University Press, 2003.

[46] E. Orowan. Zur kristallplastizitat iii. *Z. Phy.*, 89:634–659, 1934.

[47] C. Ortner and E. Süli. Analysis of quasicontinuum method in one dimension. *Math. Model. Numer. Anal.*, 42:57–91, 2008.

[48] M. Peach and J. Koehler. The forces excerted on dislocations and the stress fields produced by them. *Phys. Rev.*, 80:436–439, 1950.

[49] M. Polanyi. Uber eine art gitterstorung, die einen kristall plastisch machen konnte. *Z. Phy.*, 89:660–664, 1934.

[50] G. Richardson. Instability of a superconducting line vortex. *Physica D*, 110:139–153, 1997.

[51] A. Rosenfield. A continuous distribution of moving dislocations. *Phil. Mag.*, 24:63–69, 1971.

[52] N. Simon, E. Drexler, and R. Reed. Properties of copper and copper alloys at cryogenic temperatures. *US National Institute of Standards and Technology (USA)*, page 850, 1992.

[53] D. F. Stein and J. R. Low. Mobility of edge dislocations in silicon-iron crystals. *Journal of Applied Physics*, 31(2):362–369, 1960.

[54] S. Suresh. *Fatigue of Materials*. Cambridge University Press, 1996.

[55] E. B. Tadmor, M. Ortiz, and R. Phillips. Quasicontinuum analysis of defects in solids. *Philosophical Magazine a-Physics of Condensed Matter Structure Defects and Mechanical Properties*, 73(6):1529–1563, 1996.

[56] E. B. Tadmor, R. Phillips, and M. Ortiz. Mixed atomistic and continuum models of deformation in solids. *Langmuir*, 12(19):4529–4534, 1996.

[57] G. Taylor. The mechanism of plastic deformation of crystals. part i.-theoretical. *Proc. R. Soc. London*, 145:362–387, 1934.

[58] S. Tighe. *Macroscopic Dislocation Modelling*. DPhil thesis, University of Oxford, 1992.

[59] V. Vitek, A. Mrovec, R. Groger, J. L. Bassani, V. Racherla, and L. Yin. Effects of non-glide stresses on the plastic flow of single and polycrystals of molybdenum. *Materials Science and Engineering a-Structural Materials Properties Microstructure and Processing*, 387:138–142, 2004.

[60] R. E. Voskoboinikov, S. J. Chapman, J. R. Ockendon, and D. J. Allwright. Continuum and discrete models of dislocation pile-ups. i. pile-up at a lock. *Journal of the Mechanics and Physics of Solids*, 55(9):2007–2025, 2007.

[61] Y. Xiang, L. T. Cheng, D. J. Srolovitz, and W. N. E. A level set method for dislocation dynamics. *Acta Materialia*, 51(18):5499–5518, 2003.